WIND-TUNNEL MEASUREMENTS
IN THE WAKES OF STRUCTURES

H. G. C. Woo, J. A. Peterka,
and J. E. Cermak

1. REPORT NO. NASA CR-2806	2. GOVERNMENT ACCESSION NO.	3. RECIPIENT·ง ᴄᴀⲧᴬᴸᴼᴳ ...
4 TITLE AND SUBTITLE Wind Tunnel Measurements in the Wakes of Structures		5. REPORT DATE March 1977
		6. PERFORMING ORGANIZATION CODE
7. AUTHOR(S) H. G. C. Woo, J. A. Peterka, and J. E. Cermak		8. PERFORMING ORGANIZATION REPORT # M-210
9. PERFORMING ORGANIZATION NAME AND ADDRESS Colorado State University Fort Collins, Colorado 80523		10. WORK UNIT NO.
		11. CONTRACT OR GRANT NO. NAS8-29583
12. SPONSORING AGENCY NAME AND ADDRESS National Aeronautics and Space Administration Washington, D. C. 20546		13. TYPE OF REPORT & PERIOD COVERED Contractor
		14. SPONSORING AGENCY CODE

15. SUPPLEMENTARY NOTES

16. ABSTRACT

This report presents detailed measurements of longitudinal mean velocity, turbulence intensity, space correlations, and spectra made in the wake of two rectangular scaled models in simulated atmospheric boundary-layer winds. The model buildings were 1:50 scale models of two trailers for which corresponding field measurements are being made at the NASA, George C. Marshall Space Flight Center.

Results of a flow visualization study of the wake geometry are analyzed with some singular point theorems. Two hypothetical flow patterns of the detailed wake geometry are proposed.

Some preliminary studies of the vortex wake, effects of the model size, model aspect ratios, and boundary layer characteristics on the decay rate and extent of the wake are also presented and discussed.

17. KEY WORDS	18. DISTRIBUTION STATEMENT Cat 47

19. SECURITY CLASSIF. (of this report) Unclassified	20. SECURITY CLASSIF. (of this page) Unclassified	21. NO. OF PAGES 243	22. PRICE $8.00

*For sale by the National Technical Information Service, Springfield, Virginia 22161

FOREWORD

AUTHORS' ACKNOWLEDGMENTS

TABLE OF CONTENTS

TABLE OF CONTENTS (continued)

LIST OF TABLES

LIST OF FIGURES

LIST OF FIGURES (continued)

LIST OF SYMBOLS

Symbol	Definition
[A]	Matrix defined in equation (4.4)
A, B, n	Hot-film anemometer calibration constants
B	Surface of the obstacle
D	Depth of obstacle
D*	Characteristic length of the obstacle
E	Mean anemometer bridge voltage
E_{rms}	Root-mean-square anemometer bridge voltage
H	Height of obstacle
I	Unit matrix
J	Defined in equation (4.6)
K_1, K_2	Constant
L_B	The line where the obstacle meets the base plane
L_x, L_y, L_z	Integral length scales of turbulence in x, y, and z directions
m	Decay rate of mean velocity defect and turbulent excess
n	Mean velocity power-law exponent of boundary layer
N, S	Noddle and Saddle point
N', S'	Node and Saddle of streamline pattern on the surface
P	Plane of the base plate
Re	Reynolds number $Re = \dfrac{U(H)H}{2}$
S	Short tower
T	Tall tower
U	Mean velocity in x direction

U_{rms}	Root-mean-square of longitudinal velocity fluctuation
ΔU	Mean velocity defect $\Delta U = U_o - U$
u, v, w	Perturbation velocities in x, y, and z direction
w	Mean velocity in z direction
W	Width of obstacle
x, y, z	Space coordinates (x-streamwise, y-lateral, z-vertical)

Subscripts

o	Values in undisturbed approach flow
∞	Value outside the boundary layer
(H)	Values at one model height
e	Effective (Z_e = effective roughness length)

Greek Symbols

α	Approach wind direction
δ	Boundary-layer thickness
$\vec{\epsilon}$	Shear line vector
ϵ_x, ϵ_y	Shear stress component in x and y direction
θ	Angle between the shear vector and the x axis
λ, λ_1, λ_2	Constants
ν	Kinematic viscosity
Δ	Defined in equation (4.6)

Chapter 1

INTRODUCTION

In recent years, the number of heliports located within urban areas has increased substantially. Those heliports are frequently located where wind disturbances generated by nearby structures influence the characteristics of the wind at the landing site. As V/STOL technology advances contributing to increased popularity of small general aviation aircraft an increase in the number of small landing facilities near cities can be expected. Because small aircraft are highly sensitive to turbulence and rapid changes in wind speed, wind disturbances caused by nearby buildings may have important influences on the usability of these landing facilities. Large airports are finding increasingly larger structures built on or adjacent to the airport. The wind disturbance caused by the presence of a large hangar on at least one major airport has caused concern by pilots of commercial aircraft on final approach.

High among the environmental factors that affect aircraft performance, and hence their safety margin, are the characteristics of ambient wind incident on the aircraft. Wakes generated by buildings or other obstacles are generally characterized by increased turbulence, a mean velocity defect, and under certain conditions by organized, discrete, standing vortices. With sudden changes of mean velocity, high levels of turbulence, and with the possibility of encountering strong organized vorticity, an aircraft flying in the wake of large buildings could be subjected to large pitching or rolling moments and deterioration of aircraft control. In order to determine the

severity of safety problems related to building-wake winds and their impact on aircraft operational characteristics, the detailed characteristics of these wakes must be known. Also, if the extent to which the buildings and other obstacles near an airport affect the wind conditions can be established, then critical situations can be related to the meteorological variables such as wind speed and wind direction, so that forecasts can be made.

There are additional areas in which knowledge of building-wake structures are important. The effects of nearby buildings on wind loads imposed on a structure represent an important consideration in the design of a building. Local pressure loadings may be either increased or decreased due to the presence of a nearby building. The nature of the wind loading change depends on the overall building shapes, separation distances, and on their relative position in the approaching wind. In order to assess a structure's vulnerability to the effects of a nearby building, a specification of the building wake characteristics is required.

Diffusion of pollutants released in the wake of a building or natural obstacle will be strongly influenced by the wake characteristics. In particular, if the pollutant is released within the separation region in the lee of an obstacle or if the wake contains strong organized vorticity, the predictive model for diffusion must include the effect of these wake characteristics. Pedestrian comfort near buildings, in parks, or in plazas are all frequently influenced by the characteristics of the wind downwind from buildings.

Wakes generated by buildings or other obstacles are generally characterized, as mentioned above, by increased turbulence, mean velocity defect, and in certain situations by organized, strong vortices with axes generally parallel to the main flow direction. Under certain circumstances, however, the wake may involve mean velocity excess or turbulence defects. The wake generated by a three-dimensional surface-mounted protuberance in a turbulent boundary layer is highly three-dimensional. The characteristics of the wake (the extent of the momentum wake, the strength and extent of the vortex wake, the rate of decay of excesses and defects in the wake, etc.) are highly dependent on the overall structure height, the aspect ratio of the structure, the shape (projecting corners, step structure, round portions, etc.), approaching wind azimuth, character of the surrounding terrain (height and density of buildings and other structures, extent of vegetation and nearby topography, etc.), and in some cases the stability of the approaching wind flow. For these reasons, a simple description or generalization of building wakes does not appear to be possible.

Until recently the characteristics of building wakes have received little attention and therefore very little has been known about even the most basic characteristics of the wake behind a three-dimensional rectangular building exposed to the turbulent, planetary, boundary-layer wind. The high cost of instrumentation and data acquisition and restricted data potential of field studies have limited prototype investigations. The possibility that sufficient field information will be obtained to lead to adequate understanding and development of

theoretical or empirical models of wakes seems remote. The three-dimensionality of the problem has hindered analytical approaches also. Only recently have boundary layer wind tunnels, which have the capability of simulating atmospheric winds, been used in the study of building wakes in detail.

The formulation of a reliable prediction method for the likely flow pattern around a complex of buildings presents a severe challenge. The problem involves the interaction between a planetary turbulent boundary layer and the distribution of many shapes and sizes of buildings added with the complication that one building may be in the wake of another or that the wakes of several buildings may undergo some mutual interaction. Presently the only realistic solution to the problem is through wind tunnel experiments.

Colorado State University has had extensive experience in modeling atmospheric flow. Three large wind tunnels designed especially for modeling atmospheric flows have been constructed in the Fluid Dynamics and Diffusion Laboratory. A great deal has been published concerning the use of wind tunnels in simulating planetary boundary-layer flows and the many applications of wind tunnels to wind engineering problems. The reader may refer to a review paper in 1975 by Cermak (1) which deals extensively with the verifications between wind-tunnel and full-scale studies that have been performed. The great advantage of wind tunnel modeling over prototype studies is the large amount of data which can be obtained at low cost.

This current investigation has concentrated on wind-tunnel measurements of the flow around, and wake structures of, three-dimensional

structures of different aspect ratio submerged in a simulated atmospheric boundary layer. The studies have concentrated on defining the overall geometric structure and some other characteristics of the wakes. The studies have also been directed toward confirming the wind tunnel simulation criteria by obtaining data for comparison of laboratory and field measurements.

Most of the model studies were performed in the meteorological wind tunnel in the Fluid Dynamics and Diffusion Laboratory. This tunnel has the capability of simulating neutral, stable or unstable stratified flows. Some further descriptions of the wind tunnels used in the studies and instrumentations to perform the necessary measurements of the wakes behind obstacles will be given in Chapters 3 and 4.

Model studies in the wind tunnels have yielded: (1) substantial information about the overall geometry structure of the wake of a three-dimensional rectangular obstacle, (2) mean velocities, longitudinal turbulence intensities, two-point correlations, longitudinal energy spectra, and some vortex measurements in the wakes of two scaled models of the trailers used in the field measurements taken at the Marshall Space Flight Center, Aerospace Environment Division, Eight-Tower Atmospheric Boundary Layer Facility located in Huntsville, Alabama, (3) some information concerning the effect of the approach flow characteristics, the effects of the ratio of boundary layer thickness to model height, building height to width, building depth to width, building height to depth, and the angle of approach on the extent of the wake and the decay of mean velocity defect and turbulence defect and turbulence excess for some selected three-dimensional blocks.

In Chapter 2, a survey of related studies of the wakes is presented. The techniques used in obtaining and analyzing the experimental data and the wind tunnel test program are described in Chapter 3. In Chapter 4, techniques used in the flow visualization study are described. Based on the results and "critical point" (or singular point) analysis, a hypothesis of the detailed wake geometry is discussed. Chapter 5 presents the results and discussion of the wind tunnel measurements. In Chapter 6, some conclusions and recommendations are made.

Chapter 2

LITERATURE SURVEY

2.1 Introduction

The problem of how a turbulent boundary layer responds when it is subjected to two-dimensional or three-dimensional protuberances is highly complicated. With the present knowledge about turbulent flow, theoretical efforts must, to a great extent, rely on experimental observation and measurement. Three-dimensional wake flows, in particular, must rely heavily on experimental studies.

Considerably more work has been done to study the influence of two-dimensional surface obstacles on turbulent boundary layers than has been done for three-dimensional obstacles. Since the available information directly applicable to the characteristics of building wakes is extremely limited, additional insight can be gained from related studies such as three-dimensional free wakes and wall jets. Theoretical efforts and wind tunnel tests also provide additional guidance in the understanding of wake geometry and mechanism. The intent of this chapter is to survey and draw together related studies in these major areas.

2.2 Prototype Measurements

As has been pointed out above, little information about building wakes has been obtained from prototype measurements due primarily to the high cost of instrumentation and data acquisition and long time requirements.

The first major efforts to examine wakes of obstacles placed in a planetary boundary layer were probably the extensive field and wind tunnel measurements of the effects of windbreaks and shelterbelts.

An excellent review of the extensive literature on the effects of windbreaks and shelterbelts with a voluminous bibliography can be found in a technical note published by the World Meteorological Organization (2). This report is a summary of knowledge of effects of windbreaks and shelterbelts on microclimate, soil-climate, crop-climate, and related areas. Some of the general observations presented in this report should apply qualitatively to the study of building wakes. Of prime interest to the present investigation of building wakes was the confirmation of two factors--the roughness of soil surface and the stability of the air influencing the wind reduction by shelterbelts. The extent of wind reduction increases with decreasing surface roughness and with increasing air stability. Also of interest was the finding that the ratio of the length to the height of a shelterbelt must be at least 11.5 (with wind direction normal to the shelterbelt) if sheltering effects similar to an infinitely long belt, that is two-dimensional characteristics, were to be achieved. This report also revealed that the wind speed near the surface in the lee regains energy and momentum from the strong displacement flow (free shear layer) and that the faster the recovery, the greater the vertical wind gradient and the stronger the displacement flow. Validity of the flow characteristics was determined by measurements both in the wind tunnel and in the prototype.

Only recently have efforts been made to study the structure and other characteristics of full-scale building wakes. Measurements in the wake of a hangar at the Royal Aircraft Establishment at Bedford reported by M. J. Colmer (3) are the best field data available to date. The measurements were performed on a plateau which was fairly flat for

about 800 meters (2600 ft) upwind from the hangar. The hangar was 30 m (98 ft) long, 15 m (49 ft) wide, 10 m high and had a roof pitch of 10°. Although the hangar was isolated from other buildings, there were some airport structures reported upwind of the hangar and to the side of the approach wind vector which were approximately 200 m (650 ft) from the hangar. The sizes of these airport buildings were not mentioned in the report. There was a possibility that the hangar might have been in the meandering edge of the wake of these buildings. This may have contributed to the low frequency lateral motion of the approach wind flow mentioned in the report. Three instrumented towers are located at 5H, 14H, and 23H downwind along the centerline and one tower was located at 5H downwind and approximately 5H to the side of the centerline where H refers to the building height. In addition, a tower 18H upwind of the hangar was used to measure the approach wind conditions. The planetary boundary layer mean velocity profile had a power-law exponent of 0.18 and the thickness of the boundary layer was estimated in the report to be about 600 meters (2000 ft) (although about half that value would seem more likely for that site). Thus the ratio of the hangar height to the thickness of the boundary layer was only 1/60. The turbulence intensity (rms divided by U_∞) of the undisturbed flow at one hangar height was about 0.09. All three components of mean and fluctuating velocities in the wake at different heights were measured. From these data, turbulence intensities, auto-correlations and spectra were calculated. Only one case of experimental measurements which lasted 40 minutes was reported. Although no general conclusion could be drawn due to the limited quantity of data and thus the poor resolution of the general characteristics of the wake, this report did bring to light some interesting features of the wake flow.

From this particular field study, Colmer found that at one building
height the mean wind speed in the wake measured at 5H downstream was
substantially reduced from the undisturbed value. However, this mean
windspeed defect decayed rapidly and was nearly zero at 14H downstream.
At 23H downstream and 3H above the ground the mean windspeed was found
to be slightly less than the upstream value. This, as Colmer con-
cluded, showed that the wake diffused upwards as it moved downstream
and therefore the influence of the building would be more noticeable
higher up than near the ground. At 14H and 23H downstream, the
turbulence intensities were still different from the undisturbed value
by a larger factor than the mean windspeed defects. That is, the
turbulence intensity excess in the wake decayed more slowly than the
mean velocity defect. This finding confirms the theoretical prediction
by Hunt and Smith (42) which shall be discussed in section 2.7. The
power spectra and autocorrelation function results show that there is
more energy change closer to the ground and that the wake contains
smaller eddies than in the upstream flow. This effect is also greatest
near the ground. An interesting feature in this report is the finding
of regular lateral oscillations of the whole wake. In this particular
study, it was likely that this oscillation was due to the fluctuation
of the lateral component upstream and may be due to the wakes of the
buildings upwind and to the side of the approach wind. However, Colmer
commented that it was possible that the wake could oscillate due to some
other factor, such as the sudden change of separation point at the edge
of the building.

Several tower and flight measurements were made in the lee of a
group of buildings by Cass, Scoggins, and Chevalier (4) at a former

Air Force Base in Texas. Some general observations were made during the course of the study. The insufficient resolution of the measurement grid and the complexity of the surroundings had severely restricted the drawing of detailed conclusions about the characteristics of building wakes. An increase in turbulence levels and a decrease in mean velocities were noted when a sensor was in an anticipated wake region. It was also noted that the wake spread upward as it moved downstream. A correlation between gusts measured by tower mounted anemometers and vertical accelerations measured by aircraft mounted accelerometers was established.

Limited diffusion measurements were made in the lee of a building by Munn and Cole (5). Although diffusion data can help to some extent to establish geometry and mixing characteristics of wakes, their results were difficult to interpret primarily due to the presence of adjacent buildings.

A field measuring program is currently in progress at the NASA George C. Marshall Space Flight Center in Huntsville, Alabama to measure wake properties of small rectangular buildings. The two building shapes for which field data was obtained were rectangular structures approximately 3.25 m (10.7 ft) high and 2.44 m (8.0 ft) deep with lengths normal to the approach wind direction of 7.9 m (26.0 ft) and 26.8 m (87.9 ft). A report of these measurements is not yet available. Some preliminary data were presented in a paper at the Second U.S. National Conference on Wind Engineering Research (6). Detailed wind tunnel measurements of the wakes of the two building configurations studied in the field program are presented in this report as part of this investigation. Additional details of the field site will be given in section 3.7.

2.3 Related Flows

Several theoretical approaches have been used in an effort to un-
derstand and model three-dimensional wakes in a uniform approach flow
or three-dimensional jets in either a uniform flow or attached to a
wall. In addition, results from experiments and analysis relating to
three-dimensional free wakes and jets and to wall jets have provided
guidance for a theoretical understanding of wall wakes.

Steiger and Bloom (7,8) have examined theoretically the velocity
fields of three-dimensional viscous wakes with uniform approach flow.
Similarity solutions were obtained for general types of initial
condition with the use of the boundary layer approximation, Oseen's
linearization of the convective terms, and the assumption of constant
fluid properties for the governing equations. A similar study for
three-dimensional turbulent free wakes having elliptical cross section
have also been carried out both experimentally and analytically by
Kuo and Baldwin (9) in 1966. Constant-fluid-property, zero-pressure-
gradient, uniform approach flow were assumed. By assuming a constant
eddy diffusivity in the transverse plane but variable along the wake
centerline, an analytical solution for wake diffusion and decay in the
far-wake region were obtained from a linearized momentum equation. The
analysis predicted that the wake evolved downstream toward an
axisymmetric shape and was confirmed experimentally. In earlier
papers, Steiger and Bloom (7,8) had predicted the tendency toward
axisymmetric configurations in the far wake region by similar analytical
procedures.

Experiments to measure the characteristics of three-dimensional, turbulent, incompressible free jets were described by Sforza, Steiger and Trentacoste (10) and Trentacoste and Sforza (11). They concluded that free jets tend to a similarity structure with an axisymmetric configuration far downstream. In addition, they reported that turbulent jets were characterized by the presence of three distinct regions for the axis velocity decay. These regions were classified as follows: (1) Potential core region. (2) Characteristic decay region in which the axis velocity decay was dependent upon orifice configuration. In this region, similarity of velocity profiles was obtained for one centerline axis but not for the orthogonal axis. (3) Asymptotic (or axisymmetric) decay region in which similarity of velocity profiles was approached and identification with the generating orifice was lost. In a later report by Trentacoste and Sforza, a succinct account of the similarities between three-dimensional free wake and jet flow fields was presented. They point out as important results the fact that both flows have decay rates in the asymptotic decay region which are independent of initial generating geometry, that the characteristic decay region decay rate is a function only of the aspect ratio of the generating body (with insufficient data from wake studies to confirm their conclusion), that the growth of the mean velocity profile half-width is similar for both flows, and that certain velocity irregularities in the minor axis for large aspect ratio generating bodies are noted in both flows, these irregularities are believed to be caused by the rolling up of vortex sheets shed from the generating body and are found subsequently to die out in the asymptotic decay region.

Further similarities of the mean flow properties of these flows were shown by Sforza (13) by comparing experimental data with a quasi-axisymmetric analytical model. Since the tangential component of mean velocity is assumed to be negligible with respect to the radial component, comparison is necessarily restricted to the asymptotic decay region only.

The existence of an asymptotic decay region for free wakes and jets where identification with the generating body is lost, in addition to an apparent classical similarity structure for these flows, leads to the interesting possibility that some of these characteristics might also exist for wall jets and wall wakes in a fully developed turbulent boundary layer flow. This possibility is reinforced by the analytical solution for a two-dimensional wall jet (planar or radial) developed by Glauert (14). He found a similarity solution for a laminar jet which was also piecewise applicable to a turbulent jet if appropriate eddy viscosities were selected. An experimental investigation of the mean properties of turbulent, three-dimensional wall jets from various rectangular orifices by Sforza and Herbst (15) indicated that, in fact, the three distinct decay regions were evident. In addition, they showed that for sufficient distance from the jet origin the velocity profiles normal to the surface plate on the jet centerline did obey a similarity relationship. However, spanwise velocity distributions (parallel to the wall and perpendicular to the jet main flow) did not follow a similarity pattern. The implication, perhaps, is that similarity for wall jets appears only where the flow is nearly two-dimensional and that similarity is not applicable where three-dimensional effects become significant as near the lateral edges of the wall jet.

An excellent review paper prepared by Bearman (17) discussed recent measurements of the flow around bluff bodies in smooth and turbulent uniform flows. The effect of aspect ratio on the drag force, base pressure and flow pattern of the flat plates was described. The entrainment mechanics of the free shear layer in relation to the separation bubble was also discussed. The flow in a wake was divided into two regions by Bearman: a near wake flow region and a developed wake region. The near wake region includes the separated free shear layers and the recirculation bubble. Bearman commented that it is impossible to talk about the flow in the near wake region without considering the forces on the body since there is a strong interrelation between the two. Related studies describing the near wake config- uration and its relationship to the forces acting on the body have been given by Bearman (16,18), McLaren et al. (19,20), and Lee (21).

2.4 Three-Dimensional Wall Wakes in Uniform Flow

Aside from implications drawn above for limited field measurements and related flows, the primary guidance for building wake character- istics in the planetary boundary layer has been wind tunnel studies.

Mons and Sforza (22,23) reported velocity measurements behind a two-dimensional obstacle and two three-dimensional obstacles located at the leading edge of a flat plate. Because the obstacles were in a uniform laminar flow rather than a thick fully-developed turbulent boundary layer such as that approaching a building in the atmosphere, the results of the study were not of great value in establishing the characteristics of building wakes. An apparent transition to

turbulence in the wake region also contributed to the complexity of interpretation of the experiment. Similar to the finding of the free jets and wakes studies, they found the wall wakes behind a three-dimensional obstacle could be characterized by three distinct regions, a recirculation (trapped vortex) region, a viscous diffusion region which included the characteristic decay region, and an asymptotic decay region.

In a paper by Fiedler and Wille (24), some general characteristics (mean velocities and integral scales in the wake and pressure distributions on the model surface) in the flow structure behind finite length cylinders placed with the axis perpendicular to a uniform flow were described. The flow over the top of the blunt body was dragged into the wake. The strength of this downwash decreased with increasing aspect ratio.

2.5 Investigations of Effects of Small Protuberances in Laminar Boundary Layers

A number of investigations, for example Mueller and Robertson (25), have been performed on the effect of isolated roughness elements on laminar boundary layers. Most of these researches deal with the stability of the laminar boundary layer and on the transition from laminar to turbulent flow due to the influence of the roughness element. There is very little quantitative information in these types of studies of interest to the present study of building wakes. Nevertheless, some of the qualitative descriptions of wakes of surface protuberances in a laminar boundary layer are of use in interpreting or anticipating observations of wakes in a turbulent boundary layer.

Using flow visualization by smoke and China-clay techniques, Gregory and Walker (26) gave a detailed description of the flowfield of a three-dimensional (cylinders with height equal to diameter) protuberance in a laminar boundary layer. A system of vortices was formed in front of the obstacle which were then stretched around the obstacle in a horseshoe fashion and persisted downstream with axes parallel to the direction of the main flow. Results of smoke observation on boundary layer transition caused by a spherical roughness element was reported by Mochizuki (27). Some excellent photographs of horseshoe and trailing vortices were shown. The persistence of the horseshoe vortex was clearly evident in her photographs.

2.6 Three-Dimensional Wall Wakes in Turbulent Boundary Layers

Flow near a single hemispherical roughness element in a turbulent boundary layer was investigated and the pressure distribution on the surface of the obstacle was measured in 1938 by Jacobs (28). He discovered that the wake was unlike the momentum wake behind an obstacle in a uniform flow. There was a velocity excess on the centerline of the wake. The maximum velocity defect in the wake was observed at points equally spaced on either side of the centerline. No details were given about the approach flow characteristics, and the velocity measurements in the wake were rather limited.

An investigation of the influence of a single 4.8 mm (3/16 in.) spherical roughness element in a turbulent boundary layer on a smooth flat plate was reported by Tieleman and Sandborn (29). The boundary layer thickness was about 2.5-3.8 cm (1-1/2 in.). From the data reported,

apparently the boundary layer was developing at the measurement section. According to the report, no appreciable difference in turbulence intensities was observed when the sphere was present. The effect of the sphere on the mean velocity profile was limited to a height of the same dimension as the sphere, and the defect vanished very quickly in the downstream direction.

An experimental study of the effects of boundary layer thickness and velocity profile on the pressure distributions on isolated obstacles immersed in a turbulent boundary layer was reported by Sayre (30). Pressure distributions were measured on six models (two hemispheres, two semicylinders, and two half bodies of revolution) in three different boundary layer conditions. Since neither the power-law exponents of the mean velocity profiles nor the turbulence intensities of the approach flows were given, interpretation of the results is difficult.

The flow field about circular cylinders of finite length in a turbulent boundary layer have been studied both experimentally (flow visualization studies were included) and analytically by Roper (31,32). Since the obstacles used were cylinders, most of the studies were devoted to the behavior of the separation line and vortex shedding. Very interestingly, the horseshoe vortex was found to be elliptical in cross section downstream of the cylinder.

A review paper by Tani in 1969 (33) is a useful introduction and summary of the experimental works that have been done on the response of an equilibrium turbulent boundary layer to sudden perturbation. In addition to studies of perturbations due to sudden change of pressure

gradient, wall roughness and injection, perturbations by two-dimensional obstacles were reported. Review of the results show that the recovery of the boundary layer to equilibrium is almost instantaneous in the inner part near the wall, but rather slow in the outer part of the boundary layer initiated by reattachment, and that both the maximum turbulence intensity and maximum shear stress decay nearly exponentially with a relaxation distance of 13-18 times the boundary-layer thickness at reattachment.

Another excellent review paper of the effects of small protuberances on boundary layer flows was given by Sedney (34). The information collected in this paper is mainly experimental. For three-dimensional small protuberances, Sedney concluded that a number of common elements exist in the disturbed flow regardless of whether the boundary layer is laminar or turbulent, the speed range of the external flow, or the detailed shape of the protuberance. The fluid was found to roll up in front of the protuberance and form a horseshoe vortex around the obstacle; meanwhile spiral vortices rise up from the surface in the near wake.

Wind tunnel measurements for a two-dimensional block [1.9 cm (0.75 in.) high and 1.9 cm (0.75 in.) wide] and the first extensive measurements behind a cube [1.9 cm (0.75 in.) on each side] with one face normal to the flow submerged in an artificially stimulated thick turbulent boundary layer were made by Counihan (35). The boundary layer thickness was 15 cm (6 in.) with a power-law exponent of 0.15. The ratio of model height to boundary layer thickness was 1/8. Mean longitudinal velocities, three components of fluctuating velocities,

Reynolds stresses, space correlations of longitudinal velocity fluc-
tuations along lines parallel to the three coordinate axes, and spectra
of longitudinal, lateral, and vertical velocity fluctuations were
measured. Limitations in the instrumentation made it necessary to fix
the probe position and move the cube upstream to obtain longitudinal
variations. A systemic bias in the data could occur if the approach
flow was not in a fully developed equilibrium condition--a likely
situation since a short test-section wind tunnel with an artificially
stimulated thick turbulent boundary layer was used.

The results of Counihan (35) showed, for the cube, the significant
wake effects had disappeared at 12 cube heights downstream as compared
to the wake of the block which disappeared at 18 model heights. The
maximum vertical extent of influence on the boundary layer flow was
of the order of 1.5 model heights for the cube and 3 model heights for
the block. The wake of a two-dimensional block was found to be
more extensive than that of a three-dimensional cube and more stable as
it was not as influenced by flow laterally outside the wake. The three-
dimensional structure of the cube wake results in its more rapid
diffusion back to the original flow conditions. Counihan also observed
that turbulent integral length scales in the cube wake were smaller
than those in the block wake and both were smaller than the scales of
the undisturbed boundary layer. The only exception to this observation
was that lateral integral scales in the block wake were slightly in-
creased. A discrete eddy shedding Strouhal number of 0.15 was found
for the cube. No attempt was made to identify the three regions of
decay within the wake anticipated from the previous section. As

was pointed out by Counihan, the mean velocity decay generally agreed
with the theoretical prediction of Hunt (43). Hunt predicted that the
mean velocity defect would decay as x^{-1} in the two-dimensional case
and as $x^{-1.5}$ in the three-dimensional case.

A wind tunnel investigation of wakes of three-dimensional
obstacles submerged in a turbulent boundary layer flow were also made
by Lemberg (36) at the University of Western Ontario. The naturally
developed turbulent boundary layer used for the experiment had a
power-law exponent of approximately 0.16 and a thickness of 0.61 m
(24 in.). The models used for the study included a 10 cm (4 in.) cube,
a square cylinder with a base of 10 cm (4 in.) and a height of 15 cm
(6 in.) (these two models were oriented both with the flow normal to
one face and along the diagonal), and two circular cylinders 10 cm
(4 in.) in diameter with heights of 10 cm (4 in.) and 15 cm (6 in.)
respectively. The ratios of the model heights to boundary-layer
thickness were either 1/4 or 1/6. Measurements included longitudinal
mean velocity and turbulence intensity, as well as drag and base
moments for each obstacle.

Lemberg noted that the size of the separated flow regions were
approximately the same behind both round and sharp-edged obstacles.
The largest separated flow region was obtained with a model having a
flat front face placed perpendicular to the oncoming flow. The mean
velocity defect was found to decay as $x^{-1.58}$ for all data and the
mean velocity wake effectively vanished 15 to 18 obstacle heights
downstream. The decay of turbulence intensity was found to be slower
than for the mean velocity with power-law relationships (for sharp-edged

obstacles) decaying as $x^{-0.3}$. Extrapolated from data measured up to approximately 18 heights from the model, turbulence intensity excesses were predicted to completely disappear by about 50 model heights for the sharp-edged models and 80 model heights for circular cylinders. These distances are 3 to 5 times longer than the full-scale data of Colmer (3). The rapid decay of the turbulence behind the hangar may be expected because the obstacle height to boundary-layer thickness ratio was 1/60 for Colmer's field experiment and 1/4 to 1/6 for Lemberg's wind tunnel experiment.

In addition to his wind-tunnel measurements, Lemberg performed flow visualization studies in a water channel without boundary-layer simulation. Horseshoe vortices were observed, but no attempt was made to study the role the horseshoe vortex played in the wake of the three-dimensional obstacle.

Part of Lemberg's work was devoted to analytical investigation which was essentially an extension of Hunt's theory. Both the Hunt and Lemberg analytical treatment will be reviewed in the next section.

Some of the early results of the wind-tunnel study at Colorado State University corresponding to the NASA Huntsville field study were reported by Hansen, Peterka, and Cermak (37) and by Peterka and Cermak (38). When the model of the prototype structure was oriented with its long face normal to the wind, both the mean velocity and turbulence intensity wake were found to disappear at approximately 16 to 18 building heights downstream. When the model was oriented to a certain range of angles near 45 degrees to the approach wind (47 degrees in their study), the wake assumed a completely different

character. Longitudinal vortices were found to persist into the far wake region such that a mean velocity wake in the form of a velocity excess was found 80 model heights downwind. This was about 4 times farther than the turbulence wake which disappeared at about 18 to 20 model heights. Some model scale effects were also studied for three different model scales. The wake decay rate was found to be independent of model scale and corresponded closely to Lemberg's decay rate. Reliable measurements of the horseshoe vortex behind a three-dimensional hemisphere submerged in a turbulent boundary layer were first reported by Peterka and Cermak (38). Additional data from these two references will be discussed in greater detail in Chapter 5.

Recently, Castro and Robins (39) made some wind tunnel investigation of the effect of a thick incident boundary layer on the flow around a small surface mounted cube. A cube of 0.2 m (0.66 ft) on each side was placed in a simulated planetary boundary layer which had a thickness of 2 m (6.6 ft) and a power-law exponent of 0.24. Two orientations of the cube were studied. The cube was placed either with face on or corner on to the approach flow. A pulsed-wire anemometer was used for most of the velocity measurements. This made it possible to measure accurately the streamwise mean velocity and turbulence intensity in the near wake region. Surface pressure measurements on the cube were included in the study. The interrelation between the pressure on the surfaces of the model and the near wake flow pattern were also discussed.

The wake of the cube extended only a short distance downstream. At $x/H = 4.5$ the velocity defects were only a few percent and at

x/H = 8.5   there was no discernable deviation from the undisturbed

flow.   In Castro and Robins (39) case, the turbulence intensity at one

model height was about 26 percent (rms/U_∞).   The high turbulence level

and strong shear in the approach flow probably caused the rapid recovery

of the wake.   The effect of high turbulence intensity also showed on

the roof-corner vortices.   When the cube was placed with corner on to

both boundary layer flow and uniform flow, the vortices showed very

little effect on the longitudinal velocities in the former case as

compared with the latter.

Although the existence of vortex wakes has been known for many

years (for example, Ostrowski, Marshall, and Cermak (40) reported

the generation of vortices at the leading roof corner of a building

which was at an angle of incidence to the approach flow), not until

recently has there been an attempt [Hansen and Cermak (41)] to under-

stand the nature and physical processes of these wakes.   Experimental

and theoretical investigation of the wakes behind hemispheric and

rectangular-block (oriented with two approach wind directions) models

were reported.   Experimental measurements included mean longitudinal

velocities, mean swirl velocities and vortex strengths, longitudinal

fluctuating velocities, one-dimensional spectra, two-point space

correlations, and surface pressure distributions.   Theoretical works

included developing an inviscid model to predict the strength of the

horseshoe vortex generated by a hemisphere and to determine the effect

of vortex meander on the average strength of the vortex.   A pre-

liminary theory of combined vortex and momentum wakes developed by

Hunt was also tested.   An excellent review of literature including

the classical study of vortex structure and the related studies such as the vortices behind aircraft are also included in the report.

2.7 Theoretical and Numerical Approaches

There is no theory yet available which can predict even approximately the large scale eddy motions, the mean velocity or the turbulence velocity in the separated flow region and the near wake region of either a two-dimensional or three-dimensional obstacle submerged in a turbulent boundary layer. Some theoretical models for the far wake region have been developed.

Sforza and Mons (23) used a linearized approximation to the momentum equation with an eddy viscosity model to predict the wake of leading edge obstacles. Reasonable agreement was obtained for an obstacle whose wake was close to a two-dimensional disturbance but not for a fully three-dimensional wake.

In 1969, Hunt and Smith (42) developed a theory which related the overturning moment on the body to integrals of the wake velocity to predict the time-mean velocity in the wake behind two-dimensional and three-dimensional surface mounted obstacles in a turbulent boundary layer. Some preliminary experimental results of the mean and turbulent velocities in the wakes behind two-dimensional rectangular blocks in a simulated atmospheric boundary layer were also presented in the note. An improved theory for the mean velocity profile behind a two-dimensional body was developed by Hunt (43). Approximate Reynolds stresses and rms turbulent velocities behind two-dimensional and three-dimensional buildings were calculated. A model for two-dimensional laminar wakes was given in 1971 by Hunt (44). In this paper the

important relationship between the couple exerted on the body and the moment of momentum defect in the wake is derived in detail. Two papers with excellent introductions and summaries of the theoretical works in comparison with experimental measurements were given by Hunt (45,46). A summary of the current state of development of his wake theories can be found in two additional papers (47,48).

The theory of momentum wakes (normal wakes) developed by Hunt (43) is based on the assumption that the obstacles cause only a small perturbation to the boundary layer. This assumption imposes two basic restrictions to the application of the theory. First, the height of the protuberance must be much less than the thickness of the boundary layer in which it is immersed ($H/\delta \ll 1$). Second, the velocity defects in the wake should be small: ($|u| \ll U$). Thus, strictly speaking the theory is valid only in the far wake region.

The theory assumes that far downstream the mean velocity reverts to its upwind undisturbed values. Thus, the mean velocities in the wake can be expressed as perturbations on the approach wind velocity $U = U_0(z) + u(x,y,z)$, $V = v(x,y,z)$, $W = w(x,y,z)$, where u, v, w vanish as $x \to \infty$. It is also assumed that the approach flow mean velocity profiles obey the power law $U_0(z) = U_0(H)(z/H)^n$, where n is very small ($n \ll 1$, typically $n \approx 1/7$). Hunt made the further assumption that a constant eddy viscosity over most of the wake region (not very near the ground) can be selected to relate the perturbation shear stress to the local mean velocity gradient. Thus $\tau_{xz} \approx \bar{\nu} \frac{\partial u}{\partial z}$ and $\tau_{xy} = \bar{\nu} \frac{\partial u}{\partial y}$, where $\bar{\nu}$ is given by $\bar{\nu} \approx \gamma k^2 nHU(H)$ and k is the von Karman constant (k = 0.41), and γ is a constant which is

equal to 1.0 for a two-dimensional case and of order unity for the three-dimensional case. With the foregoing assumptions and the additional assumptions that the velocity defect profile is self-preserving and that a Gaussian distribution of velocity defect in the transverse direction exists, the equations of motion can be solved for the first order solution which can be summarized as follows for the three-dimensional case:

$$\frac{u}{U(H)} = \frac{k_2 F_2(\tilde{z}'', \tilde{y})}{[(x-a)/H]^{\frac{3+n}{2+n}}} \qquad k_2 = \frac{0.21 C_D (W/H)}{4\lambda^{1/2} \gamma [2k^2 n/(2+n)]^{\frac{3+n}{2+n}}}$$

$$F_2(\tilde{z}'', \tilde{y}) = \frac{n^{-\frac{1}{(2+n)}} \exp[-(\bar{\bar{\eta}} + \tilde{y}^2/(1.5+\bar{\eta}))]}{[\bar{\eta} + 1.5]^{1/2}}$$

$$\tilde{z}'' = \frac{(z/H)}{[(x-a)/H]^{1/2+n}} \qquad \tilde{y} = \frac{(y/H)}{[(x-a)/H]^{1/2+n} k^2 n 2\gamma}^{(2+n)}$$

$$\bar{\bar{\eta}} = \tilde{z}''^{(2+n)} [\frac{1}{2(2+n)k^2 n\gamma}] \qquad\qquad (1)$$

For the two-dimensional case:

$$\frac{U}{U(H)} = \frac{k_1}{(x/H)} F_1(\tilde{z}') \qquad k_1 = \frac{-C_D}{\delta k^2 n \Gamma^{(\frac{3+n}{2+n})}}$$

$$\bar{v} = \frac{2k^2 n U(H) H}{(2+n)} \qquad F_1(\tilde{z}') = \bar{\eta}^{\frac{1}{2+n}} e^{-\bar{\eta}}[1 + \frac{n}{2+n} \{E_i(\bar{\eta}) - \gamma_E - \ell n \bar{\eta}\}]$$

$$\tilde{z}_1 = \frac{z/H}{(x/H)^{1/2+n}} \qquad \bar{\eta} = (\tilde{z}_1)^{2+n} [\frac{1}{2k^2 n(2+n)}] \qquad (2)$$

where F_1, F_2 are similarity functions and k_1, k_2 are constants related to the overturning moment on the body. In the two-dimensional

case, the wake constant (or couple) is $C_2 = -\rho \int_0^\infty z(u-u_e)U_o(z)dz$. u_e is the velocity at the edge of the wake. In a three-dimensional wake a double integral is obtained for the similar expression $c_3 = -\rho \int_0^\infty \int_{-\infty}^\infty zuU_o(z)dydz$. x_o is the virtual origin of the similarity solution which has to be determined from experimental results. The method is to plot $[u/U_o(H)]^{-2+n/3+n}$ versus x/H and extrapolate to the x/H axis.

An important result of Hunt's theory is that it gives a universal form for plotting experimental data. In the two-dimensional case, profiles of mean velocity defect at various positions along the wake can be made to collapse to a single curve by plotting $u/U_o(H) \cdot x/H$ versus $(z/H)/[K(x/H)]^{(1/n+2)}$. K is given by $K = k^2 n$. A similar result can be obtained for the three-dimensional case by plotting $u/U_o(H) \left(\frac{x-a}{H}\right)^{3+n/2+n}$ versus $(z/H)\left(\frac{x-a}{H}\right)^{1/n+2}$. Since n is small, Hunt's theory shows that the mean velocity defect decays approximately as x^{-1} in a two-dimensional case and as $x^{-3/2}$ in a three-dimensional case.

Relations are also given by Hunt (43) for the rms turbulent velocities which have approximately a power-law behavior. For the two-dimensional case $\Delta U^2_{rms_{max}}/U_o^2(H)$ varies as $\left(\frac{x}{H}\right)^{\frac{-3+n}{2+n}}$ and for three-dimensional case $\Delta U^2_{rms_{max}}/U_o^2(H)$ varies as $\left(\frac{x}{H}\right)^{\frac{-4+n}{2+n}}$.

Hunt (48) compared his theory with some of the experimental results of Counihan (35). It was found that the similarity laws of the theory collapse the experimental measurements of mean and turbulent

velocities rather satisfactorily although the theoretical curve did not follow the data exactly. Even in the experimental results of Castro and Robins (39), where the basic assumptions used in Hunt's theory are strongly violated, the mean velocity results do seem to exhibit fair agreement with the similarity prediction. The power-law of mean velocity defect decay generally matched well with the observations for the limited data published.

Lemberg (36), in addition to his experimental works, also examined his building wake analytically. Lemberg's analytical work was essentially a combination of the variable eddy viscosities of Sforza and Mons (23) with the base moment integral concept used by Hunt (43) and includes a Gaussian distribution of longitudinal velocity in the lateral direction. Lemberg's theory differs from that of Hunt in that he does not assume a constant eddy viscosity but allows it to vary like z^α $(\bar{v}_z = kz^\alpha HU_0(h))$ where the exponent α and the constant k have to be determined by matching with experimental observations. The eddy viscosity for shear in the y direction is assumed proportional to $\bar{v}_z$ with the constant of proportionality given by the ratio of the building width to the building height $(\bar{v}_y = \bar{v}_z (W/H)^2)$. By matching his theory to his wind tunnel measurements, Lemberg found that the exponent α should be equal to the boundary-layer velocity profile power-law exponent n, but he also found that the experimental data is not sufficiently accurate to distinguish between $\alpha = n$ and $\alpha = 2n$.

Lemberg's extension of Hunt's theory does result in better agreement between the theory and experimental data, but Lemberg's theory

assumes the form of much of the solution, and it lends no further insight into the physical process in the wake. Practically, Hunt's theory is simpler to use and is probably as useful.

In addition to the theoretical efforts mentioned above, some numerical modeling efforts to develop a description of building wakes has also been attempted. The reader is referred to papers by Frost, Maus, and Simpson (49) and Hirt and Cook (50). The former paper has included a detailed survey of the wake models that are being developed. Due to the complex nature of the wake, especially the separated flow region and the near wake region, progress in numerical modeling has been rather slow. Presently there is no numerical model in existence which can completely and satisfactorily model the building wakes. Numerical modeling relies heavily on experimental observations to assist in development.

Chapter 3

DATA ACQUISITION AND ANALYSIS

The present wind tunnel studies were conducted with the intent of providing sufficient laboratory data for comparison with NASA field data and to provide more information for the understanding of the general characteristics of three-dimensional building wakes. In this chapter, the experimental facility, the general capability and limitation of the instruments used in the wake measurements, and models used to generate wakes are discussed. Particular attention is drawn to the rotating hot-film anemometer technique which has been developed recently at Colorado State University for the measurement of the three components of mean velocity in the vortices.

3.1 Similarity of Wind Tunnel Boundary Layer Flow and Natural Wind

The requirements to obtain good simulation of natural winds in the wind tunnel have been discussed by Cermak and Arya (51) and Cermak (1,52). Generally speaking, the requirements are (1) undistorted scaling of boundary geometry (geometric similarity), (2) kinematic similarity of approach flow (distributions of mean velocity and turbulence characteristics), (3) Rossby number equality, (4) Reynold's number equality, and (5) bulk Richardson number equality. For the case of strong winds considered in this study, the thermal stability is essentially neutral. Thus, thermal similarity is achieved by using isothermal flow in the wind tunnel. For localized flow investigations where coriolis effects are not important, as in this study, the Rossby number equality can be relaxed. For sufficiently

high Reynolds number ($>2 \times 10^4$) the flow around sharp-edged buildings
is essentially Reynolds number independent. Typical values encountered
are 10^7 for a 50 ft high building in the atmospheric wind and 5×10^4
to 10^5 for a scale model. Thus, acceptable flow similarity is
achieved without precise Reynolds number equality. These criteria can
be satisfied by constructing a scale model of the building and its sur-
roundings and performing the model studies in wind tunnels specifically
designed to model the important characteristics of atmospheric boundary
layer flows.

3.2 The Wind-Tunnel Facility

Except for flow visualization studies which were performed in the
Industrial Aerodynamics Wind Tunnel and a 0.6 m (2 ft) square Low
Speed Wind Tunnel, all the wake measurements were conducted in the
Meteorological Wind Tunnel located in the Fluid Dynamics and Diffusion
Laboratory at Colorado State University. A plan view of this wind
tunnel is shown in Figure 1.

The Meteorological Wind Tunnel was designed specifically to model
atmospheric boundary-layer flow. The tunnel is a closed circuit facility
with a 9 to 1 contraction ratio driven by a 400 hp variable-pitch,
variable-speed propeller. The test section is 27 m (88 ft) in length
and nominally 1.8 m (6 ft) square. The test section walls diverge
2.5 cm/3 m (1 in./10 ft), and the roof is adjustable to maintain a
zero pressure gradient along the test section. The wind speed in the
test section can be adjusted continuously from .3 to 37 mps (1 to
120 fps) and does not deviate from the set speed by more than 1/2
percent. The tunnel is equipped with a refrigeration system to maintain

the air temperature at a constant level with a deviation not more than ±0.6°C(±1°F). Though the tunnel is capable of simulating thermally stratified planetary boundary layers, all the experiments included in this report were performed with a neutral boundary-layer stratification. The facility is described in detail by Plate and Cermak. (53).

The turbulent boundary layer was tripped at the entrance of the test section with a 3.8 cm (1.5 in.) high sawtooth vortex generator and allowed to develop over the long test section with certain roughness designed to simulate prototype terrain. All the measurements presented in this report were made with the model set 17.7 m (58 ft.) from the test section entrance. A similarity profile of the turbulent boundary layer was obtained well upstream from this position. The continuous thickening of the boundary layer over the test section length used for this study is essentially of the same order as the accuracy of the measurements, and the effect is therefore considered negligible.

Four different approach flow conditions were used in various portions of this wind-tunnel study. In all the tests performed, the wind tunnel was operated at a free stream velocity of 16 mps (53 ft/sec). The first boundary layer was developed with the wind tunnel floor covered with nylon shag carpet [4 strands per square cm (26 strands per square in.) and 2.5 cm (1 in.) long] selected to produce an approach wind profile similar to that over a flat open terrain. An additional vortex generator (made of 16 right angle triangular plates, 0.3 m (1 ft) base length and 0.3 m (1 ft) high was installed at the entrance of the test section to thicken the boundary layer. With this arrangement, a fully developed boundary layer 0.71 m (28 in.) deep with a power-law exponent of 0.25 was obtained at the test site. The

vertical distributions of longitudinal mean velocity and turbulence intensity are shown in Figure 2. The measurement techniques for mean velocity and turbulence are discussed in section 3.3. The second boundary layer (shown in Figure 3) was obtained with the same arrangement as the first boundary layer except without the additional vortex generator. The boundary-layer thickness at the test site was 0.61 m (24 in.) with a power-law exponent of 0.27. It was necessary to rake the shag carpet prior to each measurement sequence and after persons walked on the carpet. The characteristics of the boundary layer were found to be repeatable over several months of use and many times of removal and installation of the carpet. The third boundary layer (shown in Figure 4) was developed over the smooth flat floor of the wind tunnel and had a boundary layer thickness of 0.38 m (15 in.) at the test site with a power-law exponent of 0.12. The fourth boundary layer was obtained by using a set of four spires at the entrance of the test section and with the boundary layer developing over the smooth flat floor. The boundary layer thus obtained as shown in Figure 5 had a thickness of 1.37 m (54 in.) with a power-law exponent of 0.09. The four different boundary layers described above are designated as Test Condition 1 through 4. A summary of these four test conditions is shown in Table 1.

The probe traversing mechanism shown in Figure 6 is composed of two units, a T-shaped carriage and a portable small carriage which can also be installed on the T-shaped carriage. The T-shaped carriage is mounted on two tracks on each side wall of the wind tunnel and can be moved manually along the test section of the wind tunnel. Once the T-shaped carriage is manually set to a test station, the vertical

and lateral motions are governed by the T-shaped carriage, and the longitudinal motion is provided by the small carriage. These motions are provided by electrical motors and can be controlled independently from outside the tunnel. The probe can be traversed vertically for 0.51 m (20 in.), laterally for 0.96 m (38 in.), and longitudinally for 0.51 m (20 in.) without manually moving the carriage to a new station. Limit switches are set so that when the carriage reaches the extreme positions, the traversing power will be interrupted. The probe position can be read from a digital voltmeter with a resolution of a few hundredths of a millimeter (several thousandths of an inch).

3.3 Velocity Measurements

Measurements of longitudinal velocity were made with two different systems. A general survey of the wake was first made with a 3/32 inch diameter pitot tube connected to an MKS Baratron Pressure Meter (Type 77). The pressure meter output and probe position output were connected to an X-Y recorder to obtain a continuous profile of dynamic pressure when the probe traversed either laterally or vertically in the wake. This preliminary survey of the mean velocities in the wake was useful in determining the extent of the wake and in locating areas where more detailed measurements should be made. In the near wake region, due to the high three-dimensionality of the flow and high turbulence intensity the pitot tube measurements could be subject to large error. However, for the far wake region where the mean flow direction is essentially in the longitudinal direction, the error due to the misalignment of the pitot tube with the mean flow

direction should be very small. The maximum error due to the presence of higher turbulence (of the order of 15 percent turbulence in most of the studies presented in this report) should fall within a few percent of the local mean velocity.

More detailed measurements of the longitudinal velocities were made with a Thermo-Systems, Inc., Model 1050 anemometer unit with a TSI-10 quartz coated cylindrical hot-film probe. This sensor has a sensing length of 0.51 mm (0.02 in.) and is 0.03 mm (0.001 in.) in diameter. The turbulent kinetic energy of the wake was at frequencies ranging up to about 2 kHz., while the frequency response of this sensor is up to 16 kHz. This is more than adequate for the present wake study. The small size of the hot film permits the detection of eddies with a frequency of approximately 5 kHz in a stream moving at 25 ft/sec. This is also adequate for the flow of interest. The anemometer unit was operated without filtering or linearization.

The probe was calibrated daily using Thermo-Systems, Inc., Model 1125 calibrator and the MKS Baratron Pressure Meter. Calibration data were fit to a variable exponent form of King's Law

$$E^2 = A + BU^n \tag{4.1}$$

using a least-squares curve fitting program. From this equation it follows, to the first order approximation, that the local turbulence intensity can be given by

$$\frac{U_{rms}}{U} \approx \frac{2E \ E_{rms}}{Bn \ U^{n-1}} \tag{4.2}$$

Mean values of the anemometer bridge output were obtained by 30 second average, using a Model 2401C Hewlett-Packard integrating digital voltmeter. Root-mean-square voltages were obtained by 60 second average of the d-c output of a DISA Model 55D35 rms voltmeter, using the same integral voltmeter.

During experiments the air temperature in the wind tunnel was always held constant with a variation not over $\pm 0.6°C$ ($\pm 1°F$). Since it was not feasible to calibrate the probe with air that had the same temperature as that in the wind tunnel, a method suggested by Bearman (54) was used to correct the error due to the temperature difference in calibration and measurements. There are two restrictions in ensuring the validity of Bearman's correction method: (1) the temperature difference must be small [less than $11°C$ ($20°F$)], (2) the wind speed must be greater than 0.9-1.5 mps (3-5 ft/sec). Both of these restrictions were met in all the measurements performed.

Careful measurements of mean velocity and turbulence intensity with and without the model in place were always made within a short period of time so that any significant error due to the day-to-day or hour-to-hour variations in test conditions or instrumentation could be kept to a minimum.

Every time a new probe was used or during a prolonged usage of the same probe, calibration was sometimes performed both before and after the day's measurements. This effort was used to check the calibration and also to assure the system accuracy and repeatability. Repeatability in turbulence intensity was better than in mean velocity.

However, the results obtained using the above measurement procedure provided acceptable accuracy even when measuring small velocity defects in the far wake region.

It must be noted that due to the high turbulence intensity and three-dimensionality of the flows, neither the hot film itself nor the use of the linearized King's Law is accurate in the near wake region. Some data within the near wake presented in this report were obtained with the instrument and technique just described. Therefore, they should be viewed as semi-quantitative data. The data in the near wake region can only show the general trends of the characteristics of the wake.

3.4 Measurements in the Organized Vortex

Measurements were made to detect possible organized vorticity in the wake region. A small paddle wheel was used as a first survey to locate areas where high streamwise vorticity in the wake existed. The four-blade paddle wheel is shown in Figure 7. It is made of 1.6 mm (.063 in.) thick balsa wood with a length of 2.5 cm (0.98 in.) and a diameter of 1.9 cm (0.75 in.). The rotations of the paddle wheel were counted visually for a 30-second period. Since the paddle wheel was used only as a flow visualization device, no attempt was made to calibrate it.

A quantitative measurement of the strength of stationary vortices in the wake with axis parallel to the main flow direction was obtained by measuring the mean cross flow velocity and direction over a grid of points spanning the suspected vortex. A new rotated, yawed hot-film probe presently under development at Colorado State University

was used to measure both cross flow velocity components in a plane normal to the main flow at each selected grid point.

The principle of operation of a rotated hot-film probe is basically the same as for an x-wire probe. When the rotated hot-film probe is used, the probe is set at several orientations to the flow (10 rotational positions were used in this study). The result is that one has more than three equations available for determing the three components of velocity. These equations can then be solved by using the least-square technique to find the three components of velocity that give the best solution to the equations. This technique resulted in highly sensitive and accurate long time average measurement (30 seconds in this study) of the three mean velocity components of any reasonably stationary vortex with axis parallel to the main flow. Resolution of cross-flow magnitude is approximately 1 percent of the longitudinal mean velocity at the point.

The probe is shown in Figure 8. Additional details of the development, testing, and operation of the probe are given by Peterka and Cermak (55) and Hansen and Cermak (41).

3.5 Measurements of Space Correlations and Spectra

Measurements of two-point correlations and one-dimensional energy spectra were obtained using the hot-film anemometers described above with a Systems Development Inc. analog-to-digital conversion unit. This system consists of a multiplexer, an analog-to-digital converter, a mini-computer for control and formatting, and a digital tape recorder. This system is capable of sampling eight channels of data simultaneously,

and the sample rate can reach up to 16,000 samples per second. The resolution of the A-D converter is 0.691 mv which is quite adequate for use with hot-film anemometer in this study. The digital tape generated by this unit is compatible with the Colorado State University CDC 6400 computer for data reduction.

Two sensors were used for two-point space correlation measurements. With one probe held fixed, the other probe was mounted on the carriage which could traverse axially, laterally, or vertically in the wind tunnel. One-minute recordings were made simultaneously for the two probes at a sample rate of 2,000 samples per second.

For data reduction the voltage record on the tape was converted into velocities using King's Law with the calibration data. The mean velocity was calculated and removed from each record to obtain fluctuating velocities. The correlation coefficients were then obtained through the multiplying, averaging, and normalization process. Only 40 seconds of the record data length were required for the correlation coefficient to reach a stationary value.

For one-dimensional energy spectrum measurements, a 70-second recording was made at each point of interest in the flow with a sample rate of 8,000 samples per second. The Nyquist frequency at this sample rate is 4 kHz which is about double that of the highest frequency found in the wakes. The method described by Bendat and Piersol (56) was used to calculate the spectrum. After removing the mean velocity from the record and tapering the fluctuating velocities with a cosine function, the Fast-Fourier-Transform (FFT) was calculated. The energy spectrum obtained was smoothed by

averaging a specified number of adjacent points. The result was
output on a hard-copy plotter, a line printer, and magnetic tape for
future access.

The FFT subroutine used (FOR2D, IBM Contributed Program Library,
Program Order Number 360 D-13.4.006) was designed to employ external
disc storage of data in the calculation. The advantage of this method
is that the length of the record that can be analyzed (and hence the
lower limit of frequency that can be calculated) is not limited by the
computer core storage capability. A detailed description and listing of
the computation technique and computer code can be found in a report by
Akins and Peterka (57).

3.6 Description of the Models

The wakes from a number of building shapes were included in the
measurement program. These models used in the wind-tunnel study
were all made of plexiglass. Three scale models of the 3.25 m
(10.7 ft) high, 7.92 m (26.0 ft) wide, and 2.44 m (8.0 ft) deep
trailer used in the first field study by NASA were tested. Results
from 1:106, 1:50, and 1:40 scale models of the structure are reported
herein and are designated as model number 1 through number 3 re-
spectively. A lengthened structure 3.25 m (10.7 ft) high, 26.8 m
(87.9 ft) wide, and 22.4 m (8.0 ft) deep was later used as the second
building for the NASA field study. A 1:50 scale model of this
lengthened structure was also used in the wind-tunnel study and is
designated as model 4 in this report.

To study the general characteristics of building wakes, additional
shapes built up from four 5.1 cm (2 in.) cubes and from one-half of

one of the cubes were used. These models are designated as model 5

through model 20. A list of all the models used is shown in Table 2.

The model dimensions in their relationship to the approach boundary-

layer flow are shown in Figure 9 along with the coordinate system and

other symbol explanations. Unless specified, the models were usually

placed with one face normal to the approach flow.

When the shag carpet was used, the model was mounted on a 1/8

inch thick steel plate. The steel plate was then placed on the carpet

so that the shag fibers extended above the height of the plate.

This arrangement made it possible to remove and replace the model

several times without elaborate anchoring procedures.

3.7 Wind-Tunnel Test Programs

3.7.1 Experimental Design to Match Field Measurements

As has been mentioned before, a primary objective of this study

is to model in the wind tunnel corresponding measurements which were

to be made in the prototype. Figures 10 and 11 show the field

measurement sites for the two building configurations studied. It

should be noted that the building was moved behind Tower 2 when it

was lengthened and the short towers of Tower 2 were moved into the

wake region. Towers 3 1/2 and 4 1/2 in Figure 10 represent wind-tunnel

measurement sites for which no corresponding field data was obtained.

Wind-tunnel measurements were designed to include the field measurement

points.

Two lines of trees were upwind of the field site. Their position

relative to the first building is shown in Figure 12. These treelines

were modeled in the wind tunnel for several of the experiments using

both nylon net screens and plastic artificial plants of scale height
and appropriate porosity. Figure 13 shows the wind tunnel set-up for
examining the effect that upwind treelines may have on the wake
characteristics. A discussion of the approach boundary layer and its
effect on the wake has been discussed in an earlier report (37).
Briefly, it was decided, based on the wind tunnel results and two
profiles of approach velocity measured in the field, that an
appropriate wind tunnel simulation would be obtained without modeling
the trees upwind. All measurements reported herein do not include
upwind trees.

3.7.2 Measurements for Model Number 2 at 0°

When the building is put with one face normal to the approach
wind, the simplest wake structure is formed. Most measurements for
model 2 were performed with the model placed in this position--the
position which corresponded with the field configuration (Figure 10).
The measurements included:

1. Horizontal Profiles of Mean Velocity and Turbulence

   a. z/H = 0.94
      x/H = 0.56 (Tower 2), 2.55 (Tower 3), 4.86, 7.17
      (Tower 4), 12.86

   b. x/H = 4.86
      z/H = 0.68, 0.78, 0.94, 1.17, 1.56

   c. z/H = 0.8
      x/H = 0.5, 1.0, 2.0, 3.0, 4.0, 6.0, 8.0, 10.0, 12.0,
      14.0, 16.0, 18.0

2. Vertical Profiles (along centerline) of Mean Velocity and
   Turbulence

   a. x/H = 0.5, 1.0, 2.0, 3.0, 4.0, 6.0, 8.0, 10.0, 12.0,
      14.0, 16.0, 18.0

3. Space Correlations (taken with the fixed points along the
    centerline at z/H = 0.94).

    a. R_{uu} (r,0,0)
        Fixed points x/H = 2.55 (Tower 3), 7.17 (Tower 4)

    b. R_{uu} (0,r,0)
        Fixed points x/H = 2.55 (Tower 3), 7.17 (Tower 4)

    c. R_{uu} (0,0,r)
        Fixed points x/H = 2.55 (Tower 3), 7.17 (Tower 4)

4. One-Dimensional Energy Spectra (y/H = 0, z/H = 0.94)
    x/H = 7.17

5. *Survey of the Free Shear Layers*

    a. Vertical Profiles (along centerline)
        x/H = -0.55, -0.36, -0.16, 0.03, 0.23, 0.42, 0.62, 0.81,
        1.20, 1.59, 1.98, 2.38, 3.16, 3.94

    b. Horizontal Profiles (z/H = 0.49)
        x/H = -0.55, -0.36, -0.16, 0.03, 0.23, 0.42, 0.62, 0.81,
        1.01, 1.20, 1.59, 1.98, 2.38, 3.16, 3.94

6. Horse-Shoe Vortex Measurements

    a. paddle wheel vorticity meter measurements at x/H = 1.56,
        3.13, 4.69

    b. rotated hot-film measurements at x/H = 1.56

3.73 Measurements for Model Number 2 at 47°

Some measurements of model No. 2 were taken with the model

turned so that the approach wind formed an angle of 47° with the normal

to the long axis of the model. This was an angle at which flow

visualization photographs show strong vortex formation on the leading

top corner of the model (Figure 14). The measurements included:

1. Horizontal Profiles of Mean Velocity and Turbulence (z/H = 0.94)
    x/H = 2.55 (Tower 3), 7.17 (Tower 4), 18.55 (Tower 5), 80.0

2. Space Correlations (taken with the fixed points along the
    centerline at z/H = 0.94)

    a. R_{uu} (r,0,0)
        Fixed points x/H = 7.17 (Tower 4), 20.0

b. R_{uu} (0,r,0)
    Fixed points x/H = 7.17 (Tower 4), 20.0

c. R_{uu} (0,0,r)
    Fixed points x/H = 7.17 (Tower 4), 20.0

3. One-Dimensional Energy Spectra (z/h = 0.94)

a. x/H = 7.17   y/H = 0.0

b. x/H = 7.17   y/H = -1.25

c. x/H = 20.0   y/H = -2.5

4. Organized Vorticity Measurements

a. paddle wheel vorticity meter measurements at x/H = 12.9

b. rotated hot-film measurements at x/H = 12.9

3.7.4 Measurements for Model Number 4 at 0°

A 1/50 scale model of the field configuration for the second

prototype structure (Figure 11) was designated as model 4. The wind

tunnel measurements included:

1. Horizontal Profiles of Mean Velocity and Turbulence

a. z/H = 0.94
    x/H = 1.0, 3.0, 4.88 (T_4), 7.0, 8.72 (S_3), 10.5,
    12.57 (S_4), 14.5, 16.44 (T_5), 20.0, 25.0, 30.0, 35.0

b. z/H = 1.93
    x/H = 4.88 (T_4), 8.72 (S_3), 12.57 (S_4), 16.44 (T_5)

c. z/H = 2.81
    x/H = 4.88 (T_4), 8.72 (S_3), 12.57 (S_4), 16.44 (T_5)

d. z/H = 3.75
    x/H = 4.88 (T_4), 8.72 (S_3), 12.57 (S_4), 16.44 (T_5)

2. Vertical Profiles of Mean Velocity and Turbulence (along centerline)

a. x/H = 1.0, 3.0, 4.88 (T_4), 7.0, 8.72 (S_3), 10.5, 12.57 (S_4),
    14.5, 16.44 (T_5), 20.0, 25.0, 30.0, 35.0, 40.0

3. Space Correlations (taken with the fixed points along the
    centerline at z/H = 0.94)

a. $R_{uu}(r,0,0)$

     Fixed points $x/H = 4.88$ (T_4), 8.72 (S_3), 16.44 (T_5)

b. $R_{uu}(0,r,0)$

     Fixed points $x/H = 4.88$ (T_4), 8.72 (S_3), 16.44 (T_5)

c. $R_{uu}(0,0,r)$

     Fixed points $x/H = 4.88$ (T_4), 8.72 (S_3), 16.44 (T_5)

4. One-Dimensional Energy Spectra

a. $x/H = 4.88$
   $y/H = 0$
   $z/H = 0.94$

b. $x/H = 4.76$
   $y/H = -4.76$
   $z/H = 0.89$

5. Survey of the Free Shear Layers

a. Vertical Profiles of Mean Velocity and Turbulence

1) $y/H = 0$
   $x/H = -0.55, -0.35, -0.15, 0.04, 0.24, 0.44, 0.64,$
   $0.84, 1.23, 1.63, 2.03, 2.42, 3.22, 4.01$

2) $y/H = 3.59$
   $x/H = -0.55, -0.35, -0.15, 0.04, 0.24, 0.44, 0.64,$
   $0.84, 1.23, 2.03$

b. Horizontal Profiles of Mean Velocity and Turbulence

1) $z/H = 0.5$
   $x/H = -0.55, -0.35, -0.15, 0.04, 0.24, 0.44, 0.64,$
   $0.84, 1.23, 1.63, 2.42, 3.22, 4.01$

3.7.5 Effect of Major Parameters on the Wake Characteristics

In order to determine the influence of parameters such as H/δ (height of building to height of boundary layer), D/W (building depth to width ratio), H/W (building height to width) and H/D (building height to depth) as well as the influence of the approach boundary-layer characteristics on the wake, a series of parametric tests were run. These tests incorporated models 1 through 20 in combination with the

four boundary layers described in section 3.2. The primary measure-
ments obtained for these tests were longitudinal profiles of mean
velocity and turbulence at $y/H = 0$ and $z/H = 1.0$. This data
provided indications of wake extent and decay rate.

The test matrix to determine the influence of H/δ and approach
boundary layer changes is shown in Table 3. The test matrix to
determine the effect of D/W on the wake is shown in Table 4. Table 5
shows the test matrix for determining the effect of H/W on the wake
decay. The tests to determine the effect of H/D are shown in
Table 6.

Chapter 4

FLOW VISUALIZATION STUDY

4.1 Introduction

At the present stage of knowledge of the structure of building
wakes, valuable insight can be gained by first investigating the
overall geometry and wake mechanisms visually. With a view to clarifying
the wake geometry and mixing mechanism, the three-dimensional motions
in the near wake region of several three-dimensional sharp-edged
rectangular models were examined qualitatively in detail.

For flow visualization studies, both smoke and oil film (also
called China clay) techniques were used. The smoke technique is able
to show not only the transient phenomena of the flow but also the
general flow pattern at any position in space by changing the position
of the smoke source. The oil film technique can show results of a
long time average of the flow pattern very near a solid surface.

The methods of phase-plane and phase-space which have proved to
be very successful in the field of nonlinear mechanics (58,59), have
also been applied to fluid flow problems recently. An excellent paper
applying this technique to the problem of viscous flows and the exten-
sion to inviscid rotational flow with slip at the boundary was given
by Perry and Fairlie (60). Mathematically, the classification of
critical points in flow pattern analysis is equivalent to the phase-
plane trajectory analysis in nonlinear mechanics. A recapitulation of
the classification of singular points in flow pattern study is presented
in the next section.

The present analysis and interpretation of the flow pattern on the turbulent boundary layer approaching three-dimensional obstacles has benefited by discussions with Dr. J. C. R. Hunt while he served as a visiting professor in the Fluid Mechanics and Wind Engineering Program at Colorado State University. By applying a theory developed by Hunt (61), the authors were able to develop a hypothesis of the general geometric structure of the wake based on a study of the flow pattern near the boundary determined from oil flows and supplemented by some visual observations of smoke flow.

4.2 Classification of Singular Points, Separation and Attachment

A singular point in flow pattern analysis is defined as that point where the shear stress and velocity are zero (Figure 15).

$$\varepsilon_x = \varepsilon_y = 0 \tag{4.1}$$

Following Hunt (61), near a singular point 0, the shear stress components ε_x and ε_y are Taylor series expandable and that terms of order higher than one may be safely ignored. That is:

$$\varepsilon_x = \frac{\partial \varepsilon_x}{\partial x} x + \frac{\partial \varepsilon_x}{\partial y} y$$

$$\varepsilon_y = \frac{\partial \varepsilon_y}{\partial x} x + \frac{\partial \varepsilon_y}{\partial y} y \tag{4.2}$$

In the case where the shear stress lines emanate from or converge into the singular point radially, then on these particular lines

$$\frac{\varepsilon_x}{\varepsilon_y} = \frac{x}{y}$$

Let $\varepsilon_x = \lambda x$, $\varepsilon_y = \lambda y$ $\tag{4.3}$

where λ is a constant. By substituting (4.3) into (4.2), we have:

$$[A - \lambda I] \begin{bmatrix} x \\ y \end{bmatrix} = 0 \qquad (4.4)$$

where

$$[A] = \begin{bmatrix} \dfrac{\partial \epsilon_x}{\partial x} & \dfrac{\partial \epsilon_x}{\partial y} \\[3mm] \dfrac{\partial \epsilon_y}{\partial x} & \dfrac{\partial \epsilon_y}{\partial y} \end{bmatrix} \quad \text{and} \quad I \text{ is the unit matrix.}$$

Solving equation (4.4) for the eigenvector (x,y), slopes of these lines which pass through the singular point can be obtained.

Real eigenvectors can be found if real eigenvalues, λ, exist. Therefore we solve

$$\det [A - \lambda I] = 0$$

or

$$\lambda^2 - \Delta\lambda + J = 0 \qquad (4.5)$$

where

$$\Delta = \frac{\partial \epsilon_x}{\partial x} + \frac{\partial \epsilon_y}{\partial y} , \quad J = \frac{\partial \epsilon_x}{\partial x} \frac{\partial \epsilon_y}{\partial y} - \frac{\partial \epsilon_x}{\partial y} \frac{\partial \epsilon_y}{\partial x}$$

(A) If $\Delta^2 - 4J \geq 0, \lambda$ has real values

$$\lambda = \Delta/2 \pm \sqrt{\Delta^2/4 - J} \qquad (4.6)$$

Let the solutions be λ_1 and λ_2.

(a) If $J > 0$,

(1) $\qquad \lambda_1 > 0, \lambda_2 > 0 \quad$ if $\Delta > 0$

(2) $\qquad \lambda_1 < 0, \lambda_2 < 0 \quad$ if $\Delta < 0$

This kind of singular point is called a node. The vertical velocity component W at a very small distance z from the surface was given by Lighthill (62) as

$$W = -1/2 \, \Delta z^2 \qquad (4.7)$$

Therefore, when $\Delta > 0$, $W < 0$ the critical point is an attachment point; when $\Delta < 0$, $W > 0$ it is a separation point. They are shown in Figure 16.

(b) If $J < 0$, the two eigenvalues are positive and negative. This is called a saddle point.

    (1) $W < 0$ if $\Delta > 0$. It is an attachment saddle.

    (2) $W > 0$ if $\Delta < 0$. It is a separation saddle.

They are shown in Figure 17.

(B) If $\Delta^2 - 4J < 0$, λ is complex. There can be no straight shear lines leading into or out of a singular point. In fact, the shear lines spiral in or out. This is called a node or sometimes a focus.

    (1) $W < 0$ if $\Delta > 0$. It is an attachment node.

    (2) $W > 0$ if $\Delta < 0$. It is a separation node.

They are shown in Figure 18 respectively.

For other examples and further discussions such as whether or not the eigenvectors are at right angles, see Lighthill (62), Perry and Fairlie (60), and Hunt (61).

In addition to classifying the singular points and considering the shear stress lines joining them, both of which can be done by observing oil film results, it is also important to count the number of nodes (ΣN) and saddles (ΣS). For a three-dimensional obstacle placed on a plane, it can be shown that on the plane (P) and on the surface (B) of the obstacle, the total number of nodes must be equal to the total number of saddles.

Namely, $(\Sigma N)_{P+B} = (\Sigma S)_{P+B}$

or $(\Sigma N - \Sigma S)_{P+B} = 0$ (4.8)

If the singular points on the surface of the obstacle are not known but the changes of the angle, $\Delta\theta$, between the shear line vector $\vec{\epsilon}$ and, say the x-axis measured on the line L_B where the body meets the plane can be inspected and calculated, then

$$(\Sigma N - \Sigma S)_P = -\left(\frac{\Delta\theta}{2\pi}\right)_{L_B} \tag{4.9}$$

These are new results given by Hunt (61) which are very important for wind tunnel flow pattern study of three-dimensional obstacles. Equation (4.9) can be very useful when it is difficult to apply the oil film technique on the sides of an obstacle. It should be emphasized that the above analysis is also applicable to flows inside or outside slots or cavities where some interesting flow patterns may appear.

The same idea used for the shear line analysis presented above can also be applied to the mean streamline pattern. It was found that saddles and nodes of mean streamline patterns could be defined in a similar way to the shear stress line. By going through the same analysis, a similar result as equation (4.8) was also given by Hunt (61)

$$(\Sigma N - \Sigma S) + 1/2 (\Sigma N' - \Sigma S') = 0 \tag{4.10}$$

where ΣN and ΣS are the numbers of nodes and saddles in the interior of the flow, and N' and S' are the numbers of nodes and saddles on the base plane and surfaces of the body. This result may be particularly appropriate for analyzing photographs of smoke patterns taken with slits or planes of intense light. This result is also applicable to an instantaneous pattern of streamlines in an unsteady flow.

Some examples of how these results can be applied are shown in section 4.4.

4.3 Flow Visualization Techniques

4.3.1 The Wind Tunnels

The flow visualization studies were conducted in both the Industrial Aerodynamics Wind Tunnel and a 0.6 m x 0.6 m (2 x 2 ft) Low Speed Wind Tunnel in the Fluid Dynamics and Diffusion Laboratory at Colorado State University (Figure 19). The Industrial Aerodynamics Wind Tunnel (Figure 20) has a test section 1.8 m (6 ft) wide by 18 m (60 ft) long with a ceiling adjustable from 1.8 m (6 ft) to 2.1 m (7 ft) high. The tunnel is a closed circuit facility and is powered by a 75 hp single-speed induction motor, 16-blade pitch control axial fan. The wind speed can be adjusted continuously from about 0 mps (0 fps) to 24 mps (80 fps). Study of the flow pattern on both the floor and surface of the model by using the oil film technique was performed in this tunnel. The tunnel was operated at its highest speed for the study. The mean velocity and longitudinal turbulence profiles are shown in Figure 21.

Some preliminary studies of the flow pattern using smoke visualization was conducted in the 0.6 m x 0.6 m (2 x 2 ft) Low Speed Wind Tunnel. The tunnel is of the open circuit type with a 2.5 m (8 ft) test section. The air speed in the tunnel is controlled by a variable speed, axial fan. The maximum wind speed in the tunnel for most of the visual study did not exceed 4 to 5 ft/sec. An approximate boundary layer simulation was obtained using spires at the entrance to the test section. This tunnel was used only for identifying qualitative characteristics of the flow.

4.3.2 Oil Film and Smoke Techniques

The oil film technique utilizes a zinc oxide powder and 'Crisco' oil mixture. The mixture ratio (in volume) is 10 percent zinc oxide powder and 90 percent Crisco oil. The model was set on a .96 m (38 in.) wide, 1.32 m (52 in.) long, and 0.3 cm (0.125 in.) thick plexiglass base plate. The surface of the model and the base plate were coated uniformly with a layer of the oil mixture. After running the wind tunnel for a period of time, the flow moved the particles of suspension into a consistent pattern. A result such as the one shown in Figure 23 took about one hour to obtain.

It has been argued that very close to the surface in a turbulent flow the mean streamlines are parallel to the mean shear stress lines but are different from mean particle paths. These differences may be quite marked in the highly turbulent flow near bluff obstacles. [Hunt (61), Lighthill (62)]. Since the oil film motions are affected by the inertia and viscosity of the oil, and are induced by pressure gradients of the flow also, the suspension particles in the oil film will not follow the random motions of the fluid particles in the flow, but will depict the mean streamline or mean shear stress line.

Titanium tetrachloride was used for the smoke study. The smoke either was released from a bronze pipe which could be held in any position in space or was injected inside the models and/or the base plate and then released from equally spaced holes on the surface of the model and base plate as shown in Figure 22. The latter method gives significantly better resolution than the single smoke source technique, especially for studying the flow pattern in the regions close to the base plate and model surfaces.

4.4   Results and Discussion

Different surface flow patterns have been observed for different aspect ratio blocks with one face normal to the approach wind. With the exception of the patterns near the side faces and at the rear attachment saddle point, much of the basic pattern is similar.

Figures 23-25 show the pattern of shear stress lines on the floor as obtained by the oil flow technique for model 2, model 7 (a cube), and model 2 at 47°. A number of features are discernible including the upstream separation line, horseshoe vortex structure, vortex rollup in the near wake, and flow reattachment region downwind.

The flow patterns for model 7 and model 2 at 47° are sketched to emphasize nodal points and saddle points in Figures 26 and 27. Due to symmetry, only half of the flow pattern for model 7 has been sketched. The object of these diagrams is to indicate how oil patterns can be interpreted using the general principles outlined in 4.2. Note that the first separation line, the first attachment line, and the second separation line of the horseshoe vortex structure in both diagrams approach so close to one another downstream that they become indistinguishable. However, they cannot in principle completely merge.

From Figure 26, it follows that there are five saddle points and seven nodes on the entire base plate. By tracing along L_B, the line where the body meets the plane, we find that $\Delta\theta = -4\pi$. Thus, this diagram satisfies equation (4.9). In Figure 27, there are five nodes and six saddles. The contribution of $\Delta\theta$ around L_B is $+2\pi$, so this diagram also satisfies equation (4.9).

Note that separation or attachment shear stress lines as ordinary
shear stress lines may or may not form closed loops. Also, it seems
that there is only one separation or attachment line which passes
through a singular point which is not a focus, although an infinite
number of shear stress lines go into or out of a node.

Based on a study of the flow pattern on the base plate and
surfaces of the model supplemented by visual observations of the smoke
pattern, two hypothetical flow patterns of the whole flow structure
about the body have been sketched--one for reattached flow and one for
unreattached flow. Figures 28-30 show the flow pattern with reattach-
ment of the free shear layer on top and both sides of the model.
Figure 28 shows the flow pattern on the top, sides, and base plate
of the model. In this figure, there are 14 nodes and 14 saddles, thus
satisfying equation (4.8). However, there are 12 attachment points
(Na = 8, Sa = 4) and 16 separation points (Ns = 6, Ss = 10), demon-
strating that there can be more separation than attachment points.
The streamline pattern in a plane perpendicular to the floor and along
the centerline of the block parallel to the flow is sketched in
Figure 29. The streamline pattern of the horseshoe vortex structure
is the same as the smoke photograph taken by E. P. Sutton and interpreted
by Perry and Fairlie (60), although Sutton's photograph was taken in
a laminar boundary layer. In Figure 29, we see that $\Sigma N = 7$,
$\Sigma S = 1$, $\Sigma N' = 0$, $\Sigma S' = 12$ (note that N' and S' are nodes and
saddles on the surface which can contribute only $+\pi$ and $-\pi$ to $\Delta\theta$),

so that from equation (4.10)

$$(\Sigma N - \Sigma S) + 1/2 \ (\Sigma N' - \Sigma S') = 7\text{-}1 - \frac{12}{2} = 0 \quad (4.11)$$

Figure 30 is a pictorial, qualitative drawing of the flow pattern. This picture shows the three-dimensionality of the mean streamline patterns presented in Figures 28 and 29.

The hypothesized flow pattern for unreattached flow over the cube is shown in Figures 31 and 32. The first of these shows the streamline pattern on the top, sides, and baseplate. There are 21 nodes and 21 saddle points. However, there are 17 attachment points (N_a = 11, S_a = 6) and 25 separation points (N_s = 10, S_s = 15). Again it shows that there can be more separation points than attachment points, but always the same number of nodes as saddles. The streamline pattern in the flow on the cube centerline showing the case for no reattachment of the free shear layer is shown in Figure 32. There are 9 nodes, 2 saddles, and 14 surface saddles. Thus, again the flow pattern satisfies equation (4.10). Note that unlike two-dimensional flow where the same streamline connects the separation to the attachment point, in three-dimensional flows there is usually no streamline which connects separation and attachment points or lines. Note also that shear stress lines (or in special cases lines of separation or attachment) may connect nodes to nodes, saddles to saddles, or saddles to nodes. There is no requirement that nodes must always be connected to saddles.

On the corner of the obstacle (see Figure 31), it seems plausible that several attachment or separation lines pass right through a singular point (it is a node in Figure 31). This may be some type

of "higher order" singular point which needs further mathematical treatment.

On the corner of the obstacle (see Figure 31), it seems plausible that several attachment or separation lines pass right through a singular point (it is a node in Figure 31). This may be some type of "higher order" singular point which needs further mathematical treatment.

The present flow visualization study shows that although the position of the critical point cannot now be predicted analytically, the singular point analysis with the arithmetic for the number of nodes and saddles provide a very effective topological means for analyzing the flow pattern as well as providing constraints in the interpretation of the flow.

Chapter 5

RESULTS AND DISCUSSION

5.1 Effect of Upwind Trees on the Wake

The effect that upwind tree lines which occur at the field site
may have on the wake characteristics was examined first. Figure 33
shows vertical profiles of longitudinal mean velocity and turbulence
intensity taken both with and without the upwind tree lines in the
tunnel but with all other experimental variables held constant. It
can be seen that the trees cause a definite but small change in the wake
strength. The effect of the trees is to give the flow approaching the
building a higher turbulence level and a higher exponent in the power-
law velocity profile--n equal to 0.33. This value is higher than those
indicated from the field measurements which have a power-law exponent
ranging from 0.23 to 0.25 and an effective roughness length of about
13 cm (5.1 in.) to 16 cm (6.3 in.).

Since the effect of the trees was small and the results of the
tests without the trees in the tunnel would be generally more applicable
(since the power-law profile without trees modeled was approximately
0.25), all subsequent measurements were made without the tree lines in
place. Also, since many of the measurements were made to understand
general wake characteristics, it was desirable not to include specific
upwind disturbances.

5.2 Wakes behind the Modeled Prototype Buildings

Extensive study in the wakes of model 2 at 0 degrees, model 2
at 47 degrees, and model 4 were made in the various boundary layers

over the carpet and the smooth floor. A summary of the measurements
and conditions is shown in the following list. The results are
presented and discussed in the following subsections.

Test Series	Model No.	Test Condition	H/δ	$Re^+(\times10^{-4})$	$\dfrac{U_{rms}(H)}{U(H)}$ (%)	Measurements
1	2	1	0.09	4.0	17.0	U, U_{rms}, correlation and spectrum
2	2 at 47°	1	0.09	4.0	17.0	U, U_{rms}, swirl velocity correlation and spectrum
3	4	2	0.11	3.8	19.5	U, U_{rms}, correlation and spectrum
4	2	3	0.17	5.6	8.0	U (free shear layer)
5	4	3	0.17	5.5	8.0	U (free shear layer)
6	2	3	0.17	5.6	8.0	swirl velocity

$$Re^+ = \frac{U(H)H}{\nu}$$

5.2.1 Mean Velocity and Turbulence Fields

In the following discussions, the mean velocity in the wake
was subtracted from the mean velocity obtained in the undisturbed
boundary layer at the same point to yield the velocity defect, while
the turbulence intensity excess was obtained by subtracting the tur-
bulence intensity in the undisturbed boundary layer from that in the
wake.

A series of vertical mean velocity defect profiles along the
wake centerline for model 2 at 0 degrees in Test Condition 1 is shown
in Figure 34. The measurements were taken from x/H = 0.5 to 18
downwind. The maximum vertical extent of the wake is of the order of

2.5H near the model to 4 to 5H at 18H downstream. A region of small

mean velocity excess extends to about 2.5H downstream. The increase

of mean velocity in this region due to the presence of the model can

easily be explained by continuity. The maximum velocity defect remains

nearly constant in elevation (about 1H) to four model heights downwind

before slowly climbing as the wake diffuses upward. It should be noted

that the result of flow visualization showed that the separation

bubble extended to about 3.5H downwind for model 2. The hot-film

anemometer is not designed to make accurate measurements in and close

to this separated region. The error in measurement tends to show a

higher mean velocity (and therefore lower mean velocity defect) than

really exists. Thus, the results shown in this area are not highly

accurate but certainly demonstrate useful qualitative information.

The profiles at x/H = 14, 16, and 18 show the flow recovers to its

undisturbed value close to the floor even though a definite wake

structure still exists above. This phenomenon implies that the wake

diffuses upward as it proceeds downstream. This wind-tunnel result is

in agreement with the field data of Colmer (3), Eimern et al. (2), and

Cass et al. (4).

Figure 35 shows the longitudinal turbulence intensity profiles

corresponding to the mean velocity profiles of Figure 34. Definite

similarities are evident between the profiles of these two figures in

the vertical extent of the wake, location of the profile maxima and

in the recovery to undisturbed conditions near the floor. The turbulence

intensity has recovered at the wall by 10H to 12H and extends higher

from the floor than is noted for the mean velocity. However, for both

the mean velocity and turbulence intensity, the wake is evident but

weak at 18H downwind.

Horizontal profiles of mean velocity and turbulence intensity provide additional insight into the nature of the wake. Horizontal profiles of both mean velocity defect and turbulence intensity excess for the same experimental configuration as for the vertical profiles are shown in Figures 36 and 37. These profiles were taken at $z/H = 0.8$ from the floor and at x/H from 0.5 to 18. Again, significant similarities are evident between the mean velocity defect and turbulence intensity excess profiles. In the region near the model, the profile maxima do not occur at the wake centerline but are displaced from 1.5 to 2.0H to the side at approximately the building edge. The displaced maxima is shortlived for the mean velocity but remains for 2H downwind for the turbulence. An interesting feature of the profiles is the secondary peak or "bump" which occurred at 2.5H to 3.5H from the wake centerline. This "bump" is observed from 2 through 12 or 14H downwind for mean velocity and from 1 through 12H for turbulence. This phenomenon which occurs at the same lateral locations in both sets of profiles is caused by the horseshoe vortex system. A simple mechanism to account for the effect of this vortex system on both the longitudinal mean and turbulence velocities can be obtained by examining the direction of rotation of the vortices. When viewed looking downwind, the right-hand horseshoe vortex rotates counterclockwise while the left-hand vortex rotates in the clockwise direction. Thus, on the inside between the vortex pair, fluid is being swept downward toward the floor. This vortex action carries high velocity and low turbulence intensity fluid from a higher position in the boundary layer nearer to the floor resulting in a locally smaller mean velocity defect and

turbulence excess. By the same token, on the outer side of the vortex
pair, the vortex action carries low velocity and high turbulence
intensity fluid from near the floor up to higher elevations resulting
in a locally larger mean velocity defect and turbulence intensity
excess. These two series of horizontal profiles show a basic deviation
from the theoretical predictions of both Hunt (43) and Lemberg (36) in
which Gaussian-type lateral profiles were assumed. Neither theory
accounted for the vortex action. An important implication of Figures
36 and 37 is that for the case of model 2 at 0 degrees for Test
Condition 1, the vortex wake does not extend with significant amplitude
farther than the momentum wake. Within the resolution of the data,
the longitudinal vorticity effects do not extend more than about 12H
to 14H downwind.

In addition to the series of vertical and horizontal profiles dis-
cussed above, additional horizontal profile measurements were obtained
at different tower locations. These data were presented in a previous
report by Hansen et al. (37). They are included again in this report
and are shown in Figures 38 to 41. Both the mean velocity and turbulence
intensity wake are symmetrical about the centerline as expected. Con-
siderable detail such as the mean velocity over-shoot region (negative
velocity defect) can be seen. Figures 40 and 41 show that at tower
3 1/2, in the lower region, both the wake structure and the actual
value of mean velocity defect and turbulence intensity excess do not
change much at different heights. This result is due, as was also
pointed out by Bearman (17), to the fact that in the near wake region,

the wake mechanism is dominated by the turbulent mixing effect instead
of turbulent diffusion. The results shown in Figures 40 and 41 show
that the wake narrows at greater heights above the floor.

The decay of both the mean velocity defect and turbulence intensity
excess in the wake of model 4 in Test Condition 2 occurred much more
slowly in comparison with the wake of model 2. This can easily be
seen by comparing Figures 42 to 45 with those discussed above for
model 2. The more rapid return of the model 2 wake to undisturbed
conditions can be attributed to the higher three-dimensional mixing
effect produced by model 2 since the width of that model is only
1/3 of that of model 4. Attention should be paid to the slightly
different test conditions for both cases. Due to the absence of the
vortex generator in the Test Condition 2 case, there is a slight
increase in turbulence intensity (from 17 percent to 19.5 percent
at 1H) for model 4, but virtually no difference in mean velocity
distribution up to 3H above the floor for both cases.

Figures 42 and 43 show vertical profiles of mean velocity defect
and turbulence intensity excess along the wake centerline for model 4.
The measurements were taken from x/H = 1.0 to 40. The basic character-
istics of the profiles are very similar to those of model 2 except that
the separated region extends to 7.0H downwind. The wake decays in a
consistent manner with increase of distance downstream. The maximum
mean velocity defect remains constant at about 0.8H up to 7H downwind,
then rises slowly to about three model heights above the floor at 35H
downstream. The velocity over-shoot region is much thicker (to about
6H at x/H = 1.0 as compared to 2.5H for model 2) and extends much
farther (to about 8.7H downstream as compared to 3.0H for

model 2). The turbulence intensity profiles of Figure 43 show
definite similarities to the mean velocity profiles. The turbulence
intensity excess has recovered at the floor by 25H while the mean
velocity defect is still quite prominent even at 40H downstream.

The horizontal profiles in Figures 44 and 45 show that the
horseshoe vortex effect appears at $z/H = 0.94$ from 7H downwind and
gradually diffuses outward as the wake proceeds downstream. This effect
is still quite evident even at 40H downwind, especially in the mean
velocity profiles. Like the model 2 wake, Figures 44 and 45 show
that the vortex wake for model 4 does not extend with significant
amplitude farther than the mean velocity or turbulence wakes. This
result implies that, with one face of the model normal to the approach
wind, strong, organized, standing vortices are not formed except for
the pair of horseshoe vortices which are not sufficiently strong to
form persistent standing vortices which remain past the momentum wake
region.

The nature of the wake of model 4 at different heights above the
floor for tower locations T_4, S_3, S_4, and T_5 are shown in Figures
46 and 47. At Tower 4, there are only slight differences in the mean
velocity and turbulence intensity from the undisturbed boundary layer
flow at 3.75H above the floor as shown in Figures 46a and 47a. How-
ever, at the same heights the differences become larger as distance
downstream increases. Interestingly, at 0.94H from the floor, the
differences show the opposite trend. This is additional evidence that
the wake diffuses upward as it proceeds downstream. The width of

the wake does not change significantly for the same heights above the floor and the maximum width within the resolution of the data does not exceed 16H (approximately twice the building width).

A comparison of Figures 42 to 44 with 34 to 37 shows dramatically the difference between the wakes of the two models. It can be concluded that the momentum wake is significantly different in persistence downwind. These data indicate a strong influence of building aspect ratio on wake extent. This feature of the wake will be explored in more depth in section 5.4. These data also have obvious implications with respect to desirable shapes of structures located near airports.

During the course of this study, the wake structure was examined to determine if the general characteristics were significantly different from the momentum wake when roof-corner vortices were generated. By observing smoke patterns around model 2, the roof-corner vortex pair was found to be the strongest and extend into the far wake region when the model was oriented with a 47 degree angle with the oncoming flow. Strong vorticity was also observed over a fairly wide range of approach wind angles. A photograph of the vortex pair when $\alpha = 47°$ is shown in Figure 14. The vortices were found to be an extremely persistent flow phenomena. The primary mechanism acting to erode or dissipate the angular momentum of such a vortex system is viscous or turbulent stress acting in such a way as to produce an opposite moment about the vortex axis. Unless this interaction occurs in the near wake where turbulence levels are high, the vortex wake shed from the building will extend much farther downwind than the momentum wake.

Figures 48 and 49 show lateral profiles of mean velocity defect and turbulence intensity excess behind model 2 placed at $\alpha = 47°$. Both the mean velocity and turbulence profiles are no longer symmetrical. This is due to the fact that the vortex generated along the longer edge of the roof and probably added to remnants of the horseshoe vortex generated at the same side of the model (the vortex generated is in the same sign) is stronger than the other roof vortex. The mean velocity excess decays fairly rapidly over the first 20H downwind. A velocity excess occurred for all profiles at different locations downwind in the region $x/H = 0.5$ to 1.0--a significant fact. This velocity excess is the portion of the wake that extended far downwind. The wake measurements were followed as far downwind as the wind-tunnel test section length allowed (80H) with virtually no measurable change in the magnitude of this velocity excess. The magnitude of this velocity excess remains relatively constant at 3 to 4 percent of U_∞. The turbulence intensity wake also extended farther downwind when the model was oriented in such a way that a strong vortex pair was generated. But no evidence of a turbulence excess or defect was found at this large distance (80H) downwind. At tower 5, the turbulence intensity shows a defect rather than an excess. However, examination of the root-mean-square of the wind velocity fluctuations at this location show that the rms values are very nearly constant across the lateral profile. The variations in the turbulence intensity are due solely to the variations of the mean wind speed.

In order to study further the vortex characteristics, some cross-flow measurements were made by using the rotated hot-film technique described in section 3.4. The results will be presented in the next section.

The mean wind speed reduction in the wake is dependent on the height at which measurements are taken. One can compare wind reduction or wake decay rate at equal heights or select the largest value at any downstream section. Selecting a height near 1H on the wake centerline gives a value always close to the cross-section maximum. Figure 50 shows the decay rate of the mean velocity wake along the centerline at $z/H = 0.94$ for model 2 at $\alpha = 0°$, $\alpha = 47°$, and model 4 at $\alpha = 0°$. The persistence of the wake containing the vortex pair is quite evident. For model 4, a short region shows a wake decay rate of $m = -1.0$, while farther downstream it decays at $m = -1.5$. For model 2, the decay rate is -1.55. These results generally agree with Hunt's (43) theoretical prediction that the perturbation velocity falls off as x^{-1} in the two-dimensional case and as $x^{-3/2}$ in the three-dimensional case.

5.2.2 Organized Vortex Measurements

The longitudinal mean velocity and turbulence data presented in the previous section indicate the presence of horseshoe vortices for the $\alpha = 0$ degree cases and roof-corner vortices in the case of model 2 at $\alpha = 47°$ (perhaps combined with the horseshoe vortex). In order to better define the vortex patterns, some cross-flow measurements were made.

With one face of the model normal to the approach wind, by using smoke visualization technique, the horseshoe vortices could be seen in front and at both sides of the model. Since the strength of the horseshoe vortices was relatively weak, they were not observed visually beyond the separation bubble. The paddle wheel vorticity meter and the rotated hot-film anemometer were therefore used to detect the presence of the vortices.

Figure 51 shows contour plots of equal streamwise vorticity in the wake of model 2 at $\alpha = 0°$. These results were reduced from the paddle wheel vorticity meter data and were taken at $x/H = 1.56$, 3.13, and 4.69 respectively. Figure 52 shows the same plot for model 2 at $\alpha = 47°$ and at $x/H = 12.9$ downwind. Since the paddle wheel vorticity meter was used only for streamwise vorticity visualization purposes, no calibration effort was attempted. Therefore there is no way to correlate the result with the strength of the longitudinal vorticity in the wake. However, these contour plots do give information about the average location of the vortex and the sense of rotation.

For model 2 at 0 degrees, the horseshoe vortex core was distinctly evident with the paddle wheel at $x/H = 1.56$ and was still detectable at $x/H = 3.13$ but had almost totally disappeared at $x/H = 4.69$. For the $\alpha = 47°$ case, the roof-corner vortex core was still strong at $x/H = 12.9$.

Quantitative, rotated hot-film measurements of the swirl velocity at the same location as Figure 51a is shown in Figure 53. This data is the first reliable measurement of the horseshoe vortex in the

$\alpha = 0°$ case for a building wake. The position of the vortex core

agrees well with the paddle wheel data. The position of the vortex

axis is approximately at $z/H = 0.25$ and $y/H = -2.4$. Since at this

location the left-hand portion of the flow is in the separation bubble,

the fluid is swept leftward into the separation bubble. The typical

swirl velocity is about 5 percent of the free stream velocity. A

plot at $z/H = 0.98$, .349, and .182 of the U component of mean

velocity defect from the rotated hot-film data is shown in Figure 54.

This figure, in conjunction with Figure 53, establishes that the

previous interpretation of the "bump" in the horizontal mean velocity

profiles was correct.

Additional cross-flow measurements were made for model 2 at

$\alpha = 47°$ and at $x/H = 12.9$ downstream. The results of these measurements

are shown in Figure 55. Typical swirl velocities at this distance

downstream are of the order of 3 to 5 percent of the free stream

velocity. The results are consistent with the paddle wheel data

shown in Figure 52 and show both a strong and a weak vortex.

As pointed out by Hansen and Cermak (41), a problem which

confronts the experimentalist attempting to measure the strength of a

vortex with a fixed position probe is that the position of a longi-

tudinal vortex in a turbulent flow is not fixed. Rather, the vortex

will meander randomly due to the large scale turbulence. This

phenomenon was observed in the early flow visualization investigation

of this wake study program. The smoke plume entrained in the vortex

was seen to move laterally and slightly vertically. Any fixed probe

placed in the flow will not be in the same position in the vortex at all times and will result in a measurement of the average swirl velocity at a fixed point in space instead of the actual swirl velocity present at any instant in the vortex. Also, the amplitude of the meander increases with increasing distance downwind. Measurements with a fixed probe will not only yield lower swirl velocity than the instantaneous swirl velocity, but will also result in measurement of a faster vortex decay rate than actually exists. Therefore, both the paddle wheel vorticity meter and rotated hot-film results presented in this section are actually smaller than in the real flow. This short discussion explains the investigator's failure in attempting to measure the cross flow at $x/H = 4.69$ for model 2 at $\alpha = 0°$ by using the same rotated hot-film technique. But the fact that the vortex can be detected at $x/H = 12.9$ for model 2 at $\alpha = 47°$ is a good indication that the instantaneous vortex strength is quite high.

For further discussion and information such as a method for correcting measurements for vortex meander and a vortex decay theory, the reader is referred to the report by Hansen and Cermak (41).

5.2.3 The Free Shear Layers

One main feature of the flow over a bluff body is its separation from the obstacle surface. The separated flow continues downstream as a free shear layer which is reasonably well defined at first and forms a boundary between the inner wake and the outer flow. A survey of the shear layers of models 2 and 4 have been included in this wake study program.

Figures 56 and 57 show two series of vertical and horizontal

profiles for the free shear layers of model 2. The vertical profiles were taken along the model centerline ranging from $x/H = -0.55$ to 3.94 downwind. The horizontal profiles were taken at $z/H = 0.5$ from the floor and at downwind locations corresponding to the vertical profiles. Both sets of profiles show definite similarities. The velocities increase sharply with distance upward or sideways from the model and then pass a "crossing point" which marks the boundary between the velocity defect and excess. The velocities reach their peak values and asymptotically approach the undisturbed conditions far from the model. The velocity gradients for the first few profiles from the leading edge of the model are very sharp and the "peak" locations are well defined. These characteristics of the profile gradually diminish as the free shear layer proceeds downstream. The location of the velocity "peak" has been arbitrarily regarded in this report as the outer boundary of the free shear layer. Based on the results presented in Figures 56 and 57, the outer boundary of the shear layer, the crossing point of velocity excess and defect, and the boundary of reserve flow region are shown in Figures 58 and 59. If the location of the vertical shear outer boundary is normalized by the model height, and the location of the lateral shear outer boundary is normalized by half of the model with (W/2), these two curves collapse satisfactorily to a single curve and grow with a power-law exponent of $m = 0.1$ as shown in Figure 60.

Since the width of model 4 is triple that of model 2, the character of the free shear layer above the model may have some differences from the

centerline profile at a position laterally distant from the centerline. This consideration led to an additional series of vertical profiles at 3.8 cm (1.5 in.) from the model edge.

Two sets of vertical profiles on model 4 are plotted in the same form as for the results of model 2 in Figures 61 and 62. Comparing these two sets of mean velocity profiles, some apparent differences in character of the shear layers can be seen. For the set of mean velocity profiles taken along the centerline of the model, no velocity "peak" phenomenon above the crossing point for mean velocity defect and excess has been found. Unlike the vertical mean velocity profiles on the centerline of model 2, the vertical mean velocity profiles of model 4 on the centerline approach the undisturbed flow rather smoothly. This feature makes the upper boundary of the shear layer difficult to define precisely. The edge of the shear layer was thus selected by picking a similar point of curvature in the profile. However, for the series of profiles taken at 3.8 cm (1.5 in.) from the model edge (y/H = -3.54 laterally from the centerline) the "peak" phenomenon is quite apparent especially for the first few profiles from the leading edge of the model. Figures 63 and 64 show the positions of the upper boundaries of the shear layers as well as the locations of the crossing points and reverse flow regions for these two sets of data. Along the centerline the shear layer and crossing points of mean velocity defect and excess rise much higher than along the y/H = 3.54 line at the corresponding locations downstream and grow at a higher rate.

Figure 65 shows a series of horizontal mean velocity profiles taken at about one-half of the height of model 4. The effect of the

horseshoe vortex can be seen in the profiles from x/H = 2.42 downstream. This is not found for model 2 at the same location. The lateral shear layer outer boundary, location of the crossing point and the reverse flow region are shown in Figure 66. The results from model 4 show that the growth of the shear layer and the crossing point of mean velocity defect or excess are quite complicated. Some efforts to collapse the data have been tried without success.

It should be noted that the results of both models 2 and 4 show that on the side and top faces, no free shear layer reattachment occurs.

5.2.4 Space Correlations and Spectrum Measurements

Velocity correlations in the wake region can provide useful information about the physical size of eddies in the wake turbulence. Two-point velocity correlations were measured in the wake of model 2 at $\alpha = 0°$, model 2 at $\alpha = 47°$, and model 4 at $\alpha = 0°$ to determine the influence of the building on the macro scale of turbulence.

Figures 67, 68, and 69 show the longitudinal, lateral and vertical space correlations of the longitudinal component of turbulence for model 2 at both $\alpha = 0$ and $\alpha = 47°$. Figures 70, 71, and 72 show the same data for model 4 at $\alpha = 0°$. The integral scales determined by integration of the correlation curves to the first zero crossing point (estimated crossing point for some curves) are listed in Table 7. It should be pointed out that due to the presence or absence of the vortex generator at the entrance of the test section, there are some slight changes in the integral scales of the approaching winds. In the presence of the vortex generator (model 2 cases), the integral

scales were Lx = 20.0 cm (7.90 in.), Ly = 4.3 cm (1.68 in.), and

Lz = 8.7 cm (3.42 in.). In the absence of the vortex generator

(model 4 cases), the integral scales were Lx = 25.1 cm (9.88 in.),

Ly = 4.1 cm (1.63 in.), and Lz = 7.4 cm (2.91 in.). The results show

that for model 2 and model 4 at $\alpha = 0°$, all three turbulent scales are

reduced by the presence of the model. That is, the model has the effect

of adding turbulence to the wake but at scales smaller than the

boundary-layer scales. The scales are appreciably smaller close to

the model than farther down in the wake. These results are in agree-

ment with the data of Counihan (35).

By comparing the data for model 2 at 47 degrees with the others,

it can be seen that the vortex wake is more highly structured than the

momentum wake. At x/H = 20.0, all the three correlations are larger

in the vortex wake than those in the undisturbed boundary layer. This

apparently is due to the presence of the well structured large-scale

vortex. One effect of the vortex, at the measurement location, was

to bring fluid from higher in the boundary layer (and hence with

larger scales) to locations closer to the surface. The integral scale

results can be explained by this mechanism.

One-dimensional turbulent kinetic energy spectra were measured

and calculated at several locations in the wakes and at the corresponding

heights in the undisturbed boundary layer. The purpose of the spectrum

measurements was to find out how the turbulent kinetic energy is re-

distributed in the wake and also to find out whether there is any vortex

shedding or discrete meander frequency to the motion of the wake or

the horseshoe vortex. All the spectra data presented in this section

show a distinct inertial subrange and viscous dissipation range.

Figure 73 shows the normalized spectrum for the undisturbed boundary at z/H = 0.94 for Test Condition 1. A normalized spectrum behind model 2 for α = 0° is shown in Figure 74. A comparison of Figures 73 and 74 shows a slight shift of energy to the higher frequencies due to the presence of model 2. Very interestingly, in the α = 47° case behind model 2, there is virtually no difference with the α = 0° case as can be seen by comparing Figure 75 with 74. There is some scatter in the points at the low frequency end of the spectrum. This scatter could be reduced by lengthening the duration of the velocity record. Figures 76 and 77 were calculated to determine whether or not there was turbulent kinetic energy concentrated in some specific frequency range in the direct path of the vortex. The results show there is only a slight shift in the spectrum in the x/H = 7.17 and y/H = -1.25 case (Figure 76) and almost no detectable difference in the x/H = 20.0 and y/H = -2.5 case (Figure 77).

Spectra for model 4 are shown in Figures 78 to 80. There is virtually no difference in the spectra due to the presence of model 4 as compared with the undisturbed boundary layer.

Spectra measurements have shown that the structure of the turbulence in the wake returns to its undisturbed spectral distribution more quickly than the mean velocity wake returns to its undisturbed state. No evidence of a discrete vortex shedding frequency or vortex meander frequency was found in the cases presented.

5.3 Evaluation of the Hunt Momentum Wake Theory

Hunt's momentum wake theory (43) for both two-dimensional and three-dimensional buildings in a turbulent boundary layer was compared with the experimental results of Counihan (35) in the second half of

the same report by Hunt himself. It was found that the similarity

relationships of the theory described the behavior of the wake

reasonably well. The numerical values were not precisely correct, but

the theory as a whole was sufficiently accurate for practical purposes as

indicated by Hunt. Lemberg's (36) wind-tunnel data and Castro and Robins

(39) experimental data has been compared by Hunt (47) with his theory.

Despite the fact that some of the basic assumptions in the theory are

strongly violated in some cases, the experimental results generally

did follow the basic similarity prediction of the theory fairly well.

Several sets of the wind tunnel data obtained in the present wake

study program were used to evaluate Hunt's theory. The first data

were two series of vertical and horizontal mean velocity profiles in

the wake of model 2. The boundary-layer thickness was 0.71 m (28 in.),

the model height $H = \delta/9.8$, the power-law exponent $n = 0.25$, and the

upwind longitudinal local turbulence intensity at the height of the

model was 19 percent. Measurements of mean velocities were made over

the range $0.5 \leq x/H \leq 18.0$. The virtual origin, a, of the similarity

solution was estimated by plotting $[\Delta U_{max}/U(H)]^{-\frac{2+n}{3+n}}$ against x/H

and extrapolating. This plot, as shown in Figure 81a, is not very

linear. It is likely that there is no region where the similarity

solution exists at all. A similar finding has also been reported by

Castro and Robins (39) based on their wind tunnel data. The curve in

Figure 81a was approximated by a straight line and the virtual origin,

a, was found to be -0.65H. This value is small and of the same order

of magnitude as that of Counihan's data reported by Hunt (43,47).

In order to obtain the numerical values for the theoretical prediction,

the values of C_D, λ, and γ must be determined. The drag coefficient was estimated to 1.5 (from wind tunnel data obtained from personal communication with R. Akins, Colorado State University). For the sake of simplicity, following the same procedure suggested by Hunt (47), we also assumed $\lambda = 1$ and chose γ to give reasonable agreement with the theoretical and experimental values. The value of γ was found to be 1.56. Figure 81b shows that the shapes of the experimental and theoretical curves are in reasonable agreement. The discrepancy between the two curves possibly demonstrates the inadequacy of the constant eddy viscosity concept.

According to the theory, the wake should spread sideways exponentially like $e^{-(y/H)^2/(\lambda k\, x/H)}$, where λ is a constant. An effort to collapse the horizontal mean velocity defect data by plotting $\ln[U(y)/U(y=0)]$ as a function of $(y/H)/(x/H)^{1/2}$ [as shown by Hunt (47)] did not succeed. Apparently, in our case the effect of the horseshoe vortex was sufficiently strong that the theory based only on momentum loss and neglecting longitudinal vorticity could not adequately describe the lateral characteristics of the wake. It should be noted that while he served as a visiting professor in the Fluid Mechanics and Wind Engineering Program at Colorado State University in 1975, J. C. R. Hunt initiated a small perturbation theory for a combined vortex and momentum wake. A portion of this new theory has been briefly discussed and given a preliminary test by Hansen and Cermak (41).

The second set of data used to test Hunt's theory are three series of mean velocity defect data taken at one model height downwind along the centerline of model 1, 2, and 3. The data were taken under

test condition 3 which had a power-law exponent n = 0.12. The boundary layer height and model height ratio was 12.3, 5.9, and 4.6 respectively for model 1, model 2, and model 3. The upwind longitudinal local turbulence intensity at the model height was respectively 9.6 percent, 8 percent, and 7.2 percent. Since from the series of vertical profiles taken along the centerline of model 2, the maximum mean velocity defects at different locations downstream are found all to be about the same as that at one model height, and since all the three models mentioned here have the same aspect ratios, the maximum mean velocity defects are all assumed to be at one model height. In other words, $[\Delta U_{max}/U(H)]$ is approximated by $[\Delta U(H)/U(H)]$. Based on this approximation, we were able to calculate the virtual origins of the similarity plot for the three models. Again, the plots $\Delta U(H)/U(H)$ vs. x/H were all found to be not very linear. Based on a straight line approximation the virtual origins were found to be approximately -0.65H for all the three models. The mean velocity decay is plotted in the universal form of Hunt's theory as shown in Figure 81c. The data collapse well. The numerical values of the theoretical curve were obtained with $C_D = 1.5$, $\lambda = 1$ and $\gamma = 3.05$.

The width of model 4 is triple of that of model 2. It was considered that in regions close to the model Hunt's theory for the time mean velocity profile behind a two-dimensional building might apply. The series of vertical mean velocity defect profiles taken along the centerline of model 4 in test condition 2 were thus used to check this possibility. The first test was to compare the maxima of ΔU at a given x/H with the theory. $\Delta U_{max}/U(H)$ was plotted against $(x/H)^{-1}$.

found that the data did not fall on a straight line. As in the
three-dimensional case, this suggested that no region in the wake of
model 4 existed where Hunt's universal plot for two-dimensional building
was valid. Despite this finding several plots of $(\Delta U/U(H))x/H$ against
$(z/H)/x/H)^{\frac{1}{2+n}}$ for the data near the model were made. The results
did show that the data had no tendency to collapse into a single curve.
The decay of the mean velocity wake of model 4 is believed to be more
of a "three-dimensional" type especially in the far wake region. The
velocity decay profile for model 4 shown in Figure 50 confirms that
there is no clear region where a x^{-1} decay rate is dominant
indicating a two-dimensional flow regime.

Figures 82a and 82b show that if we plot the series of mean velocity
defect data taken along the centerline of model 4 in Hunt's universal
form for three-dimensional wake, the data collapse fairly well. The
virtual origin of the similarity plot in this case was found to be
approximately -6.0H as shown in Figure 82a. The numerical values of the
theoretical curve were obtained with $C_0 = 1.4$, $\lambda = 1$ and $\alpha = 0.95$.
Thus the three-dimensional character of the wake was established.

According to Hunt's theoretical prediction, the longitudinal
turbulent velocity excess should decay with a relationship like

$$\Delta U_{\substack{rms \\ max}}^2/U_0^2 (H) \simeq \frac{10K^2 n\alpha K_2}{(2+n)[\frac{x-a}{H}]^{(\frac{4+n}{2+n})}} \qquad dF_2(0,\tilde{z}")/d\tilde{z}"\Big|_{max} \quad \text{for three-}$$

dimensional cases. By using the experimental results of Figures 81b
and 82b, we find that the maximum values of $K_2(dF_2(0,\tilde{z}")/d\tilde{z}")$ are

5.02 and 58.3 respectively for models 2 and 4. By substituting proper theoretical and experimental values of the additional turbulence in the wakes of the models is shown in Table 8. The table indicates that the theory seems to give a good estimate for the turbulence level if x/H is large enough to be beyond the recirculation region. In both cases, the experimental values reach almost stationary values downstream of the recirculation region. Figure 83 shows the turbulent velocity excess decay for both models 2 and 4 follows the theoretical power-law prediction remarkably well.

The results of this section show that along the wake centerline where the swirl effect of the horseshoe vortex is not too strong, Hunt's theory does work well even close to the near wake region where the small perturbation approximations are not strictly valid. Off-centerline profiles are not well described by Hunt's theory due to the disturbing effects of the longitudinal vorticity.

5.4 Effects of the Model Height and Aspect Ratios on the Decay Rate of the Wake.

A series of measurements have been conducted for models with different aspect ratios and sizes in order to investigate in more generality the decay rate of building wakes. The data were all taken downwind at one model height along the centerline (y=0). The mean velocity defects were plotted in the form U_o/U versus x/H, and the turbulence intensity excesses were plotted as $\frac{U_{rms}}{U} / \frac{(U_o)_{rms}}{U_o}$ versus x/H. Figures 84 to 111 show the data. The decay rate m is defined as either

$$U_o/U = k_1 (\frac{x}{H})^m$$

or
$$\frac{U_{rms}}{U} \Big/ \frac{(U_o)_{rms}}{U_o} = k_2 \left(\frac{x}{H}\right)^m \qquad (5.1)$$

The advantage of plotting the data in this way is that the three regions of decay as reported by Sforza (13) are readily evident. The separation region shows essentially a constant value, the characteristic decay region develops downstream, and an asymptotic decay region develops at a different power-law decay rate in the far wake region. The matching point between the three regions is not sharp but forms smooth transitions so that, alternatively, one could consider the entire curve to be smooth without any definite region of power-law decay. When the data is plotted in this form, many of the curves for models of the same aspect ratios take on similar shapes so that only a factor in x/H must be applied to reduce those data to a common curve. At this time, no rational method of selecting those pertinent variables is evident.

If the far wake region, for example as shown in Figure 104, indicates an asymptotic decay region, then for three-dimensional wakes, the asymptotic decay region is not entirely independent of the generating body as is the case for related flows discussed earlier. Significant differences in slopes, for example, are evident in this region. Colmer's data placed on this type of plot (Figures 84 and 85) indicate that care should be taken in selecting gross parameters of that prototype wake from the two data locations since they fall into two different decay regions of the wake. A list of all the models under different test conditions with their ranges of the three wake regions and decay rates can be found in Table 9. It should be noted that, for some cases, the ranges of the three regions can be quite different for the mean velocity defect wake and the turbulence intensity excess wake.

5.4.1 Effects of H/δ

Figures 84 to 87 show the effect of model size on the wake structure for two shapes--the first NASA prototype structure and a cube. The measurements for both mean velocity and turbulence intensity show the important result that the decay rate, m, is independent of H/δ over the range examined, but the extent of the wake does depend on H/δ. Thus, to properly model a building wake the value of H/δ must be scaled for the model and the prototype.

For a three-dimensional obstacle immersed in a turbulent boundary layer, the effect of the approaching flow on the wake depends not only on the characteristics of the boundary layer but also on the size of the obstacle compared to the boundary layer thickness, the aspect ratios of the obstacle, and its particular orientation. The major parameters in the approaching flow which affect the wake flow are the turbulence intensity (or the mean velocity shear) and the scale of the energy-containing turbulence.

The addition of turbulence to the incident flow affects both the steady and the fluctuating velocity near the building. Consequently, this will directly effect the pressure distribution on the surface of the building. In the recirculation region of the wake, the free shear layers entrain fluid from the separated base cavity. The rate of entrainment depends on the state of the free shear layers. Increasing the turbulence level in the incident flow will increase the mixing effect between the free shear layer and the near wake [Bearman (17), Lee (21)] resulting in the enhancement of entrainment. This effect will cause an increase in the base pressure and consequently a reduced drag on the body. The couple (which is related to the drag force)

acting on the body can be related to the momentum defect of the u
component of the mean velocity. This is the reason that, with higher
turbulence level in the incident flow, a lower mean velocity defect is
observed in the near wake. In the case of three-dimensional blocks,
as was pointed out by Counihan (35), the far wake was dispersed by
both convection of outer flow into the wake region and by diffusion.
Increasing the turbulence intensity will increase both of these mixing
modes. This mechanism explains the more rapid recovery of the wake for
a smaller model as shown in Figures 84 to 87.

Models 1 and 2 are almost an even factor of 2 different in size
as are the cubes, models 5 and 7. For the cubes, the mean velocity
wake does not change decay characteristics with size, while for models
1,2, and 3 with a 2.44 factor in W/H and 0.75 in D/H, a factor in x/H
is required to make the curves coincident. Thus, for test condition 1
and for mean velocity, the effects on the wake of changing the H/δ
ratio are dependent also on the aspect ratios. For the turbulence
excess wake, factors in x/H are needed in both model sets to cause
collapse of the data to a single set. We may conclude from this that if
similarity relations can be found for three-dimensional wakes, they must
differ for mean velocity and turbulence characteristics.

Very interestingly, under test conditions 3 and 4, the "shift"
in the mean velocity wake disappears for models 1,2, and 3, although
for the turbulence wake it still exists as can be seen from Figures
88 to 91. For models 5,6, and 7, the results under these two test
conditions are shown in Figures 92 to 95. For the mean velocity wake, the
curves do not collapse as well as under test condition 1, especially for

model 5 under test condition 4 where the shift in x/H is quite noticeable in the characteristic decay region (Figure 94). If the results under these two test conditions for each set of models are compared, it is evident that there is only a small change in the characteristics of the curves, even though the power-law exponent n and H/δ values vary considerably. Careful comparison of the incident flow for test conditions 3 and 4 shows there is not much difference in mean velocity profile, turbulence level (and possibly turbulence scale) deep in the boundary layer where the models sat.

In recent years there have been some studies of turbulence, shear, and turbulence scale effects on the flow around two-dimensional bluff bodies. A theory of turbulent flow around two-dimensional bluff bodies by Hunt (63) can be summarized briefly as:

$L_x/D^* \gg 1$ along the mean stagnation streamline
$\sqrt{\overline{u^2}}$ attenuates like the mean flow

$L_x/D^* \ll 1$ $\sqrt{\overline{u^2}}$ will be amplified because of vortex stretching

where L_x is the integral scale and D^* is the characteristic length of the body. The results by Hunt show how the turbulence amplification approaching the body depends on the size of the building relative to the scale of the incidence turbulence. For small scale eddies, due to the stretching of vortex lines, some component of the turbulent velocity will be amplified. The amplification of the turbulence component near the building possibly will affect both the pressure distribution on the surface of the building and the entrainment mechanism of the separated shear layer.

In the mixing region of the wake, only eddies of a scale comparable with the scale of the wake can appreciably affect the wake mixing properties. This mixing mechanism, which cannot be adequately modeled by existing turbulence eddy viscosity models, determines the characteristics of the wake in this region. The scale of the eddies in this region is believed to be greatly influenced by the geometry (or characteristic length) of the model. It should be emphasized that this characteristic length should not simply mean the model height; instead it should be viewed in a more generalized sense including combinations of the height, the width, the depth, and the aspect ratios.

In view of the above arguments, there seems no simple way to explain satisfactorily the "shift" phenomenon in x/H which exists for certain aspect ratio models under some test conditions. Turbulence intensities at the building height do not provide an empirical basis for collapsing the curves. Additional theoretical and experimental understanding of the nature of the mean flow and turbulence immediately around the building are required before a satisfactory collapse of these data can be obtained.

Figures 96 to 103 show the results for models 17 to 20 under test conditions 3 and 4. Models 17 and 19 are only half the depth of models 5 and 7 respectively. Models 18 and 20 are only half the width of models 5 and 7 respectively. The change of D/H from 1 to 0.5 (from models 5,7 to 17,19) cause some change in the characteristics of the wake. Surprisingly, models 18 and 20, although they have the same aspect ratios, show different decay rates. One plausible explanation is that the free shear layer reattached to the model for model 20 but not for model 18. If this explanation is correct, it provides an additional complication for predicting the extent of building wakes.

Note that by increasing the power-law exponent n, the wake disappeared faster as a result of increasing shear and turbulence. This effect can be easily seen by comparing the results for the various models under the three different test conditions. Note also that the higher the n value the greater the tendency for the separated flow to reattach at the top of the model [Bearman (17)].

Since the horseshoe vortex formation is closely related to the shear in the approaching flow, a correct modeling of the shear distribution in the approach flow is apparently required. The formation of the vortex wake should not be Reynolds number dependent for a sharp-edged building, but the vorticity decay rate may be Reynolds number dependent as pointed out by Saffman (64) and Hansen and Cermak (41). Additional investigations including wind-tunnel modeling of this effect are required.

5.4.2 Effects of D/W

The models used for this study are listed in Table 4. All the model heights were two inches ($H/\delta = 0.07$), namely, the influence of model height with respect to the boundary layer height is excluded. However, the H/W and H/D values are not kept at the same values for the models. Actually the effects of both D/W and H/W are inseparable. For models 10, 13, and 16, the effect of H/D have also been included. The difference in H/D values may cause some effect on the wake decay rate as discussed in the previous section. The results are shown in Figures 104 to 107. The results for each model can also be found in Table 8. Some general conclusions can be drawn:

1) Decay rates for both the mean velocity wake and turbulence wake decrease as the value of D/W increases, except between models 7 and 10

where there is a jump. 2) The extent of the wake decreases as

D/W increases, reaches a minimum value for model 7, then increases.

3) The extent of the recirculation and characteristic decay regions

generally follow the same trend.

5.4.3 Effects of H/W

The models used for this study are listed in Table 5. The effects

of H/δ should be considered for models 8, 11, and 14. For models

15, 12, 9, 7, and 18, H/δ = 0.07, H/D = 1.0. Actually H/W and

D/W change in the same way. Thus, as mentioned before, the effect

of H/W and D/W are inseparable. As the value of H/W (or D/W)

increases, the wake decay rate continuously decreases as does the

extent of the wake.

5.4.4 Effects of H/D

The models used for this study are listed in Table 6. For models

16, 13, 10, 7, and 17 the effects of H/δ and H/W are excluded. As

H/D increases (or D/W decreases), the wake decay rate generally in-

creases smoothly, except for model 7 where there is a drop both in the

decay rate and extent of the wake. Otherwise, there is not much change

in the extent of the wake.

5.4.5 Remarks

Most experiments and theories for three-dimensional wakes have

determined that the velocity defect $(U_o - U/U_\infty)$ decays as $(x/H)^{-3/2}$.

The present results show this to be valid only for certain aspect ratios.

A series of mean velocity decay profiles for several selected models

are shown in Figure 112. The decay rate for models 15 and 12 with

width-to-height ratios of 4 to 1 and 3 to 1 show very nearly a -1.5 power-law decay exponent. However, the decay rate drops to approximately -1.2 as the width-to-height ratio drops to 1.0 (note $H/\delta = 0.07$ for all these three models and the data was obtained $Z = H$). For model 14 ($W/H = 0.25$), the decay rate drops to approximately -1.0. The lower decay rate does not necessarily indicate a wake extending farther downstream in nondimensional coordinates since the decay began almost immediately downstream from the mode for the tall structures while the decay for the low, wide structure did not begin until 3 to 5H downstream. The tall narrow structures which showed the -1.0 slope may be too tall in relation to the boundary-layer thickness (0.12δ and 0.29δ) to fit Hunt's (43) theoretical prediction. The slopes shown in Figure 112 represent the characteristic decay region. For only one case, the cube, could transition to another decay rate far downstream be detected which might signal the existence of an asymptotic region (dotted line).

The decay of turbulence intensity excess in the wakes of the same set of models is shown in Figure 113. The same systematic variation in slope is evident. It should be noted that since the measurements were all taken at one model height ($z = 1H$) along the wake centerline, $\Delta^2 rms(maximum)$ is approximated by $\Delta^2 rms(H)$. Slopes were found to be more difficult to assign to the turbulence case since, for the low models, straight line segments were not clearly evident. The lower models show for a part of their decay region, a decay rate of approximately -2 as predicted by Hunt's (43) theory. Three regions can be observed in the curves although the asymptotic decay region is tenuously defined and exists, if at all, only for very small values of turbulence intensity excess.

Chapter 6

CONCLUSIONS AND RECOMMENDATIONS

Detailed measurements of longitudinal mean velocity, turbulence intensity, space correlations, and spectra were made in the wake of two rectangular scaled block models of two trailers for which corresponding field measurements are being made by NASA. The block models were deeply submerged in turbulent boundary layers. The approach velocity profile was similar to that of a neutrally stable, natural wind over a lightly forested grass plain and was selected to closely model conditions at the Eight-Tower Planetary Boundary Layer Test Site of the NASA George C. Marshall Space Flight Center.

Measurements were made with the wind approaching normal to the long face of the models (0° wind). The wakes were found to be symmetrical about their centerline, diffused upward as the wakes proceeded downstream, and persisted to approximately 18 building heights downstream for the shorter model. For the longer model, the wake was found still quite detectable at 40 building heights downstream. The horseshoe vortex effects were quite evident for both cases. Scales of turbulence in the wakes were generally less than those in the undisturbed flows. Spectra measurements showed that the energy distribution of the turbulence in the wake returned to its undisturbed state very quickly.

Some preliminary studies of the vortex wake were conducted in this wind tunnel study program. Longitudinal mean velocity, turbulence intensity, space correlations, spectra and cross-flow measurements were obtained for the shorter model with 47 degree azimuth to the incident

flow. With the model in this orientation, the wake assumed a completely different character. Standing longitudinal vortices were formed in the wake, and the result was a much slower wake decay rate. At 80 building heights downwind a velocity excess was still evident and had the same value as the excess at locations near the model. The space correlation measurements showed that the presence of the vortex generating obstacle can cause an increase in the turbulence scales. However, spectra measurements have shown that the structure of the turbulence in a vortex wake returns to its undisturbed state more quickly than in the mean velocity wake.

Results of the flow visualization study were analyzed with some singular point theorems. Two hypothetical flow patterns of the whole flow structure about the body were proposed, which bears further experimental and mathematical treatment.

Models of different aspect ratios were used to study the effects of the boundary layer height with respect to the model height and the aspect ratios of the model on the decay rate of the wake. Preliminary results showed that to properly model the wake of a building, the relative heights of the building and the boundary layer must be modeled.

For a three-dimensional block submerged in a turbulent boundary layer, as the flow passes over and around the obstacle, the vortex lines must be stretched. Vorticity is concentrated near the stagnation point, and a streamwise component of vorticity (horseshoe vortex) is induced. The piling up of vortex lines in front of the obstacle induce secondary vortices in the opposite direction which were observed in the flow visualization study presented in this report. Since the obstacle

was sitting on the floor, the viscous effects were important. The vorticity stretching, concentration of vorticity in front of the protuberance, streamwise vorticity, and viscous effects must all be considered. The configuration of a three-dimensional obstacle wake is complicated indeed. The formation, size, strength, and extent of the vortices and the mechanism of interaction among the vortices in front and around the obstacle are virtually unknown. The shapes of structures susceptable to generation of strong vorticity, and the range of approach flow direction for which significant vorticity is generated has not been investigated. Theoretical models such as the one developed by Hunt are still relatively crude and provide only gross wake properties. Their applicability is limited but of practical interest in many situations.

It is evident that considerable additional effort is required in theoretical developments, in wind tunnel testing, and in field testing before building wake characteristics can be predicted with a high degree of confidence. While the present investigation has extended the range of wake measurements considerably, it has also revealed the need for further investigation of vortex structure in wakes and for further detailed measurements in the wakes of a wider range of building shapes. The data show, for example, that the wake characteristics of tall, narrow buildings and low, long buildings are significantly different. Furthermore, neither the characteristics for a building of complex shape nor for a group of buildings has been investigated.

REFERENCES

1. Cermak, J. E., "Applications of Fluid Mechanics to Wind Engineering," 1974 Freeman Scholar Lecture, ASME Journal of Fluids Engineering, Vol. 97, Ser. 1, No. 1, March 1975.

2. Eimern, J. V., Karschon, R., Razumova, L. A., and Robertson, G. W., "Wind Breaks and Shelterbelts," World Meteorological Organization Technical Note No. 59, WMO-No. 147, T.P. 70, 1964

3. Colmer, M. J., "Some Full-Scale Measurements of the Flow in the Wake of a Hangar," ARC-CP-1166, November 1970.

4. Cass, S. D., Scoggins, J. R., and Chevalier, H. L., "Low-Altitude Atmospheric Turbulence around an Airport," J. Aircraft, Vol. 10, No. 3, March 1973, pp. 157-163.

5. Munn, R. E., and Cole, A. F. W., "Turbulence and Diffusion in the Wake of a Building," Atmospheric Environment, Pergamon Press, Vol. 1, 1967, pp. 33-43.

6. Frost, W., Fichtl, G., Connell, J. R., and Hutto, M. L., "Mean Horizontal Wind Profiles Measured in the Atmospheric Boundary Layer about a Simulated Block Building," Second U.S. National Conference on Wind Engineering Research, Conference Preprints, Colorado State University, June 1975.

7. Steiger, M. H., and Bloom, M. H., "Three-Dimensional Viscous Wakes," Journal of Fluid Mechanics, Vol. 14, 1962, pp. 233-240.

8. Steiger, M. H., and Bloom, M. H., "Three-Dimensional Effects in Viscous Wakes," AIAA Journal, Vol. 1, 1963, pp. 776-782.

9. Kuo, Y. H., and Baldwin, L. V., "Diffusion and Decay of Turbulent Elliptic Wakes," AIAA Journal, Vol. 4, No. 9, September 1966, pp. 1566-1572.

10. Sforza, P. M., Steiger, M. H., and Trentacoste, N., "Studies on Three-Dimensional Viscous Jets," AIAA Journal, Vol. 7, No. 7, July 1969, pp. 1380-1383.

11. Trentacoste, N., and Sforza, P. M., "Further Experimental Results for Three-Dimensional Free Jets," AIAA Journal, Vol. 5, No. 5, May 1967, pp. 885-891.

12. Trentacoste, N., and Sforza, P. M., "Some Remarks on Three-Dimensional Wakes and Jets," AFOSR Scientific Report, AFOSR 68-0892, PIBAL Report No. 68-9, April 1968.

13. Sforza, P. M., "A Quasi-Axisymmetric Approximation for Turbulent, Three-Dimensional Jets and Wakes," AIAA Journal, Vol. 7, No. 7, July 1969, pp. 1380-1383.

14. Glauert, M. B., "The Wall Jet," Journal of Fluid Mechanics, Vol. 1, 1956, pp. 625-643.

15. Sforza, P. M., and Herbst, G., "A Study of Three-Dimensional, Incompressible Turbulent Wall Jets," AIAA Journal, Vol. 8, No. 2, February 1970, pp. 276-283.

16. Bearman, P. W., "An Investigation of the Forces on Flat Plates Normal to a Turbulent Flow," Journal of Fluid Mechanics, Vol. 46, Part 1, 1971, pp. 177-198.

17. Bearman, P. W., "Some Recent Measurements of the Flow around Bluff Bodies in Smooth and Turbulent Streams," Symposium on External Flows, Bristol University, July 1972, pp. B.1-B.15.

18. Bearman, P. W. and Trueman, D. M., "An Investigation of the Flow around Rectangular Cylinders," Aeronautical Quarterly, August 1972, pp. 229-237.

19. Mclaren, F. G., Sheratt, A. F. C., and Morton, A. S., "Effect of Free Stream Turbulence on the Drag Coefficient of Bluff Sharp-edged Cylinders," Nature, Vol. 223, August 23, 1969, pp. 828-829.

20. Mclaren, F. G., Sheratt, A. F. C., and Morton, A. S., "Effect of Free Stream Turbulence on the Drag Coefficient of Bluff Sharp-edged Cylinders," Nature, Vol. 224, November 29, 1969, pp. 908-909.

21. Lee, B. E., "The Effect of Turbulence on the Surface Pressure Field of a Square Prism," Journal of Fluid Mechanics, Vol. 69, Part 2, 1975, pp. 263-282.

22. Mons, R. F., and Sforza, P. M., "The Three-Dimensional Wake behind an Obstacle on a Flat Plate," AFOSR Scientific Report, AFOSR 68-1666, PIBAL Report No. 68-20, 1968.

23. Sforza, P. M., and Mons, R. F., "Wall-Wake: Flow behind a Leading Edge Obstacle," AIAA Journal, Vol. 8, No. 12, December 1970, pp. 2162-2167.

24. Fiedler, H. E., and Wille, R., "Some Observations in the Near Wake of Blunt Bodies," AIAA Journal, Vol. 8, No. 6, June 1970, pp. 1140-1141.

25. Mueller, T. J., and Robertson, J. M., "A Study of the Mean Motion and Turbulence Downstream of a Roughness Element," Developments in Theoretical and Applied Mechanics, Vol. 1, 1965, pp. 326-340.

26. Gregory, N., and Walker, W. S., "The Effect of Transition of Isolated Surface Excrescences in the Boundary Layer," R & M 2779, Pt. 1, 1955, Aeronautical Research Council, England.

27. Mochizuki, M., "Smoke Observation on Boundary Layer Transition caused by a Spherical Roughness Element," Journal of the Physical Society of Japan, Vol. 16, No. 5, May 1961, pp. 995-1000.

28. Jacobs, W., "Flow behind a Single Roughness Element," Ing. Arch. 9, 1938, STS order No. 5734, pp. 343-355.

29. Tieleman, H. W., and Sandborn, V. A., "A Three-Dimensional Single Roughness Element in Turbulent Boundary Layer," A report prepared for U.S. Army Research Grant DA-AMC-28-043-64-G-9, October 1965.

30. Sayre, C. L., Jr., "An Experimental Study of the Effects of Boundary Layer Thickness and Velocity Profile on the Pressure Distributions on Objects Immersed in the Boundary Layer," Report No. M.E. 595(19), M.E. Department, University of Maryland, February 1965.

31. Roper, A. T., "The Wake Region of a Circular Cylinder in a Turbulent Boundary Layer," Colorado State University, M.S. Thesis, 1965.

32. Roper, A. T., "A Cylinder in a Shear Layer," Ph.D. Dissertation, Civil Engineering Department, Colorado State University, 1967.

33. Tani, Itiro, "Review of Some Experimental Results on the Response of a Turbulent Boundary Layer to Sudden Perturbations," AFSOR-IFR-Stanford Conference, Vol. 1, 1969, pp. 483-494.

34. Sedney, R., "A Survey of the Effects of Small Protuberances on Boundary Layer Flow," AIAA Journal, Vol. 11, No. 6, June 1973, pp. 782-792.

35. Counihan, J., "An Experimental Investigation of the Wake behind a Two-Dimensional Block and behind a Cube in a Simulated Boundary Layer Flow," CERL Laboratory Note No. RD/L/N 115/71, June 1971.

36. Lemberg, R., "On the Wakes behind Bluff Bodies in a Turbulent Boundary Layer," Research Report Engineering Science, BLWT-3-73, The University of Western Ontario, April 1973.

37. Hansen, A. C., Peterka, J. A., and Cermak, J. E., "Wind-Tunnel Measurements in the Wake of a Simple Structure in a Simulated Atmospheric Flow," Contract Report CER73-74ACH-JAP-JEC43, June 1974, Colorado State University; also NASA CR-2540, April 1975.

38. Peterka, J. A., and Cermak, J. E., "Turbulence in Building Wakes," 4th International Conference on Wind Effects on Buildings and Structures, London, United Kingdom, September 1975.

39. Castro, I. P., and Robins, A. G., "The Effect of a Thick Incident Boundary Layer on the Flow around a Small Surface Mounted Cube," Central Electricity Generating Board Report R/M/N795, January 1975.

40. Ostrowski, J. S., Marshall, R. D., and Cermak, J. E., "Vortex Formation and Pressure Fluctuations on Buildings," Proceedings, International Res. Seminar on Wind Effects on Buildings and Structures (Ottawa), Vol. 1, University of Toronto Press, Toronto, 1971, pp. 459-484.

41. Hansen, A. C., and Cermak, J. E., "Vortex-Containing Wakes of Surface Obstacles," Project THEMIS Technical Report No. 29, CER75-76ACH-JEC16, Colorado State University, December 1975.

42. Hunt, J. C. R., and Smith, G. P., "A Theory of Wakes behind Buildings and Some Provisional Experimental Results," CERL Note RD/L/N 31/69, 1969.

43. Hunt, J. C. R., "Further Aspects and Theory of Wakes behind Buildings and Comparison of Theory with Experiments," CERL RD/L/R/1665, 1970.

44. Hunt, J. C. R., "A Theory for the Laminar Wake of a Two-Dimensional Body in a Boundary Layer," Journal of Fluid Mechanics, Vol. 49, Part 1, 1971, pp. 159-178.

45. Hunt, J. C. R., "The Effect of Single Building and Structures," Phil. Trans. Roy. Soc. Lond., A 269, 1971, pp. 457-467.

46. Hunt, J. C. R., "Some Theories for the Mean and Turbulent Velocity Distributions in Flows around Bluff Bodies," A paper presented at the Symposium on External Flows, July 1972.

47. Hunt, J. C. R., "Wakes behind Buildings," A paper presented to the Atmospheric Environment Committee of the Aeronautical Research Council for their meeting on October 23, 1974.

48. Counihan, J., Hunt, J. C. R., and Jackson, P. S., "Wakes behind Two-Dimensional Surface Obstacles in Turbulent Boundary Layers," Journal of Fluid Mechanics, Vol. 64, part 3, 1974, pp. 529-563.

49. Frost, W., Maus, J. R., and Simpson, W. R., "A Boundary Layer Approach to the Analysis of Atmospheric Motion over a Surface Obstruction," NASA CR-2182, 1973.

50. Hirt, C. N., and Cook, J. L., "Calculating Three-Dimensional Flows around Structures and over Rough Terrain," Los Alamos Scientific Laboratory, LA-DC-13289, 1971.

51. Cermak, J. E., and Arya, S. P. S., "Problems of Atmospheric Shear Flows and their Laboratory Simulation," AGARD Conference Proceedings, No. 48, 1970, pp. 12.1-12.16.

52. Cermak, J. E., "Laboratory Simulation of the Atmospheric Boundary Layer," AIAA Journal, Vol. 9, No. 9, September 1971, pp. 1746-1754.

53. Plate, E. J., and Cermak, J. E., "Micrometeorological Wind Tunnel Facility, Description and Characteristics," Fluid Dynamics and Diffusion Laboratory Report, CER63EJP-JEC9, Colorado State University, 1963.

54. Bearman, P. W., "Corrections for the Effect of Ambient Temperature Drift on Hot-Wire Measurements in Incompressible Flow," DISA Information Bulletin No. 11, 1970.

55. Peterka, J. A., and Cermak, J. E., "A Wind Model for an Elevated STOL-Port Configuration," NASA CR-2450, 1974.

56. Bendat, J. S., and Piersol, A. G., Random Data: Analysis and Measurement, Wiley-Interscience, New York, 1971.

57. Akins, R. E., and Peterka, J. A., "Computation of Power Spectral Densities and Correlations using Digital FFT Techniques," Fluid Dynamics and Diffusion Laboratory Report, CER75-76REA13, Colorado State University, 1975.

58. Stoker, J. J., Nonlinear Vibration, Interscience Publishers, Second printing, September 1966.

59. Minorsky, N., Nonlinear Oscillations, Krieger Publishing Company, Huntington, New York, 1974.

60. Perry, A. E., and Fairlie, B. D., "Critical Points in Flow Patterns," Adv. Geophys., Vol. 18B, 1974, pp. 299-315.

61. Hunt, J. C. R., Personal Communication, 1975.

62. Lighthill, M. J., [Article in Laminar Boundary Layer (edited by L. Rosenbead)], Oxford Press, 1963, pp. 48-88.

63. Hunt, J. C. R., "A Theory of Turbulent Flow around Two-Dimensional Bluff Bodies," Journal of Fluid Mechanics, Vol. 61, 1973, pp. 625-706.

64. Saffman, P. G., "The Structure of Turbulent Line Vortices," The Physics of Fluids, Vol. 16, No. 8, August 1973, pp. 1181-1188.

TABLE 1

BOUNDARY LAYER CHARACTERISTICS

Test Condition	$\delta(m)$	$\delta(in.)$	n	$z_e(mm)$	$z_e(in.)$	Development
1	0.71	28	0.25	4.3	0.17	carpet, vortex generator
2	0.61	24	0.27	6.1	0.24	carpet
3	0.38	15	0.12	0.11	0.0042	flat plate floor
4	1.37	54	0.09	0.048	0.0019	spires, flat plate floor

TABLE 2

BUILDING MODEL DIMENSIONS

Model	H (height)		W (width)		D (depth)	
	cm	in.	cm	in.	cm	in.
1	3.10	1.22	7.54	2.97	2.31	0.91
2	6.50	2.56	15.88	6.25	4.88	1.92
3	8.26	3.25	20.14	7.93	6.20	2.44
4	6.40	2.52	53.59	21.10	4.80	1.89
5	10.16	4.00	10.16	4.00	10.16	4.00
6	7.62	3.00	7.62	3.00	7.62	3.00
7	5.08	2.00	5.08	2.00	5.08	2.00
8	10.16	4.00	5.08	2.00	5.08	2.00
9	5.08	2.00	10.16	4.00	5.08	2.00
10	5.08	2.00	5.08	2.00	10.16	4.00
11	15.24	6.00	5.08	2.00	5.08	2.00
12	5.08	2.00	15.24	6.00	5.08	2.00
13	5.08	2.00	5.08	2.00	15.24	6.00
14	20.32	8.00	5.08	2.00	5.08	2.00
15	5.08	2.00	20.32	8.00	5.08	2.00
16	5.08	2.00	5.08	2.00	20.32	8.00
17	5.08	2.00	5.08	2.00	2.54	1.00
18	5.08	2.00	2.54	1.00	5.08	2.00
19	10.16	4.00	10.16	4.00	5.08	2.00
20	10.16	4.00	5.08	2.00	10.16	4.00

TABLE 3

TEST MATRIX FOR H/δ AND BOUNDARY LAYER EFFECTS

Test Series	Model	H (in.)*	Approach Flow Condition	H/δ	$\frac{U_{rms}(H)}{U(H)}$ (%)
	1	1.22	1	0.04	21
1	2	2.56	1	0.09	17
	3	3.25	1	0.12	15.6
	5	4.00	1	0.14	14.8
2	6	3.00	1	0.11	16
	7	2.00	1	0.07	18
	1	1.22	4	0.02	10.4
3	2	2.56	4	0.05	9
	3	3.25	4	0.06	8.3
	5	4.00	4	0.07	7.8
4	6	3.00	4	0.06	8.6
	7	2.00	4	0.04	9.4
	17	2.00	4	0.04	9.4
5	19	4.00	4	0.07	7.8
	18	2.00	4	0.04	9.4
6	20	4.00	4	0.07	7.8
	1	1.22	3	0.08	9.5
7	2	2.56	3	0.17	7.8
	3	3.25	3	0.22	7
	5	4.00	3	0.27	6.3
8	6	3.00	3	0.20	7.2
	7	2.00	3	0.13	8.4
	17	2.00	3	0.13	8.4
9	19	4.00	3	0.27	6.3
	18	2.00	3	0.13	8.4
10	20	4.00	3	0.27	6.3

*Note: 2.54 cm = 1 in.

TABLE 4

TEST MATRIX FOR D/W EFFECTS

Model	H (in.)*	Test Condition	H/δ	D/W	H/W	H/D
15	2	1	0.07	0.25	0.25	1.00
12	2	1	0.07	0.33	0.33	1.00
17	2	1	0.07	0.50	1.00	2.00
9	2	1	0.07	0.50	0.50	1.00
7	2	1	0.07	1.00	1.00	1.00
10	2	1	0.07	2.00	1.00	0.50
18	2	1	0.07	2.00	2.00	1.00
13	2	1	0.07	3.00	1.00	0.33
16	2	1	0.07	4.00	1.00	0.25

*Note: 2.54 cm = 1 in.

TABLE 5

TEST MATRIX FOR H/W EFFECTS

Model	H (in.)*	Test Condition	H/δ	H/W	D/W	H/D
15	2	1	0.07	0.25	0.25	1.0
12	2	1	0.07	0.33	0.33	1.0
9	2	1	0.07	0.50	0.50	1.0
7	2	1	0.07	1.00	1.00	1.0
18	2	1	0.07	2.00	2.00	1.0
8	4	1	0.14	2.00	1.00	2.0
11	6	1	0.21	3.00	1.00	3.0
14	8	1	0.29	4.00	1.00	4.0

*Note: 2.54 cm = 1 in.

TABLE 6

TEST MATRIX FOR H/D EFFECTS

Model	H (in.)*	Test Condition	H/δ	H/D	D/W	H/W
16	2	1	0.07	0.25	4.0	1.0
13	2	1	0.07	0.33	3.0	1.0
10	2	1	0.07	0.50	2.0	1.0
7	2	1	0.07	1.00	1.0	1.0
17	2	1	0.07	2.00	0.5	1.0
8	4	1	0.14	2.00	1.0	2.0
11	6	1	0.21	3.00	1.0	3.0
14	8	1	0.29	4.00	1.0	4.2

*Note: 2.54 cm = 1 in.

TABLE 7

RATIOS OF THE INTEGRAL LENGTH SCALES OF TURBULENCE
IN THE WAKES OF MODELS 2 AND 4 TO CORRESPONDING
SCALES IN THE UNDISTURBED BOUNDARY LAYER

	Model 2	Model 2 at 47°	Model 4
Longitudinal Scale			
x/H = 2.55	0.52		
x/H = 7.17	0.73	1.20	
x/H = 20.00		1.13	
x/H = 4.88			0.59
x/H = 8.72			0.66
x/H = 16.44			0.67
Vertical Scale			
x/H = 2.55	0.35		
x/H = 7.17	0.59	0.93	
x/H = 20.00		1.04	
x/H = 4.88			0.71
x/H = 8.72			0.87
x/H = 16.44			0.98
Lateral Scale			
x/H = 2.55	0.52		
x/H = 7.17	0.84	0.95	
x/H = 20.00		1.36	
x/H = 4.88			0.70
x/H = 8.72			0.90
x/H = 16.44			0.88

TABLE 8

EXPERIMENTAL AND THEORETICAL TURBULENCE DECAY COMPARISON

Model 2

$\frac{x}{H}$	$\Delta U^2_{rms\,max}/U_o^2 (H) \{\frac{x-a}{H}\}^{(\frac{4+n}{2+n})}$	Theoretical Value
0.5	.129	
1.0	.247	
2.0	1.311	
3.0	.808	
4.0	1.021	
6.0	1.290	1.461
8.0	1.413	
10.0	1.483	
12.0	1.449	
14.0	1.912	
16.0	1.217	
18.0	2.262	

Model 4

$\frac{x}{H}$	$\Delta U^2_{rms\,max}/U_o^2 (H) \{\frac{x-a}{H}\}^{(\frac{4+n}{2+n})}$	Theoretical Value
1.0	3.421	
3.0	5.488	
4.88	8.910	
7.0	9.341	
8.72	10.384	
10.5	11.116	
12.57	10.961	11.08
14.5	11.735	
16.44	12.519	
20.0	10.092	
25.0	8.302	
30.0	10.153	
35.0	11.886	
40.0	10.733	

TABLE 9

POWER-LAW DECAY RATES AND DOWNSTREAM EXTENT
FOR THE VARIOUS MODELS AND TEST CONDITIONS

Test Condition 1

Model	Recirculation Region		Characteristic Decay Region		Asymptotic Decay Region	
1 *	0.0H	2.5H	(-.52)	5.5H	(-.17)	15.0H
**	0.0H	2.5H	(-.65)	5.5H	(-.25)	15.0H
2	0.0H	3.0H	(-.52)	8.0H	(-.17)	23.0H
	0.0H	3.0H	(-.63)	9.0H	(-.24)	23.0H
3	0.0H	3.0H	(-.52)	10.0H	(-.17)	26.0H
	0.0H	3.0H	(-.70)	12.0H	(-.24)	26.0H
4	0.0H	5.0H	(-6.2)	15.0H	(-.14)	55.0H
	0.0H	7.0H	(-.93)	18.0H	(-.33)	40.0H
5	0.0H	1.0H	(-.24)	6.0H	(-.06)	25.0H
	0.0H	1.0H	(-.46)	7.0H	(-.09)	25.0H
6	0.0H	1.0H	(-.24)	6.0H	(-.06)	22.0H
	0.0H	1.0H	(-.47)	7.0H	(-.07)	20.0H
7	0.0H	1.5H	(-.24)	4.5H	(-.06)	13.0H
	0.0H	1.5H	(-.48)	4.6H	(-.08)	18.0H
8	0.0H	0.5H	(-.24)	2.5H	(-.06)	14.0H
	0.0H	0.5H	(-.47)	3.5H	(-.14)	16.0H
9	0.0H	1.2H	(-.37)	5.0H	(-.13)	20.0H
	0.0H	2.0H	(-.52)	9.0H	(-.14)	21.0H
10	0.0H	1.3H	(-.29)	5.0H	(-.10)	21.0H
	0.0H	1.75H	(-.60)	5.0H	(-.015)	22.0H
11	0.0H	0.3H	(-.25)	1.15H	(-.04)	90.0H
	0.0H	0.5H	(-.41)	3.0H	(-.14)	13.0H
12	0.0H	2.5H	(-.46)	8.0H	(-.14)	21.0H
	0.0H	3.0H	(-.69)	9.0H	(-.38)	19.0H
13	0.0H	2.0H	(-.18)	6.5H	(-.10)	21.0H
	0.0H	1.5H	(-.37)	5.5H	(-.12)	28.0H
14	0.0H	0.25H	(-.28)	1.0H	(-.03)	7.0H
	0.0H	0.30H	(-.54)	1.6H	(-.19)	11.0H
15	0.0H	2.5H	(-.61)	9.0H	(-.15)	26.0H
	0.0H	3.5H	(-.78)	9.5H	(-.22)	25.0H
16	0.0H	2.0H	(-.18)	6.5H	(-.10)	23.0H
	0.0H	2.0H	(-.44)	5.0H	(-.12)	21.0H
17	0.0H	1.0H	(-.50)	4.5H	(-.05)	20.0H
	0.0H	1.25H	(-.65)	6.0H	(-.10)	23.0H
18	0.0H	1.1H	(-1.5)	5.5H	(-.04)	20.0H
	0.0H	1.2H	(-.34)	5.5H	(-.06)	20.0H

* First line indicates mean velocity decay rates

** Second line indicates turbulence intensity decay rates

TABLE 9 (continued)

Test Condition 3 Model		Recirculation Region		Characteristic Decay Region		Asymptotic Decay Region	
1	*	0.0H	3.0H	(-.92)	8.0H	(-.12)	38.0H
	**	0.0H	4.0H	(-.97)	13.0H	(-.54)	35.0H
2		0.0H	3.0H	(-.91)	8.0H	(-.11)	42.0H
		0.0H	4.0H	(-.98)	15.0H	(-.45)	45.0H
3		0.0H	3.0H	(-.92)	8.0H	(-.11)	45.0H
		0.0H	4.0H	(-.98)	16.0H	(-.30)	47.0H
5		0.0H	1.0H	(-.42)	4.5H	(-.05)	20.0H
		0.0H	1.5H	(-.71)	10.0H	(-.26)	28.0H
6		0.0H	1.5H	(-.43)	4.5H	(-.05)	20.0H
		0.0H	1.5H	(-.71)	9.0H	(-.25)	30.0H
7		0.0H	1.5H	(-.43)	4.0H	(-.05)	20.0H
		0.0H	1.5H	(-.71)	9.0H	(-.25)	27.0H
17		0.0H	1.5H	(-.83)	4.0H	(-.07)	20.0H
		0.0H	2.0H	(-1.02)	7.0H	(-.25)	27.0H
19		0.0H	1.5H	(-.84)	4.5H	(-.07)	17.0H
		0.0H	2.0H	(-1.02)	8.0H	(-.37)	28.0H
18		0.0H	1.2H	(-.11)	5.0H	(-.02)	25.0H
		0.0H	1.0H	(-.41)	7.0H	(-.12)	30.0H
20		0.0H	1.0H	(-.17)	4.5H	(-.03)	20.0H
		0.0H	1.5H	(-.43)	8.5H	(-.16)	30.0H

Test Condition 4							
1.	*	0.0H	2.5H	(-.86)	8.0H	(-.12)	30.0H
	**	0.0H	3.0H	(-.88)	15.0H	(-.32)	35.0H
2		0.0H	3.0H	(-.87)	8.0H	(-.12)	32.0H
		0.0H	3.5H	(-.88)	18.0H	(-.38)	42.0H
3		0.0H	3.0H	(-.89)	7.5H	(-.11)	38.0H
		0.0H	3.0H	(-.88)	20.0H	(-.35)	50.0H
5		0.0H	2.0H	(-.35)	5.5H	(-.04)	30.0H
		0.0H	2.0H	(-.63)	10.0H	(-.25)	37.0H
6		0.0H	1.5H	(-.33)	4.5H	(-.04)	28.0H
		0.0H	1.5H	(-.63)	9.0H	(-.25)	36.0H
7		0.0H	1.0H	(-.33)	4.5H	(-.04)	30.0H
		0.0H	1.5H	(-.63)	8.0H	(-.25)	40.0H
17		0.0H	1.25H	(-.70)	4.0H	(-.04)	29.0H
		0.0H	1.75H	(-.83)	7.5H	(-.21)	35.0H
19		0.0H	1.4H	(-.70)	4.5H	(-.04)	29.0H
		0.0H	2.0H	(-.83)	9.0H	(-.25)	32.0H
18		0.0H	1.0H	(-.12)	4.5H	(-.02)	40.0H
		0.0H	1.0H	(-.31)	6.0H	(-.09)	50.0H
20		0.0H	1.0H	(-.13)	5.0H	(-.02)	40.0H
		0.0H	1.0H	(-.50)	6.0H	(-.17)	40.0H

* First line indicates mean velocity decay rates

** Second line indicates turbulence intensity decay rates

PLAN

ELEVATION
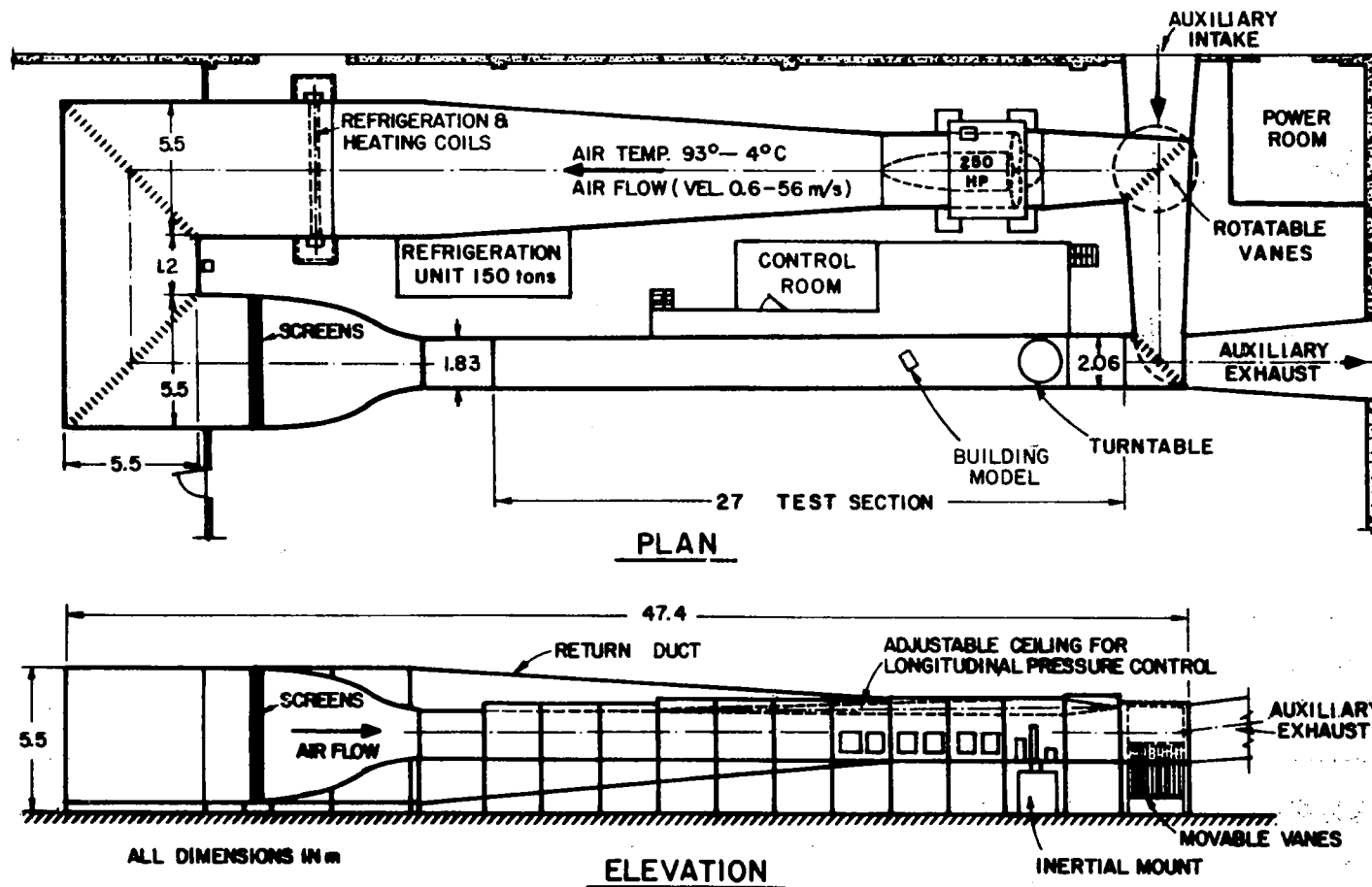
Figure 1.   Meteorological Wind Tunnel at Colorado
State University
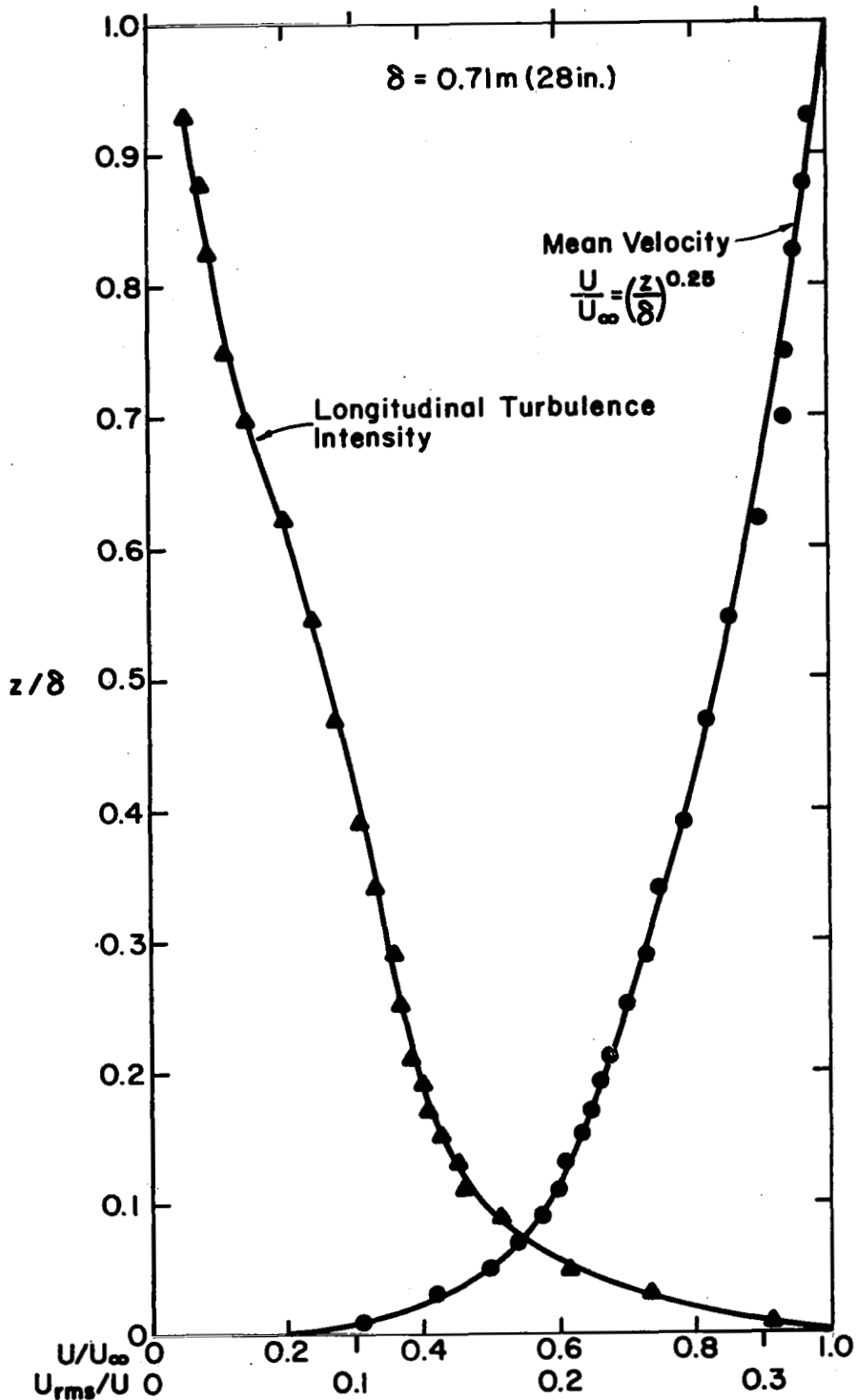
Figure 2. Mean Velocity and Turbulence Intensity Profiles
for Test Condition 1
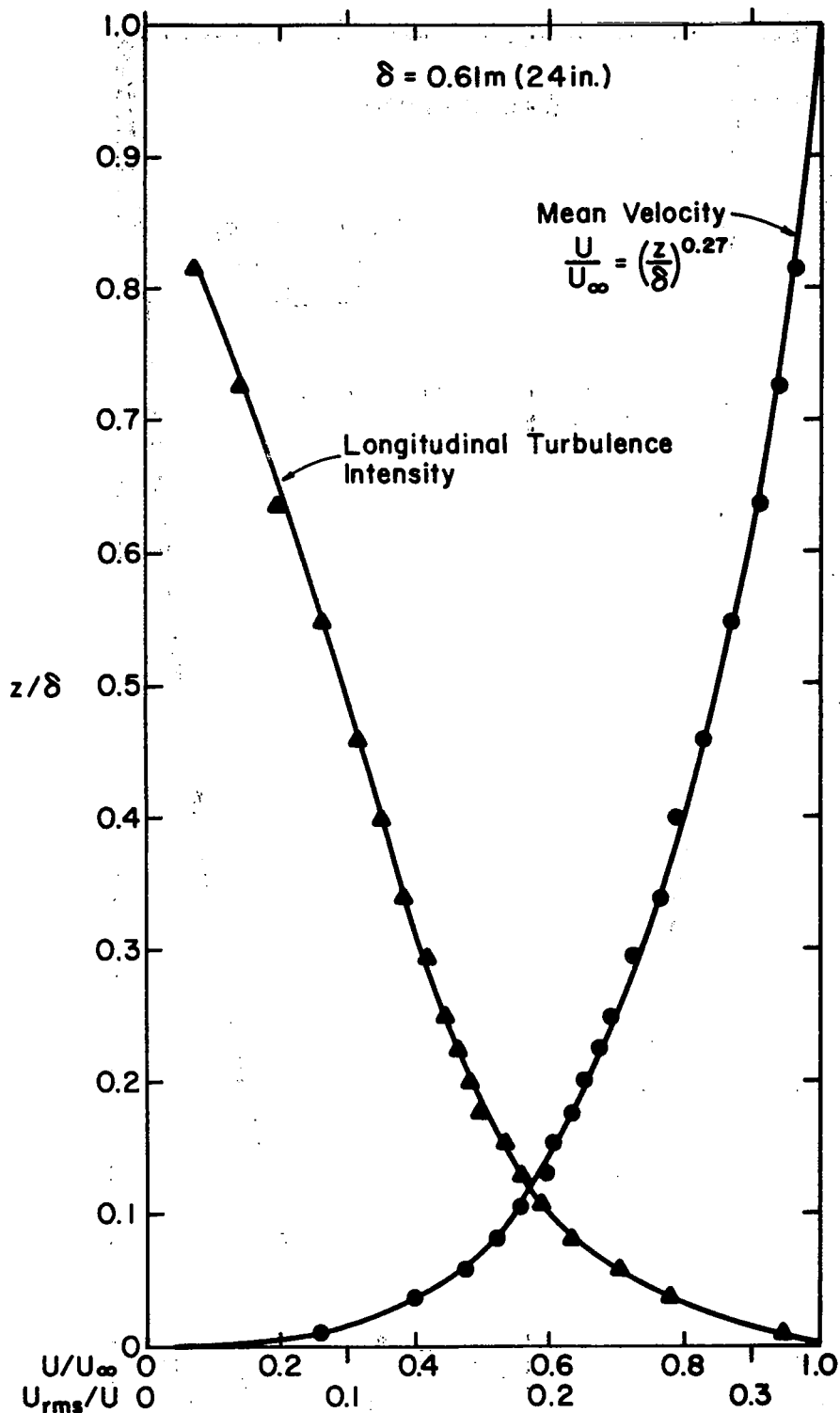
Figure 3. Mean Velocity and Turbulence Intensity Profiles
for Test Condition 2
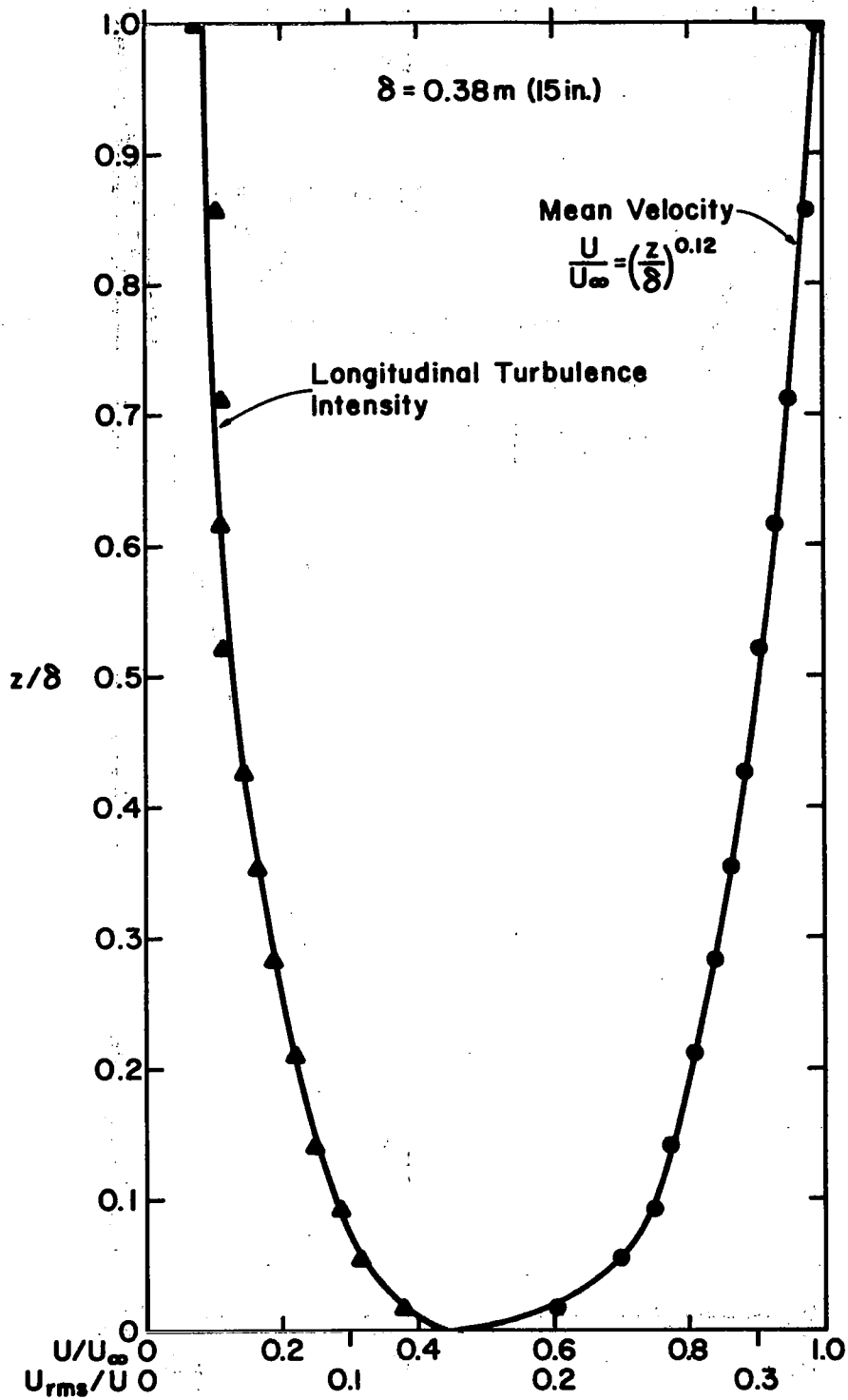
Figure 4. Mean Velocity and Turbulence Intensity Profiles
for Test Condition 3
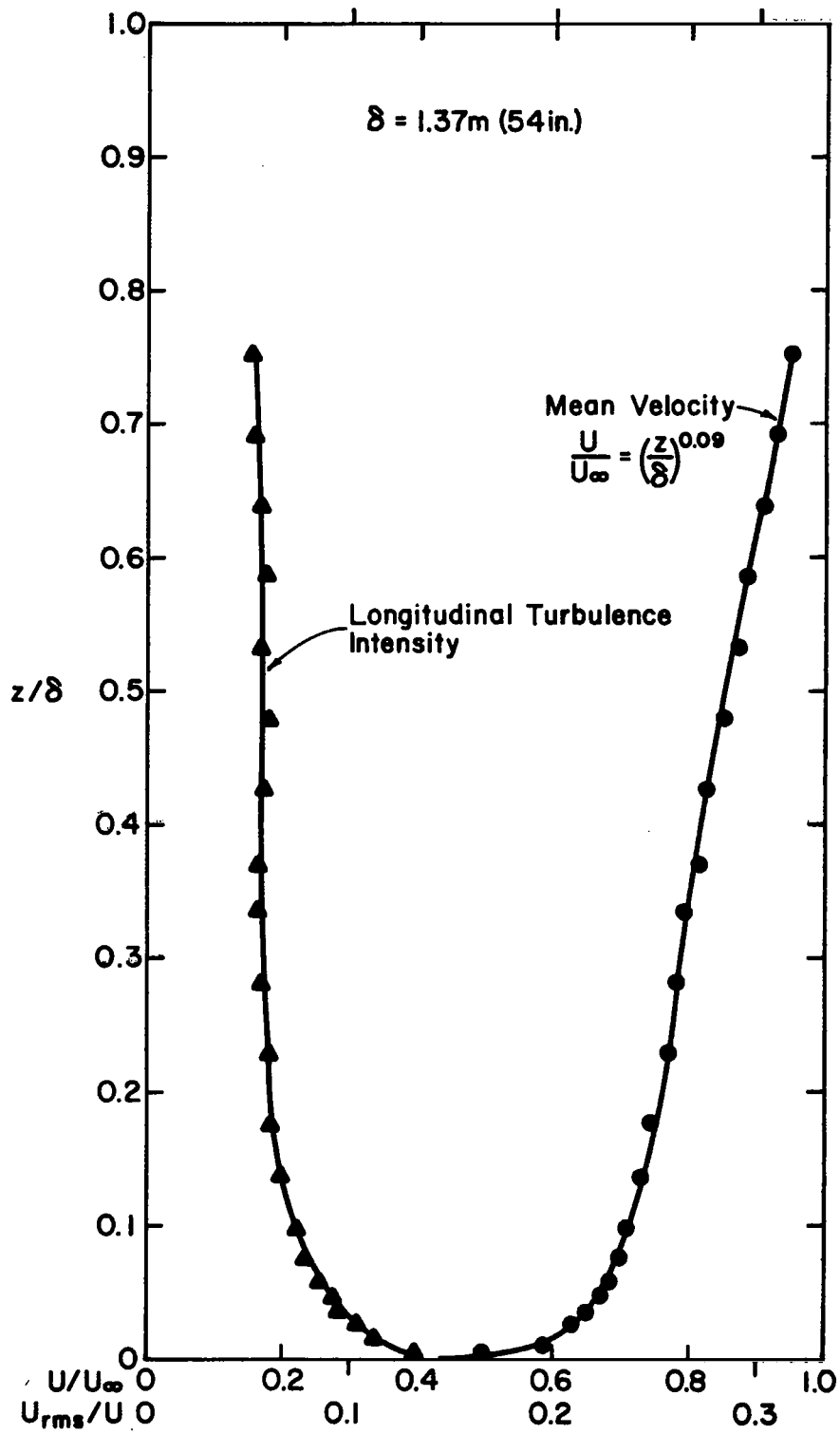
Figure 5. Mean Velocity and Turbulence Intensity Profiles
for Test Condition 4
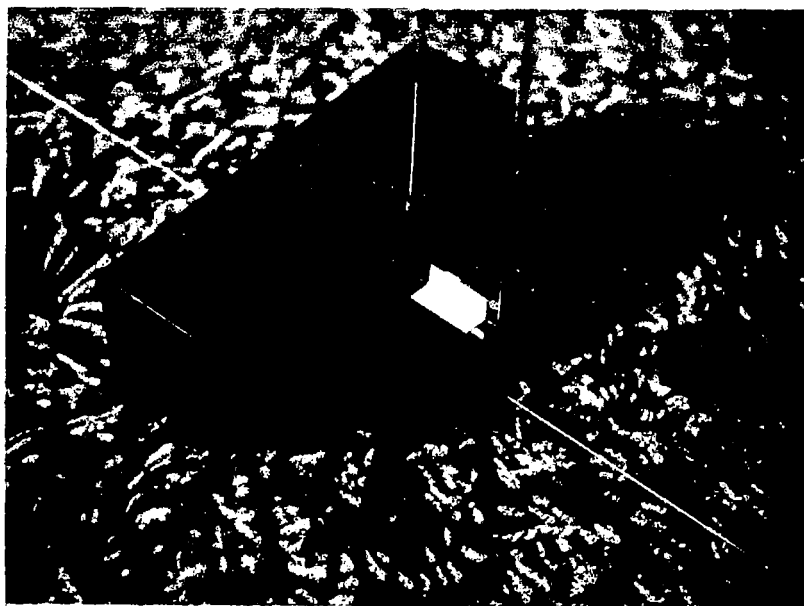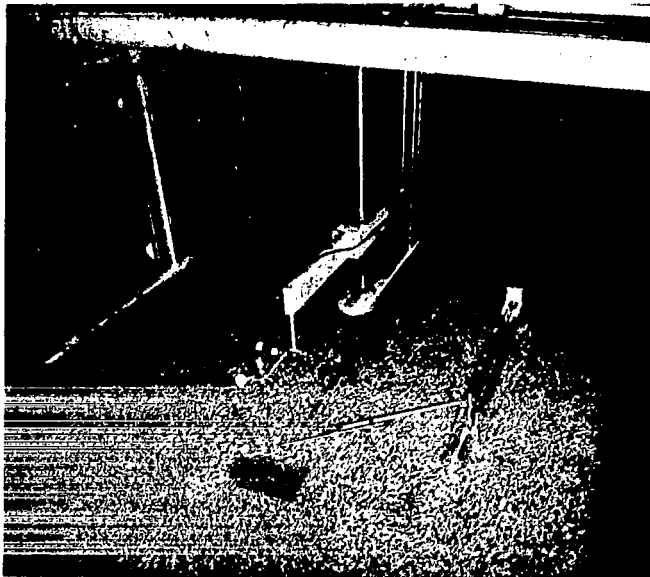
Figure 7. Paddle Wheel Vorticity Meter
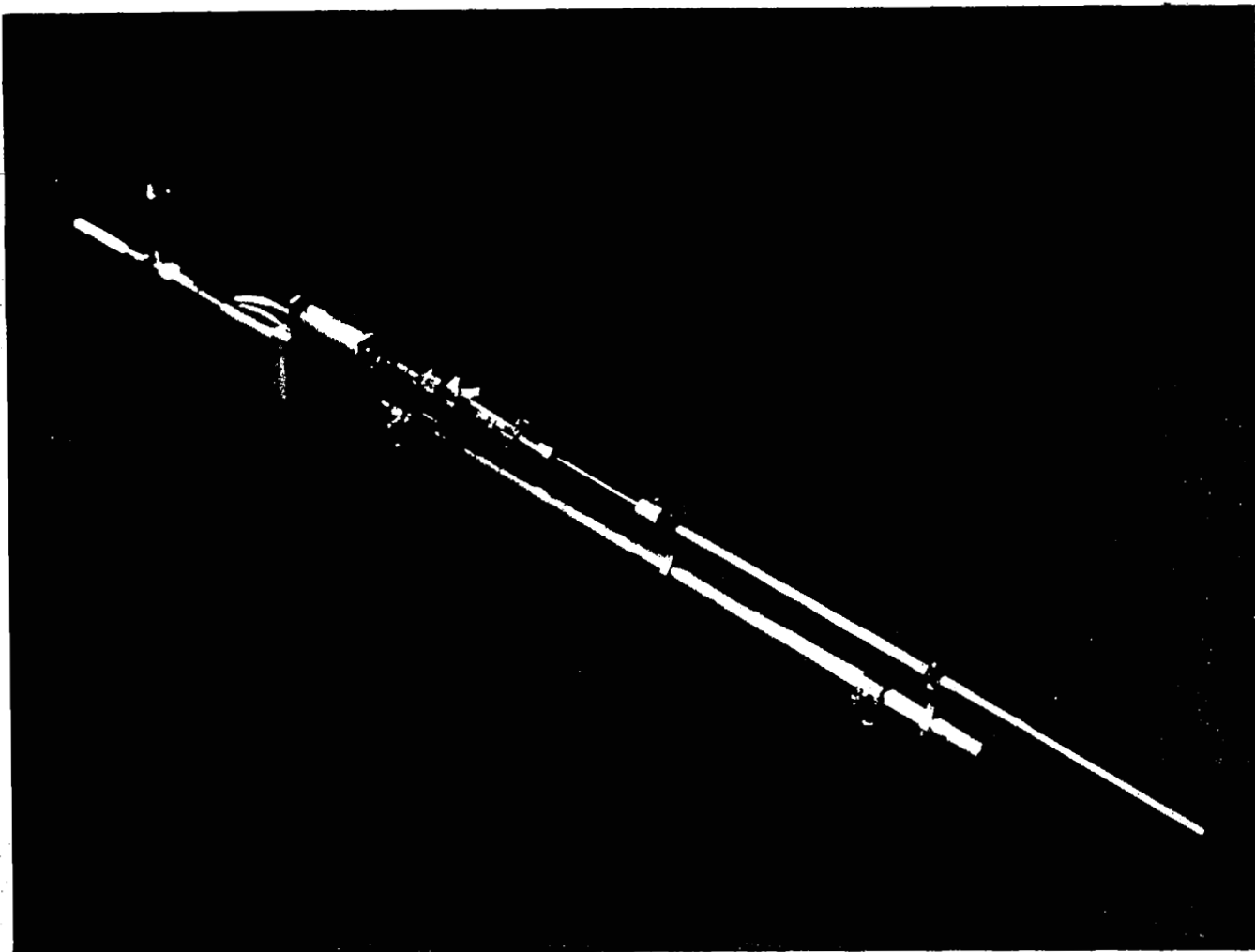
Figure 8. Rotated Hot-Film Probe
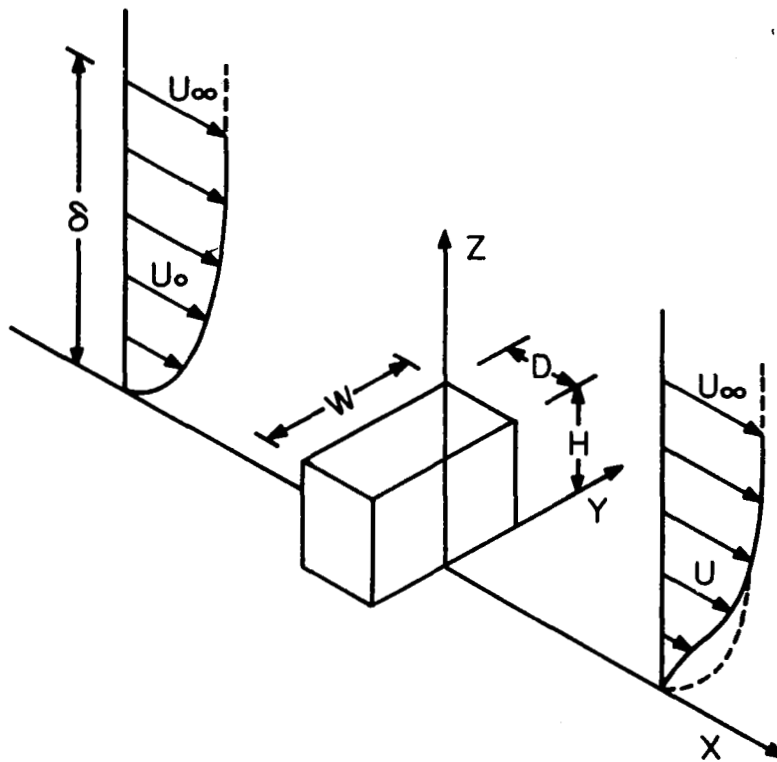
Figure 9. Model Coordinate System and Symbol Definition
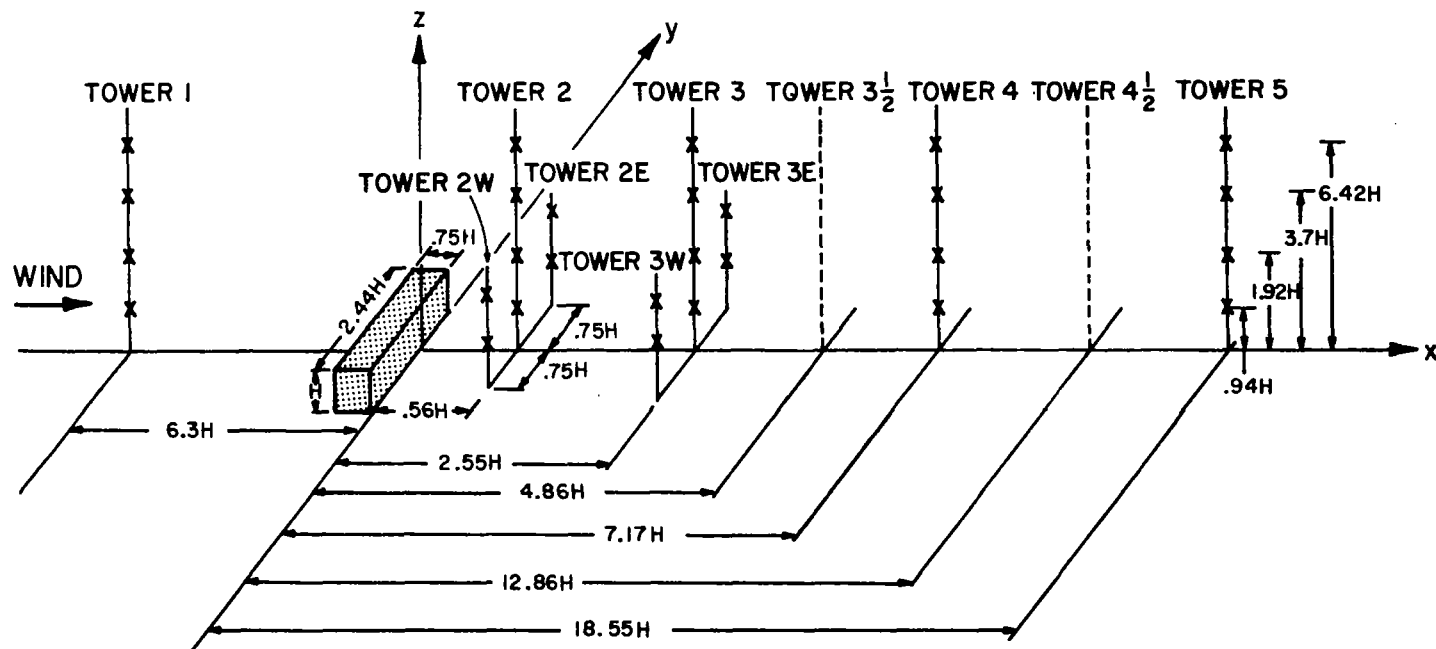
Figure 10. Schematic View of the NASA, George C.
Marshall Space Flight Center Boundary-
Layer Facility for the First Building
(Not to Scale)
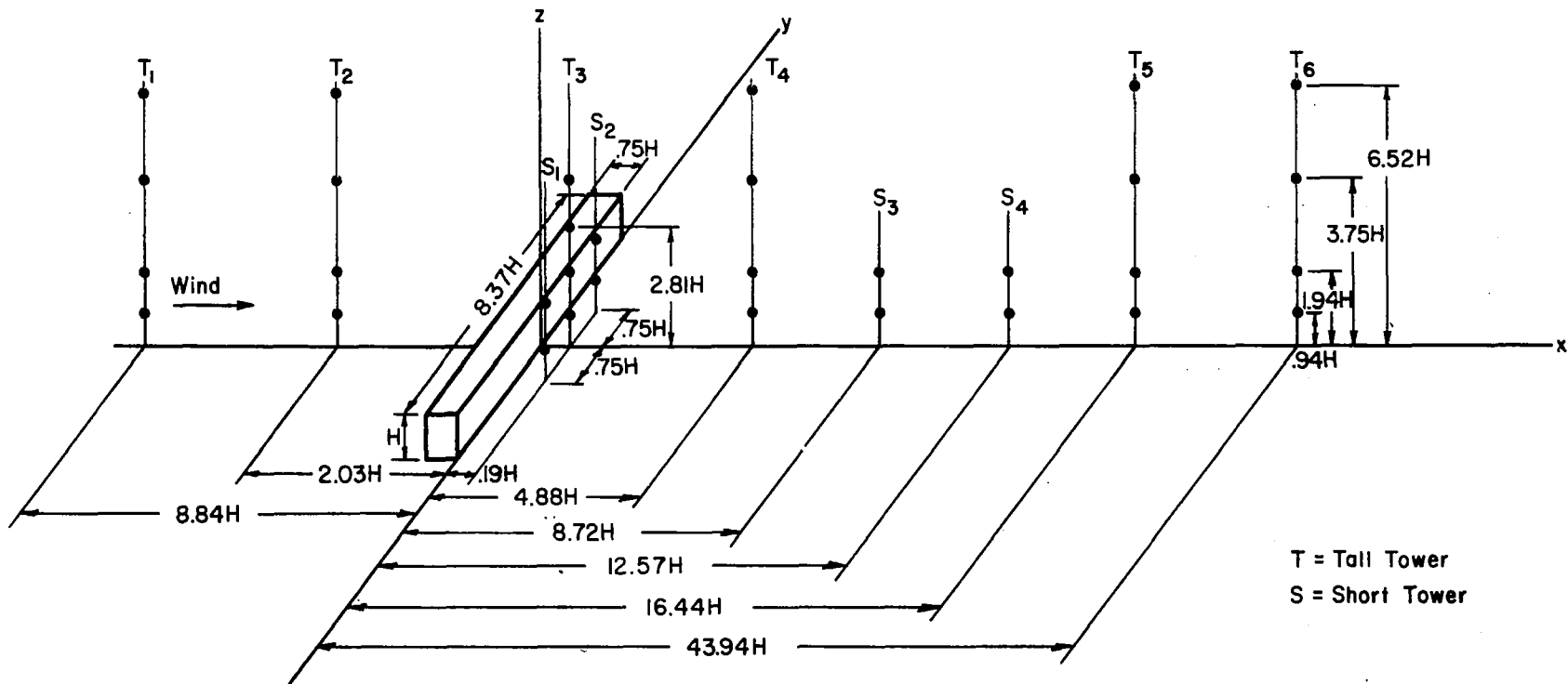
Figure 11. Schematic View of the NASA, George C. Marshall
Space Flight Center Boundary-Layer Facility
for the Second Building (Not to Scale)
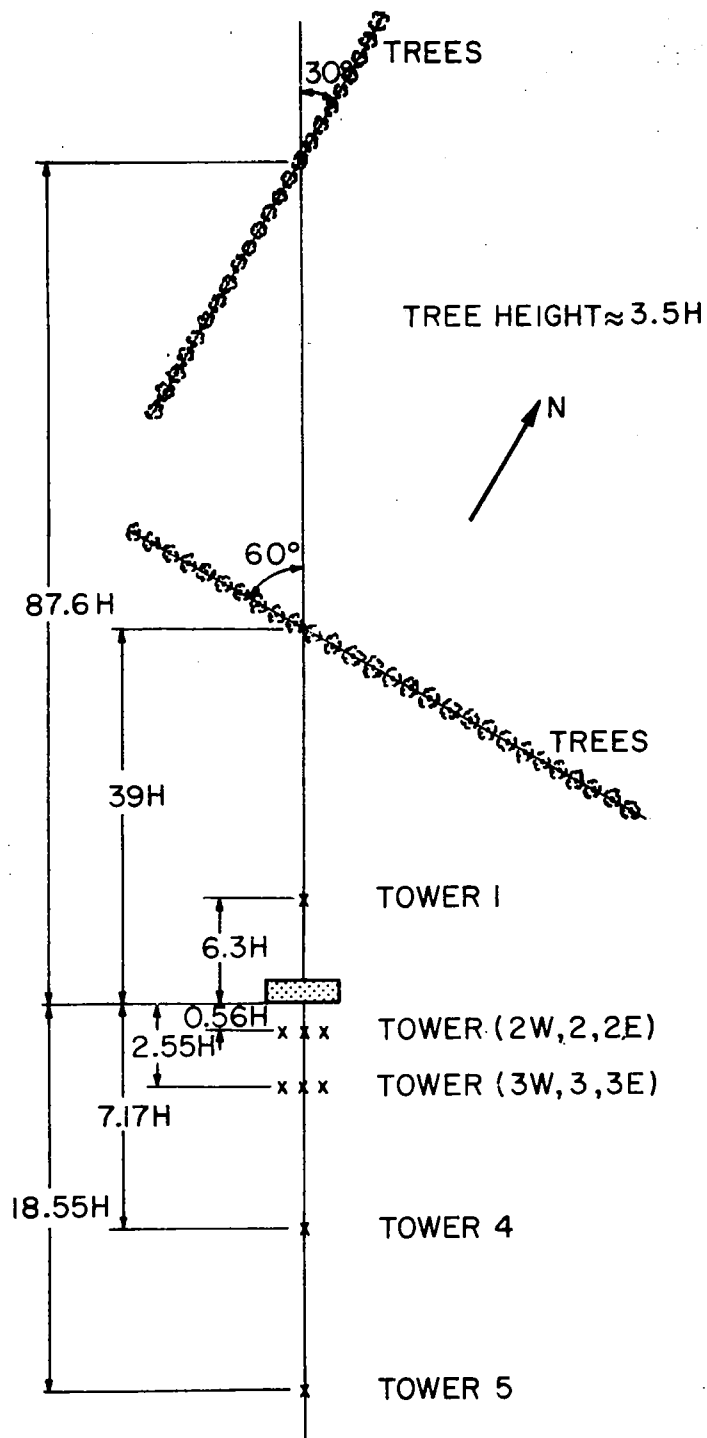
Figure 12. Plan View of the NASA, George C. Marshall Space Flight
Center Boundary-Layer Facility for the First Building
(Not to Scale)

Figure 13. Wind Tunnel Experimental Configuration
with Upwind Trees Included
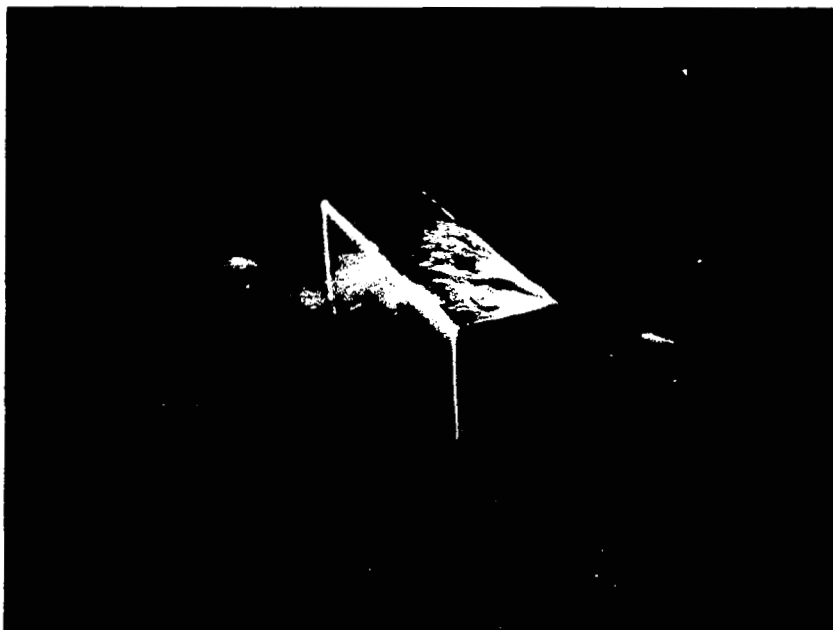
Figure 14. Flow Visualization of the Roof-Corner Vortices with
the Wind Approaching at 47 Degrees to the Normal to
the Long Face of the Building ($\alpha = 47°$)
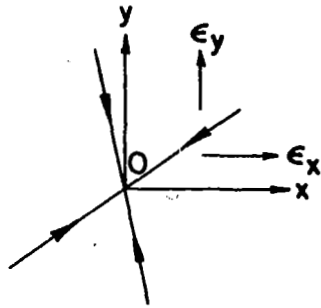
Figure 15. Singular Point, $\epsilon_x = \epsilon_y = 0$
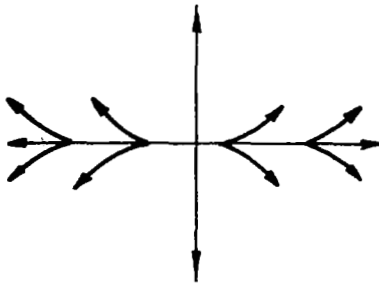
(a) $\Delta > 0$ Attachment Point
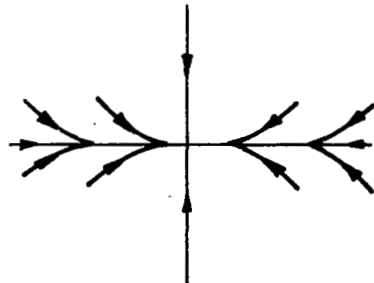
(b) $\Delta < 0$ Separation Point

Figure 16. Node Points, $\Delta^2/4 \geq J > 0$, λ has Real Values
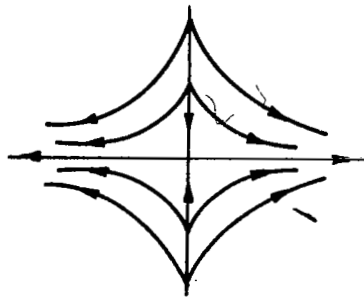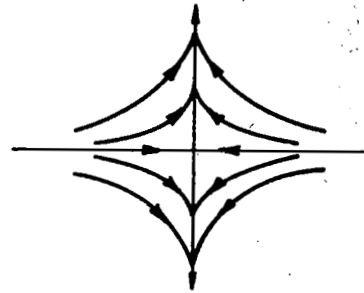
(a) $\Delta > 0$ Attachment   (b) $\Delta < 0$ Separation

Figure 17. Saddle Points, $\Delta^2/4 \geq J$, $J < 0$
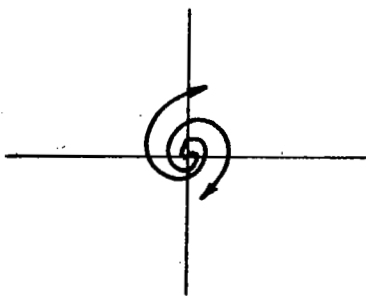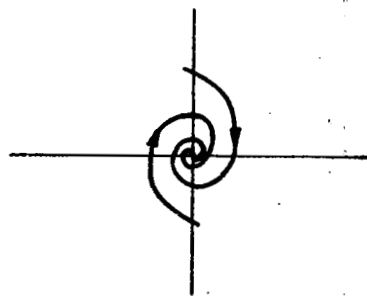
(a) $\Delta > 0$ Attachment   (b) $\Delta < 0$ Separation

Figure 18. Nodes (Foci), $J > \Delta^2/4$, λ is Complex
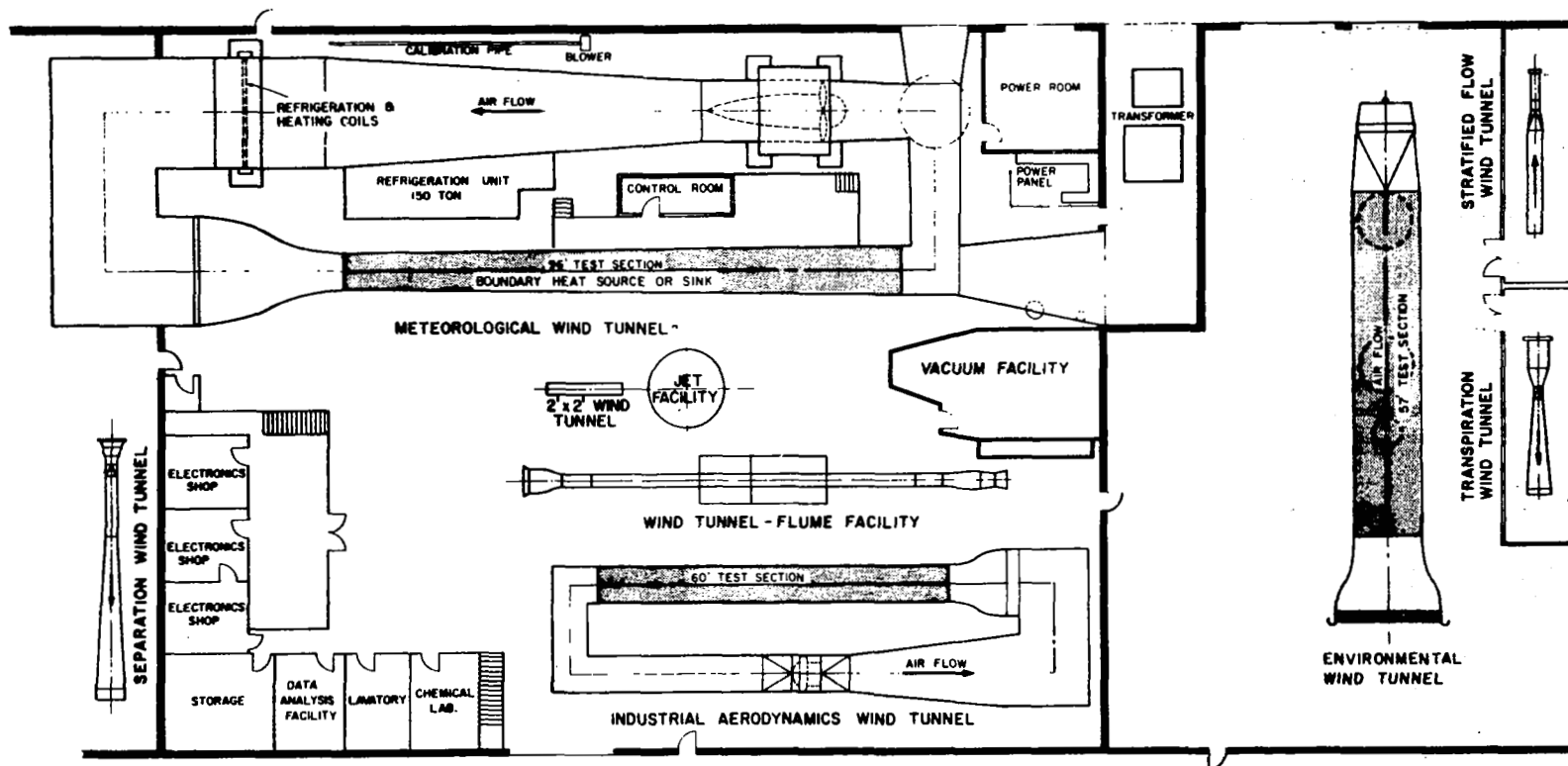
Figure 19. Fluid Dynamics and Diffusion Laboratory
at Colorado State University
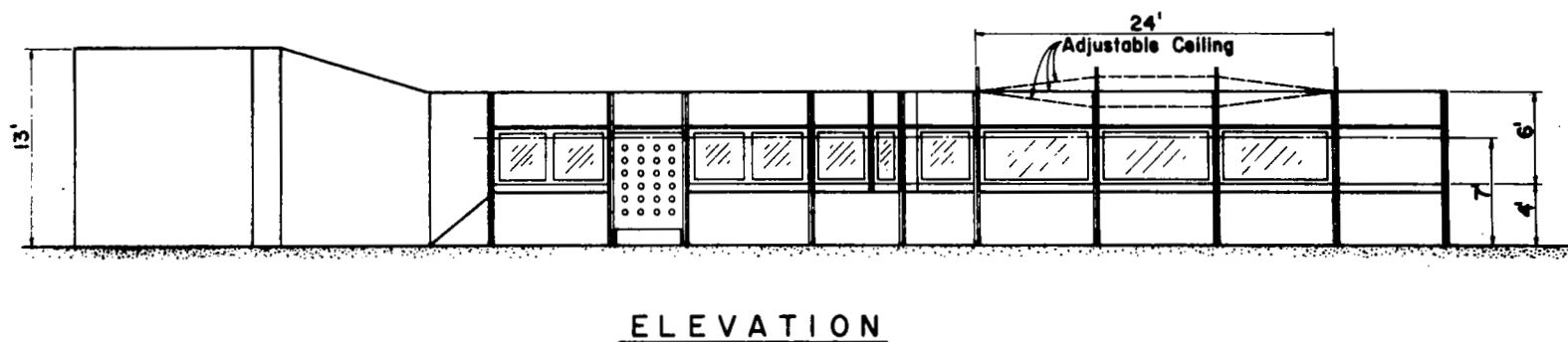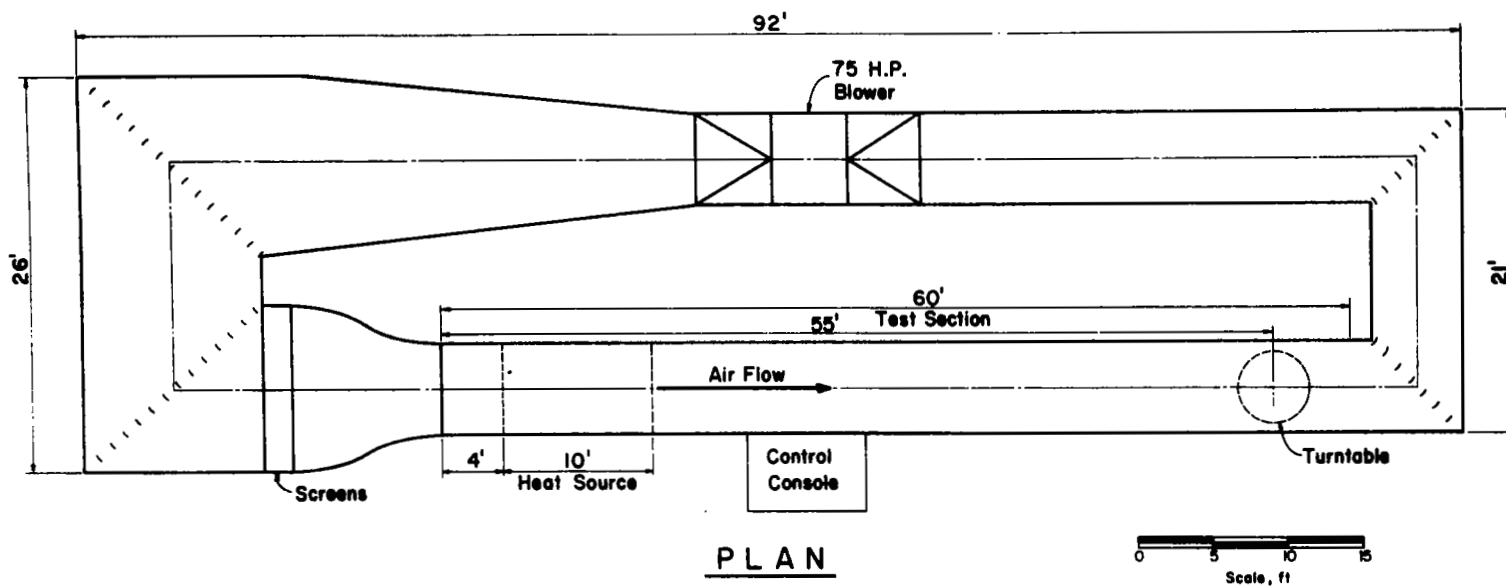
Figure 20.   Industrial Aerodynamics Wind Tunnel
at Colorado State University
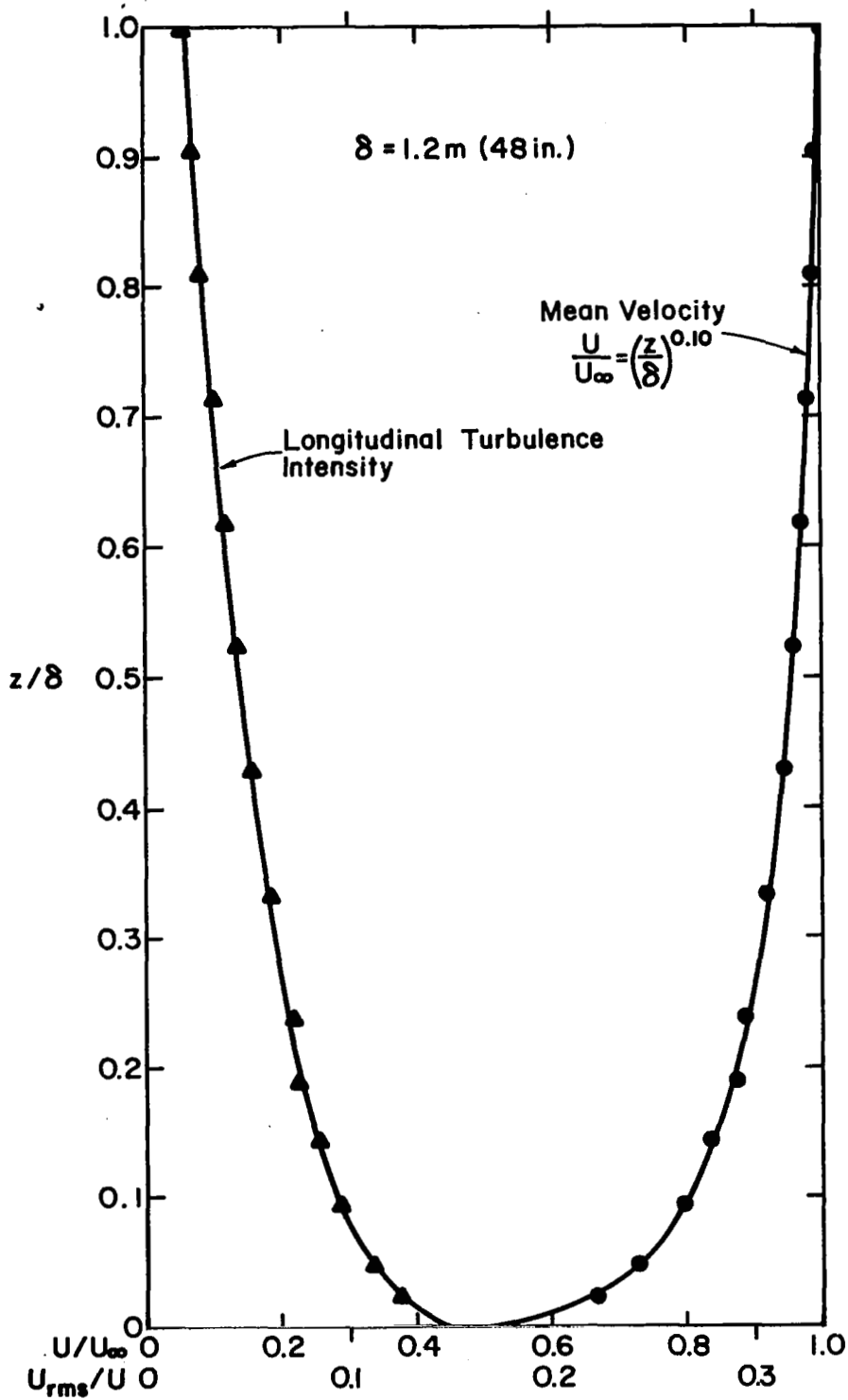
Figure 21. Mean Velocity and Turbulence Intensity
Profiles for the Oil Flow Tests
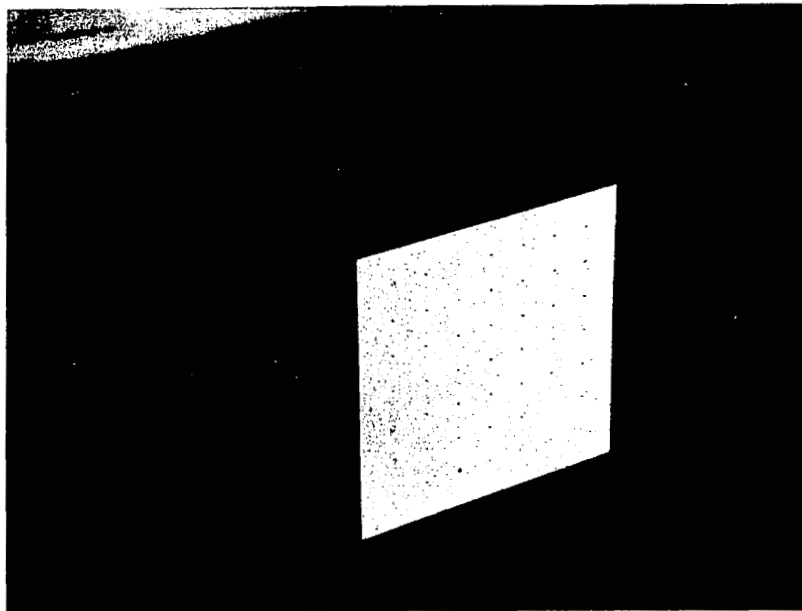
Figure 22. Model Used for Smoke-Visualization Tests
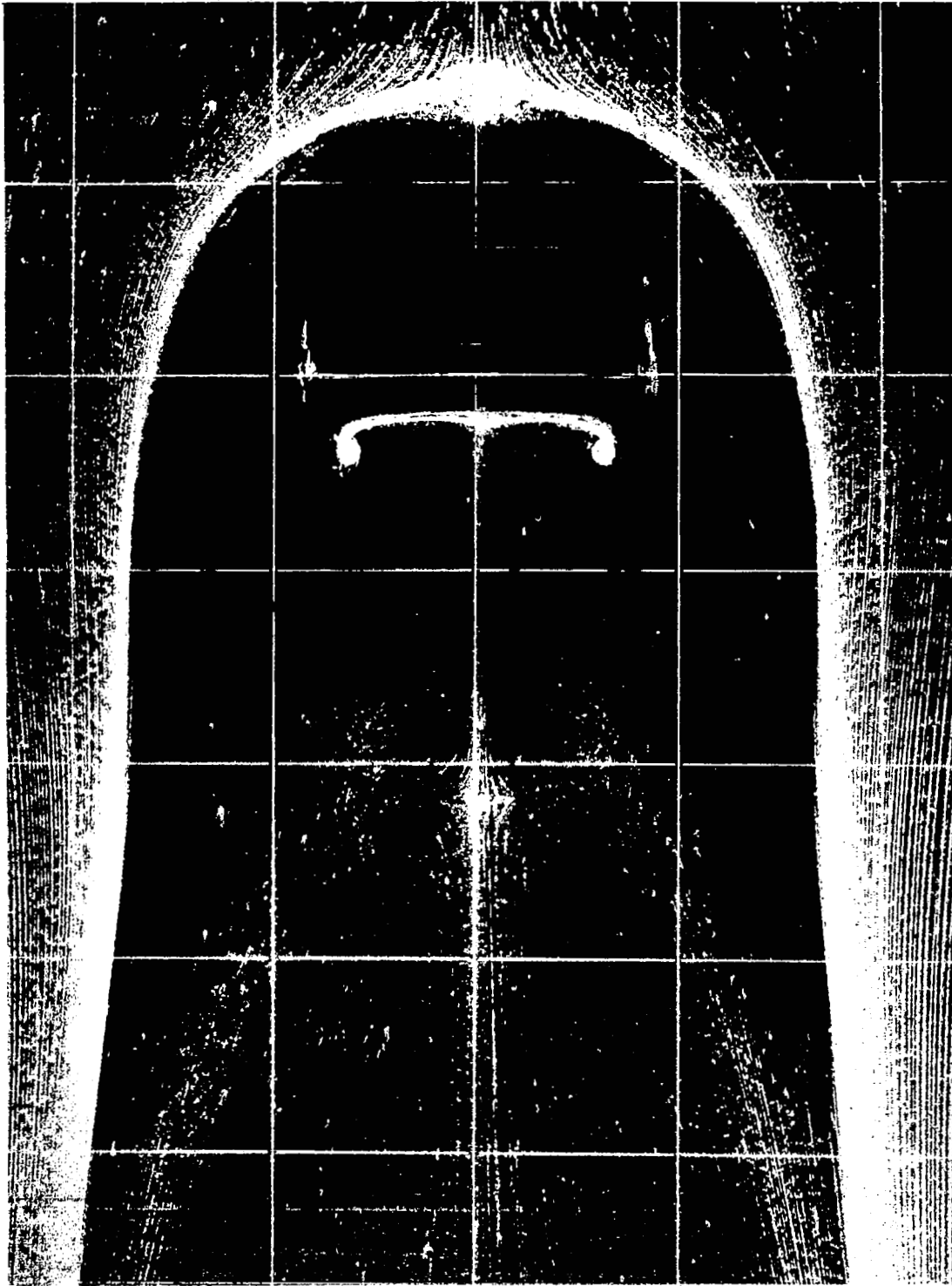
Figure 23. Oil Flow Pattern for Model 2. Grid Size
is 10.2 cm (4.0 in.)
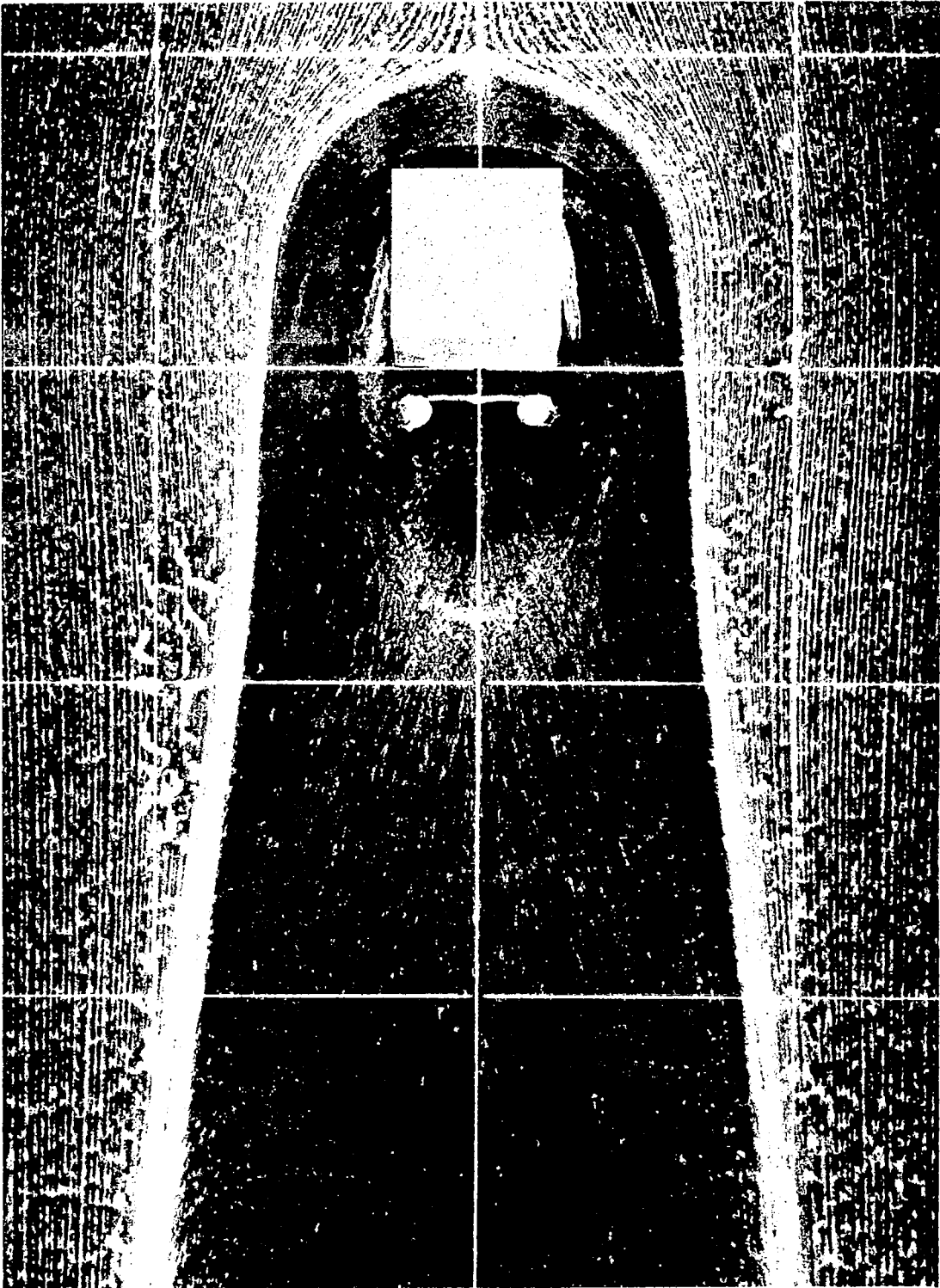
Figure 24. Oil Flow Pattern for Model 7. Grid Size
is 10.2 cm (4.0 in.)

Figure 25.   Oil Flow Pattern for Model 2 at 47
             Degree Flow Direction.   Grid Size
             is 10.2 cm (4.0 in.)
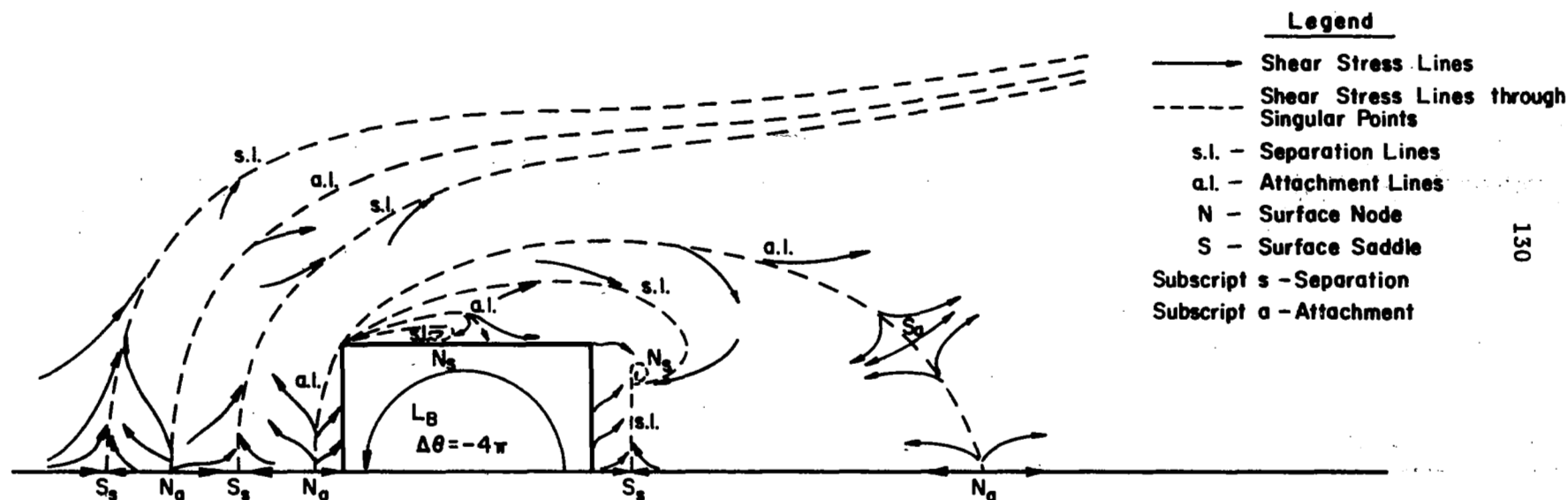
Figure 26. Shear Stress Lines and Streamlines on the
Baseplate for Flow around Model 7
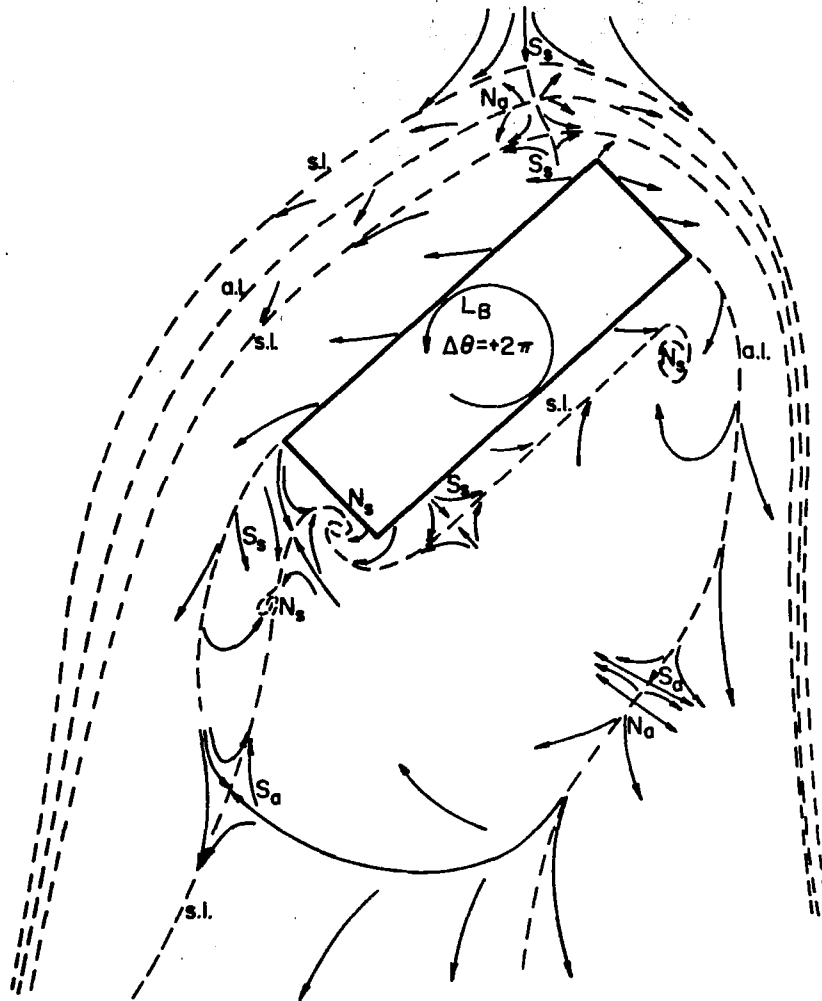
Figure 27. Shear Stress Lines and Streamlines on the Baseplate for Flow around Model 2 at α = 47 Degrees (See Figure 26 for Legend)
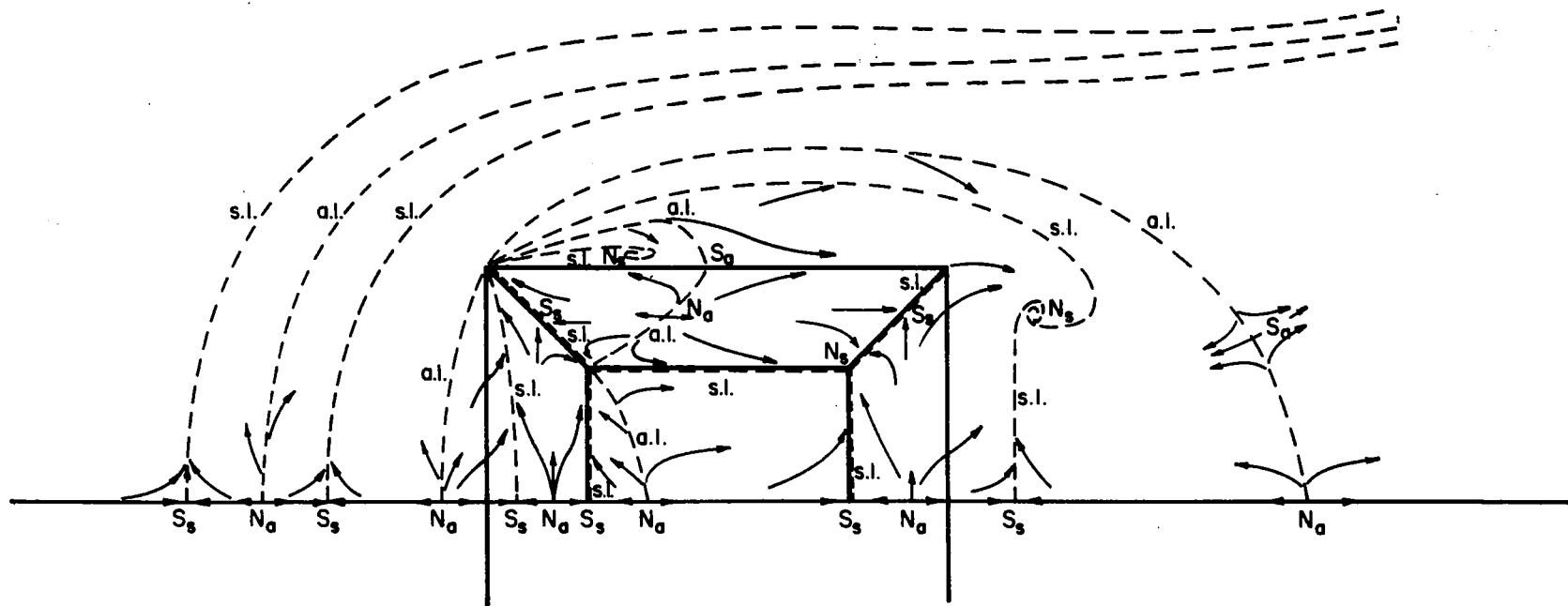
Figure 28. Hypothetical Shear Stress Lines and Streamlines for the Flow
around Rectangular Blocks with Reattachment of the Free
Shear Layer (See Figure 26 for Legend)

Legend

N — Node of Streamline Pattern

S,S′ — Saddles of Streamline Pattern

Subscript s — Separation

Subscript a — Attachment

N — Surface Node

S — Surface Saddle

Streamline

Primary
Horseshoe Vortex
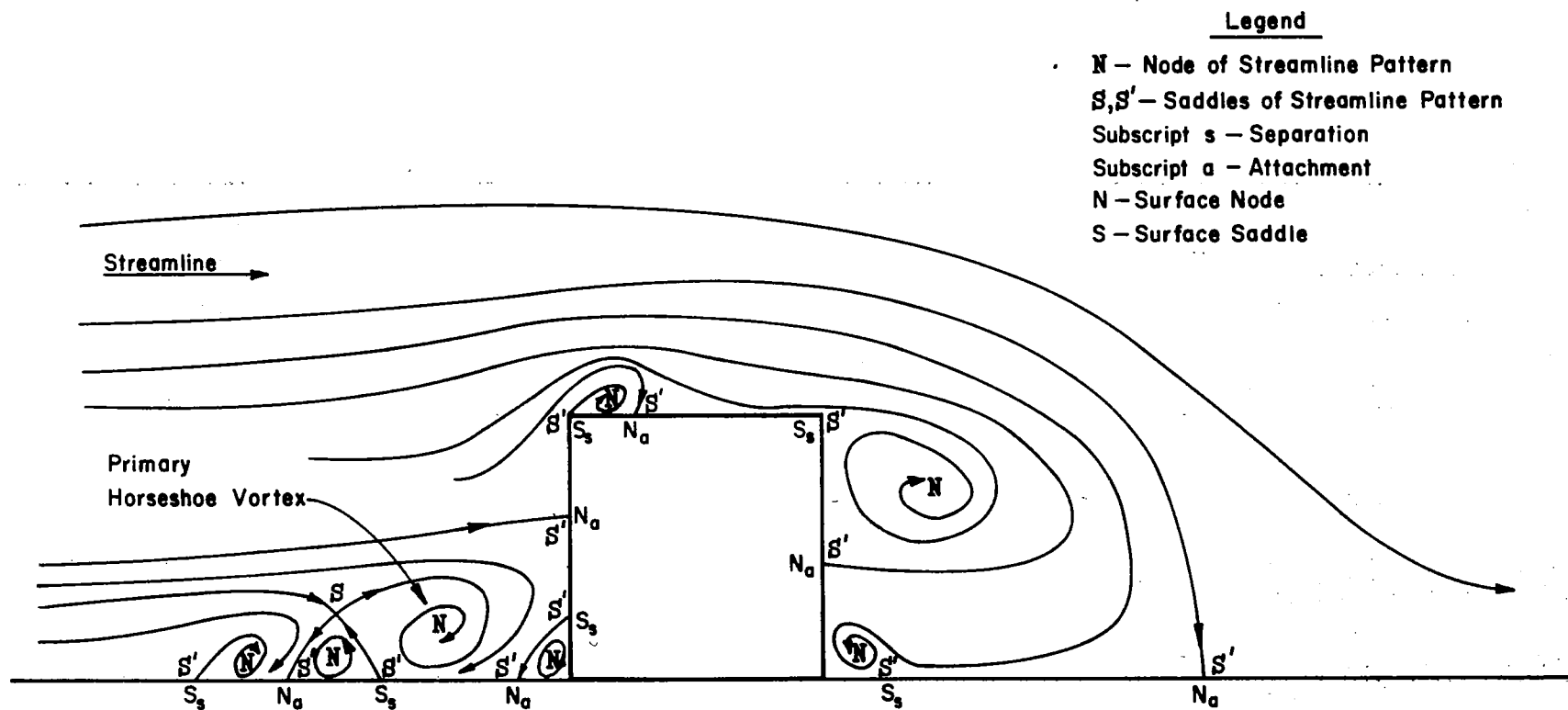
Figure 29.   Streamlines in the Flow on the Centerline for
Rectangular Blocks with Reattachment of the
Free Shear Layer
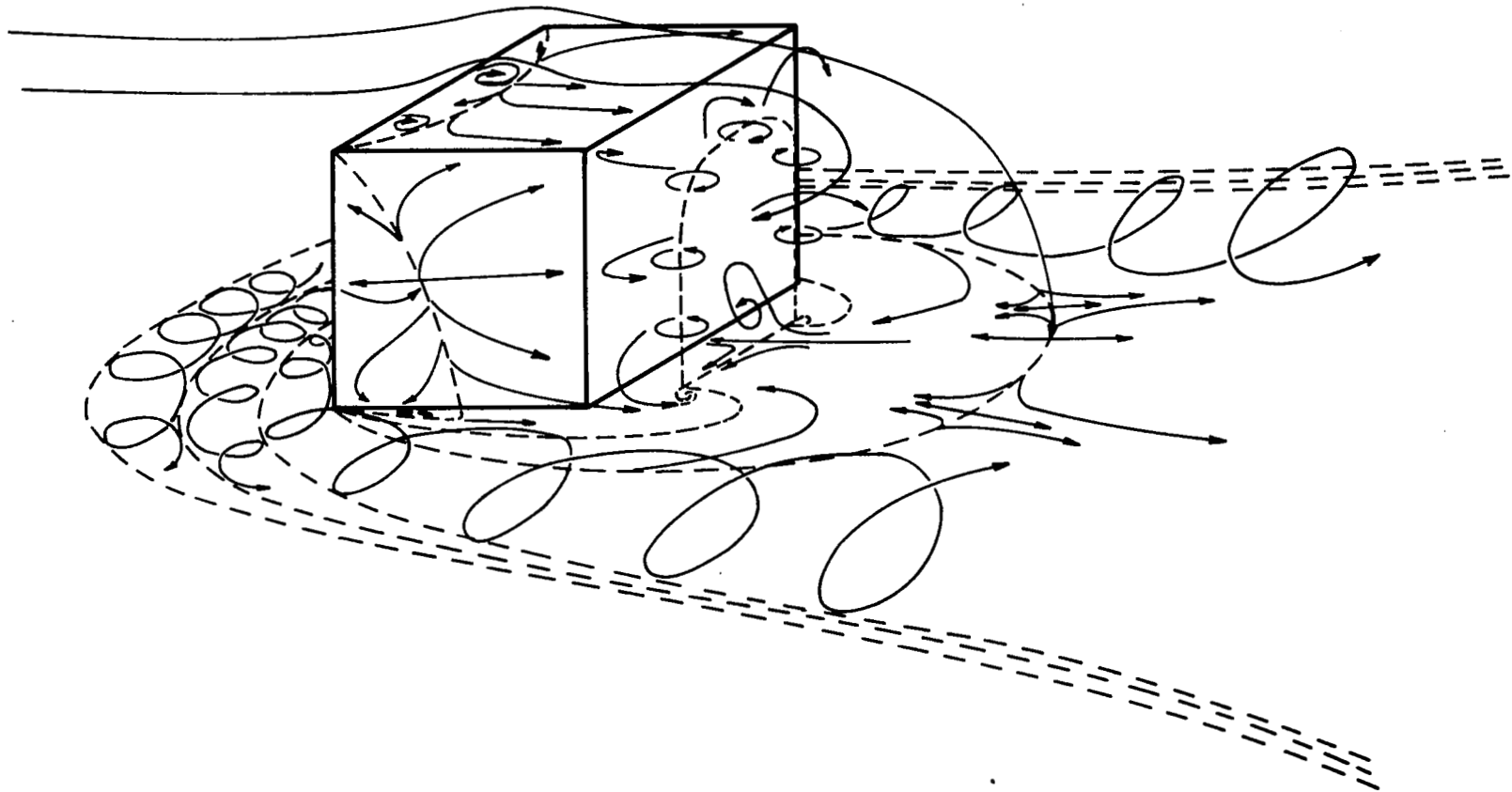
Figure 30. Flow Pattern around a Rectangular Block with Reattachment
of the Free Shear Layer
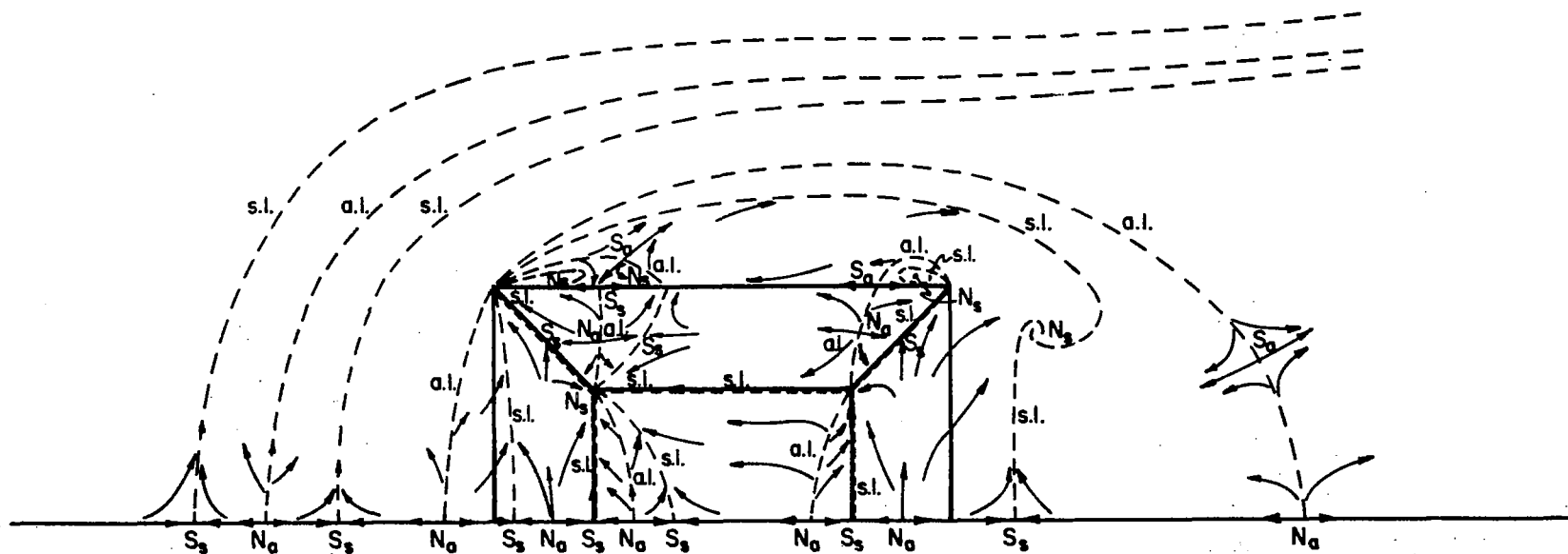
Figure 31. Hypothetical Shear Stress Lines and Streamlines for Flow
around Rectangular Blocks with No Reattachment of the
Free Shear Layer (See Figure 26 for Legend)
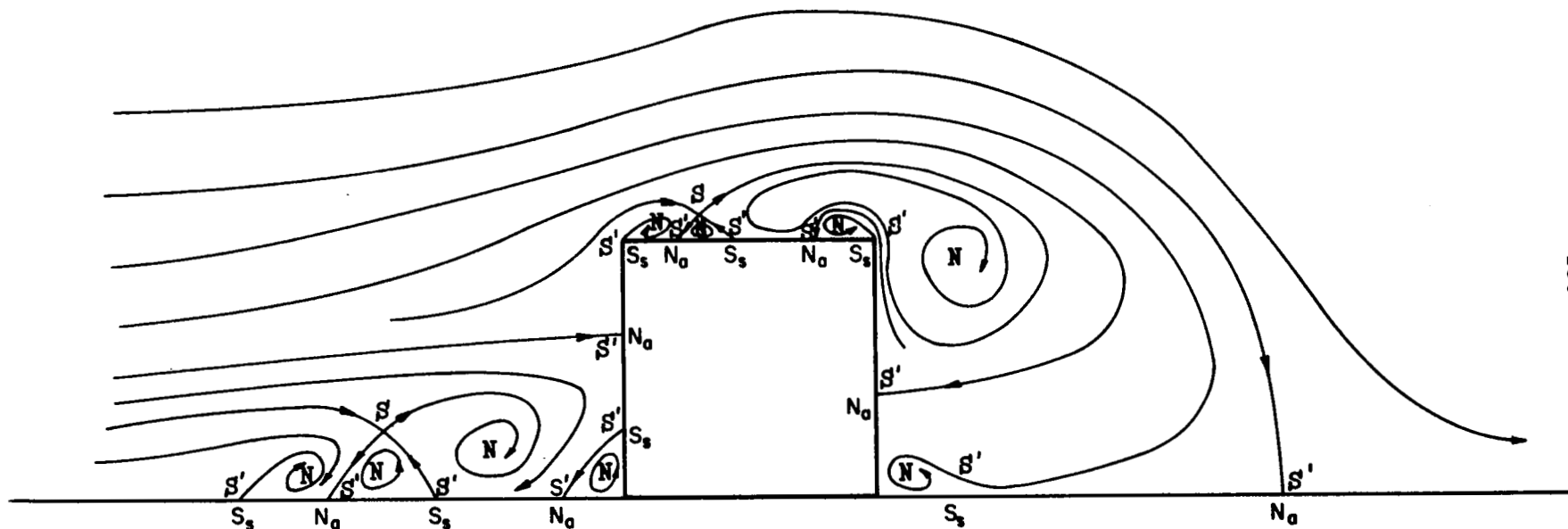
Figure 32. Streamlines in the Flow on the Centerline for
Rectangular Blocks with Reattachment of the
Free Shear Layer (See Figure 29 for Legend)
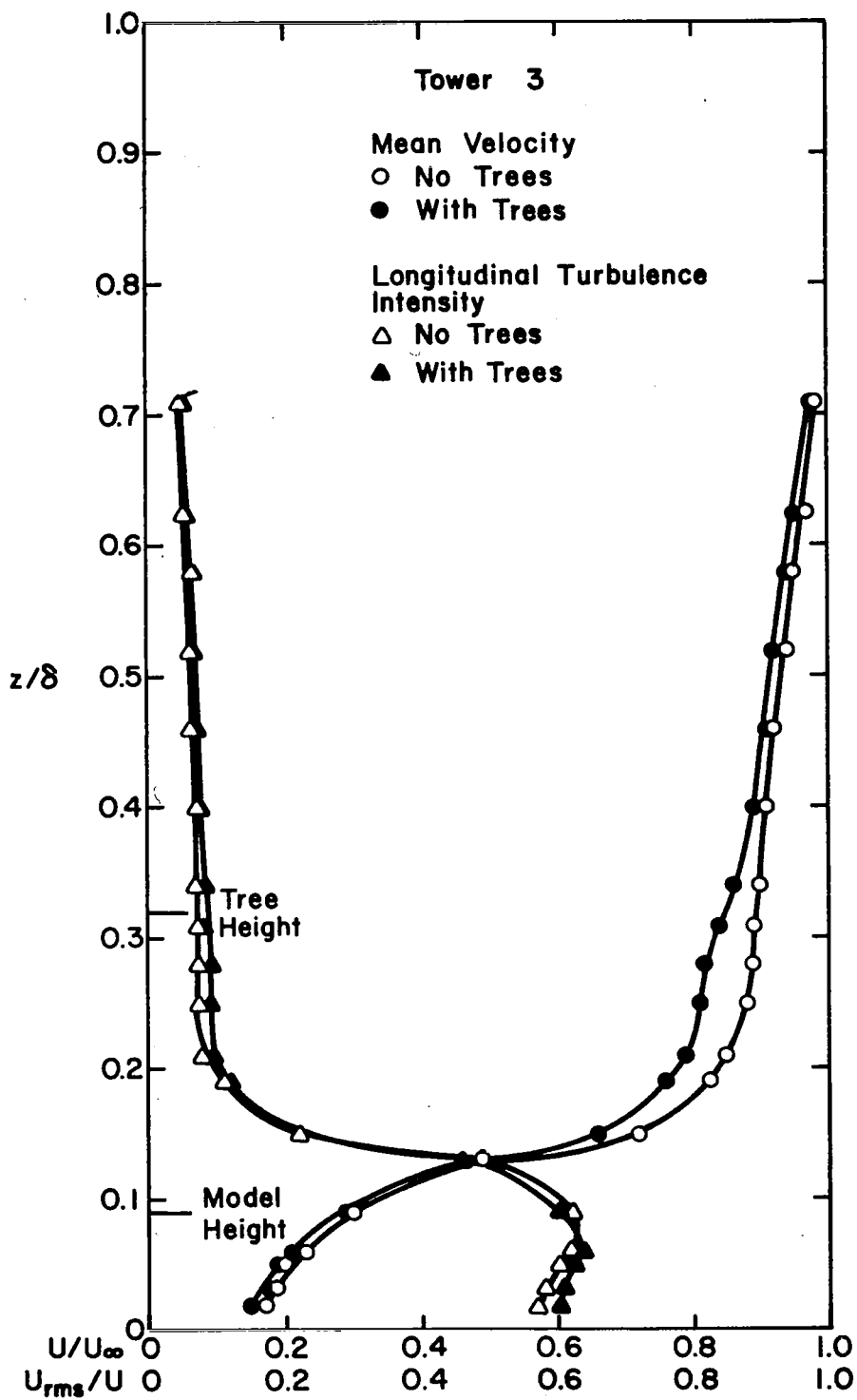
Figure 33.   Tree Influence on Longitudinal Mean Velocity and
Turbulence Intensity behind Model 2
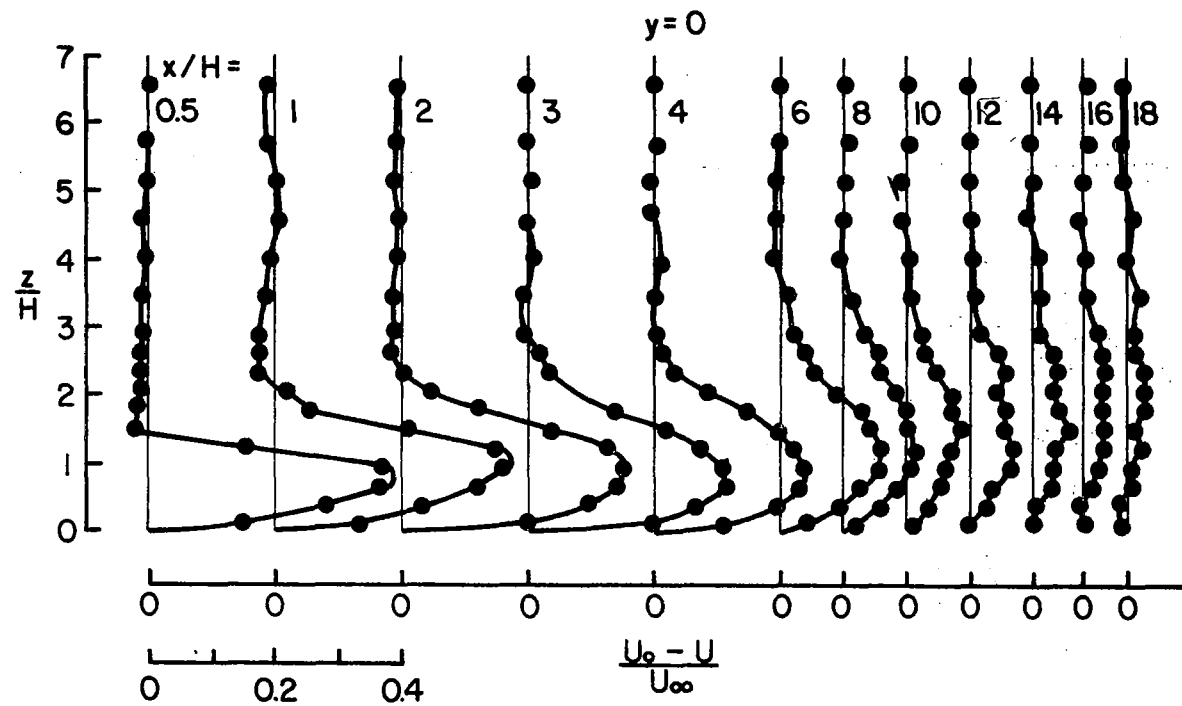
Figure 34.   Vertical Profiles of Mean Velocity Defect
behind Model 2 for Test Condition 1
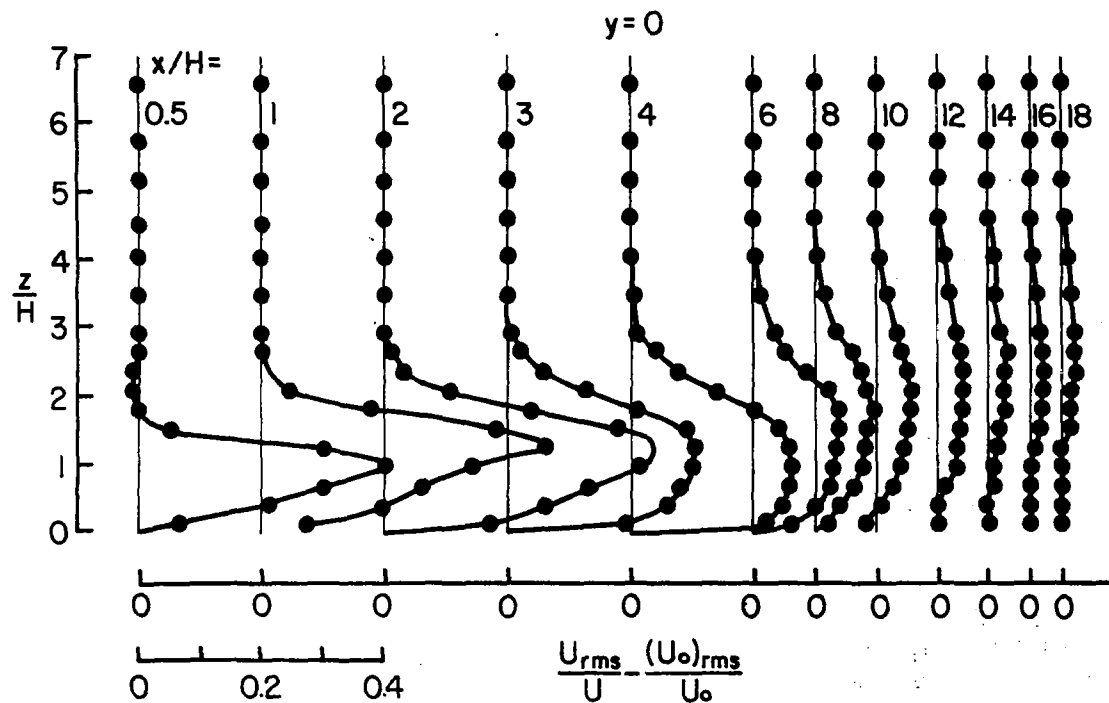
Figure 35. Vertical Profiles of Turbulence Intensity Excess behind Model 2 for Test Condition 1

139
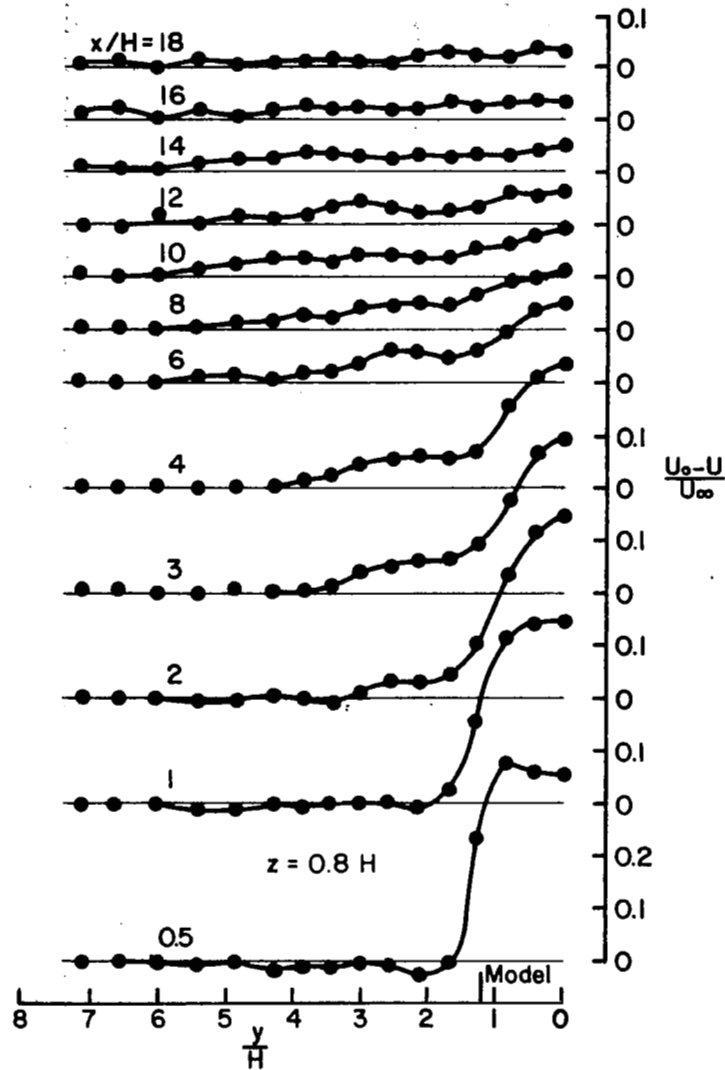
Figure 36. Horizontal Profiles of Mean Velocity Defect
behind Model 2 for Test Condition 1
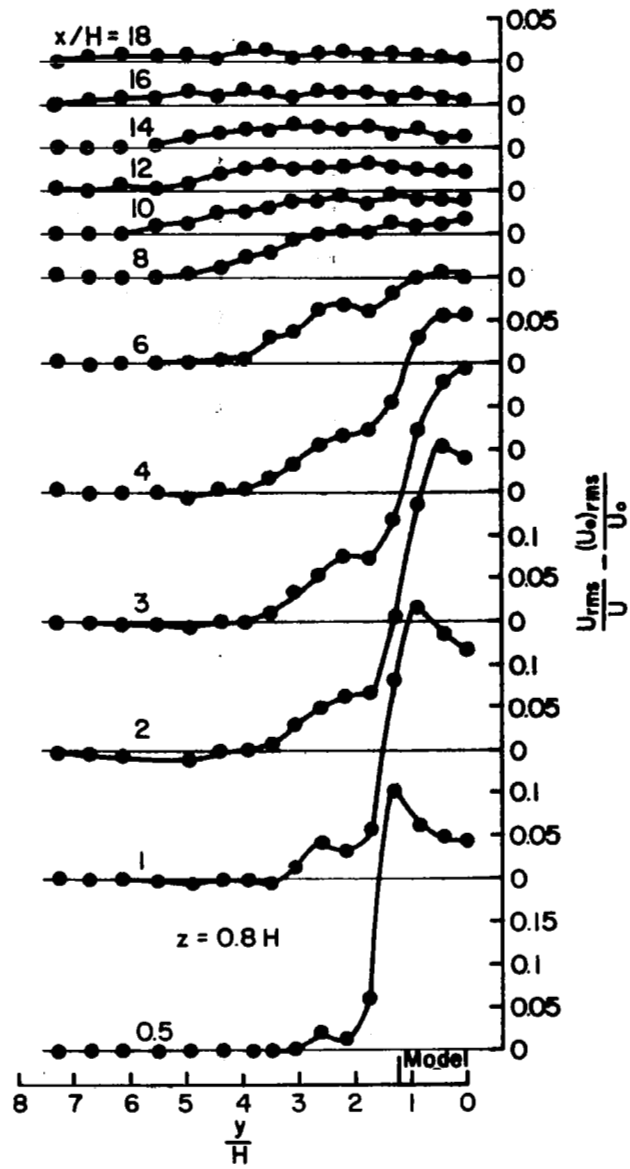
Figure 37. Horizontal Profiles of Turbulence Intensity Excess
behind Model 2 for Test Condition 1
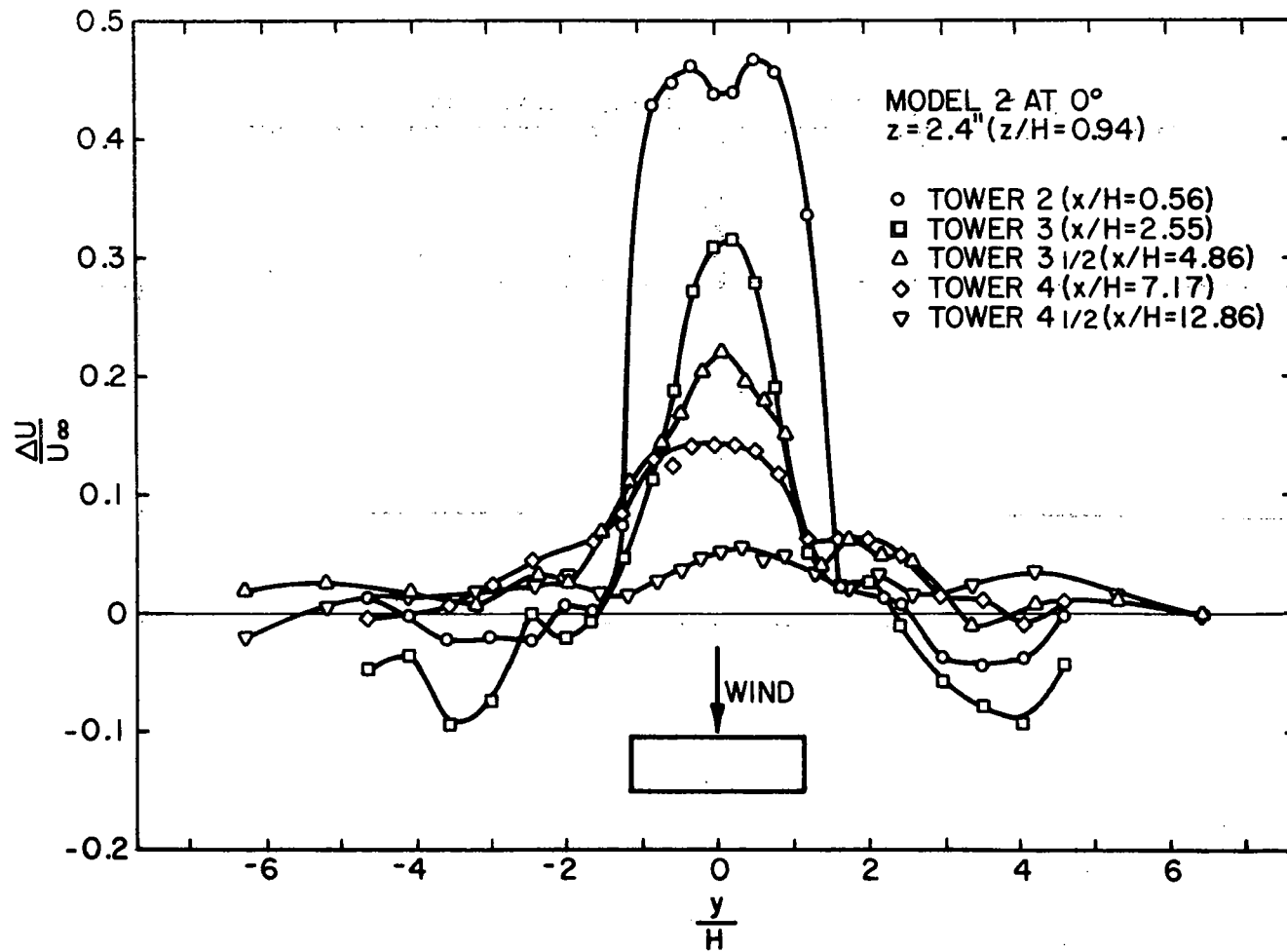
Figure 38. Additional Horizontal Profiles of Mean Velocity
Defect behind Model 2 for Test Condition 1 (37).
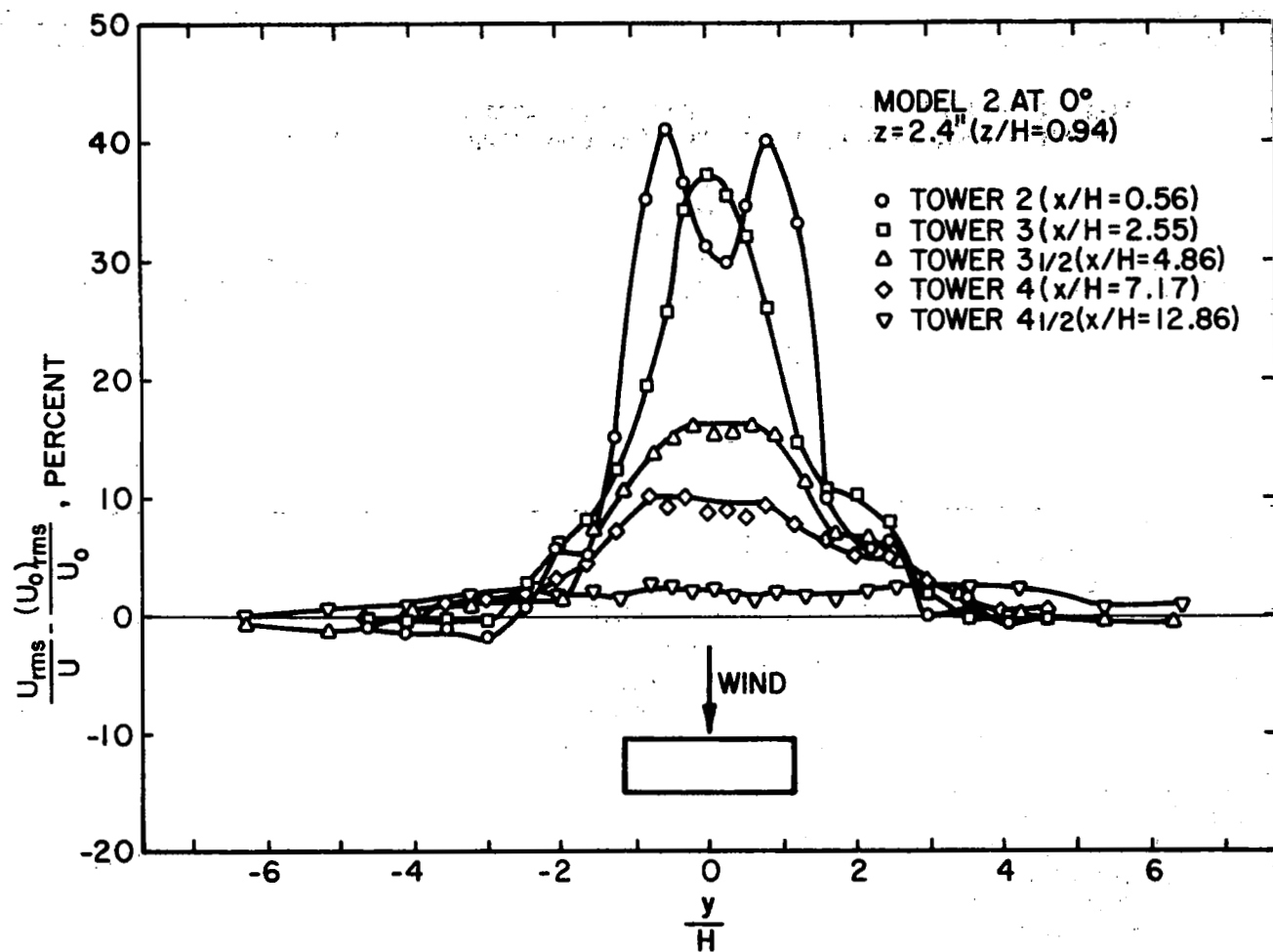
Figure 39. Additional Horizontal Profiles of Turbulence Intensity Excess behind Model 2 for Test Condition 1 (37).
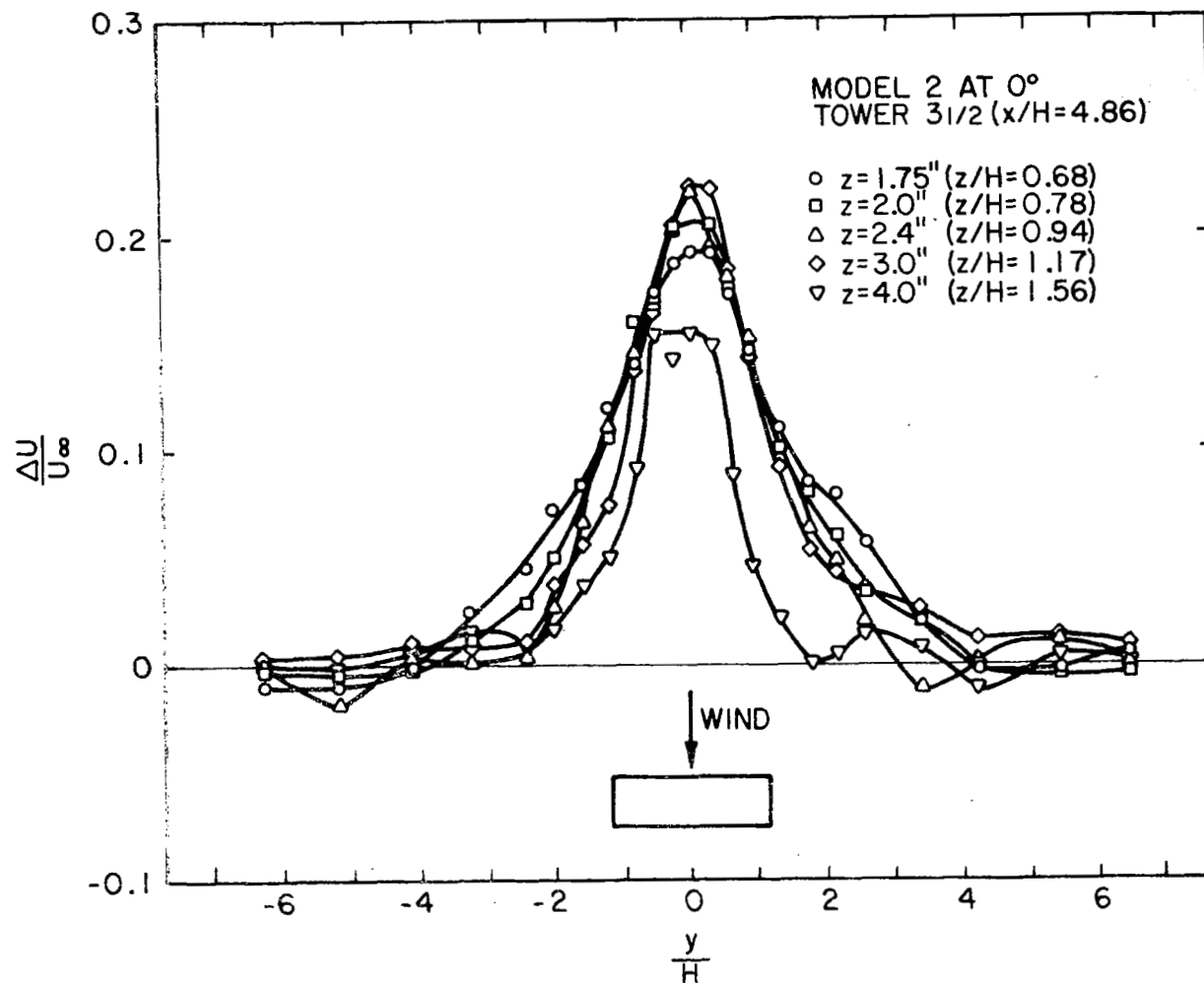
Figure 40. Horizontal Profiles of Mean Velocity Defect at Several
Elevations behind Model 2 for Test Condition 1 (37).
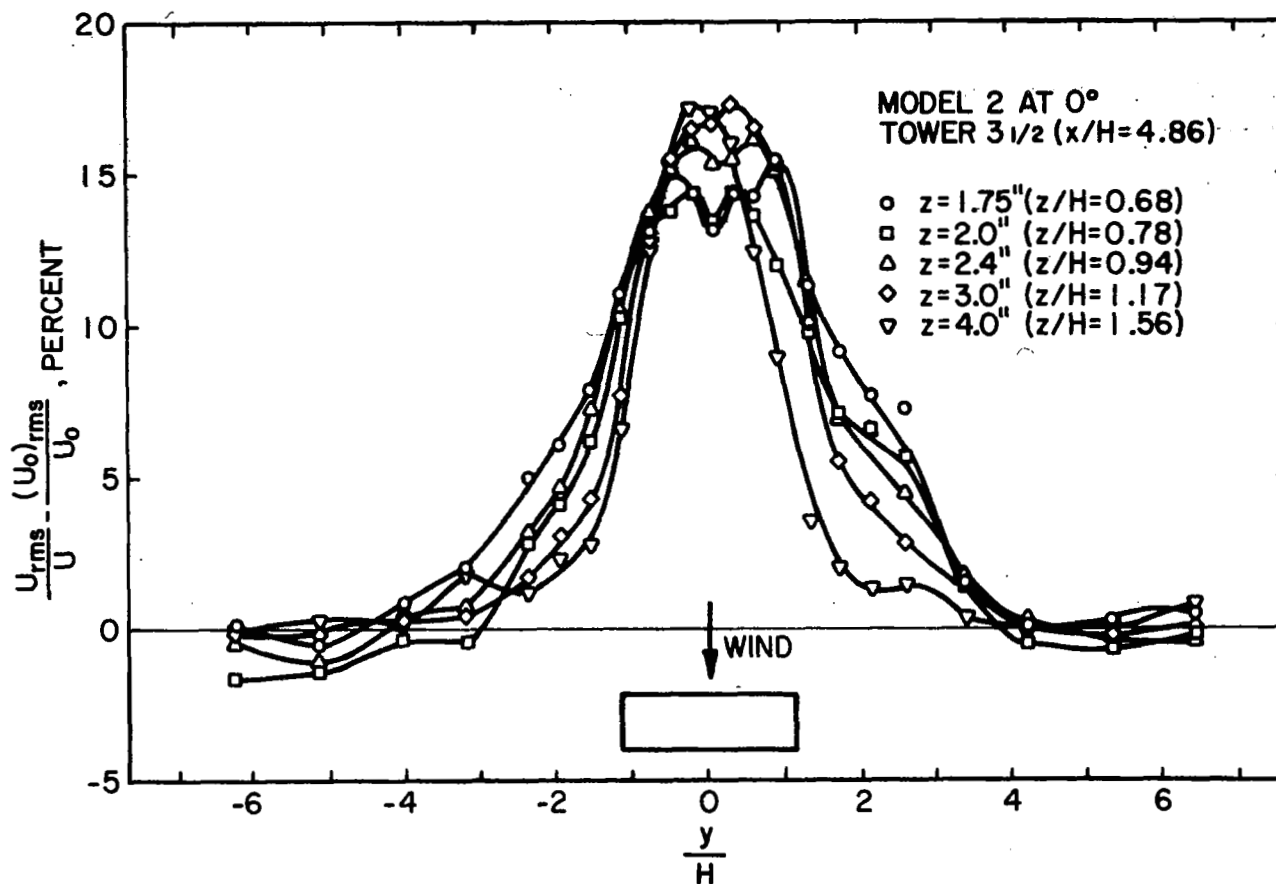
Figure 41.   Horizontal Profiles of Turbulence Intensity Excess at
Several Elevations behind Model 2 for Test Condition 1 (37).

$$\frac{x}{H}=1.0 \quad 3.0 \quad 4.88(T_4) \quad 7.0 \quad 8.72(S_3) \quad 10.5 \quad 12.57(S_4) \quad 14.5 \quad 16.44(T_5) \quad 20.0 \quad 25.0 \quad 30.0 \quad 35.0 \quad 40.0$$

$$\frac{U_o-U}{U_\infty}$$
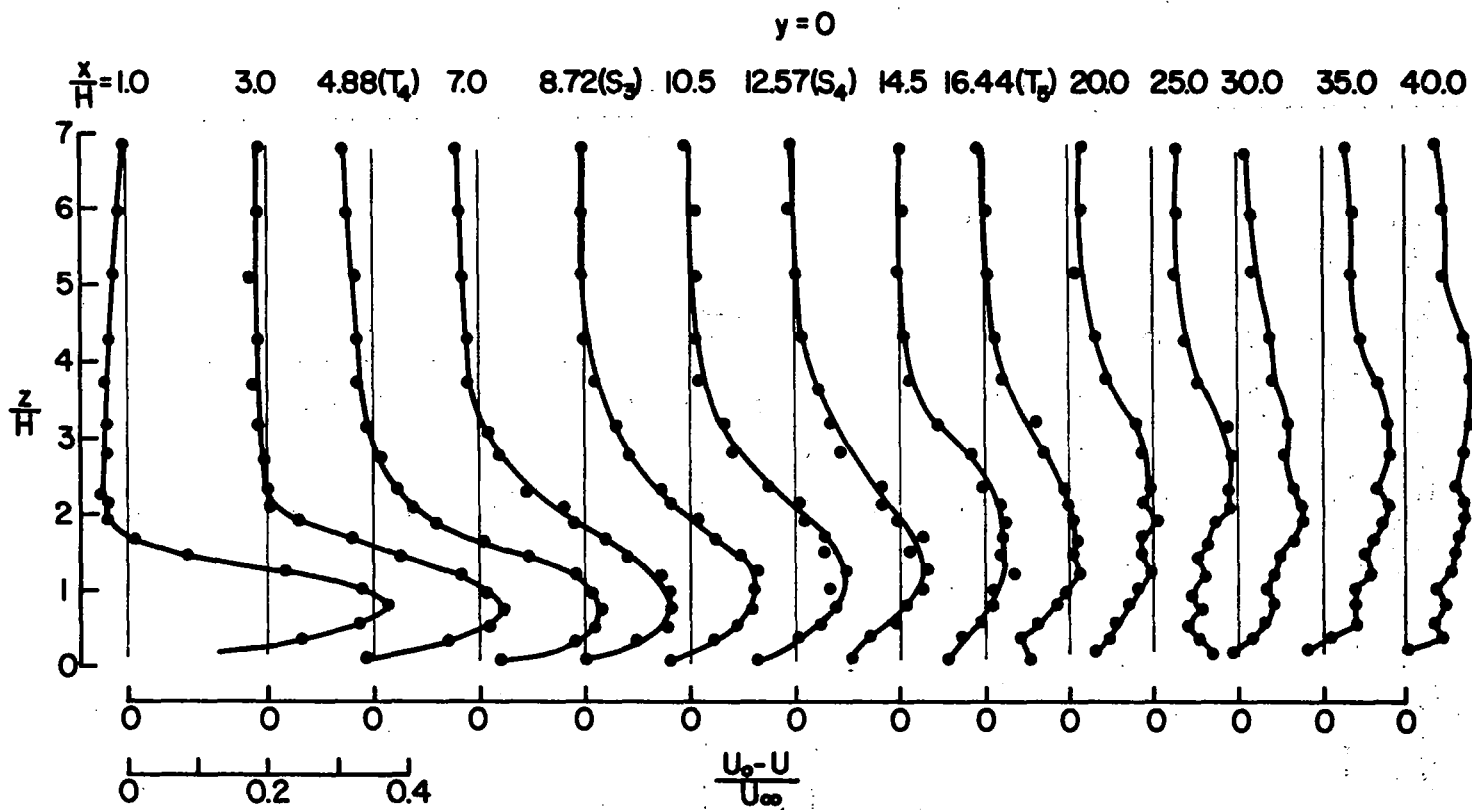
Figure 42.   Vertical Profiles of Mean Velocity Defect behind Model 4 for Test Condition 2
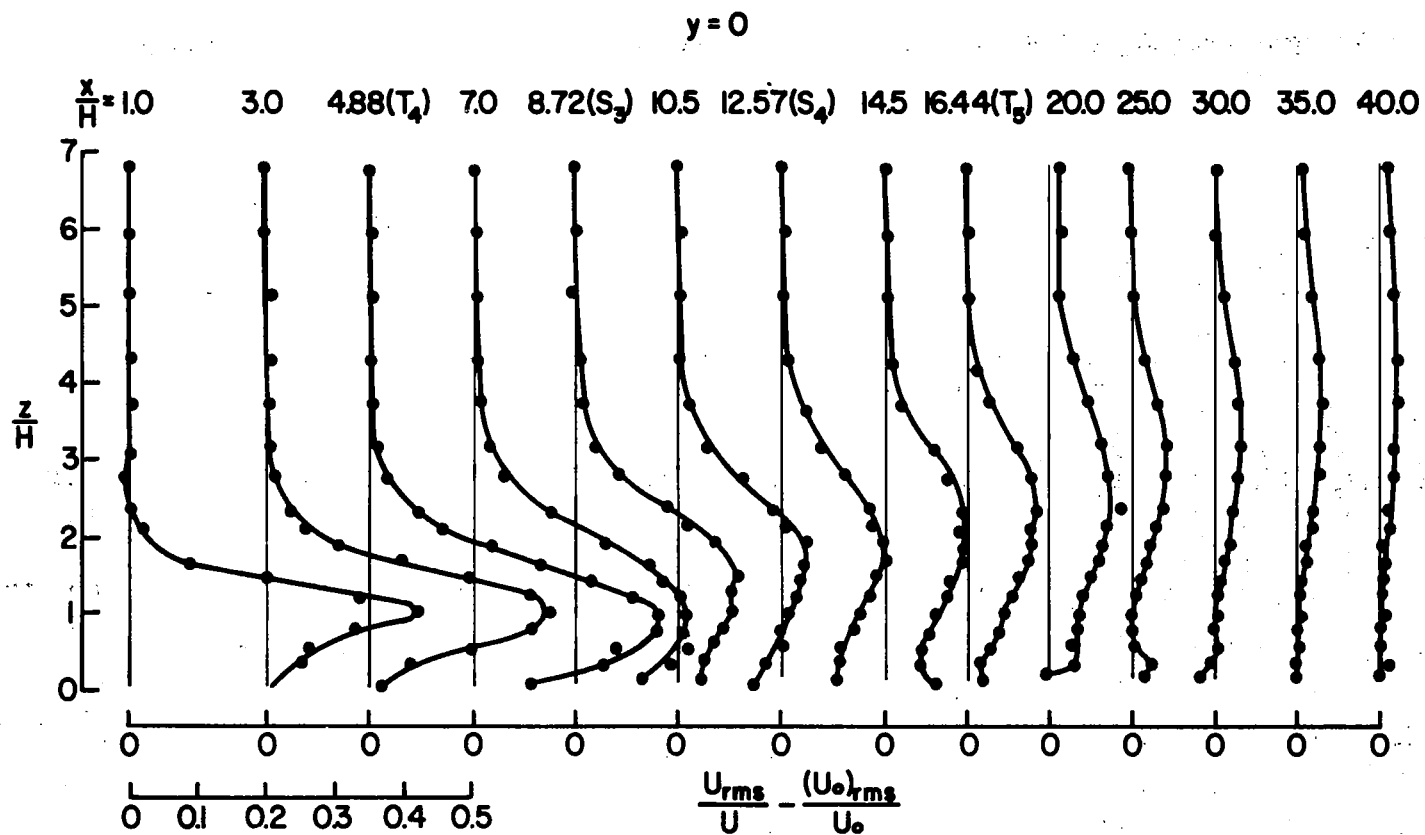
Figure 43. Vertical Profiles of Turbulence Intensity Excess behind Model 4 for Test Condition 2
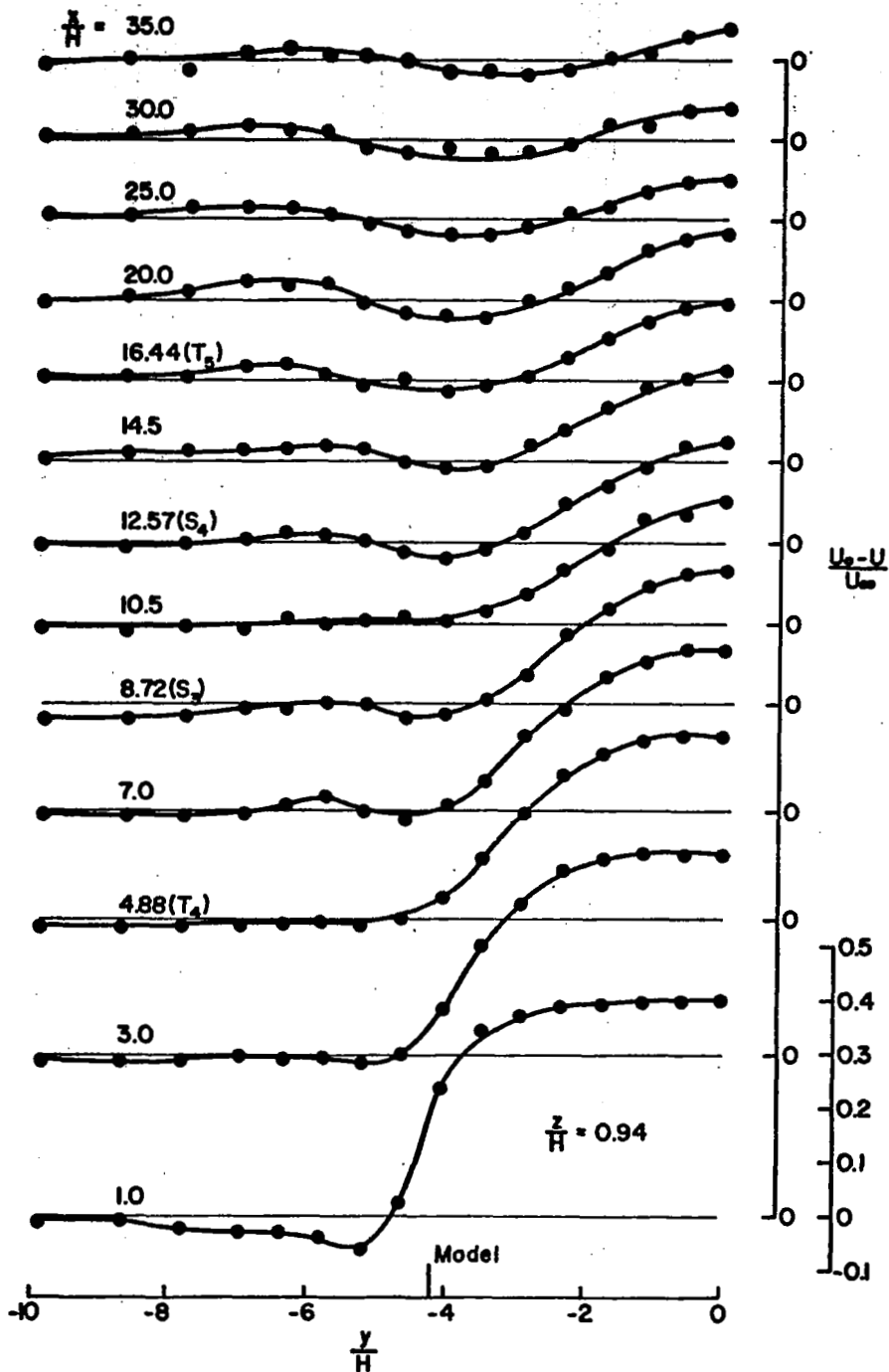
Figure 44. Horizontal Profiles of Mean Velocity Defect behind Model .4 for Test Condition 2
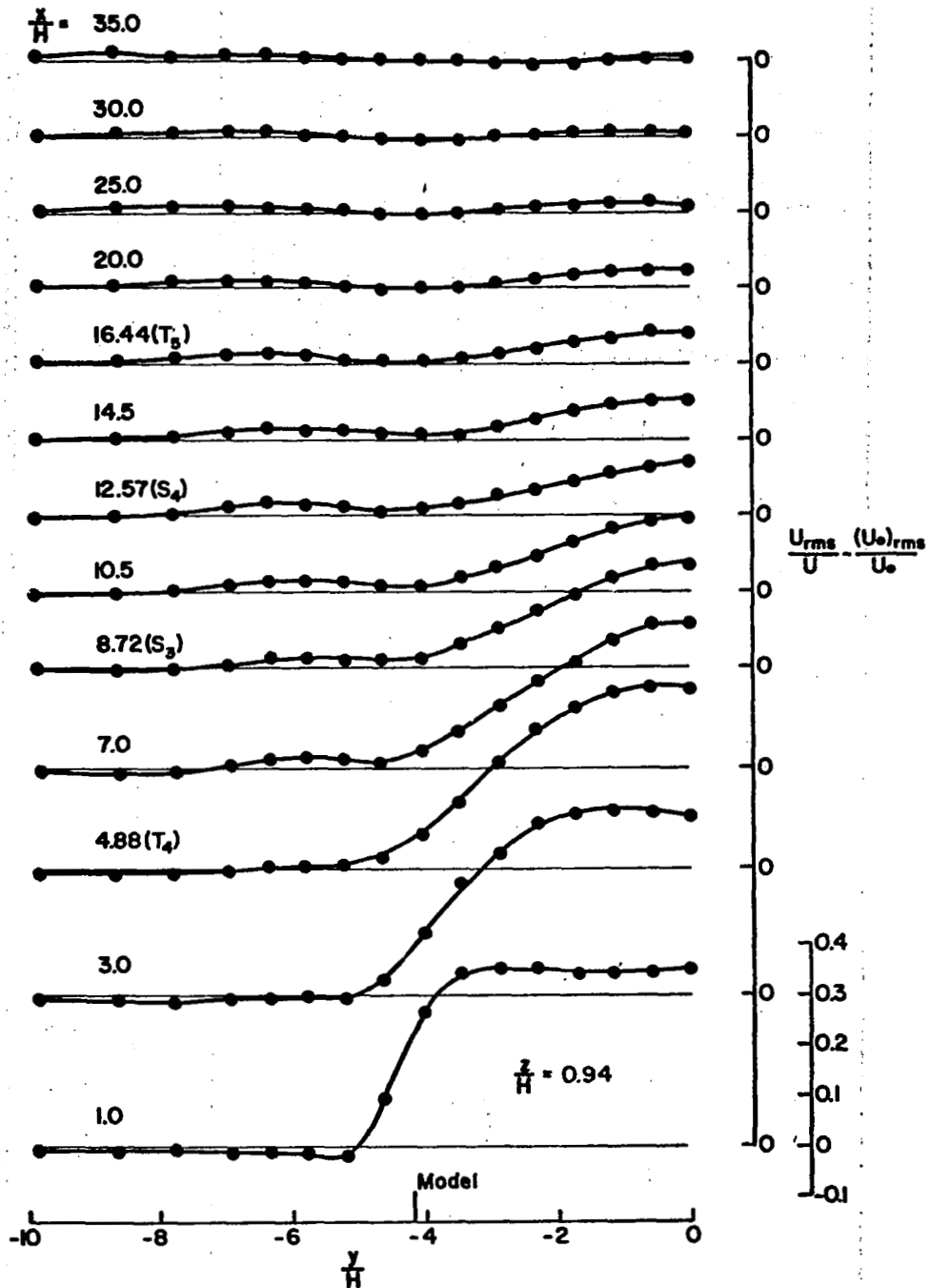
Figure 45. Horizontal Profiles of Turbulence Intensity Excess behind Model 4 for Test Condition 2
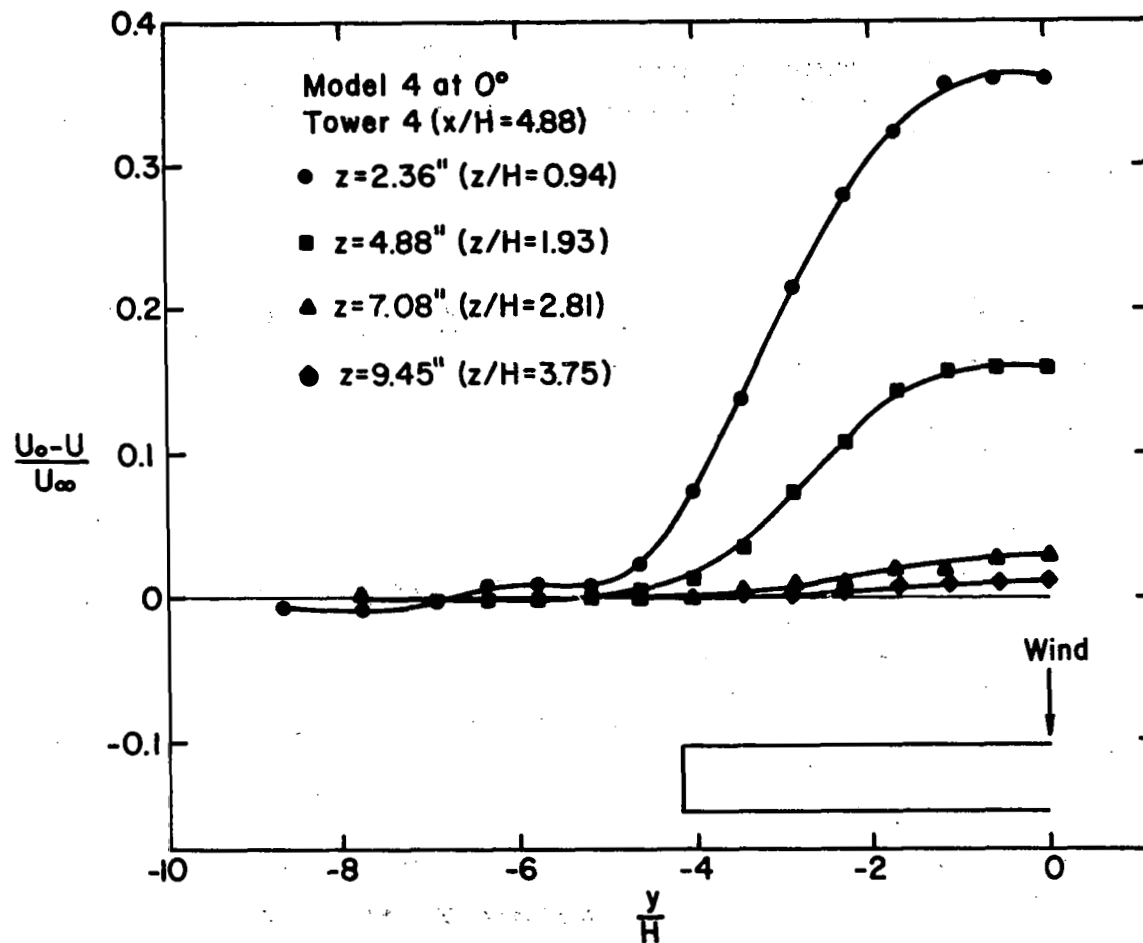
Figure 46a. Horizontal Profiles of Mean Velocity Defect at Several Elevations and Downstream Positions behind Model 4 for Test Condition 2
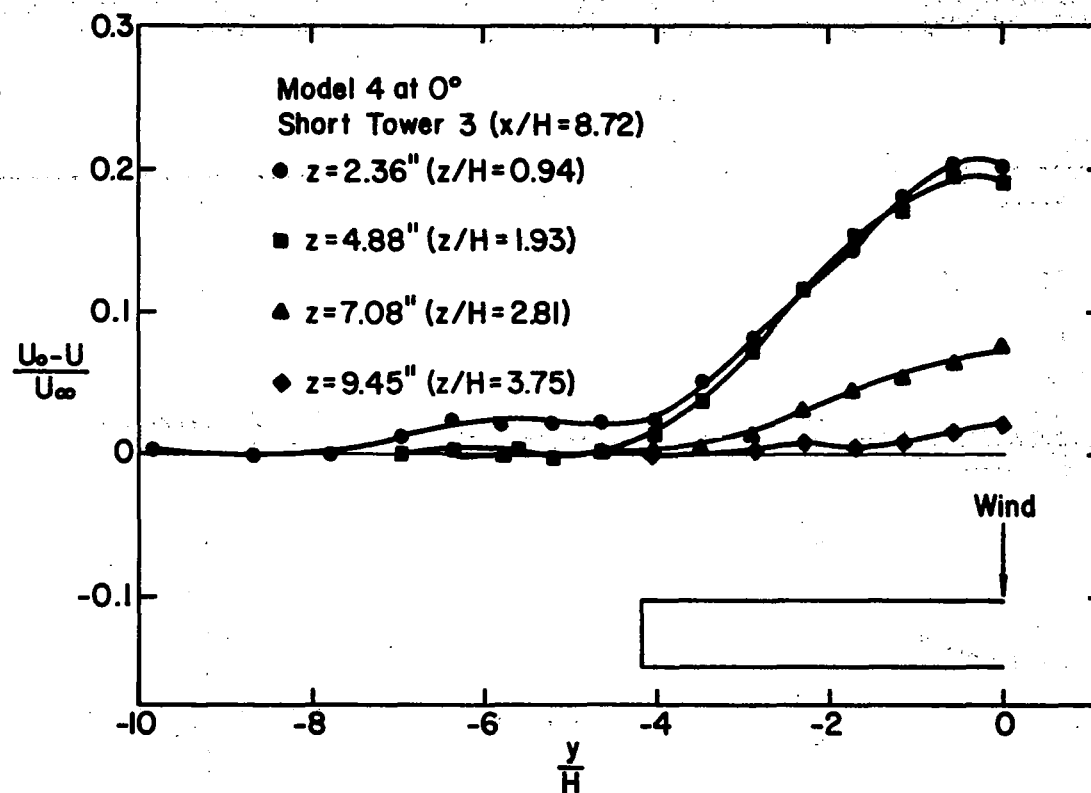
Figure 46b. Horizontal Profiles of Mean Velocity Defect at Several Elevations and Downstream Positions behind Model 4 for Test Condition 2
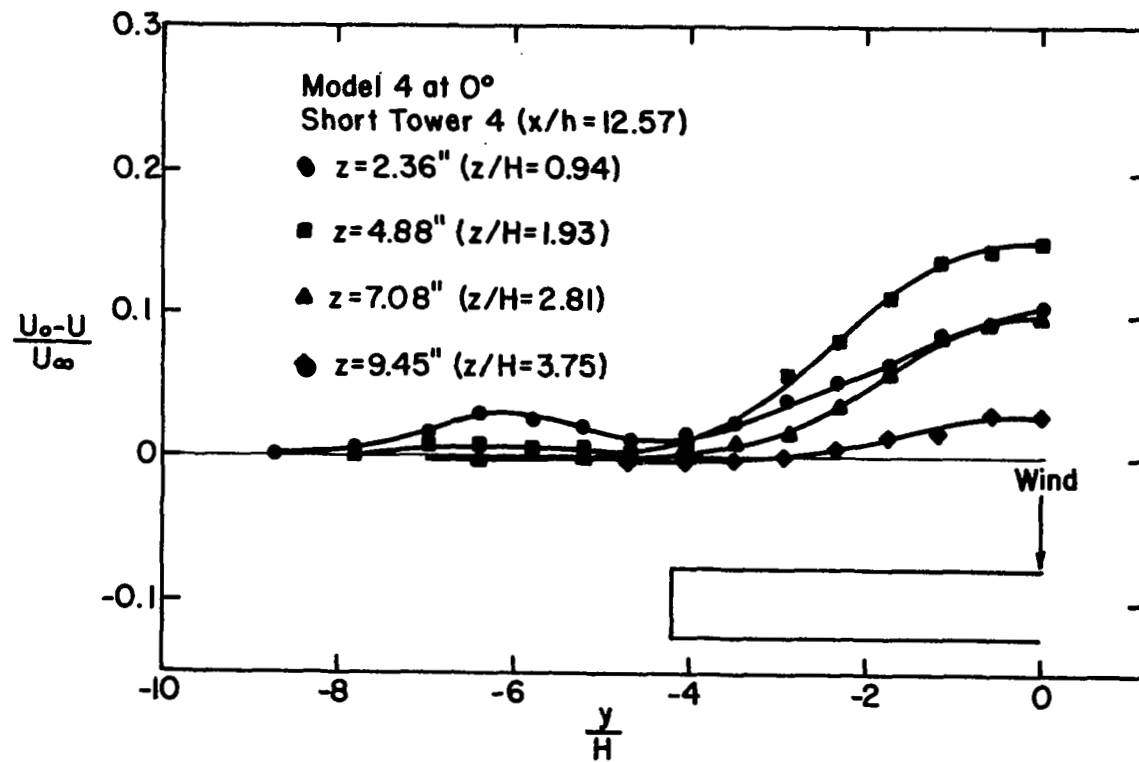
Figure 46c.   Horizontal Profiles of Mean Velocity Defect at Several Elevations and Downstream Positions behind Model 4 for Test Condition 2
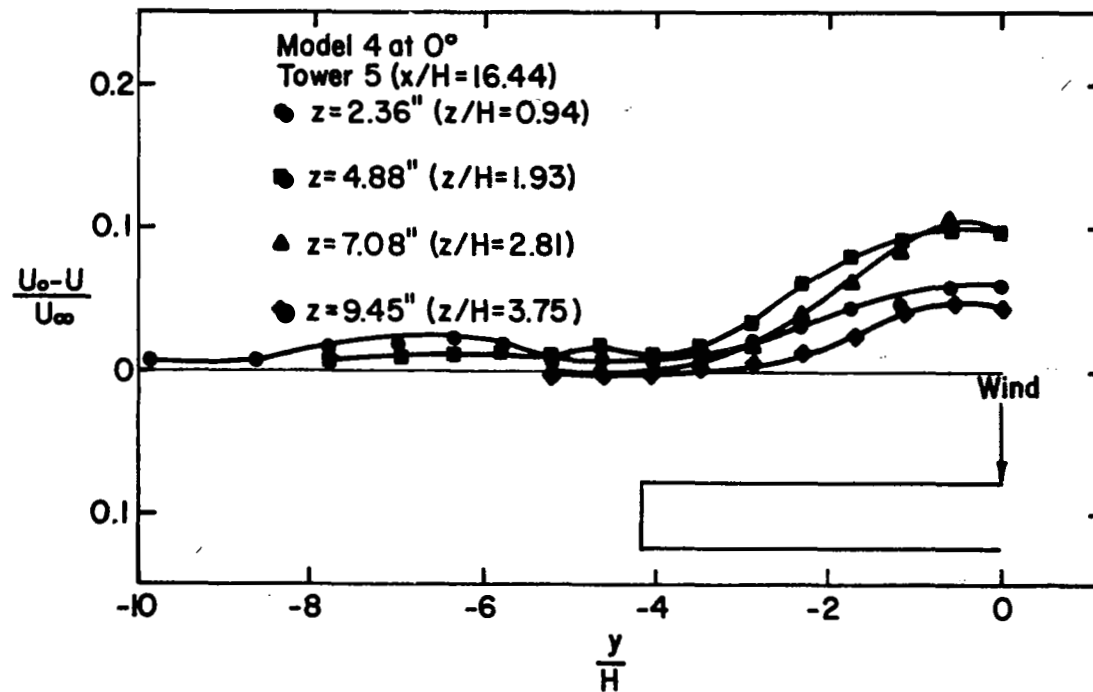
Figure 46d. Horizontal Profiles of Mean Velocity Defect at Several Elevations and Downstream Positions behind Model 4 for Test Condition 2
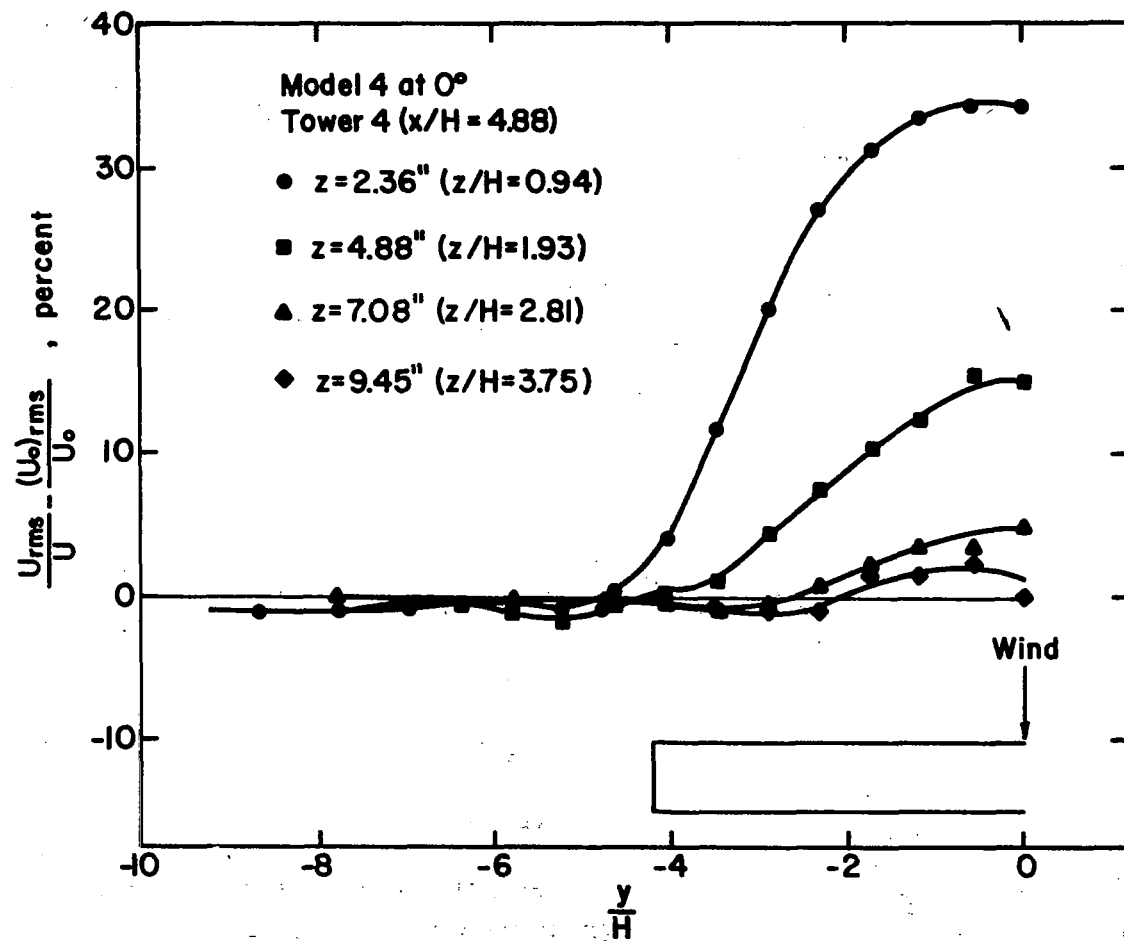
Figure 47a. Horizontal Profiles of Turbulence Intensity Excess at Several Elevations and behind Model 4 for Test Condition 2
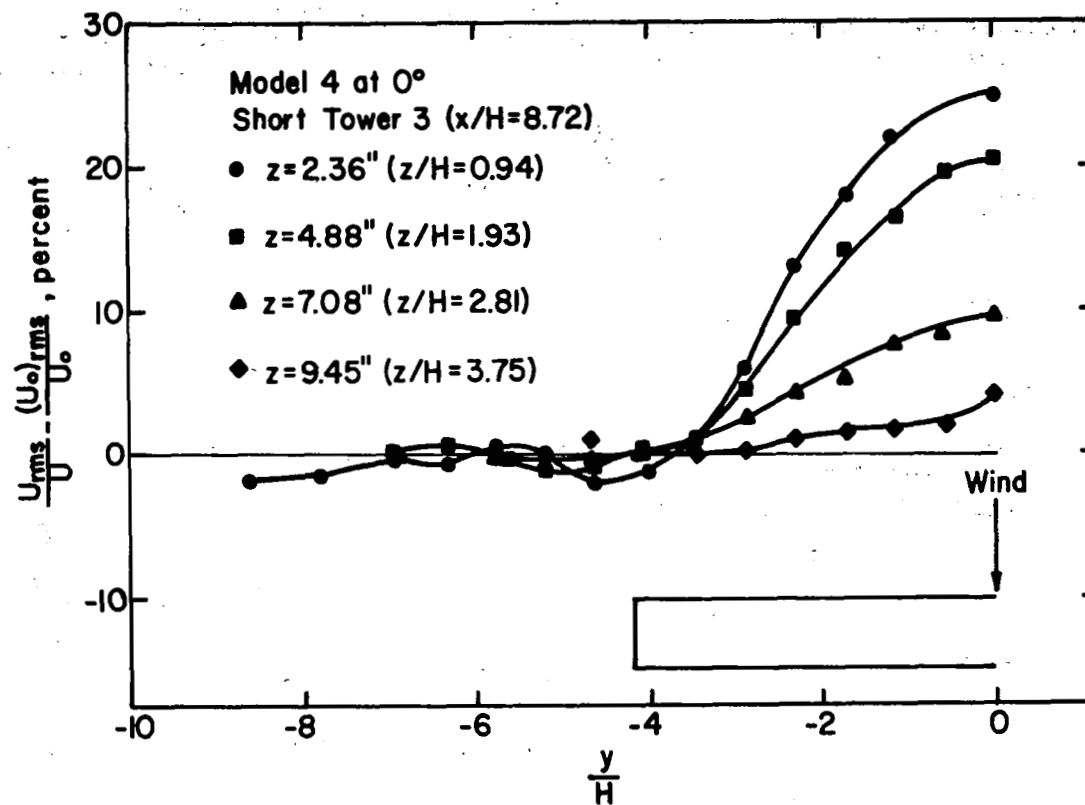
Figure 47b. Horizontal Profiles of Turbulence Intensity Excess at
Several Elevations and Downstream Positions behind
Model 4 for Test Condition 2
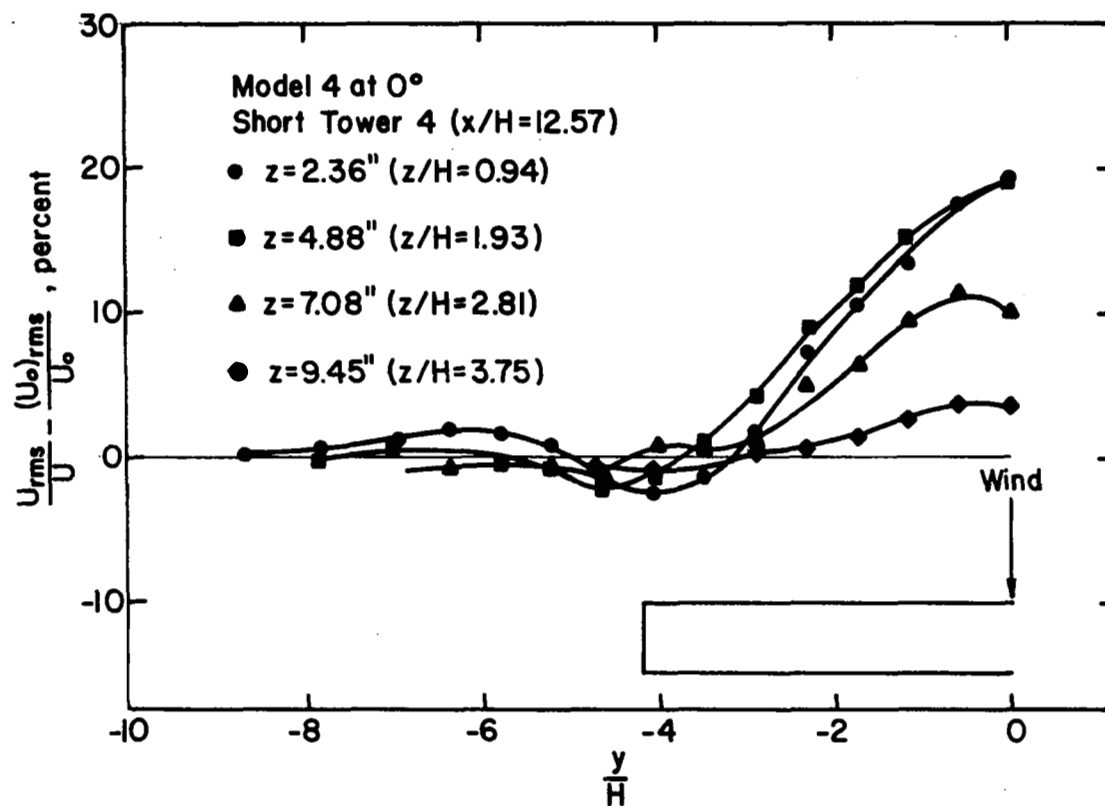
Figure 47c. Horizontal Profiles of Turbulence Intensity Excess at Several Elevations and Downstream Positions behind Model 4 for Test Condition 2
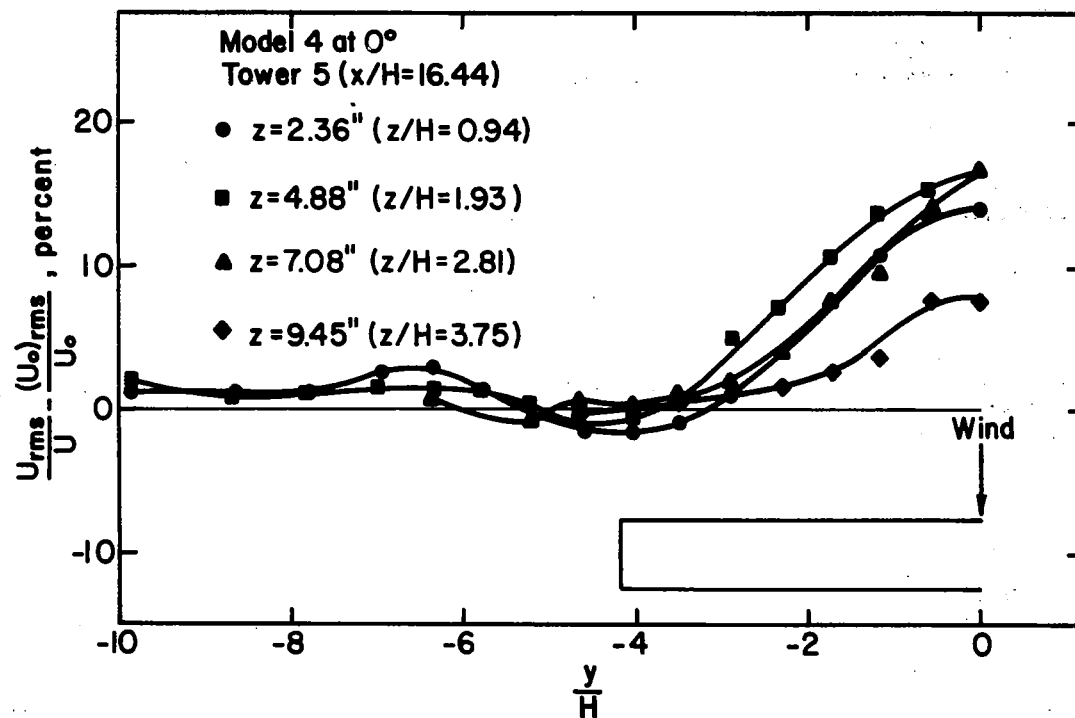
Figure 47d. Horizontal Profiles of Turbulence Intensity Excess at
Several Elevations and Downstream Positions behind
Model 4 for Test Condition 2
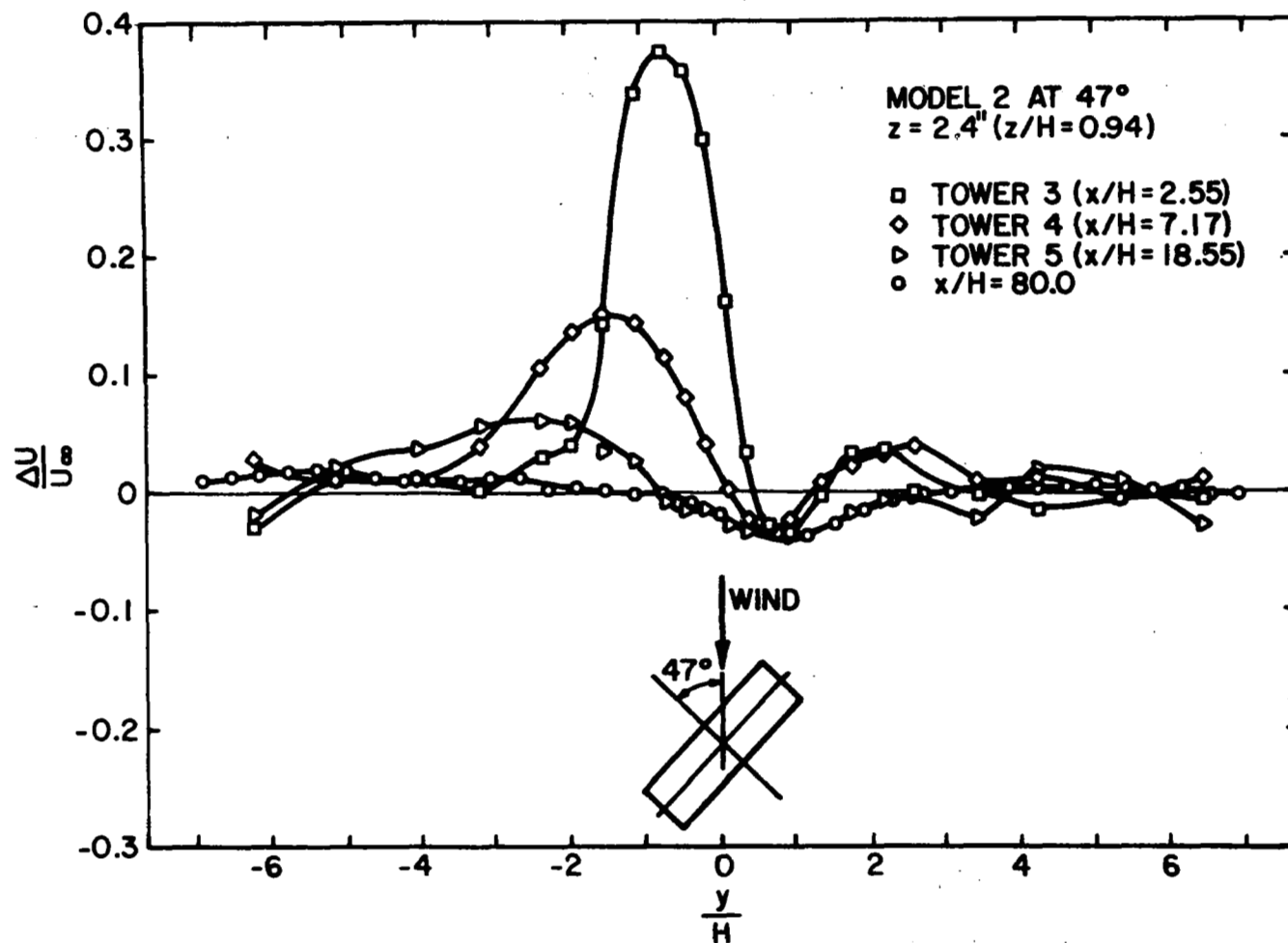
Figure 48. Horizontal Profiles of Mean Velocity Defect
behind Model 2 at 47 Degrees for Test Condition 1
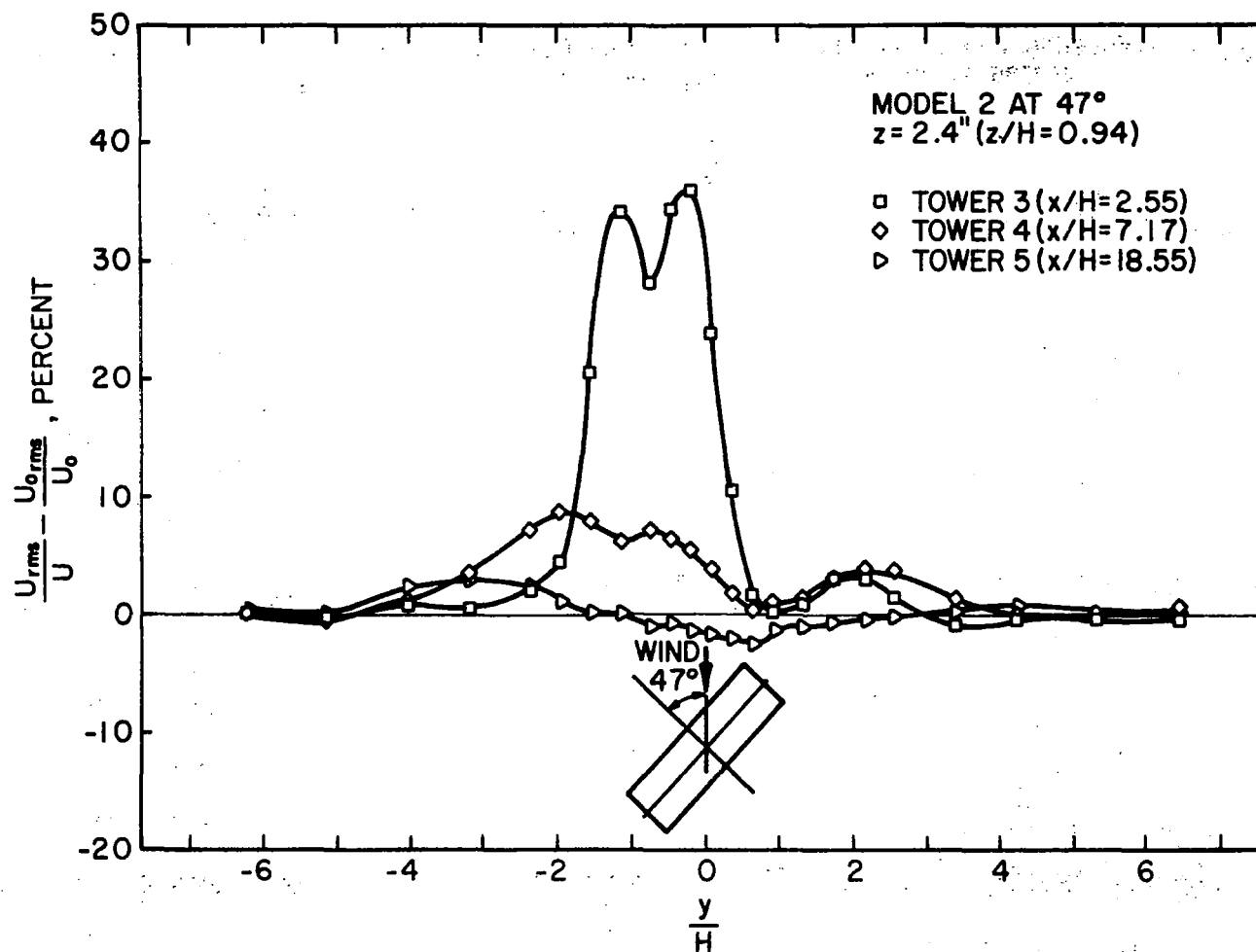
Figure 49. Horizontal Profiles of Turbulence Intensity Excess behind
Model 2 at 47 Degrees for Test Condition 1
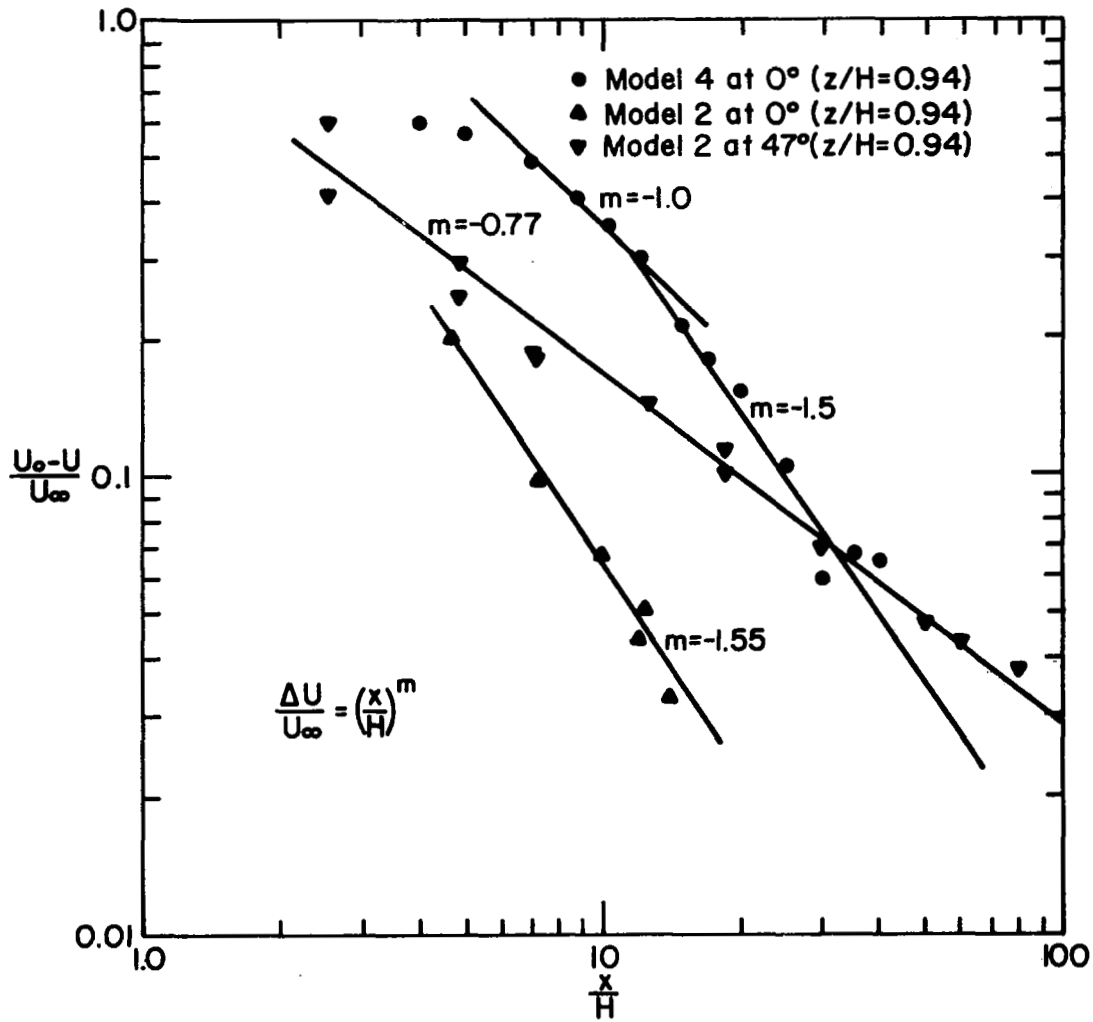
Figure 50. Decay of Mean Velocity Defect with Distance for
Model 2 at α = 0 and 47 Degrees and Model 4 at
α = 0 Degrees
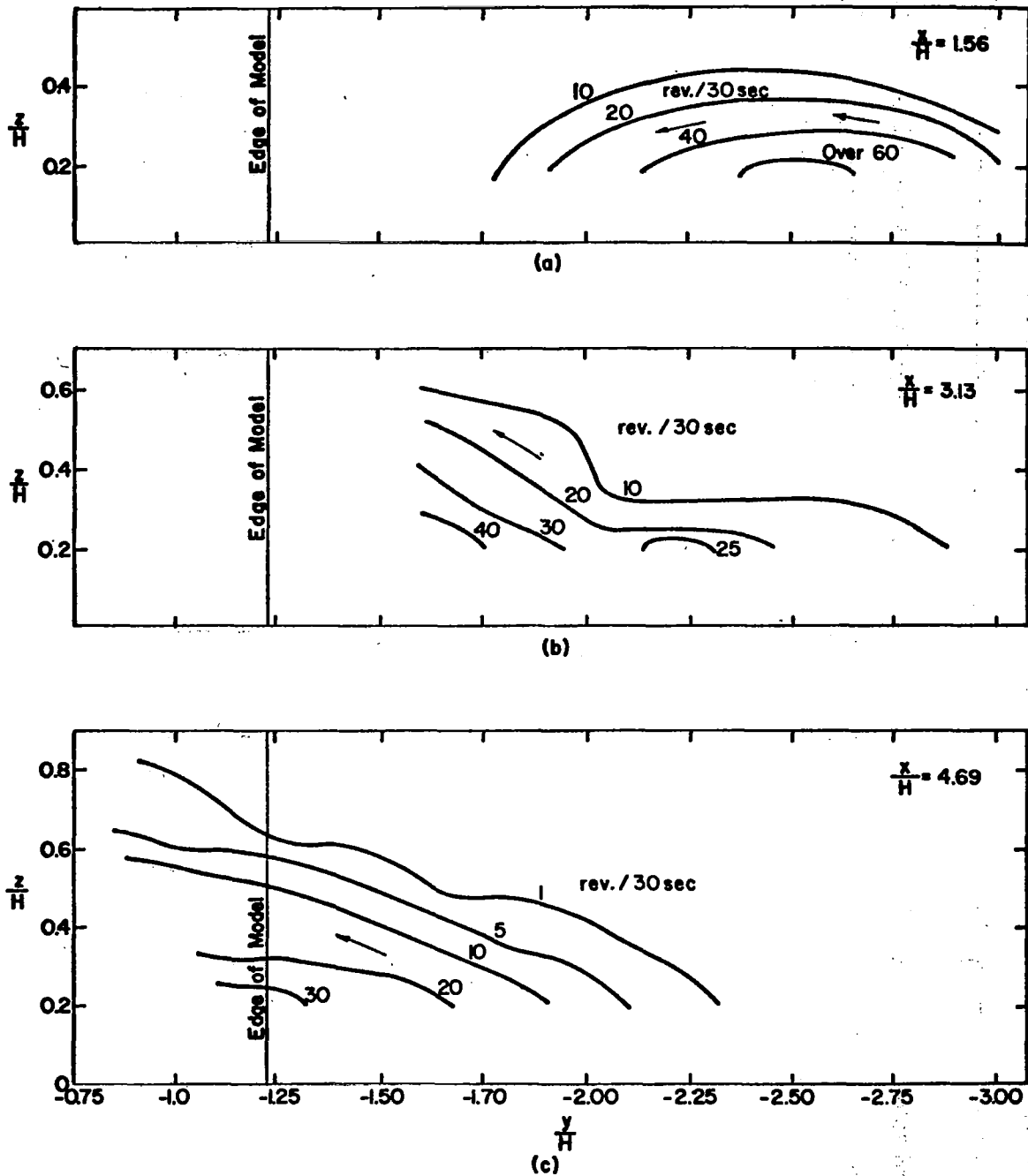
Figure 51.   Contours of Constant Streamwise Vorticity behind Model 2
at α = 0 Degrees from Paddle Wheel Vorticity Meter
(Viewed Looking Downwind)
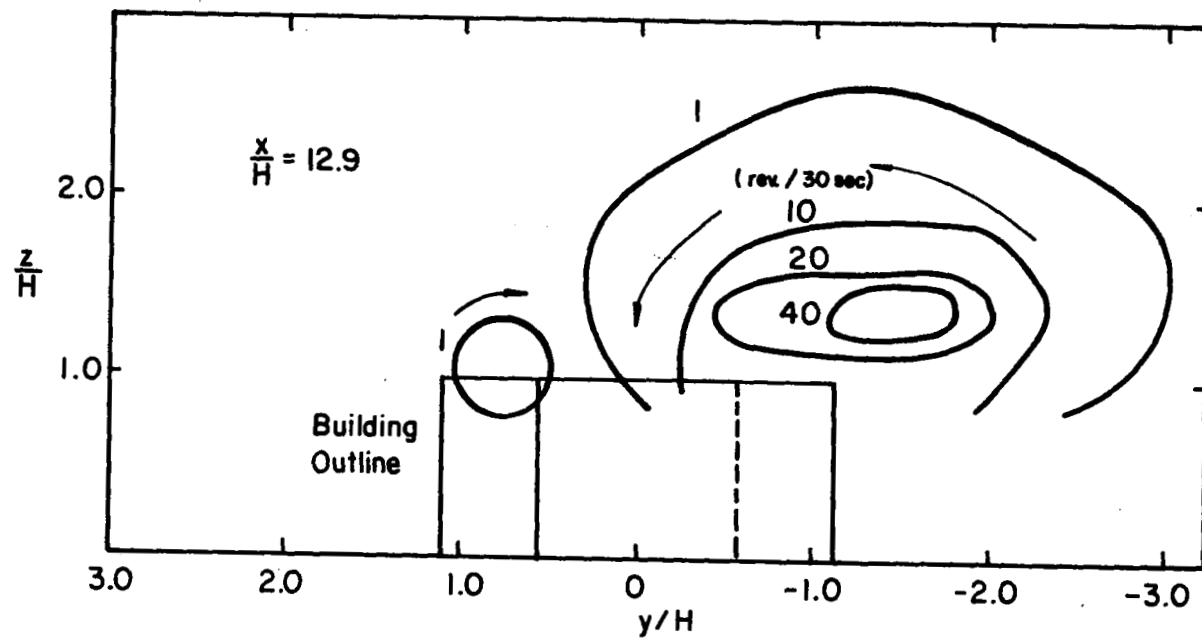
Figure 52. Contours of Constant Streamwise Vorticity behind Model 2 at α = 45 Degrees from Paddle Wheel Vorticity Meter (Viewed Looking Downwind)
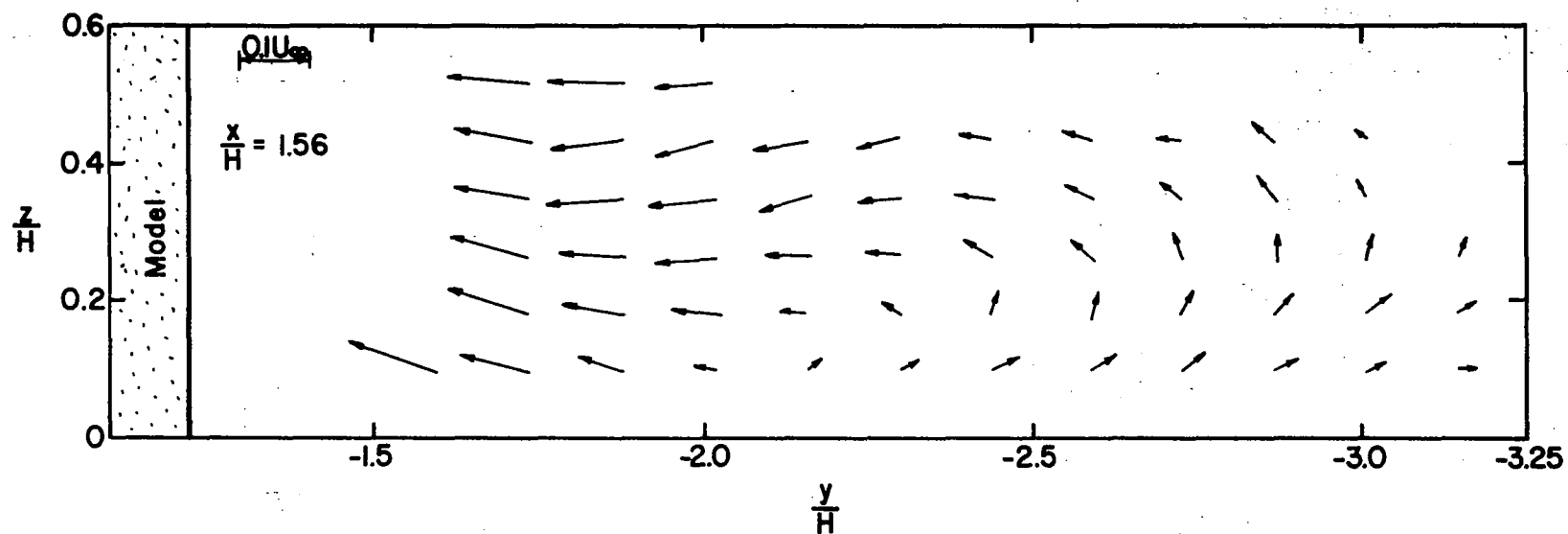
Figure 53. Cross-Flow Velocity Vector Distribution behind Model 2
at α = 0 Degrees (Viewed Looking Downwind)
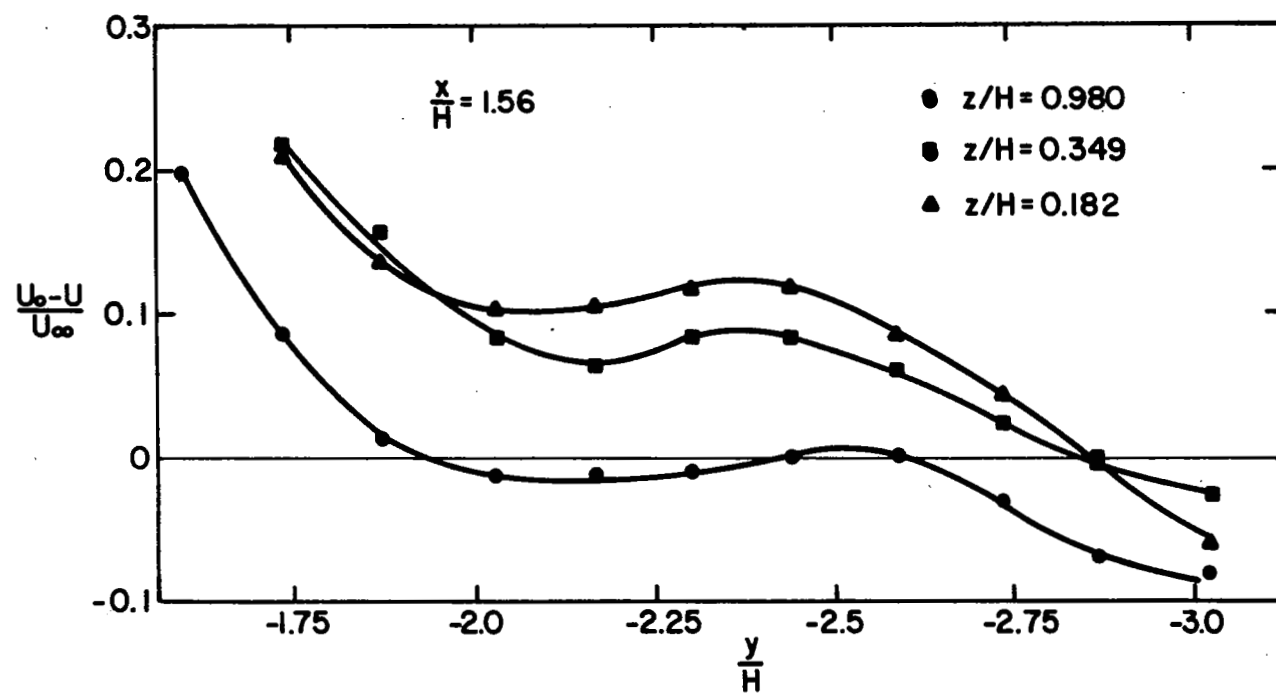
Figure 54. Horizontal Profiles of Longitudinal Mean Velocity Defect
behind Model 2 at α = 0 Degrees (from Rotated Hot-Film Data)
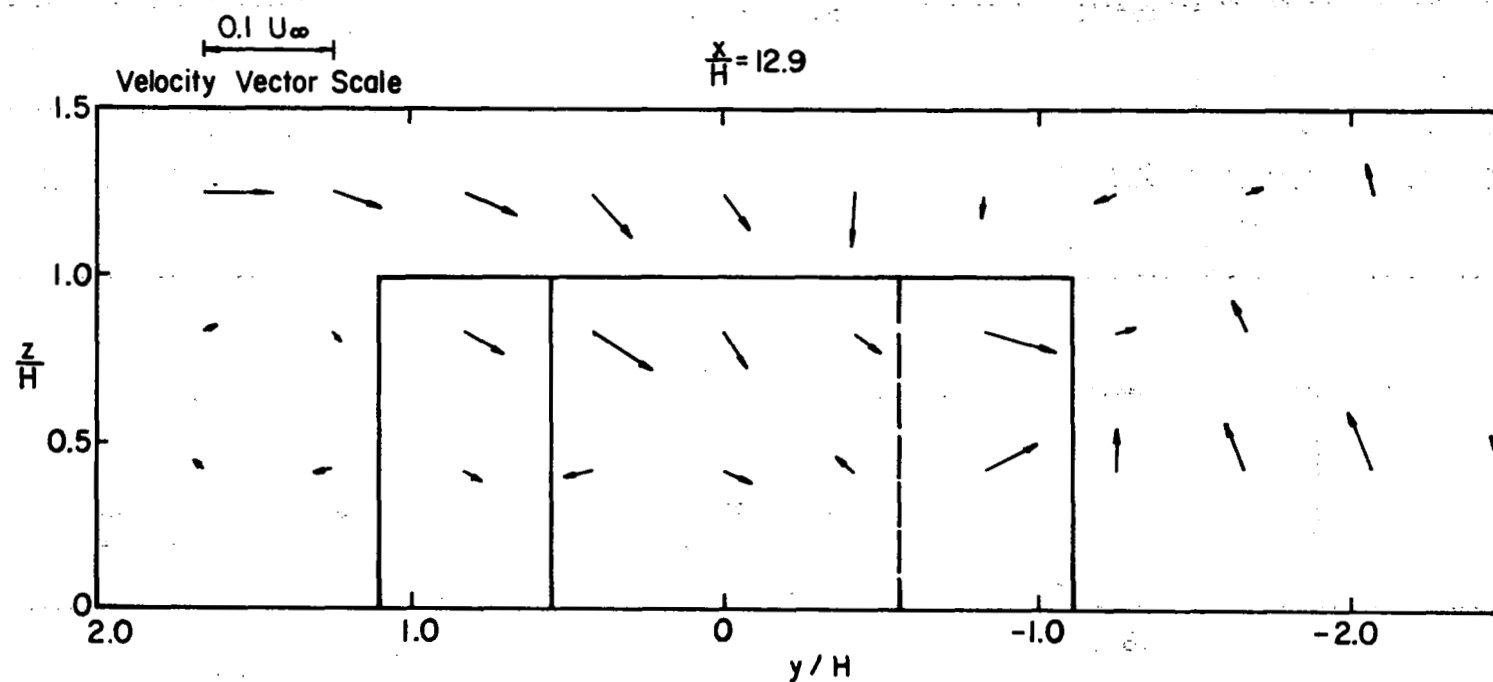
Figure 55. Cross-Flow Velocity Vector Distribution behind
Model 2 at α = 47 Degrees (Viewed Looking Downwind)
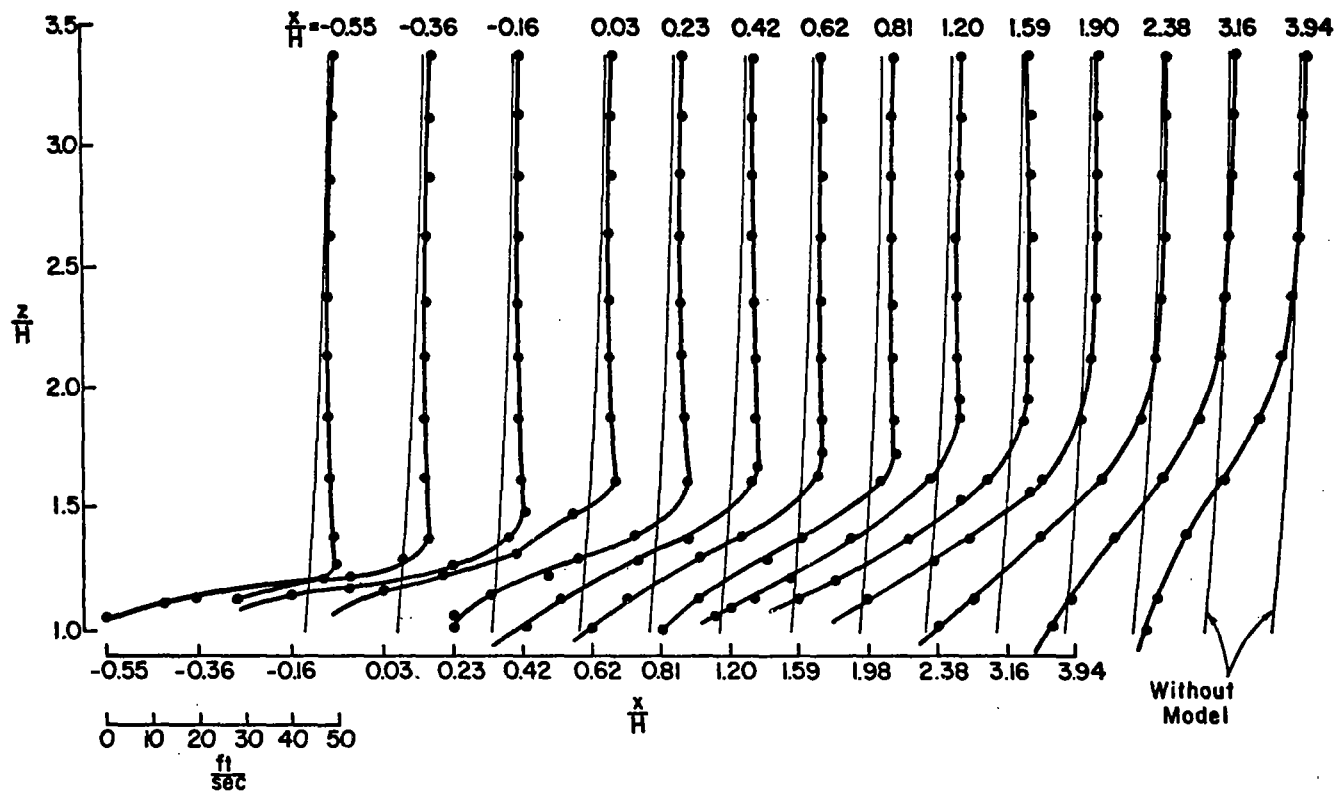
Figure 56. Vertical Profiles of Mean Velocity in the Free Shear Layer
on the Centerline above Model 2 at 0 Degrees for Test Condition 1
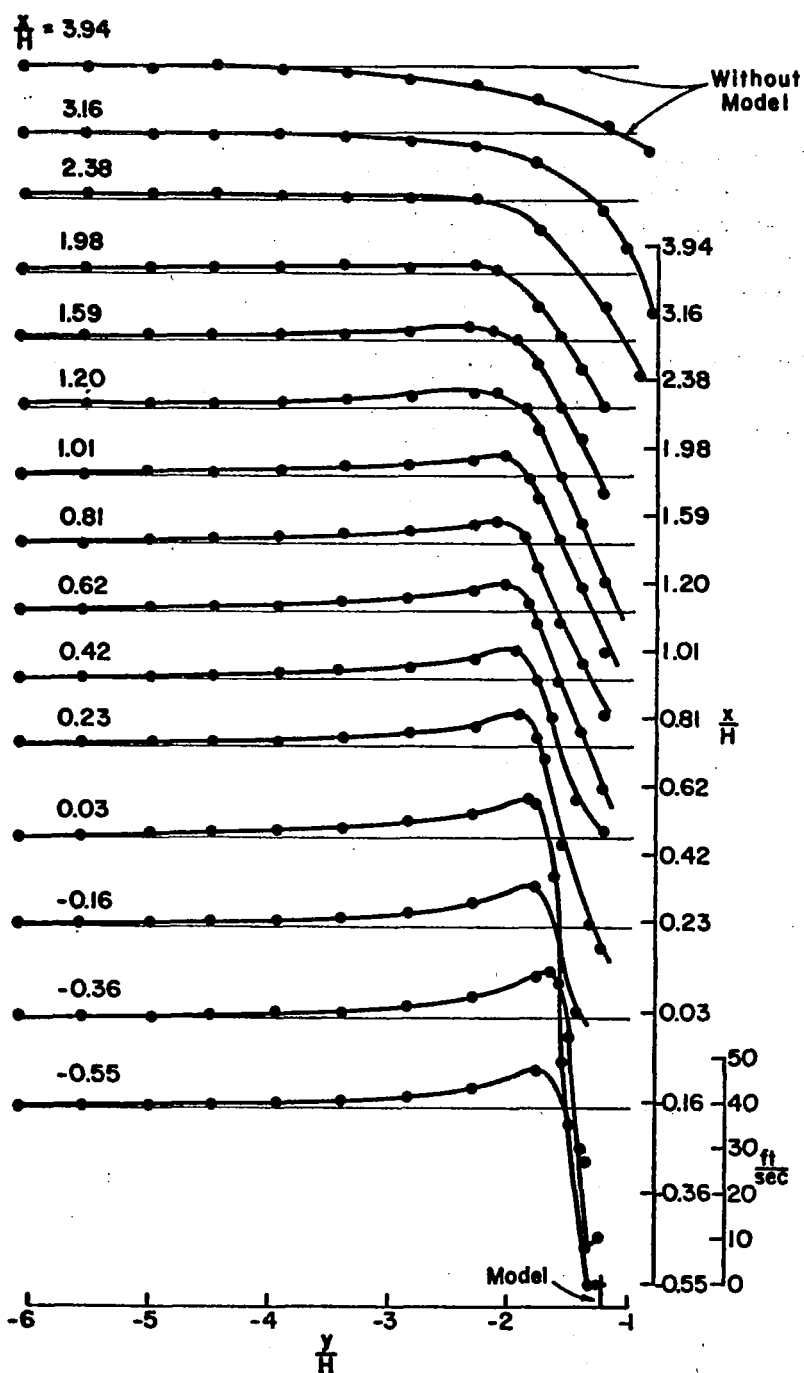
Figure 57. Horizontal Profiles of Mean Velocity in the Free Shear Layer
of the Side of Model 2 at 0 Degrees for Test Condition 1
(at z/H = 0.5)
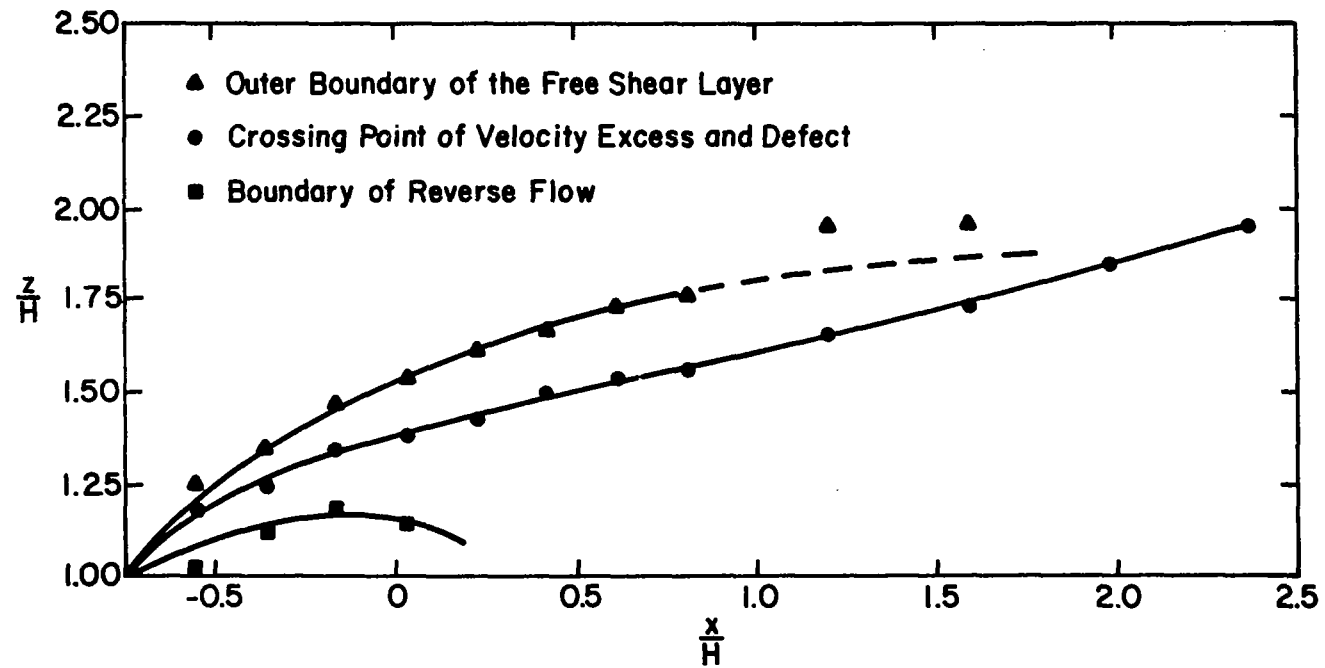
Figure 58. Boundaries of the Free Shear Layer above
Model 2 on the Centerline
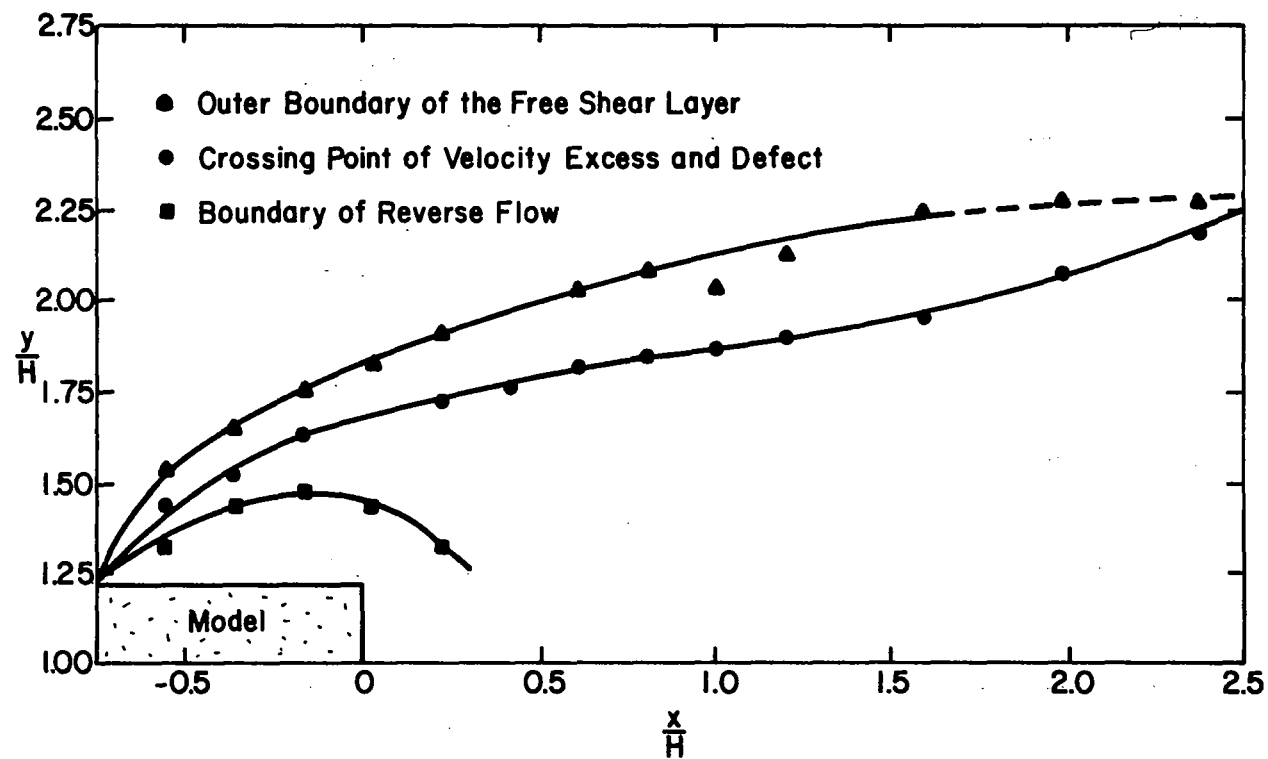
Figure 59.   Boundaries of the Free Shear Layer at
             the Side of Model 2 at z/H = 0.5
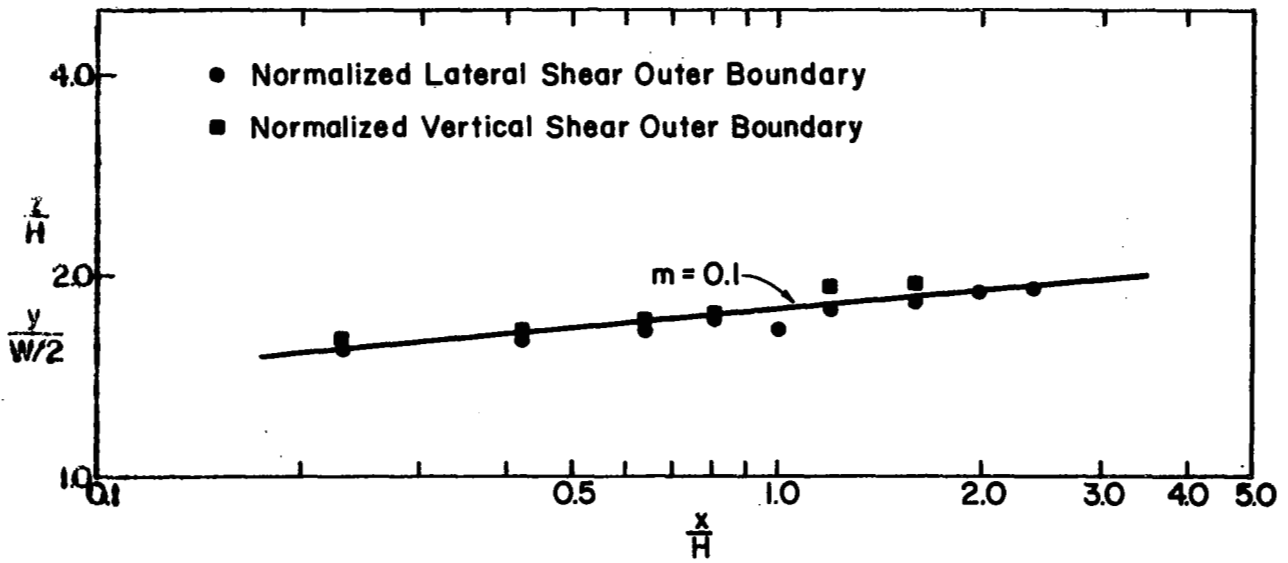
Figure 60. Normalized Vertical and Horizontal
Shear Layer Outer Boundary for Model 2
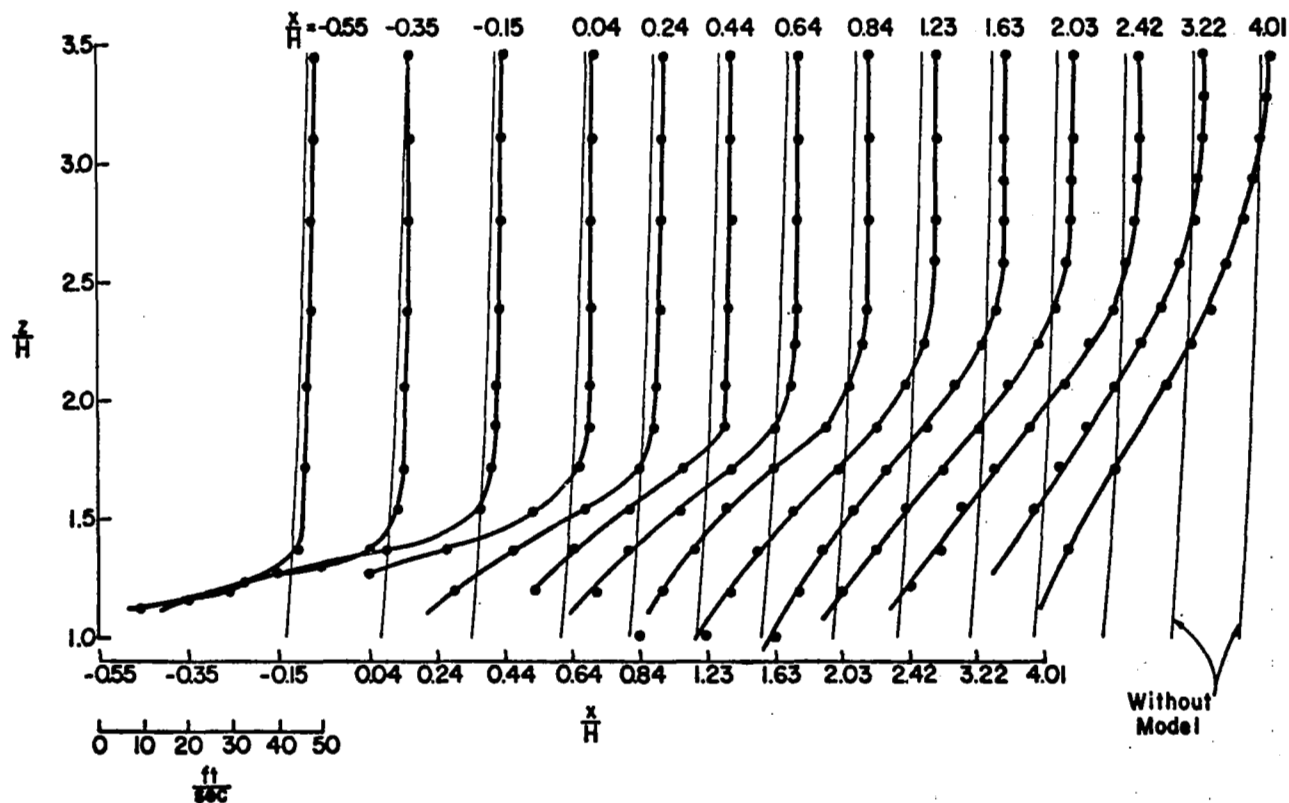
Figure 61. Vertical Profiles of Mean Velocity in the Free Shear Layer on the Centerline above Model 4 at 0 Degrees for Test Condition 2
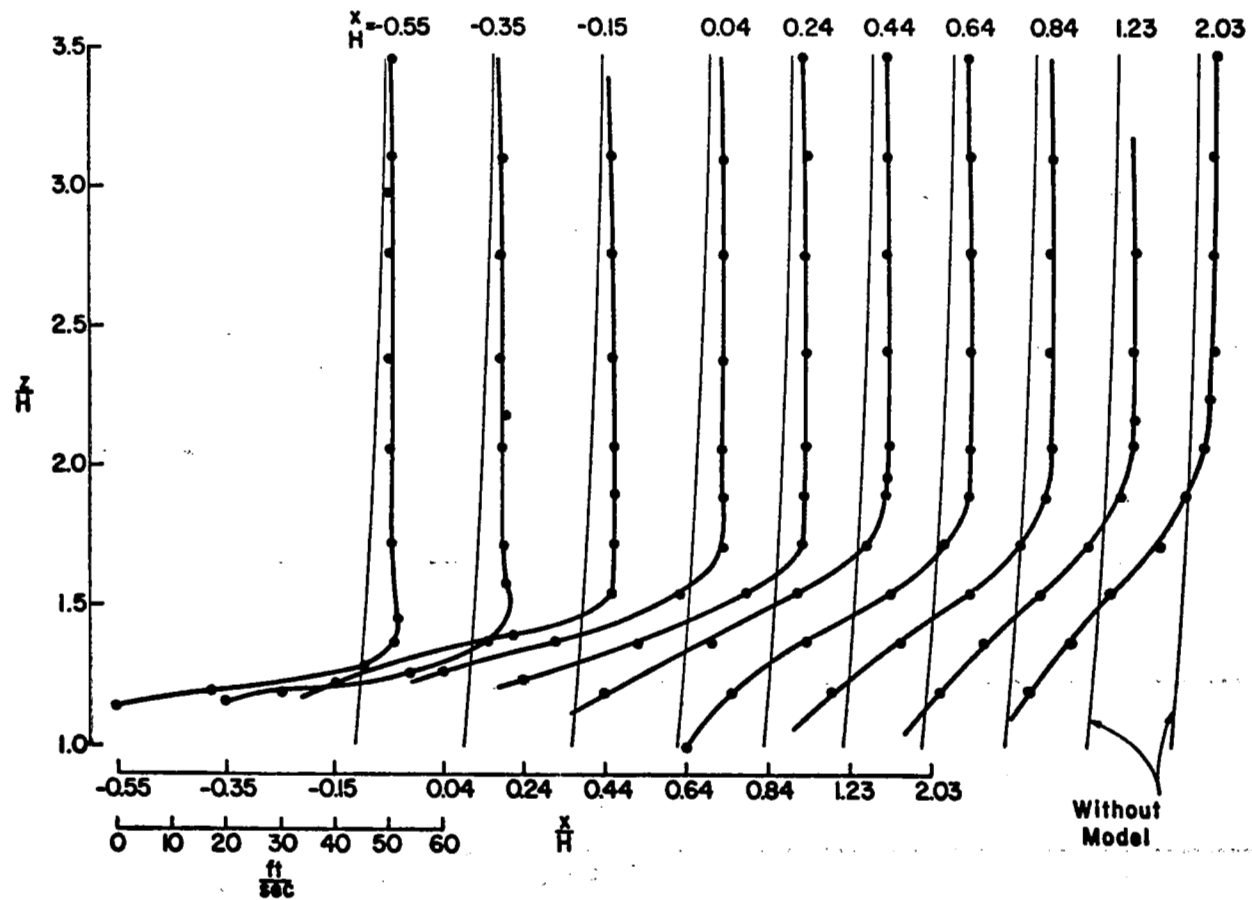
Figure 62. Vertical Profiles of Mean Velocity in the Free Shear Layer
at y/H = -3.54 above Model 4 at 0 Degrees for Test Condition 2
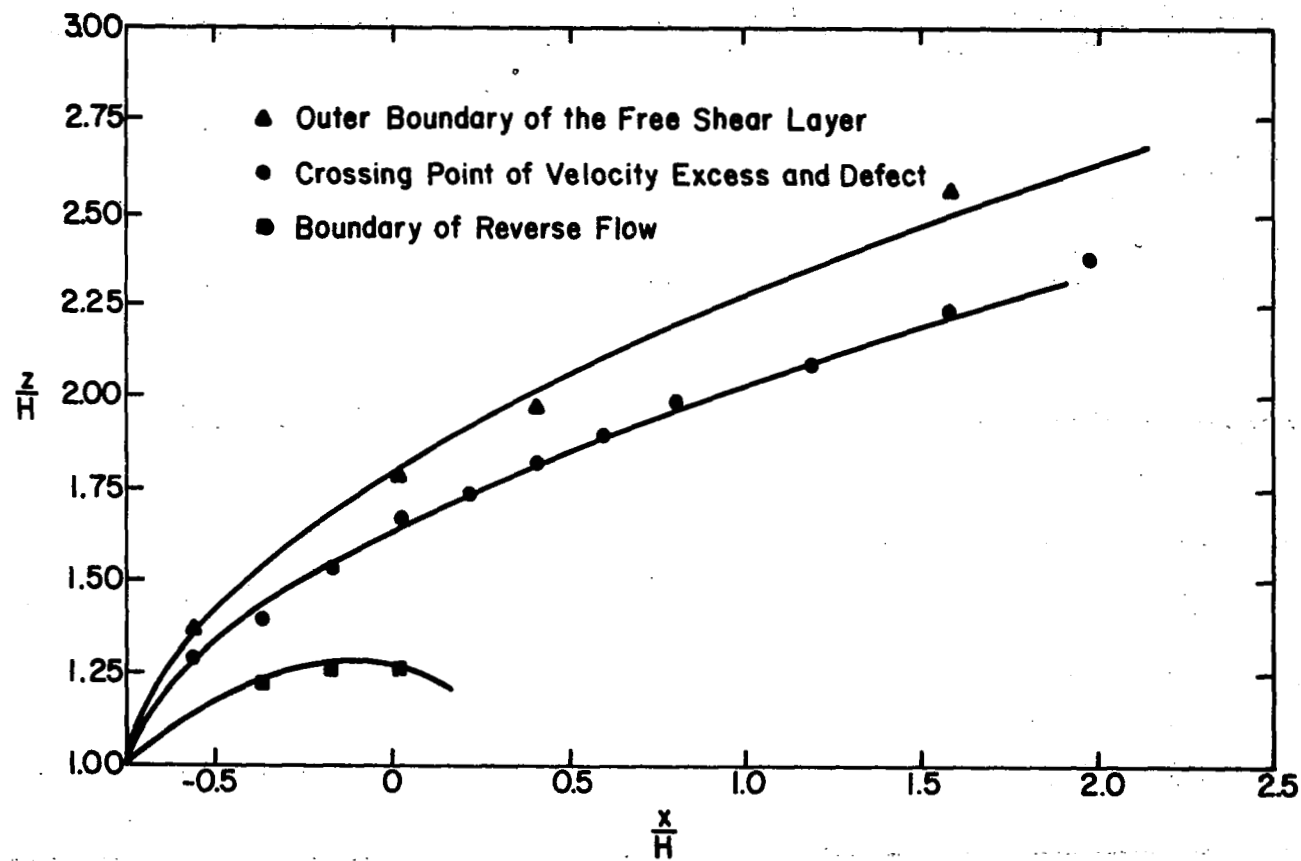
Figure 63.   Boundaries of the Free Shear Layer above Model 4 on the Centerline
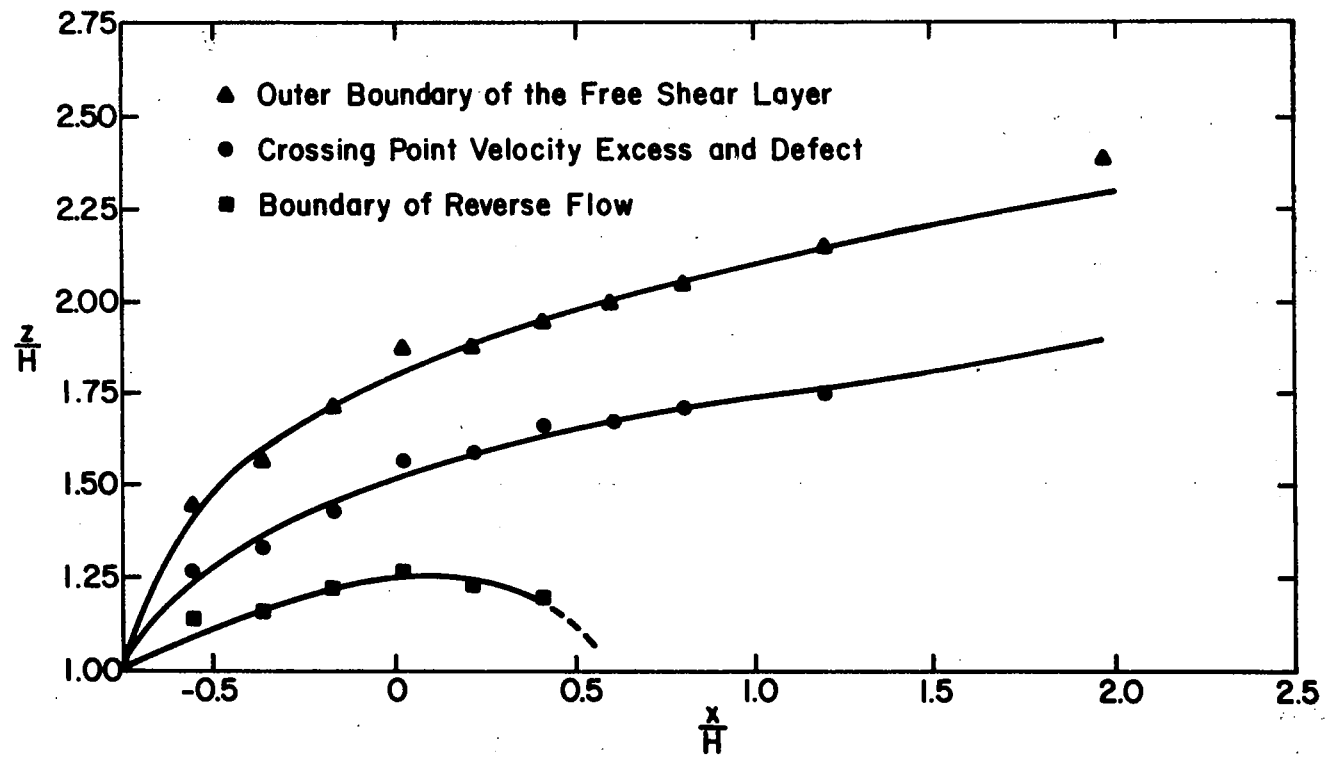
Figure 64. Boundaries of the Free Shear Layer above Model 4 at y/H = -3.54
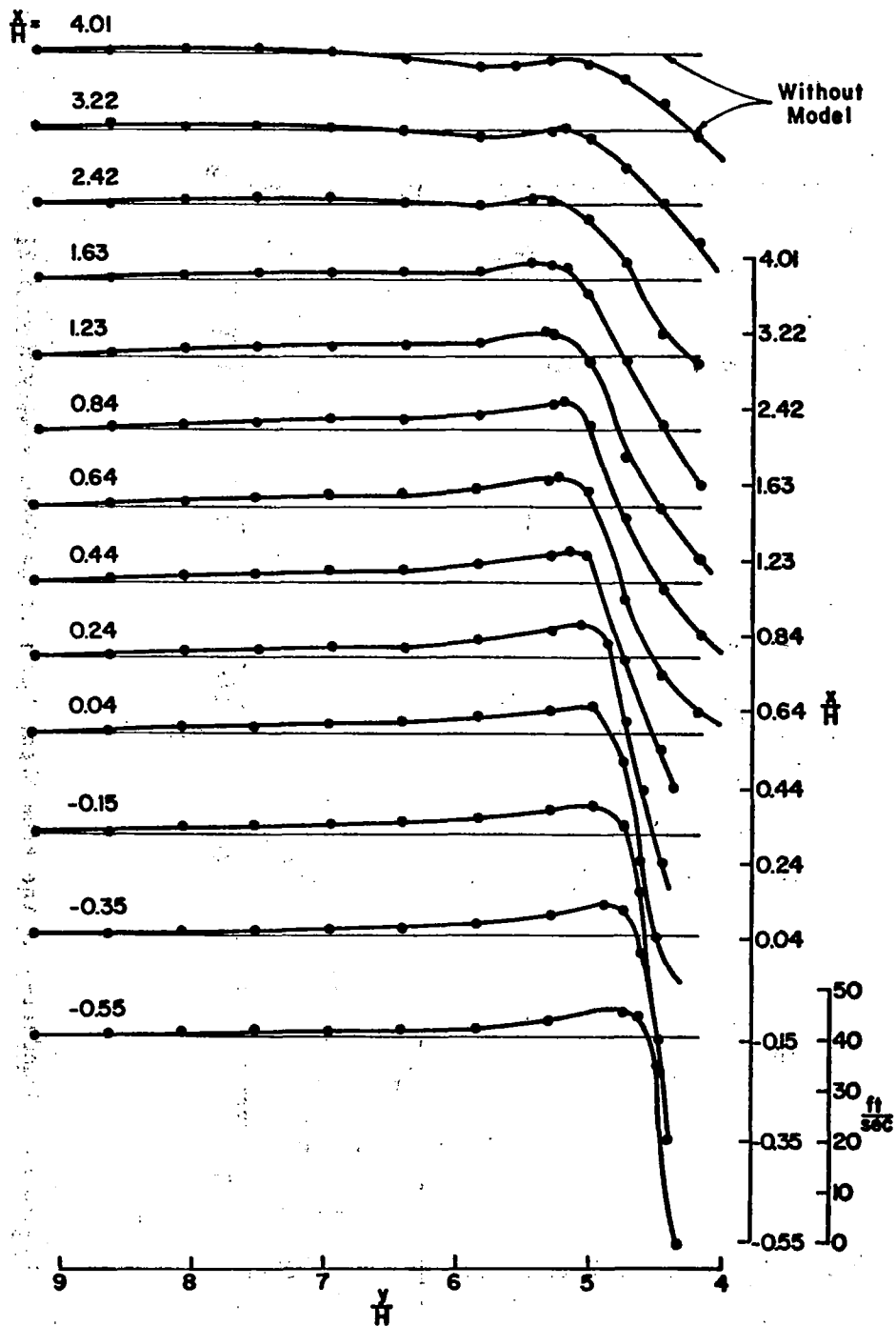
Figure 65. Horizontal Profiles of Mean Velocity in the Free Shear
Layer at the Side of Model 4 at 0 Degrees for Test
Condition 1 (at z/H = 0.5)
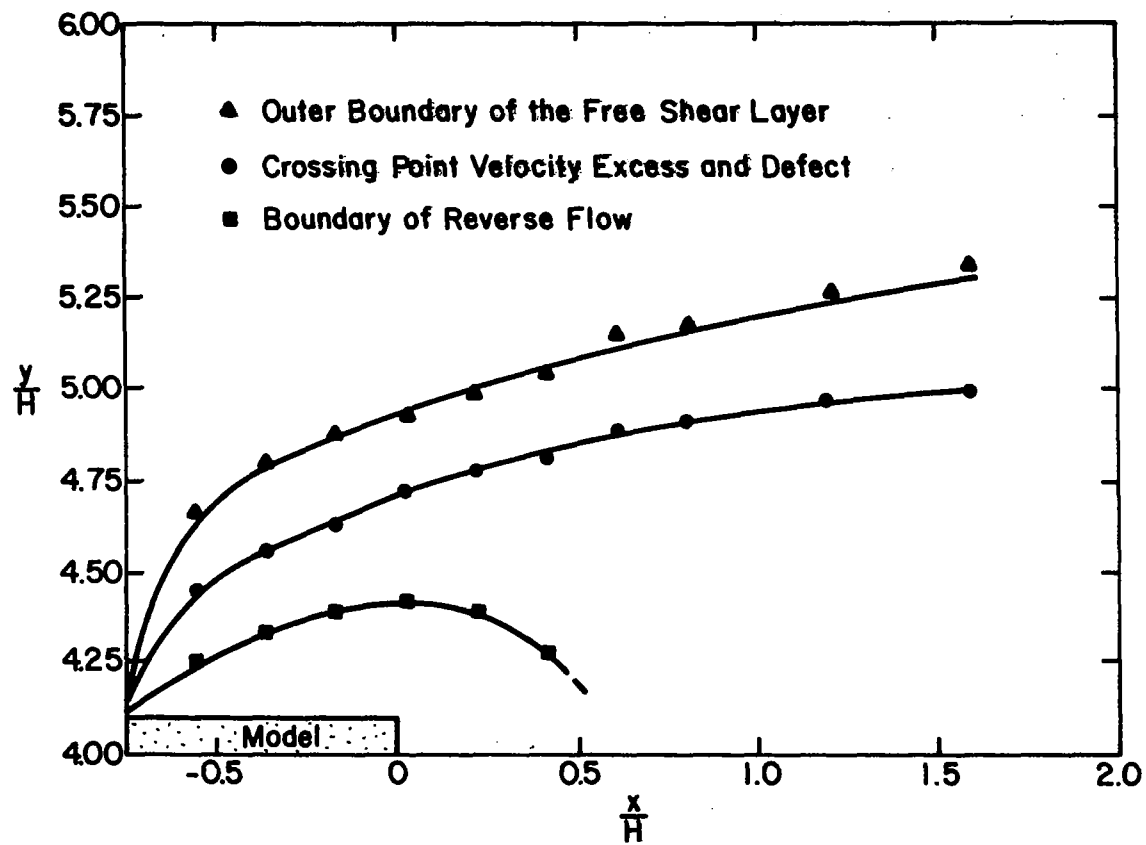
Figure 66.   Boundaries of the Free Shear Layer at the Side of Model 4 at z/H = 0.5
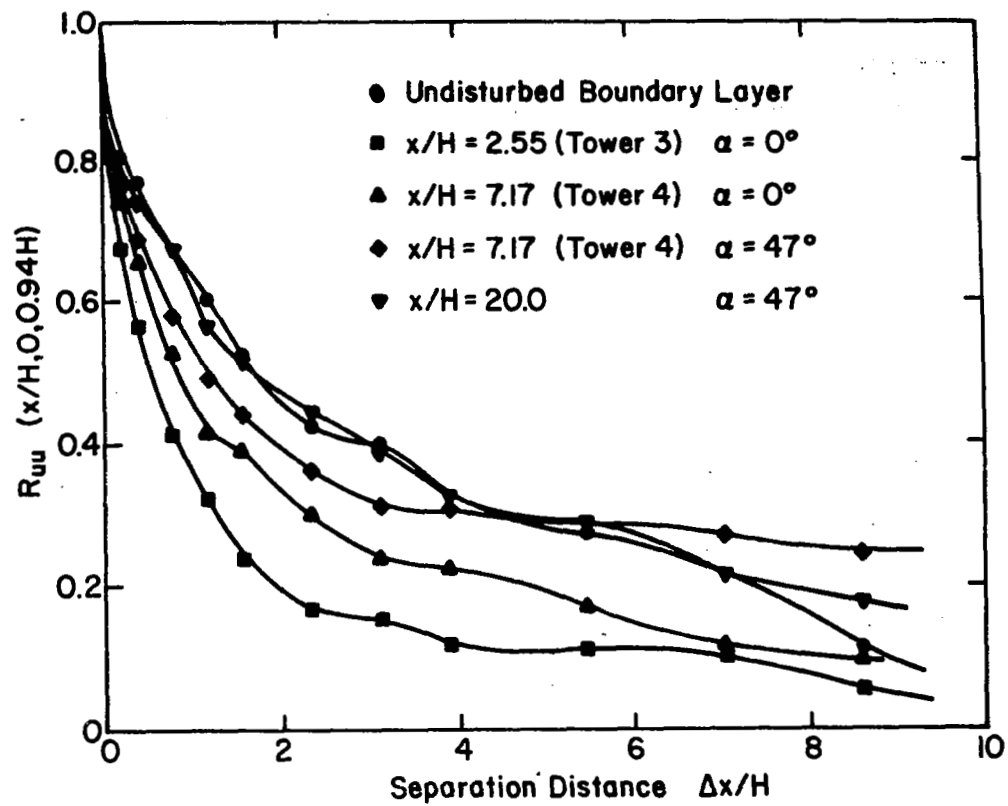
Figure 67. Longitudinal Space Correlations of Longitudinal Velocity Fluctuations behind Model 2 (Fixed Point at y/H = 0.0, z/H = 0.94)
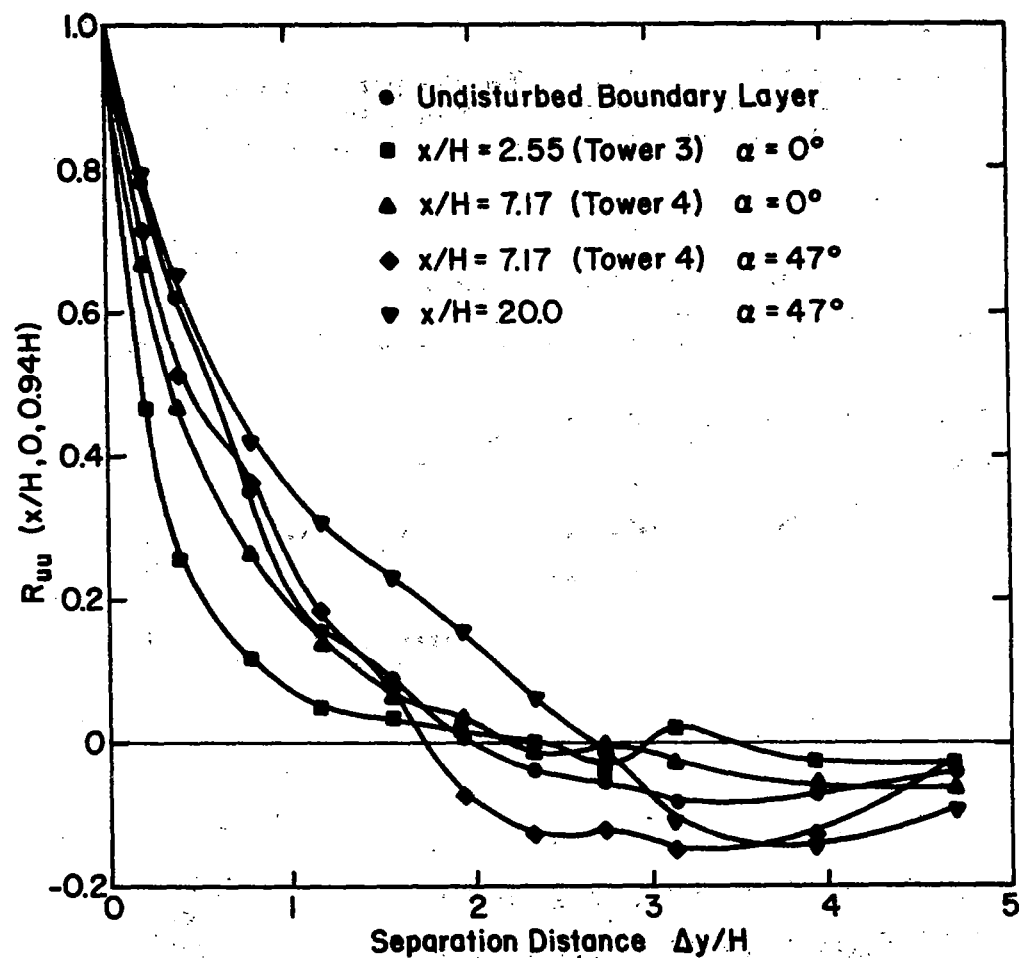
Figure 68. Lateral Space Correlations of Longitudinal Velocity Fluctuations behind Model 2 (Fixed Point at y/H = 0.0 z/H = 0.94)
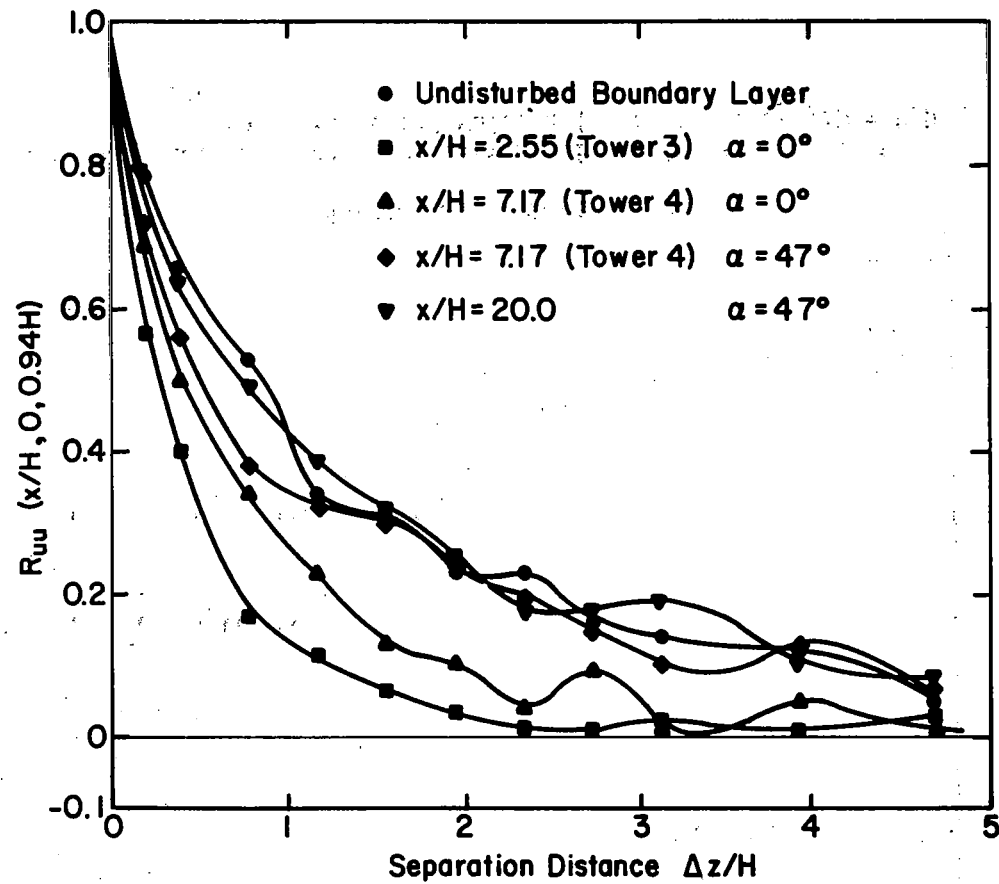
Figure 69. Vertical Space Correlations of Longitudinal Velocity
Fluctuations behind Model 2 (Fixed Point at
y/H = 0.0, z/H = 0.94)
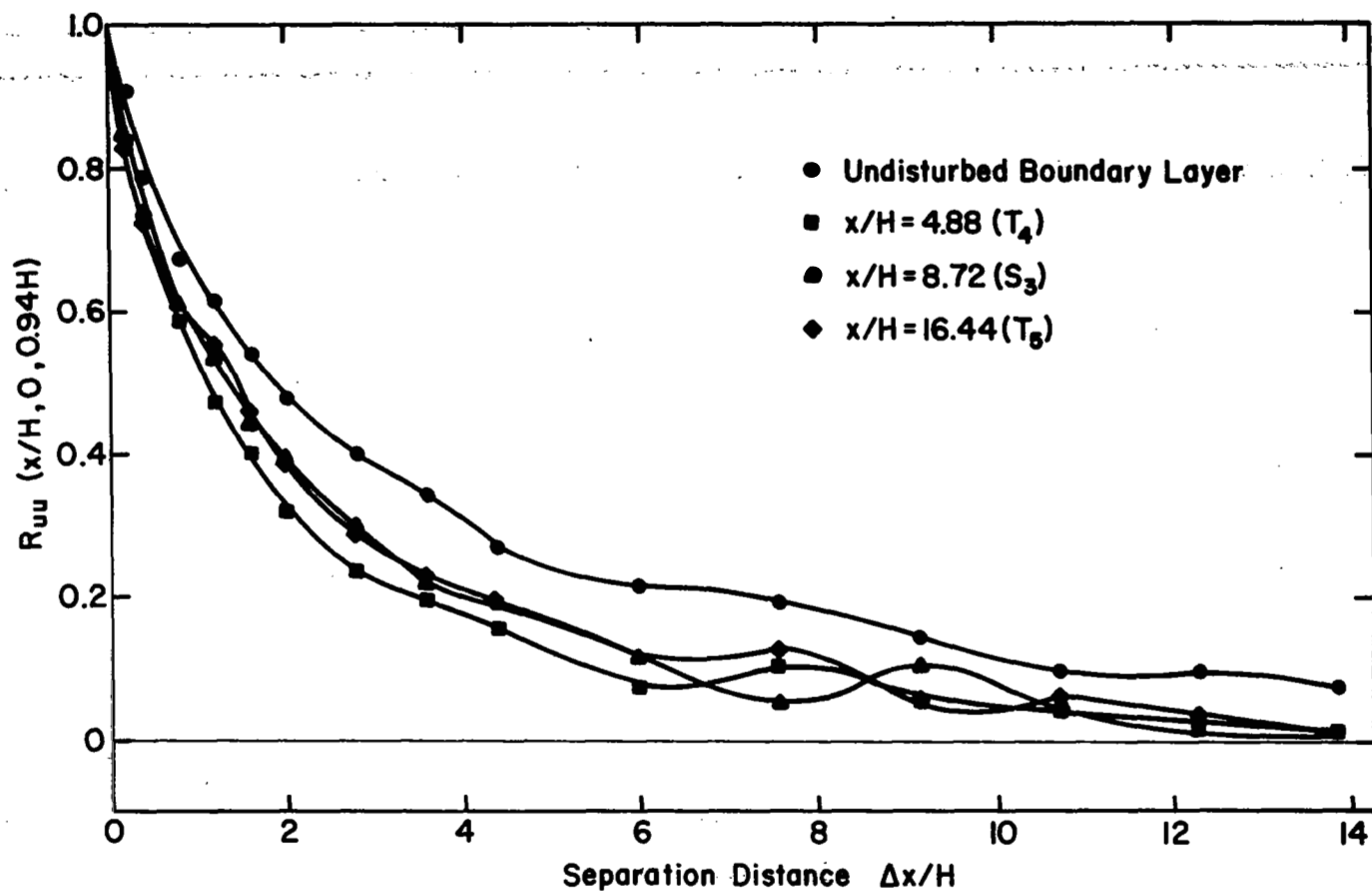
Figure 70. Longitudinal Space Correlations of Longitudinal
Velocity Fluctuations behind Model 4 (Fixed Point
at y/H = 0.0, z/H = 0.94)
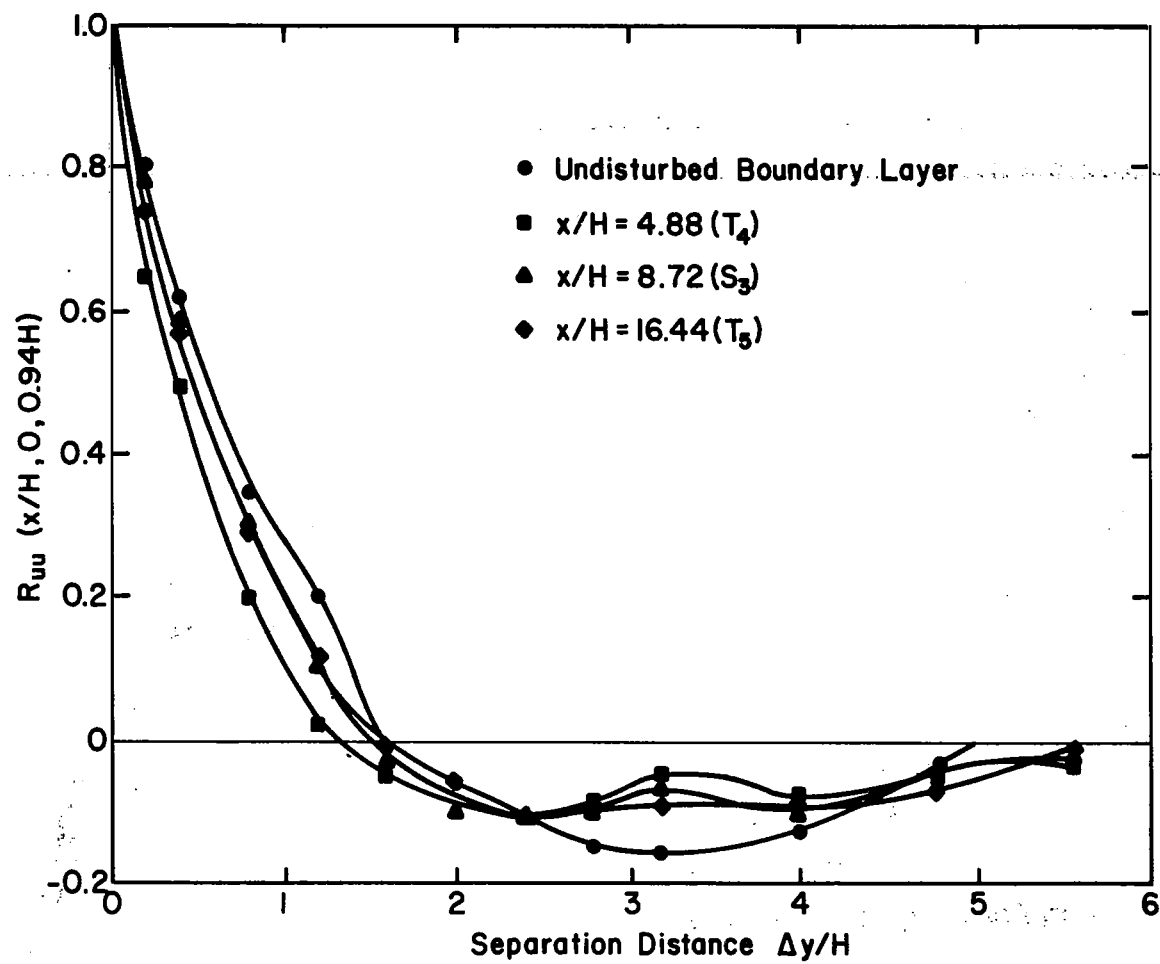
Figure 71. Lateral Space Correlations of Longitudinal
Velocity Fluctuations behind Model 4 (Fixed Point
at y/H = 0.0, z/H = 0.94)
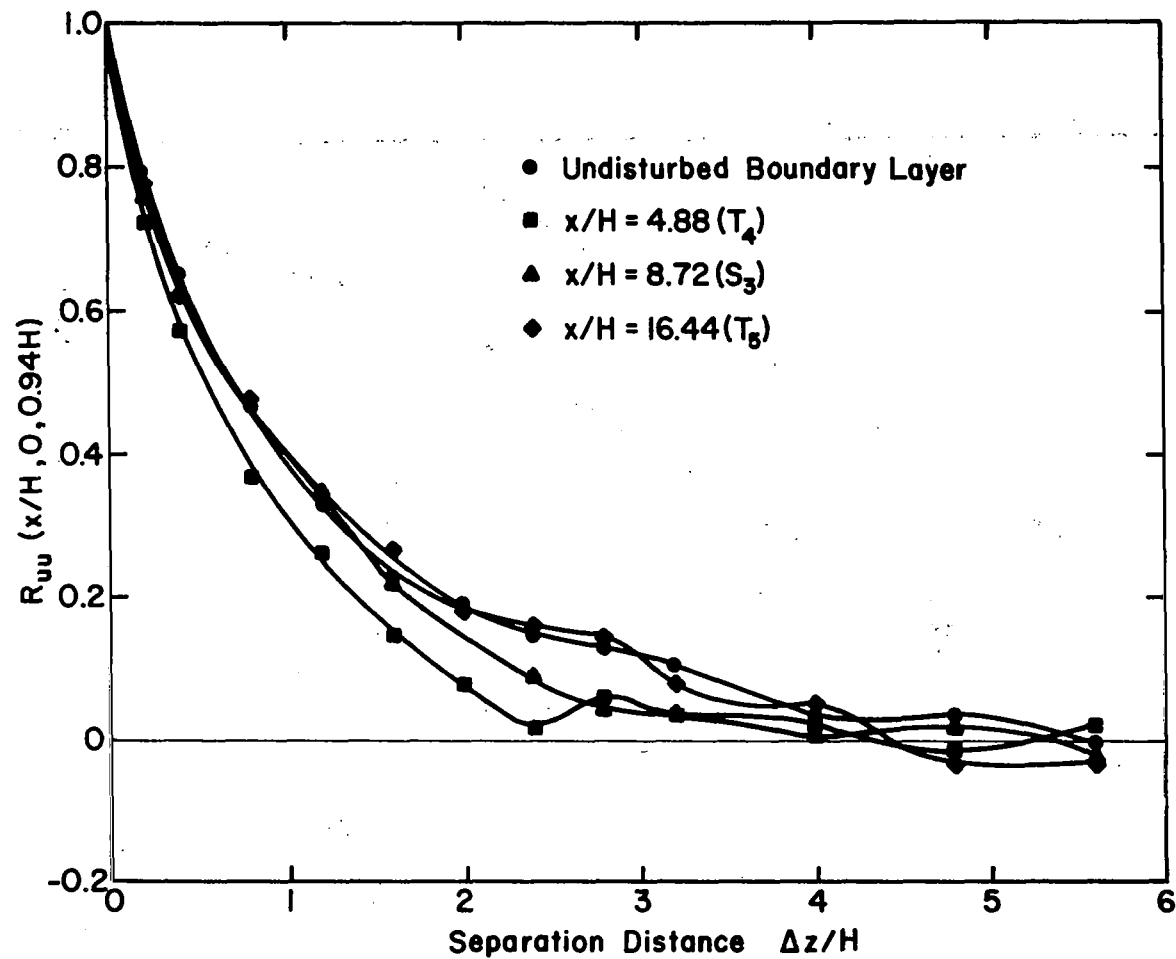
Figure 72.   Vertical Space Correlations of Longitudinal Velocity
Fluctuations behind Model 4 (Fixed Point at
y/H = 0.0, z/H = 0.94)
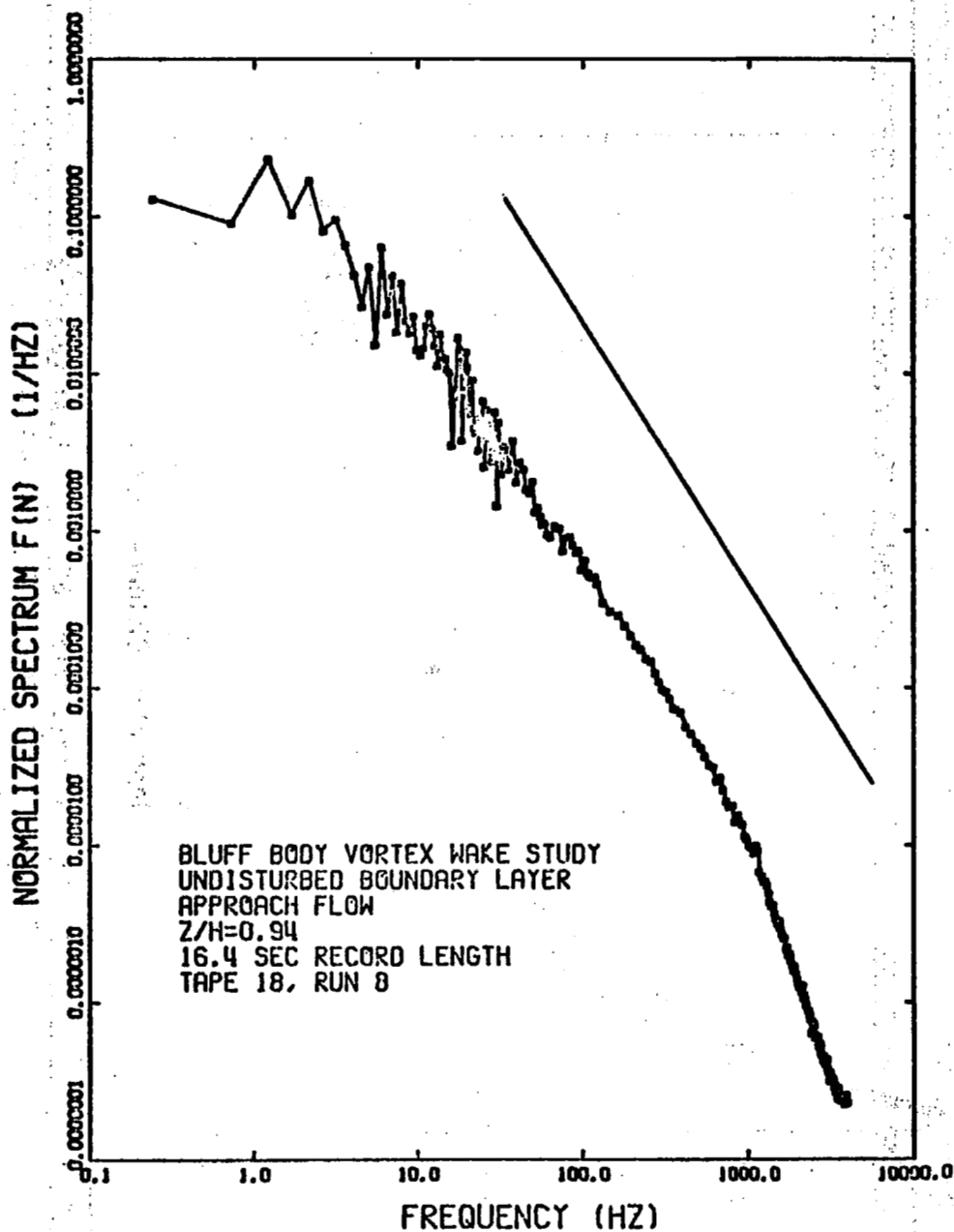
Figure 73. Normalized One-Dimensional Velocity Spectrum in the Undisturbed Boundary Layer at z/H = 0.94 for Test Condition 1
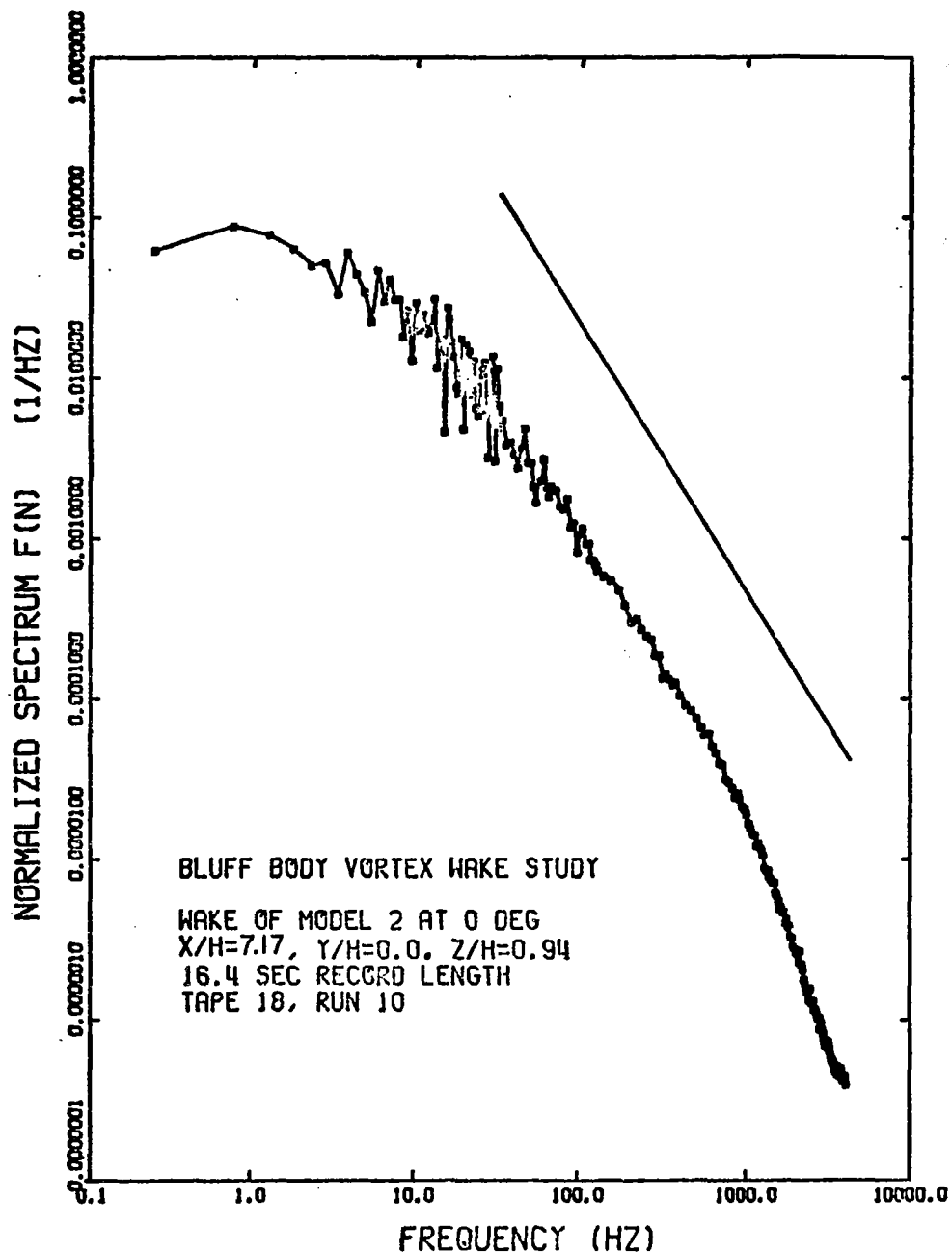
Figure 74. Normalized One-Dimensional Velocity Spectrum behind
Model 2 at α = 0 Degrees for Test Condition 1
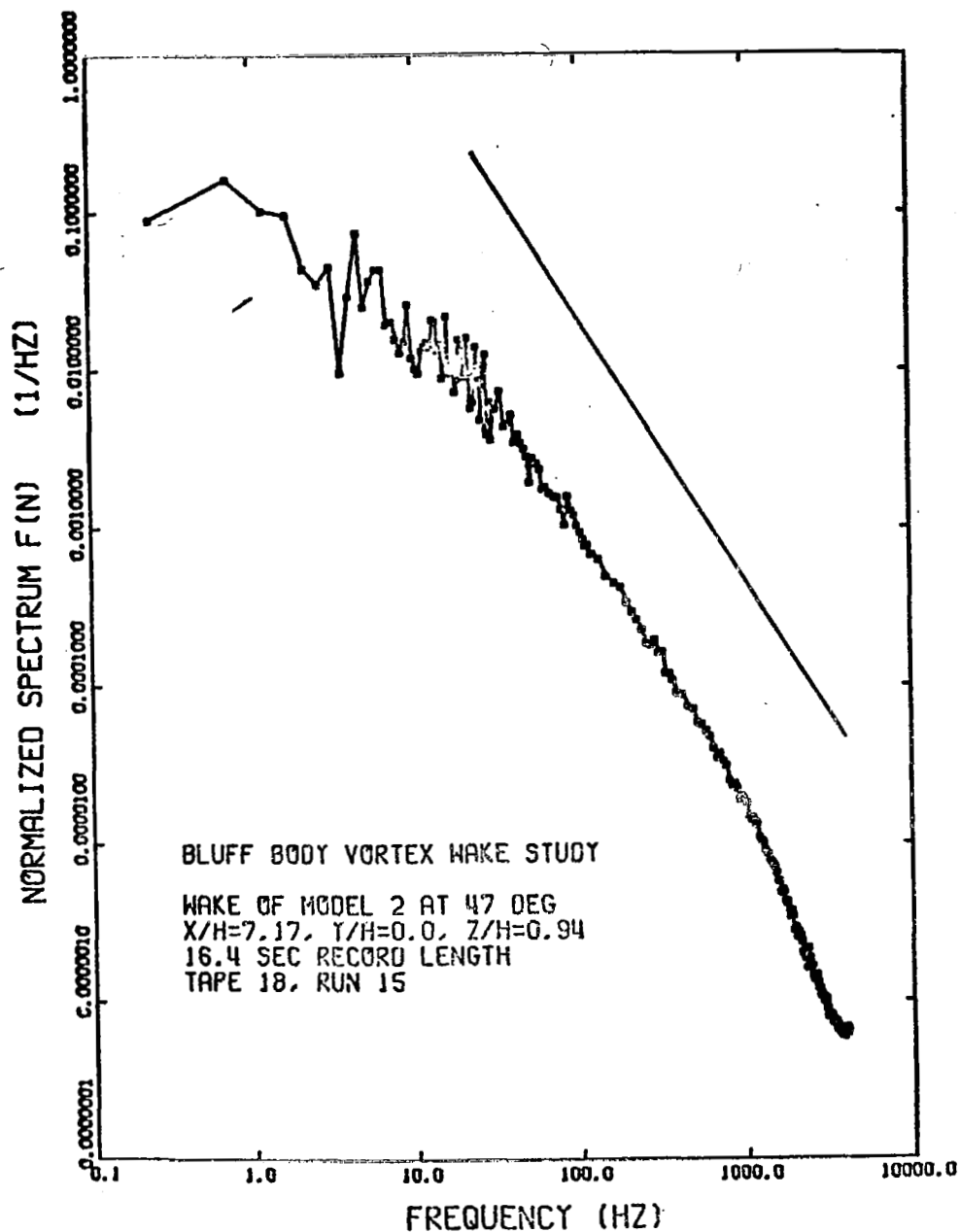
Figure 75. Normalized One-Dimensional Velocity Spectrum
behind Model 2 at α = 47 Degrees for Test
Condition 1
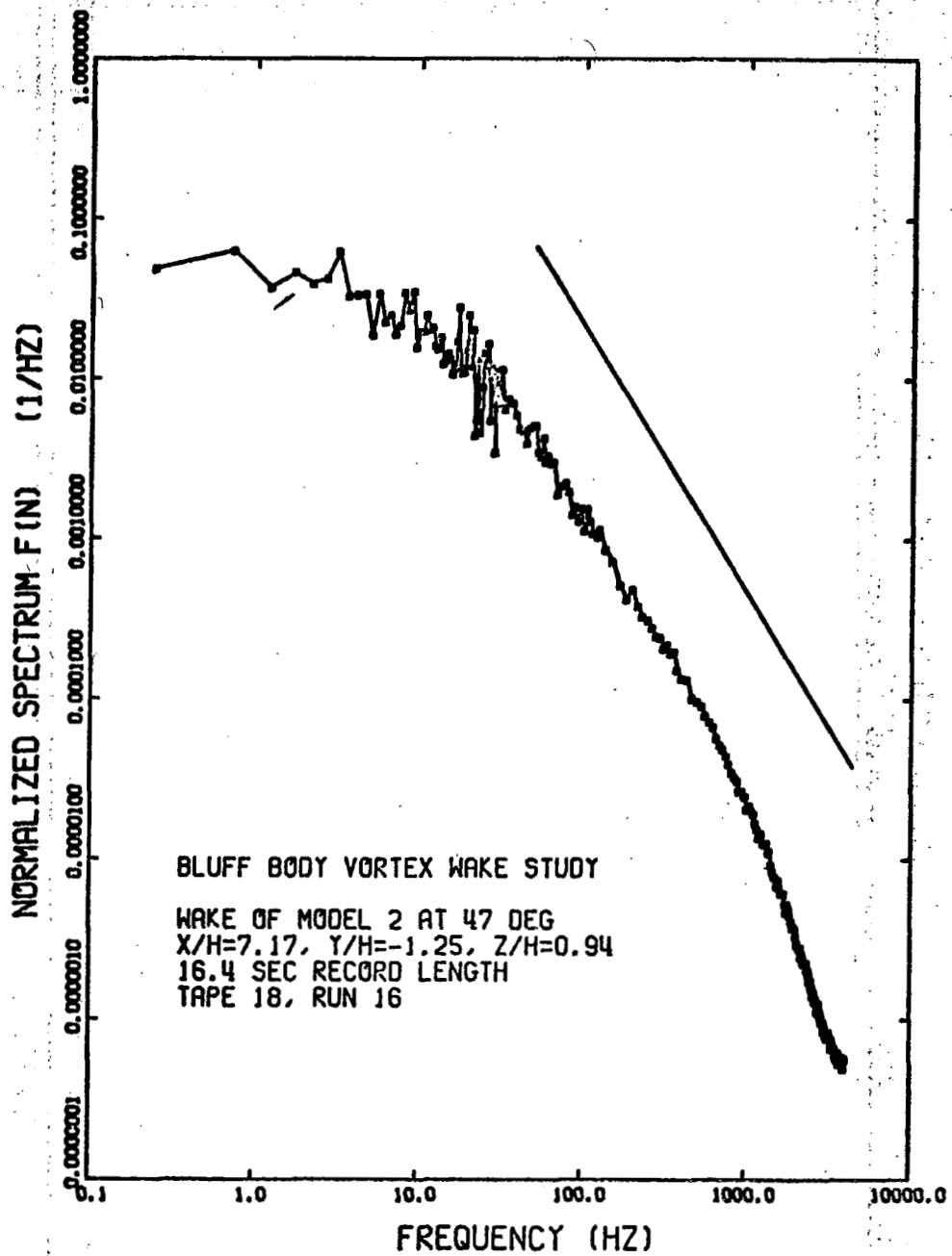
Figure 76. Normalized One-Dimensional Velocity Spectrum behind
Model 2 at α = 47 Degrees for Test Condition 1

BLUFF BODY VORTEX WAKE STUDY

WAKE OF MODEL 2 AT 47 DEG
X/H=20., Y/H=-2.5, Z/H=0.94
16.4 SEC RECORD LENGTH
TAPE 18, RUN 22
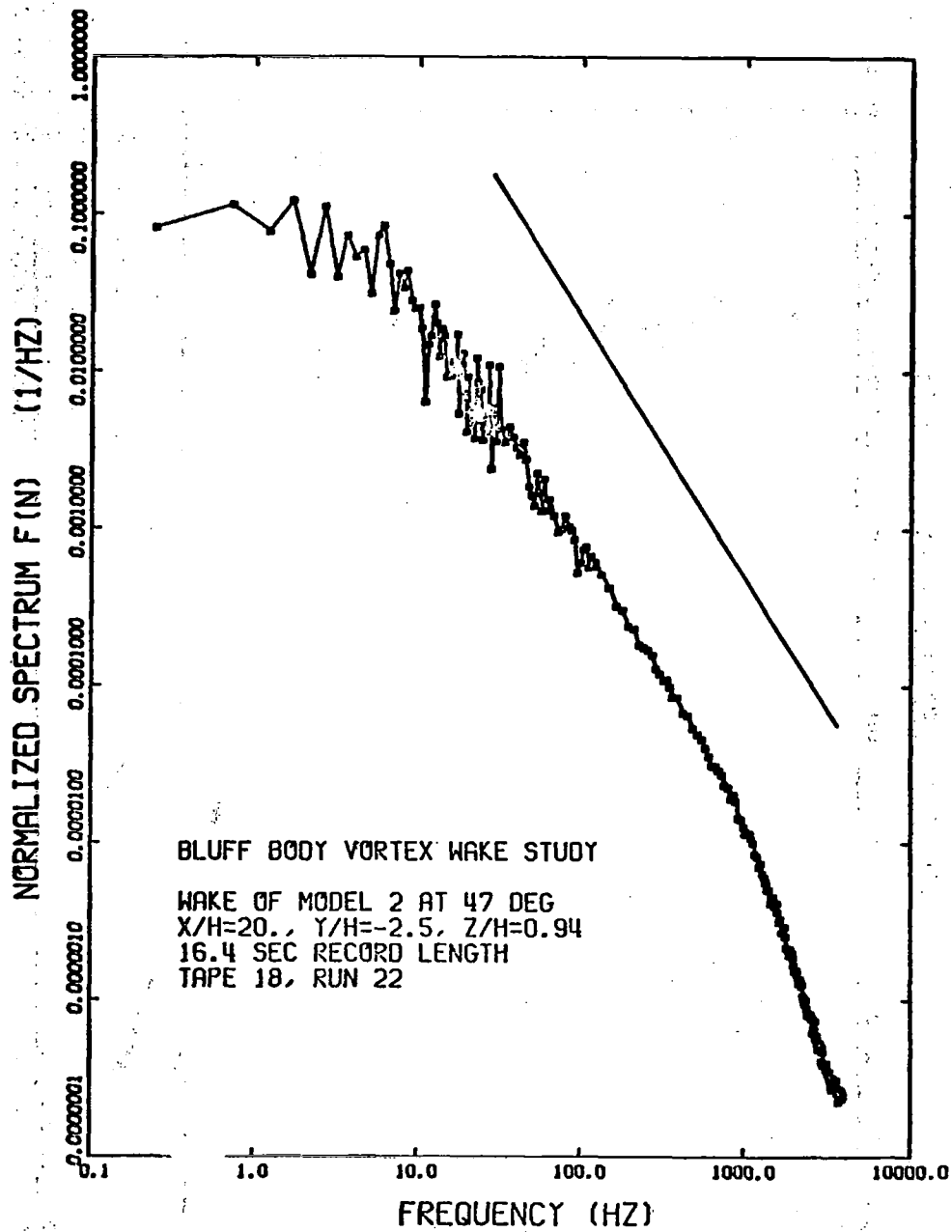
Figure 77. Normalized One-Dimensional Velocity Spectrum behind
Model 2 at α = 47 Degrees for Test Condition 1
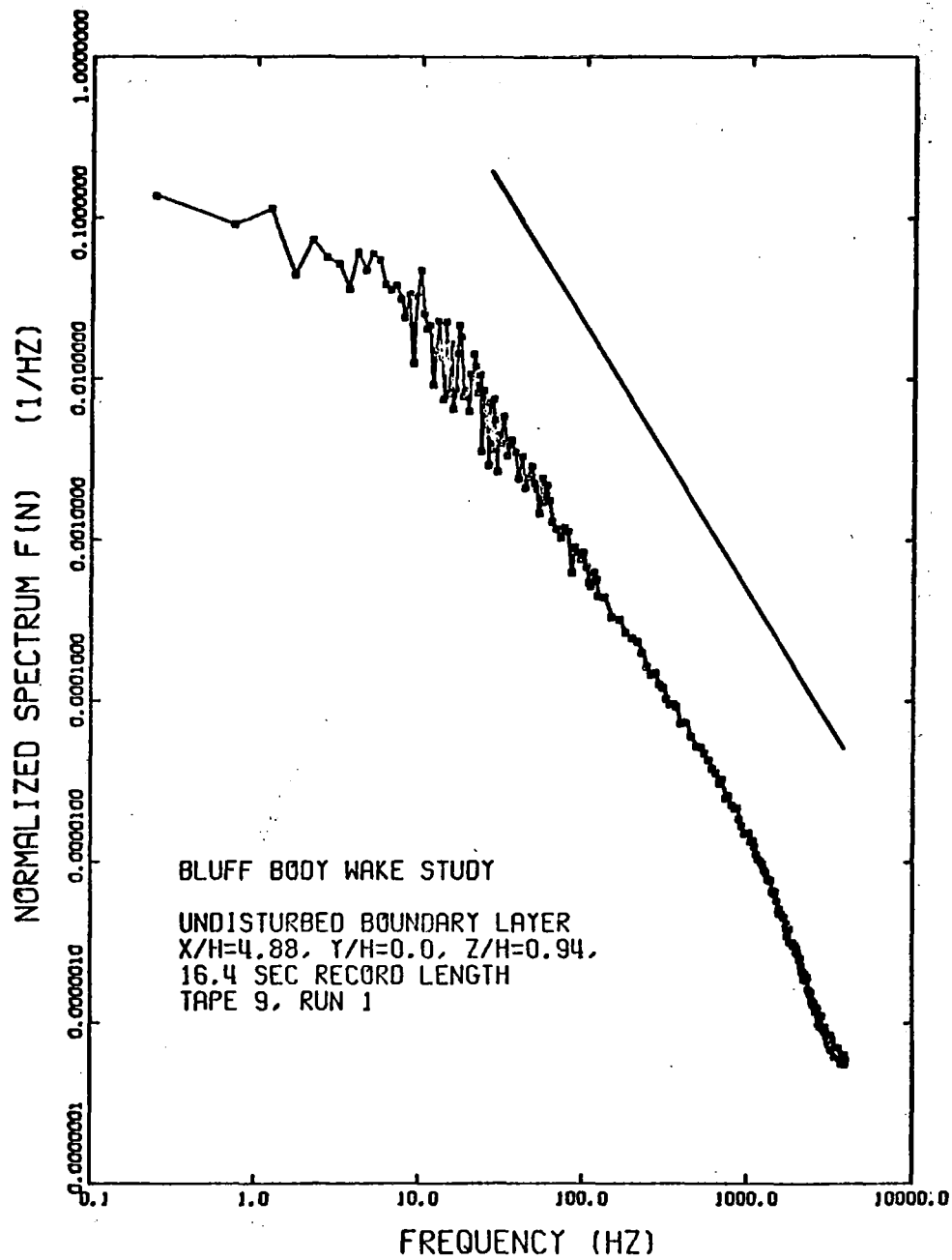
Figure 78. Normalized One-Dimensional Velocity Spectrum behind Model 4 at α = 0 Degrees for Test Condition 2
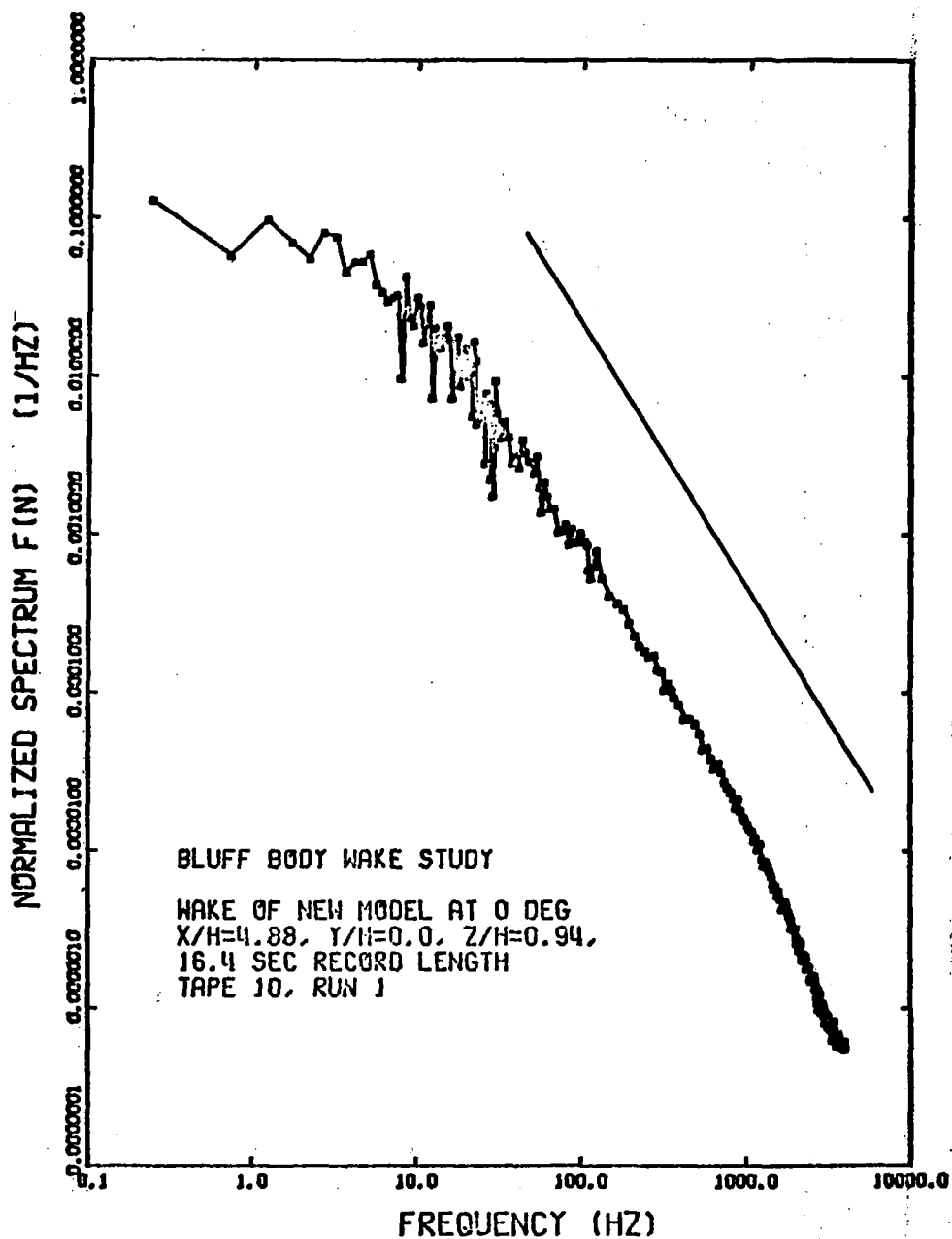
Figure 79.   Normalized One-Dimensional Velocity Spectrum behind
Model 4 at α = 0 Degrees for Test Condition 2
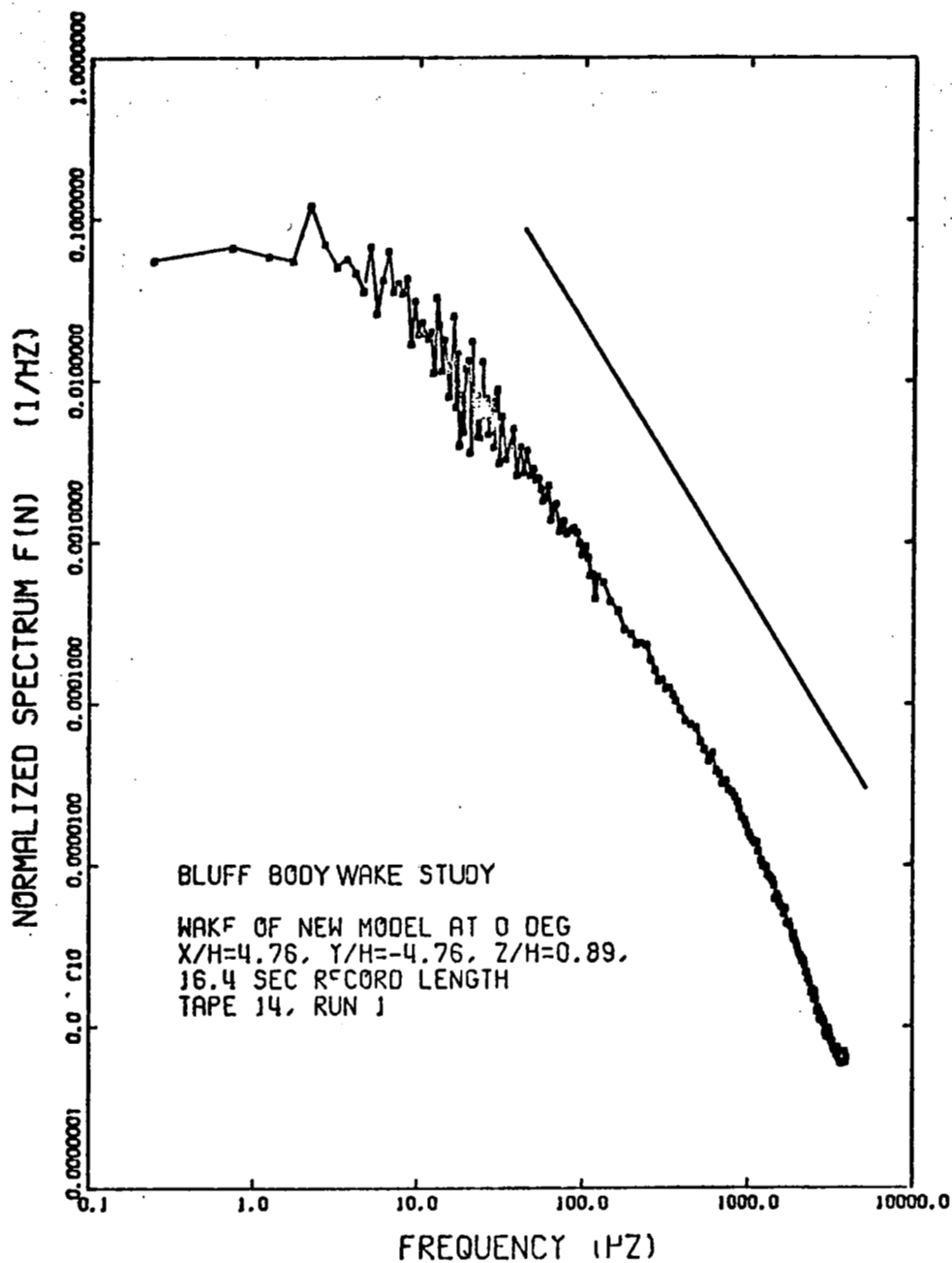
Figure 80.   Normalized One-Dimensional Velocity Spectrum behind
Model 4 at α = 0 Degrees for Test Condition 1
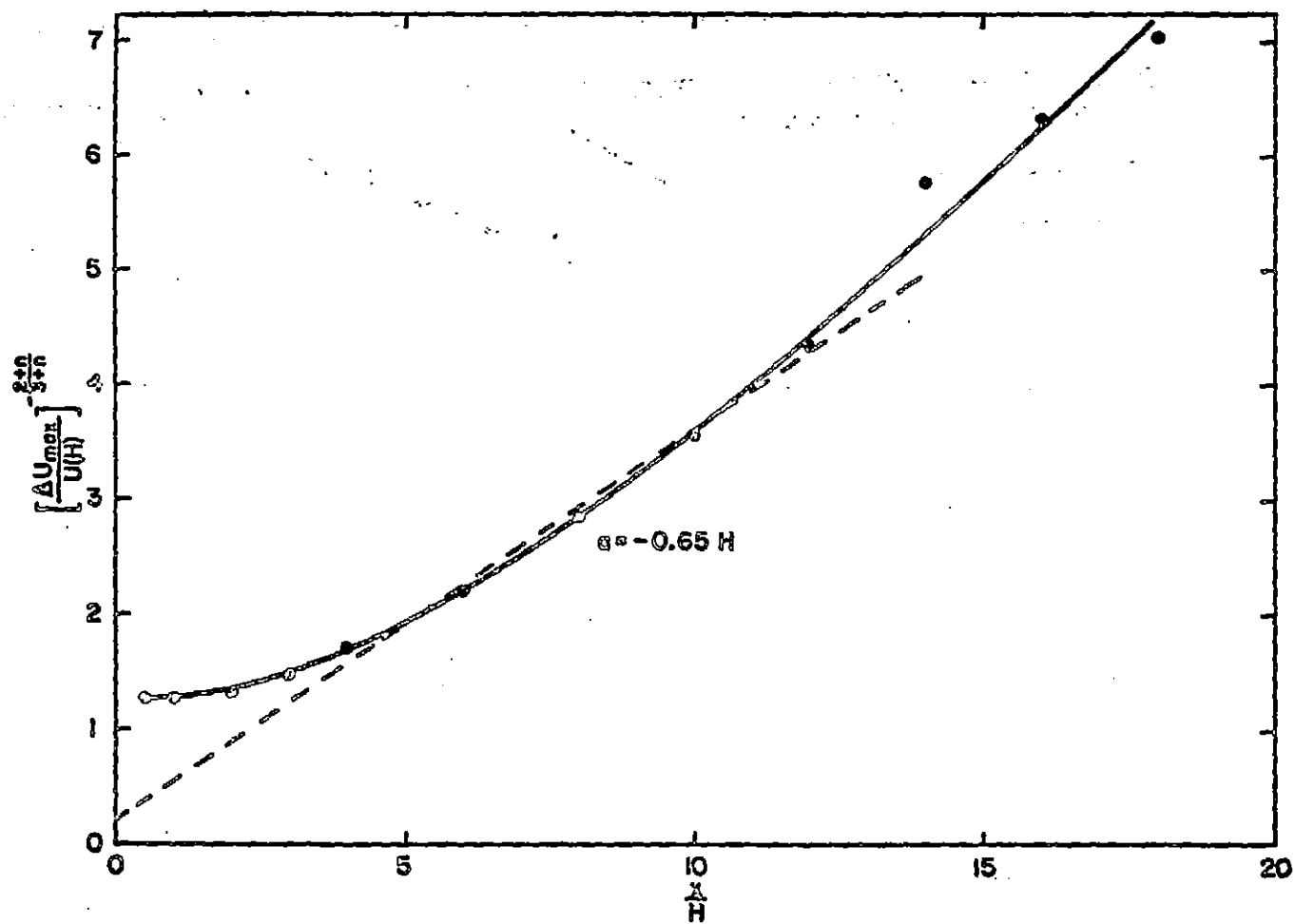
Figure 81a. Determination of the Virtual Origin for the Model 2 Wake for Comparison with Hunt's Theory
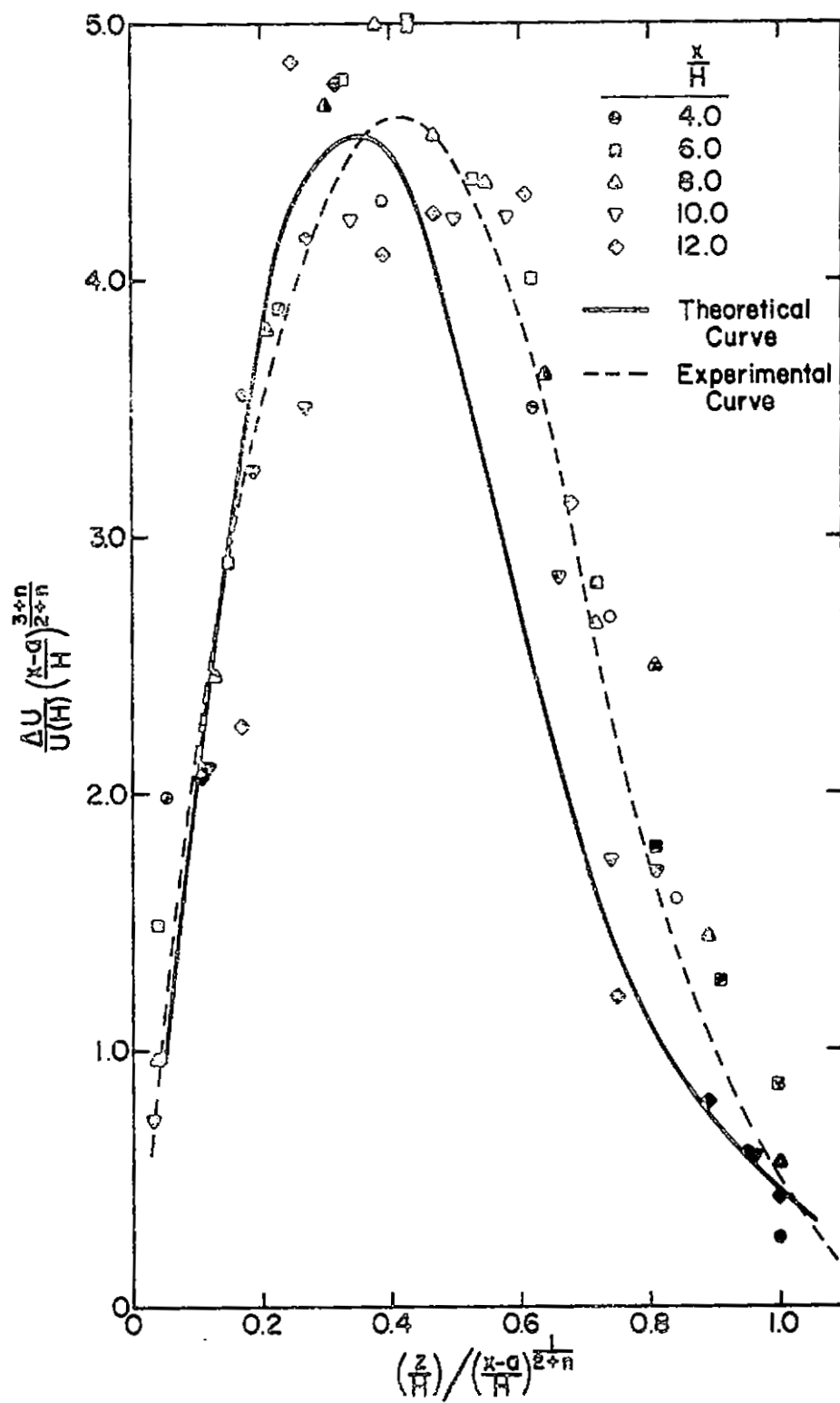
Figure 81b. Comparison of the Model 2 Wake with Hunt's Theory
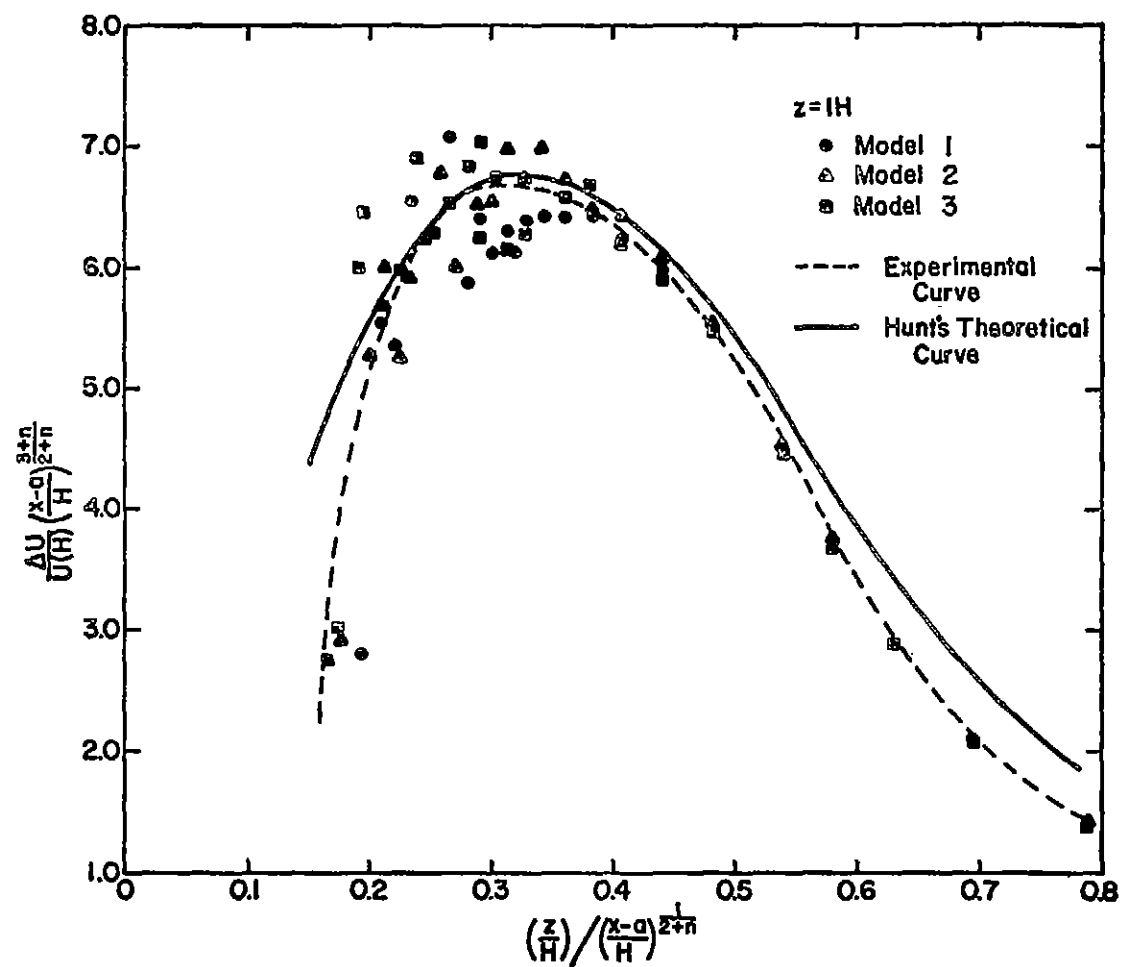
Figure 81c.   Comparison of the Wakes of Models 1, 2, and 3 with Hunt's Theory
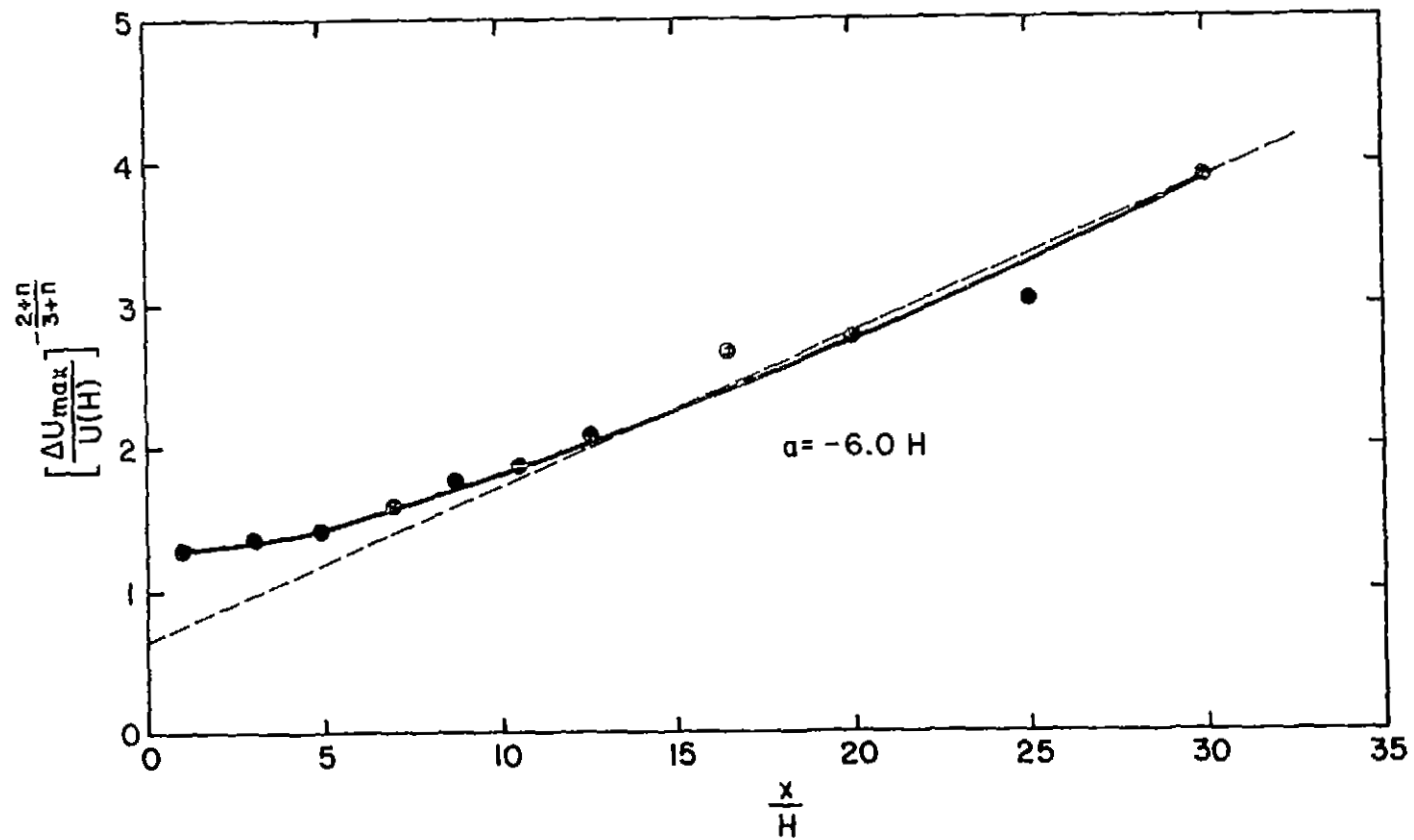
Figure 82a. Determination of the Virtual Design for the Model 4 Wake for Comparison with Hunt's Theory
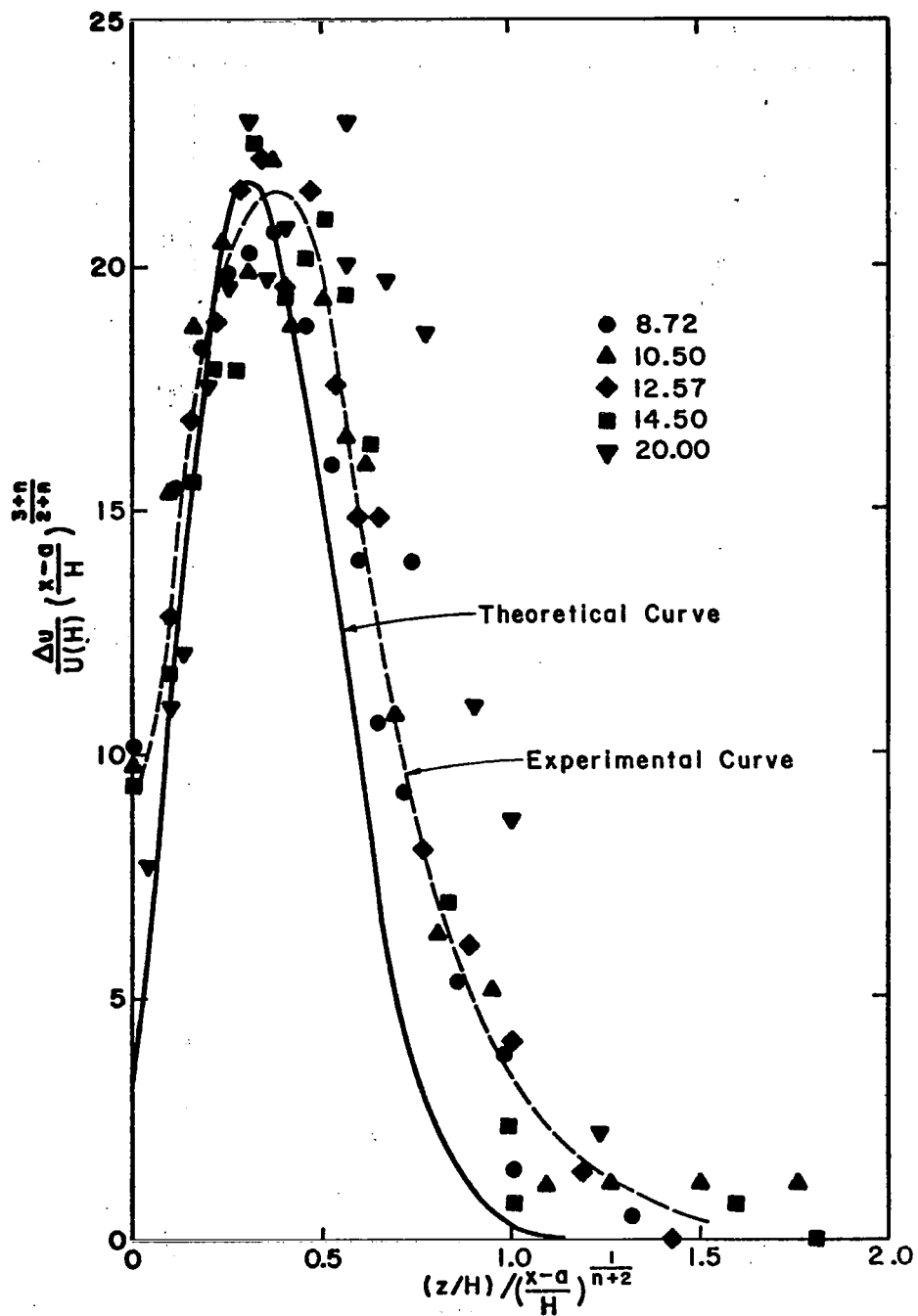
Figure 82b.   Comparison of the Model 4 Wake with Hunt's Theory
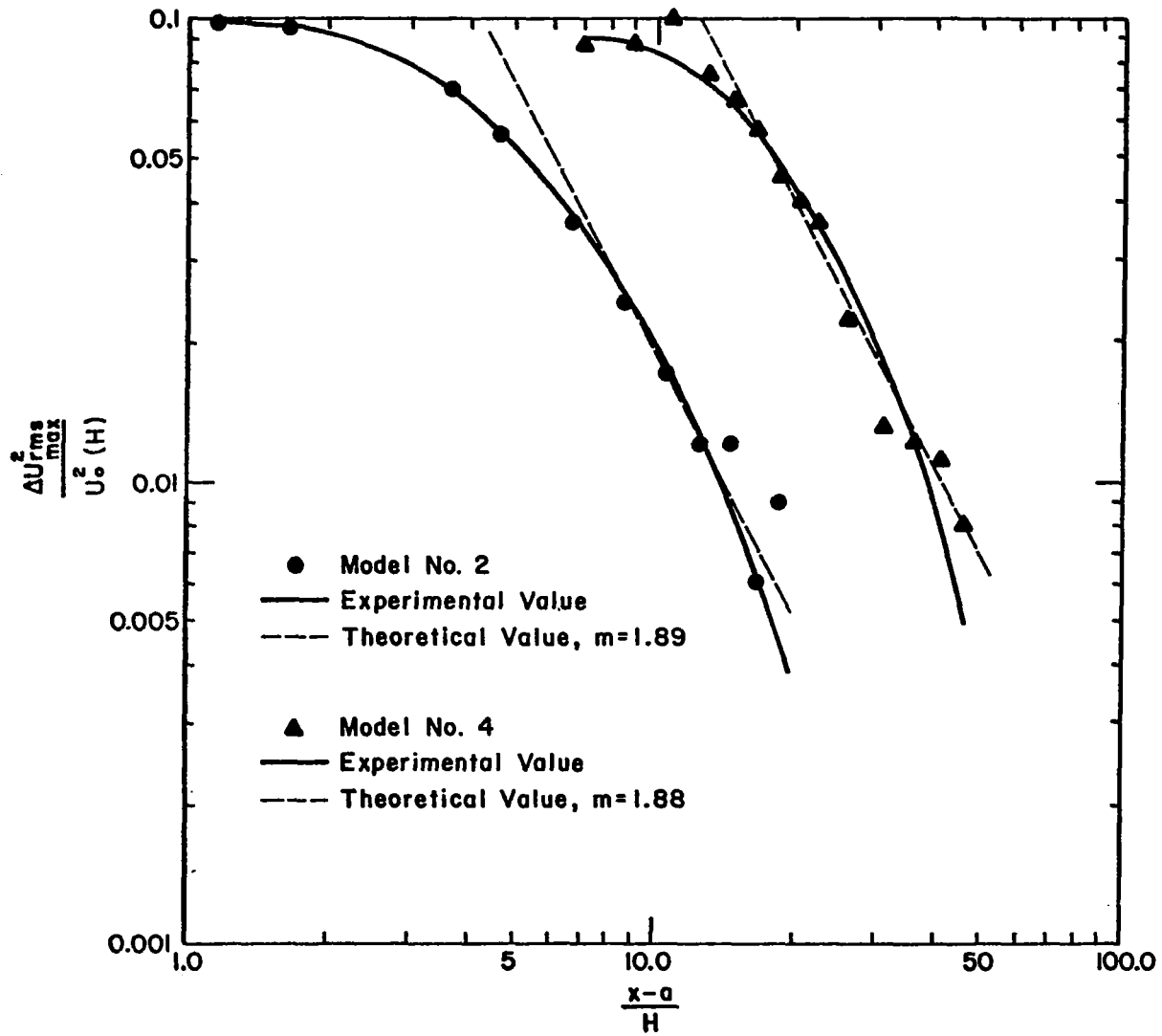
Figure 83. Turbulent Velocity Excess Decay Behind Models 2 and 4
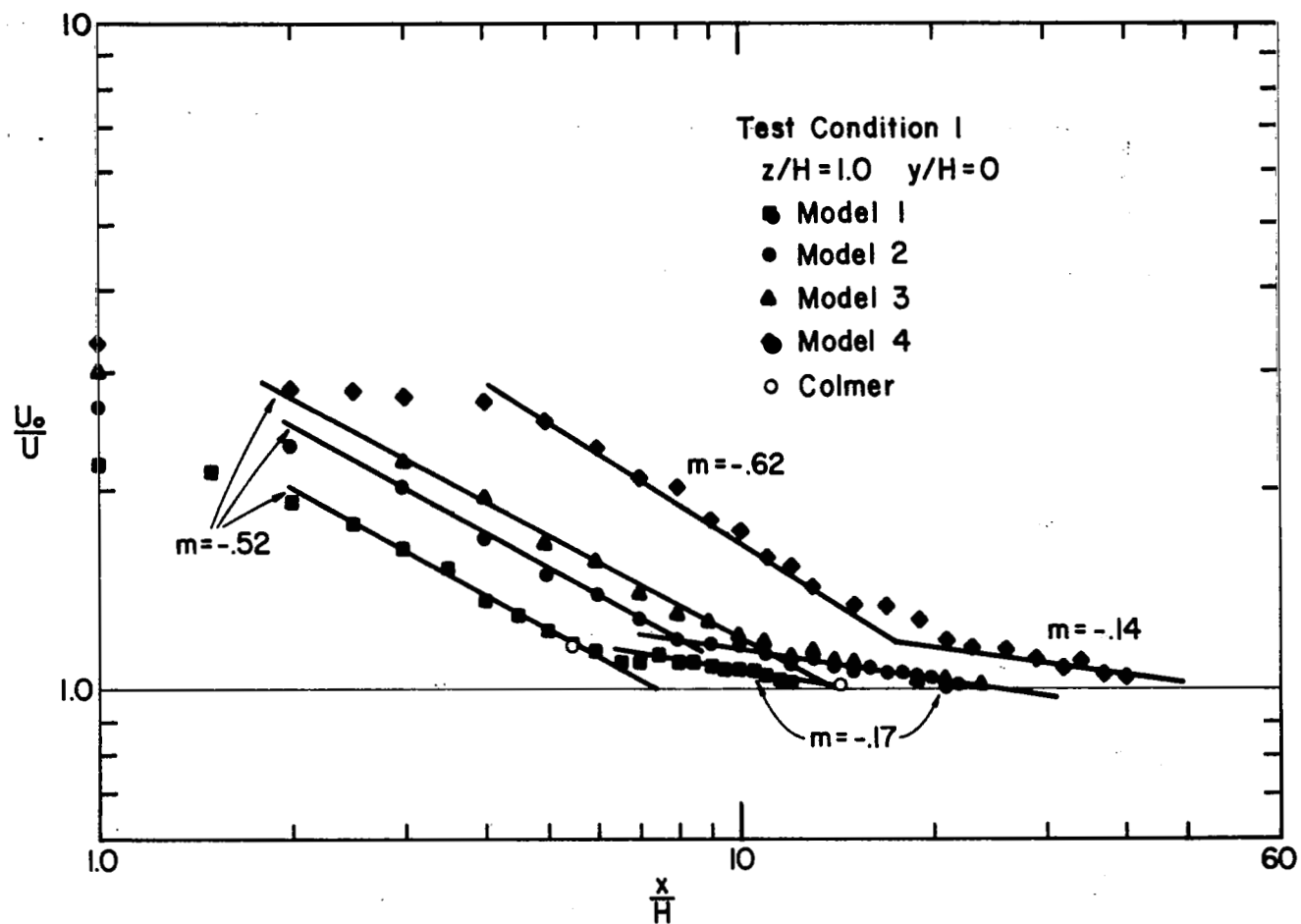
Figure 84.   Decay of the Ratio U_O/U along the Centerline
(Test Condition 1, models 1,2,3)

Figure 85. Decay of the Ratio $\dfrac{U_{rms}}{U}\Big/\dfrac{(U_o)_{rms}}{U_o}$ along the Centerline

(Test Condition 1, models 1,2,3)
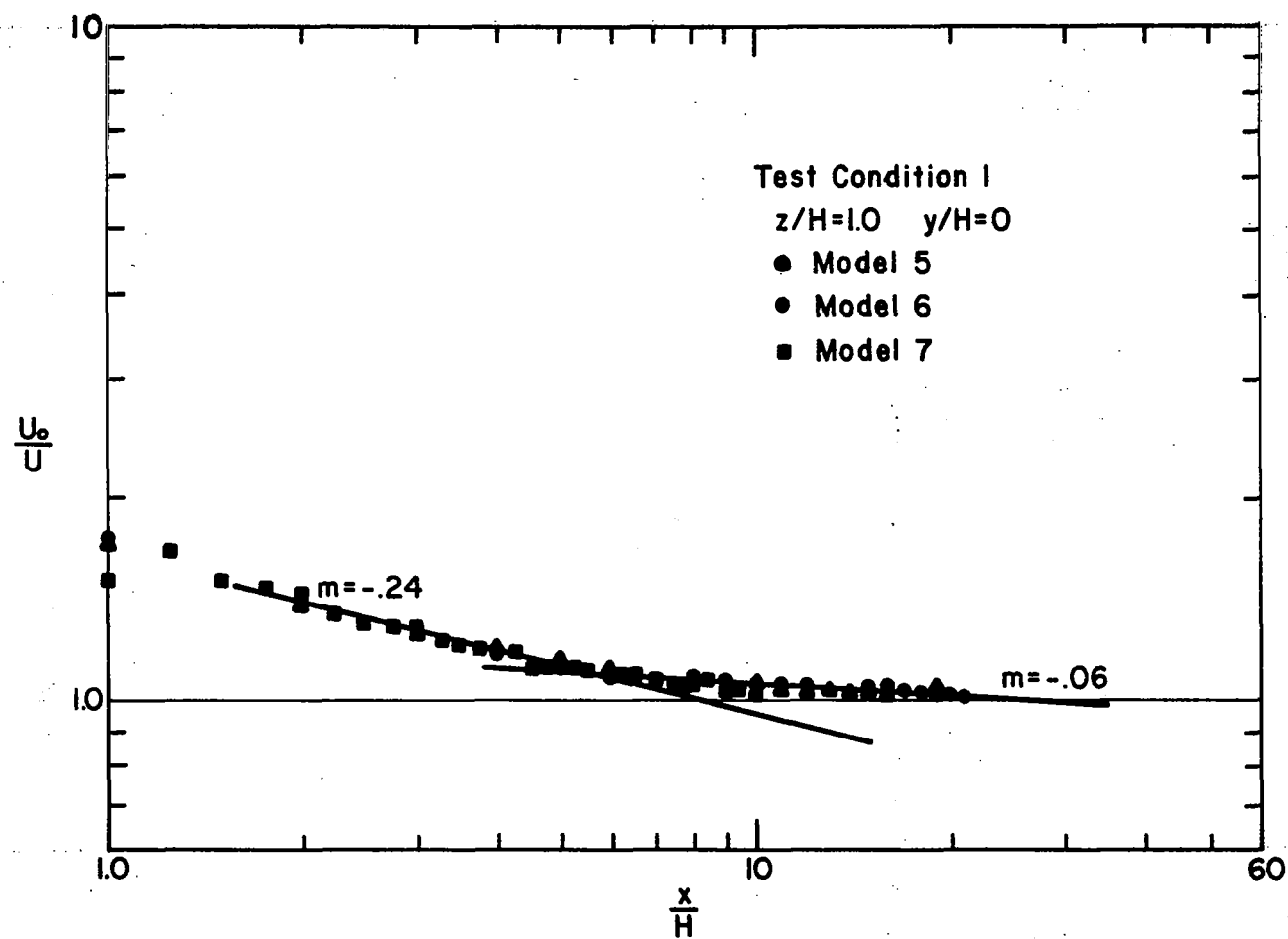
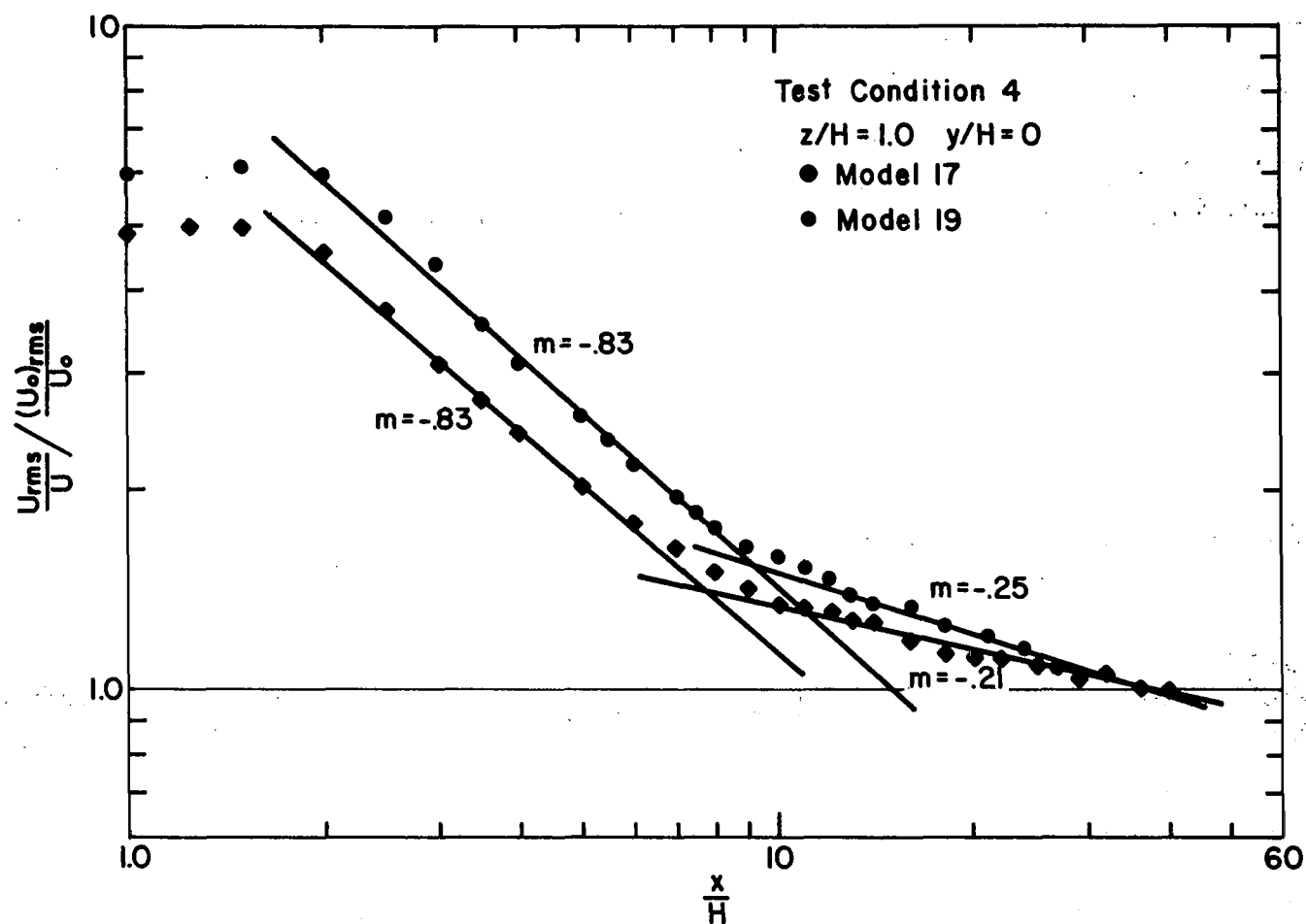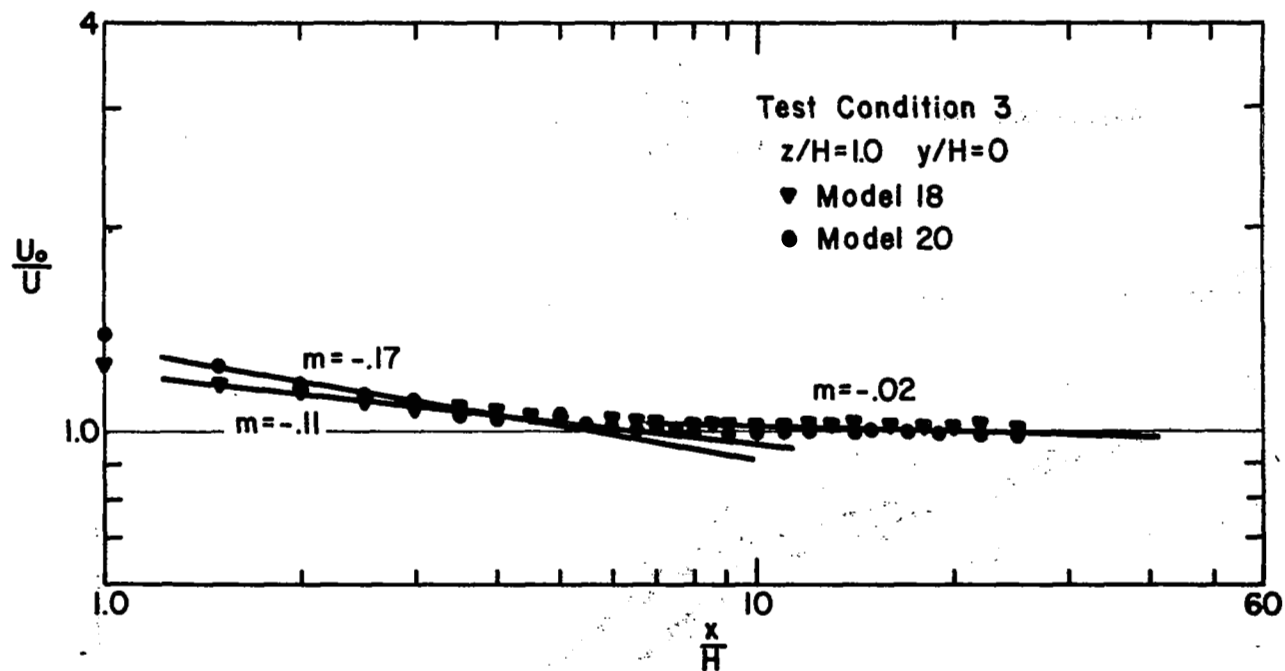Figure 86. Decay of the Ratio U_0/U along the Centerline
(Test Condition 1, models 5,6,7)
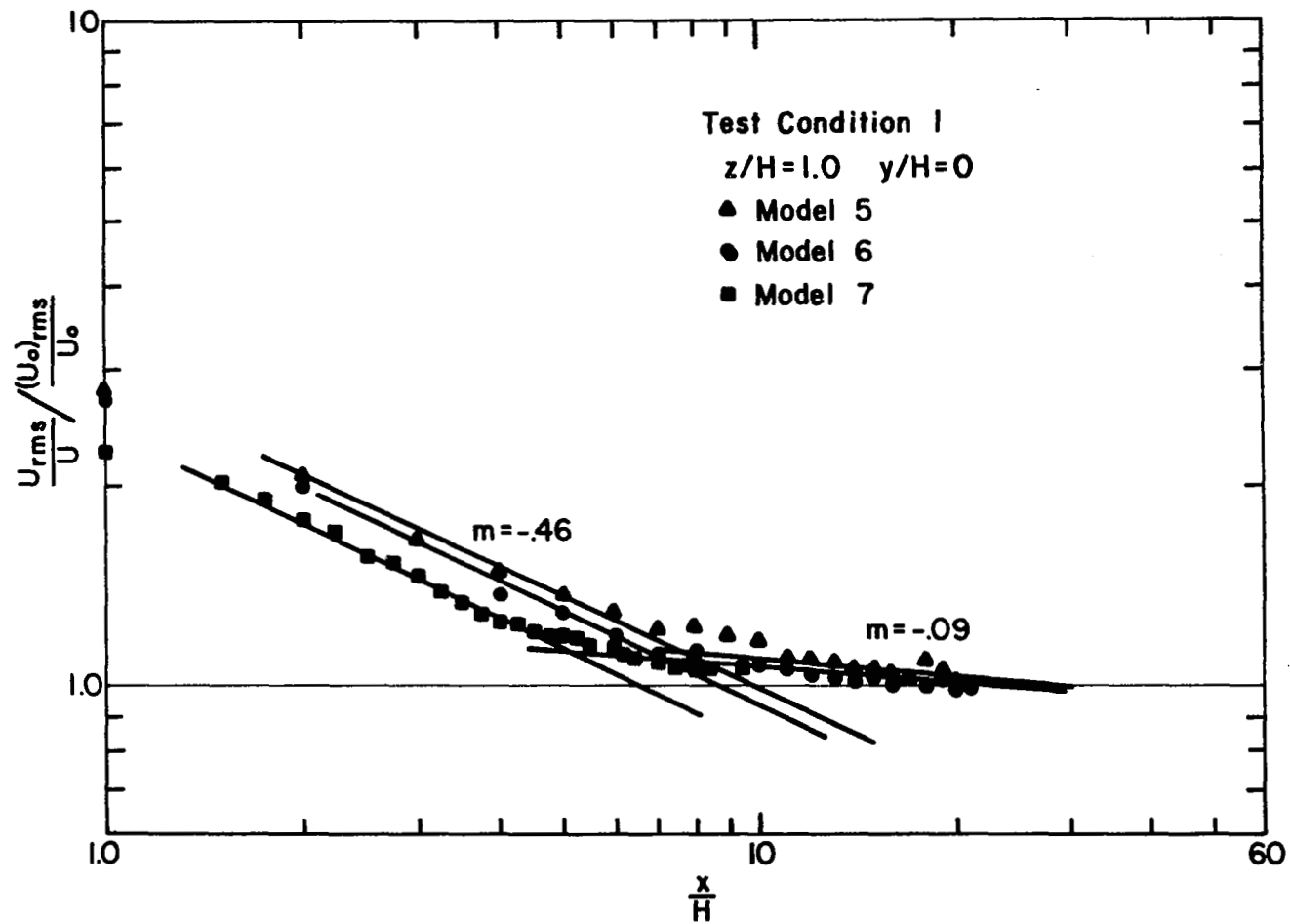
Figure 87. Decay of the Ratio $\dfrac{U_{rms}}{U}/\dfrac{(U_o)_{rms}}{U_o}$ along the Centerline

(Test Condition 1, models 5,6,7)
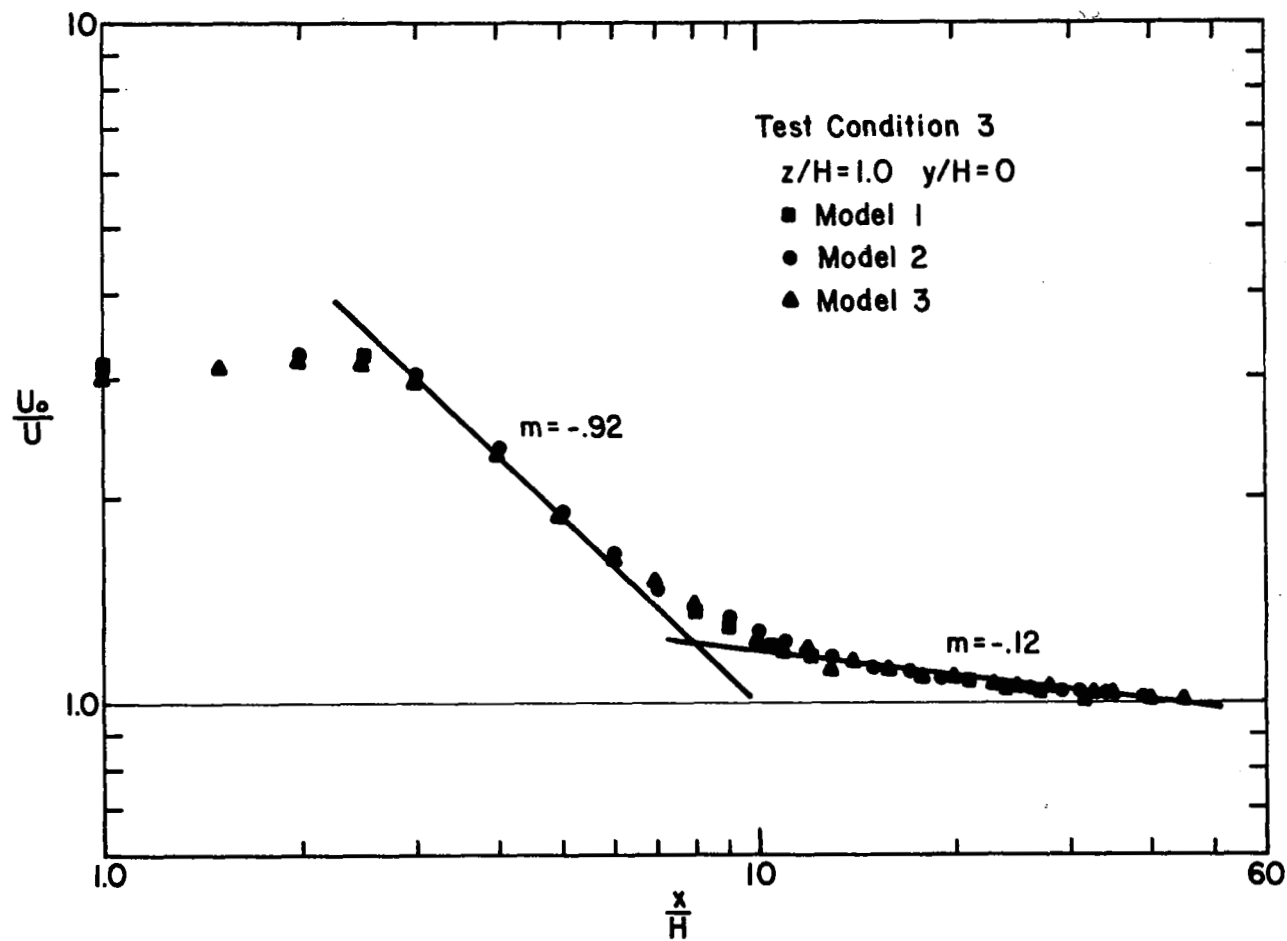
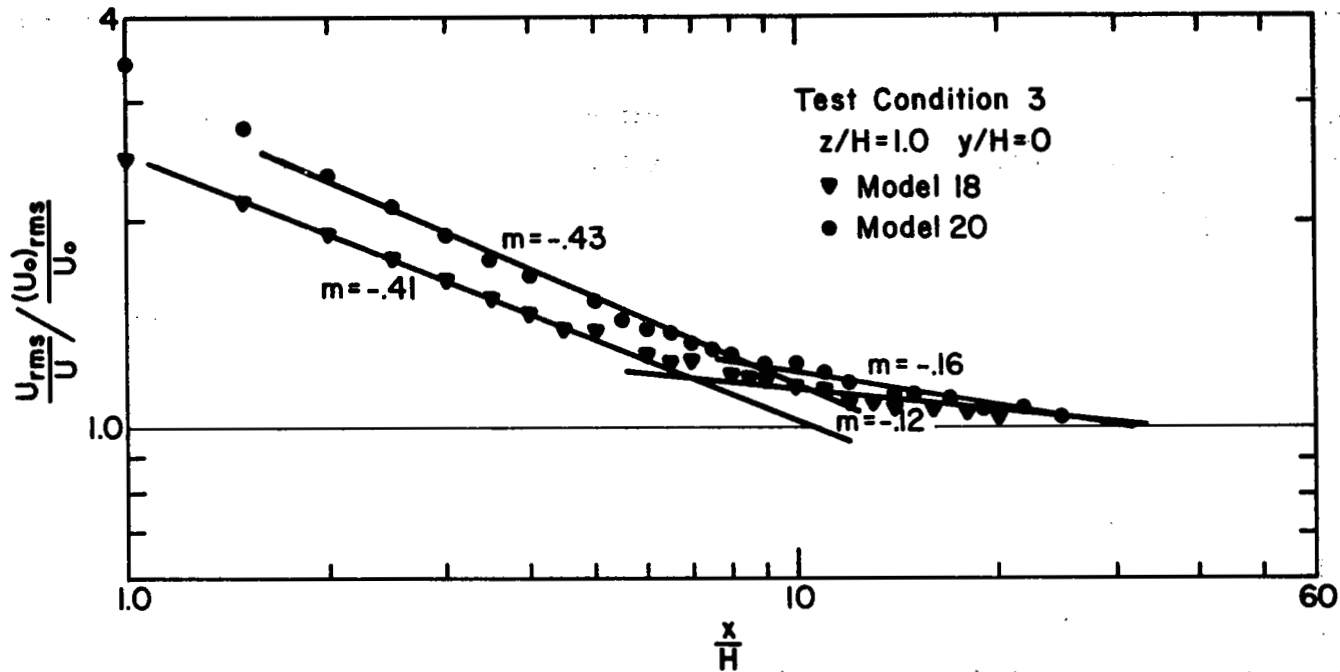Figure 88. Decay of the Ratio U_o/U along the Centerline
(Test Condition 3, models 1,2,3)
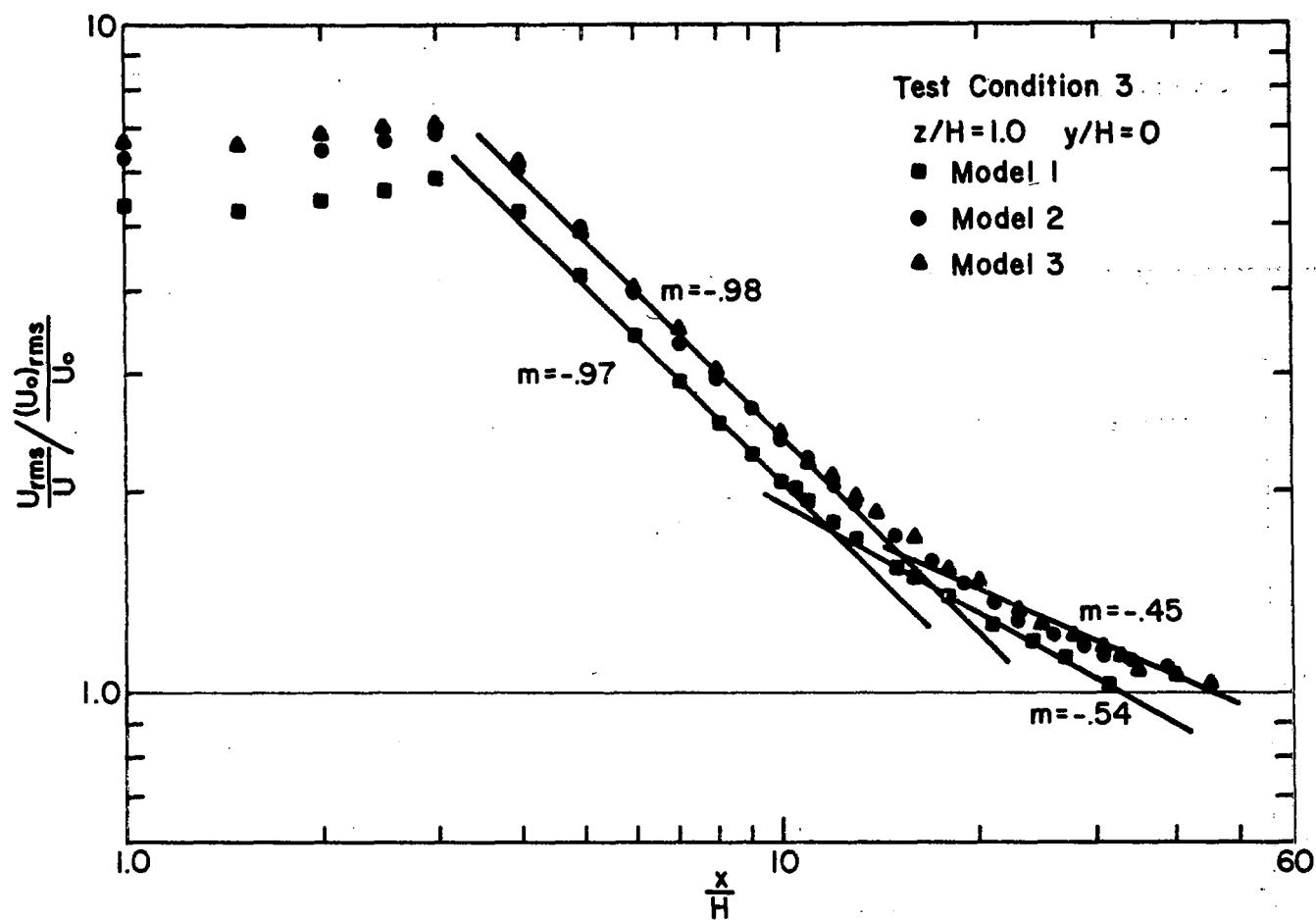
Figure 89.   Decay of the Ratio $\dfrac{U_{rms}}{U}/\dfrac{(U_o)_{rms}}{U_o}$ along the Centerline
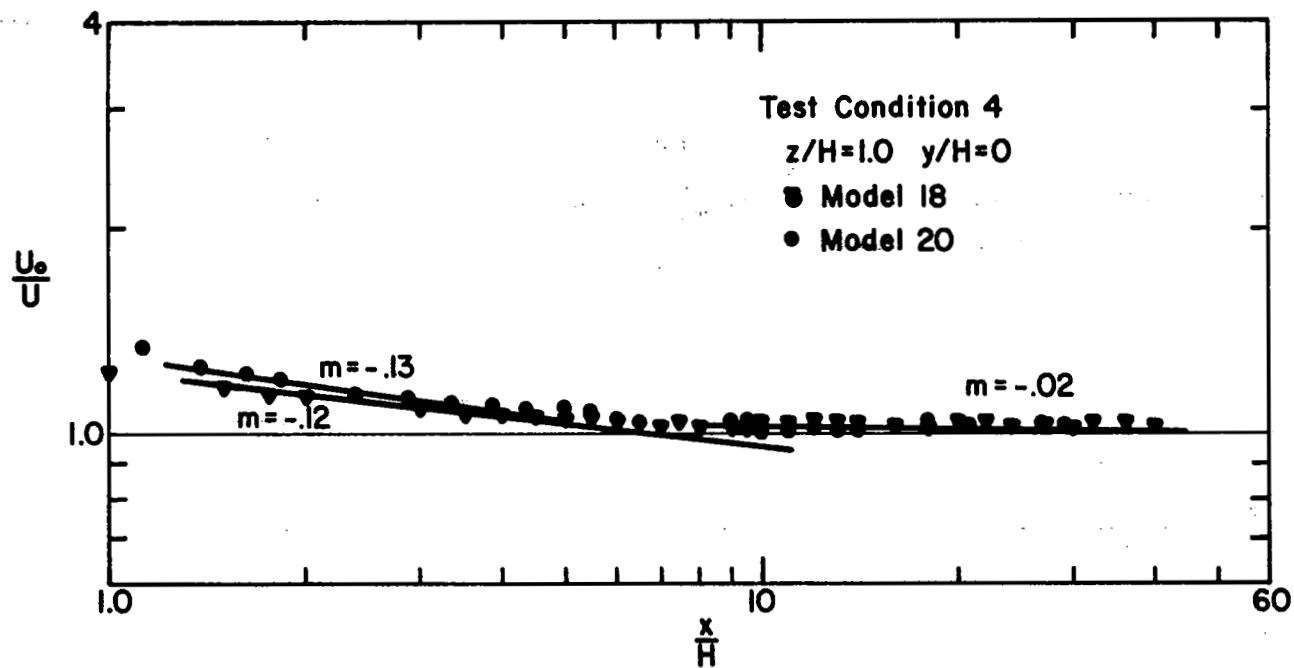
(Test Condition 3, models 1,2,3)
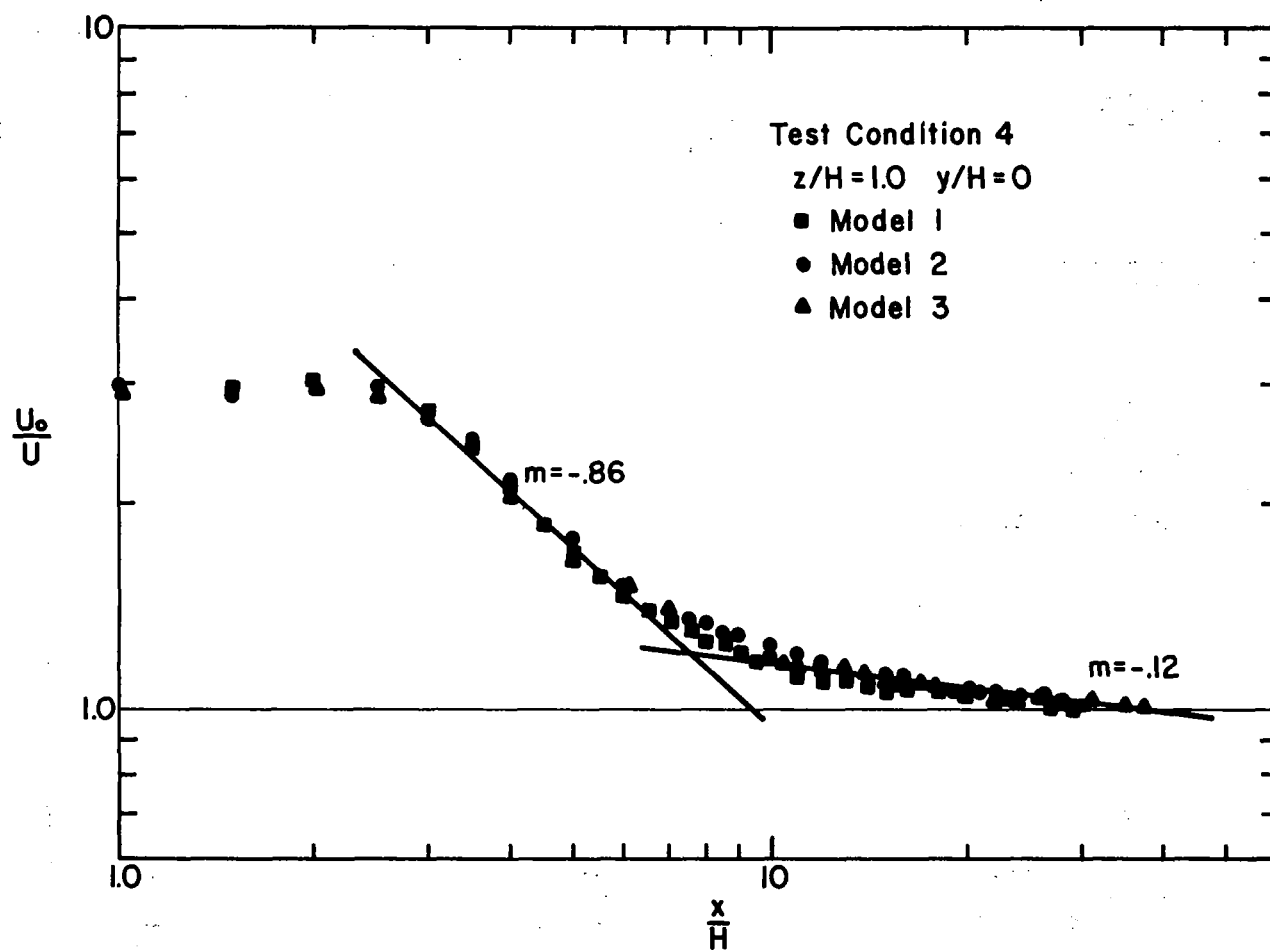
Figure 90.   Decay of the Ratio U_o/U along the Centerline
(Test Condition 4, models 1,2,3)
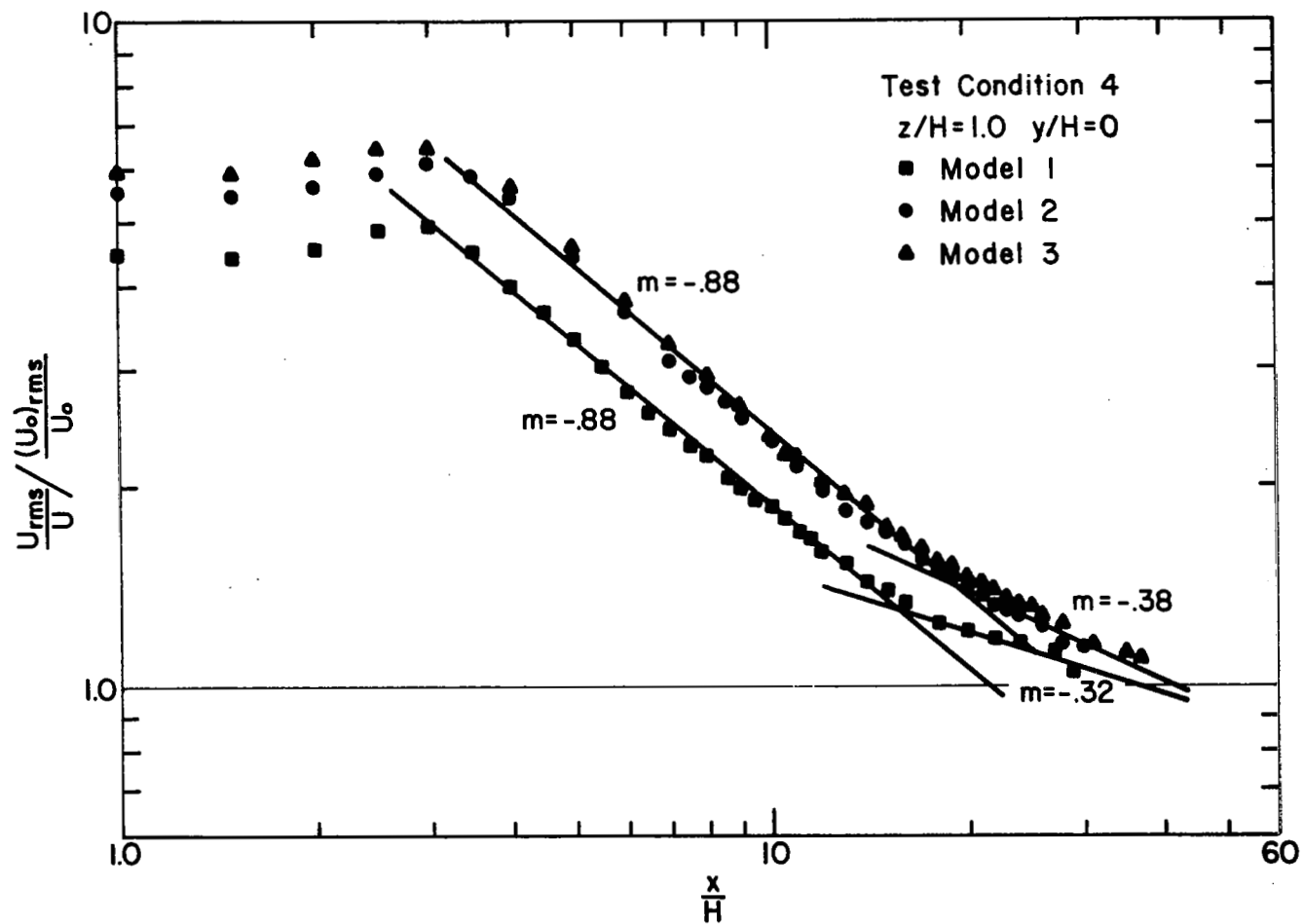
Figure 91.   Decay of the Ratio $\dfrac{U_{rms}}{U}\Big/\dfrac{(U_o)_{rms}}{U_o}$ along the Centerline

(Test Condition 4, models 1,2,3)
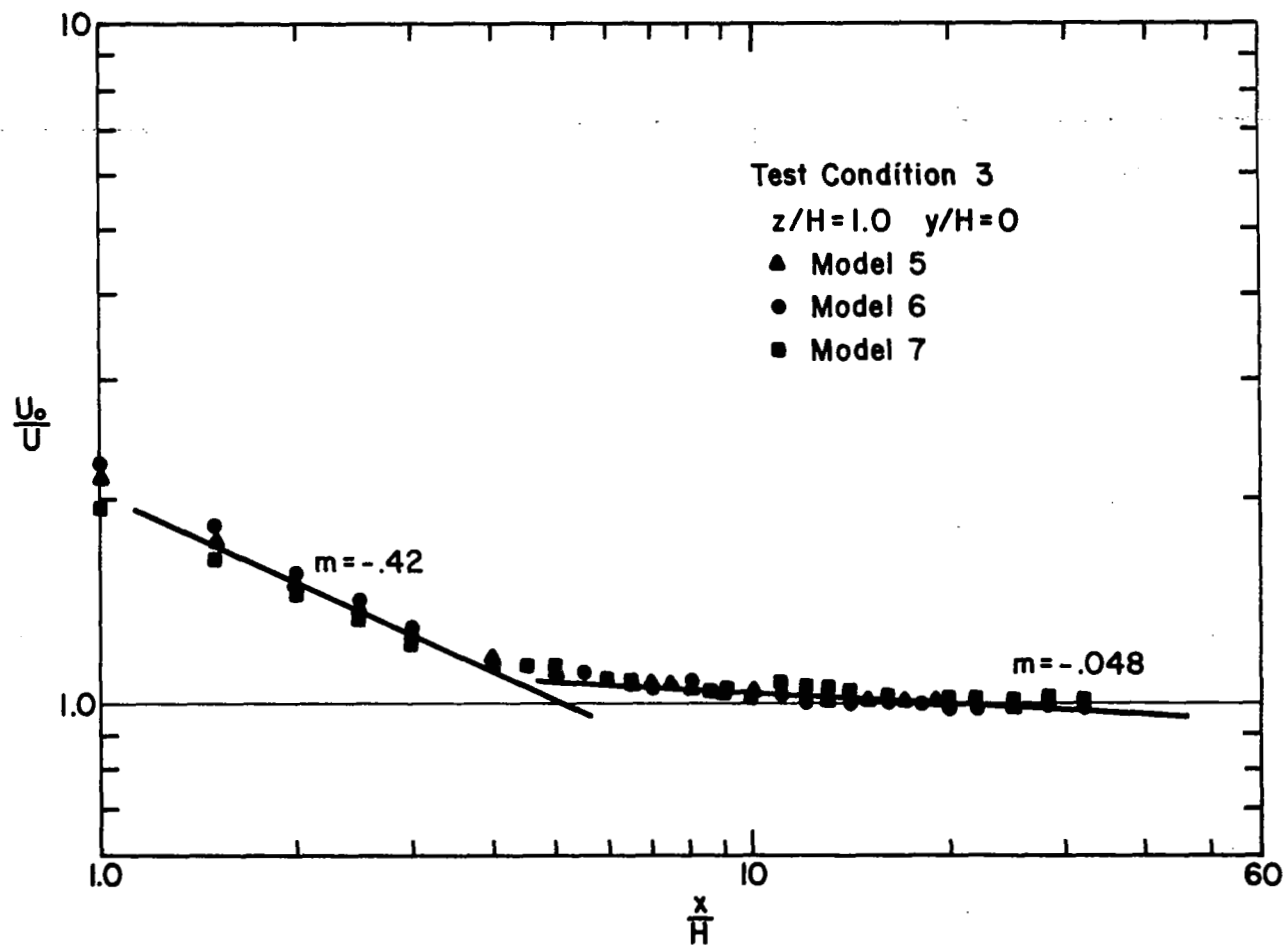
Figure 92. Decay of the Ratio U_o/U along the Centerline
(Test Condition 3, models 5,6,7)
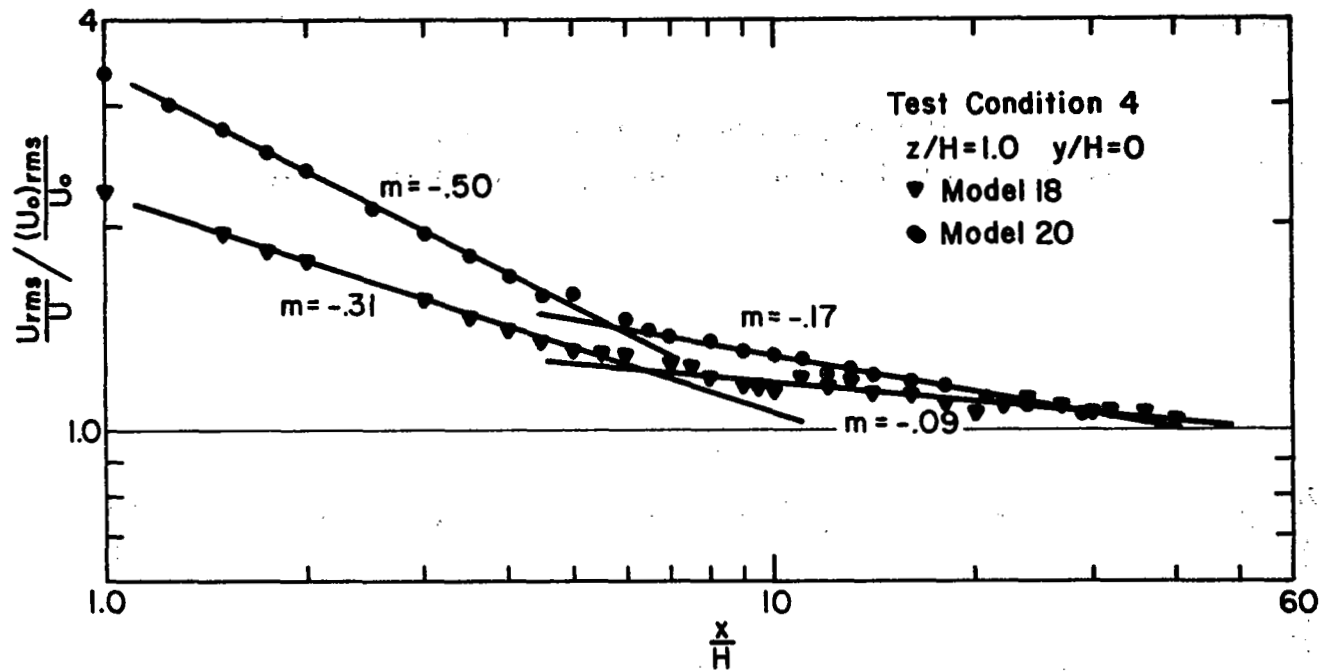
Figure 93. Decay of the Ratio $\dfrac{U_{rms}}{U}/\dfrac{(U_o)_{rms}}{U_o}$ along the Centerline
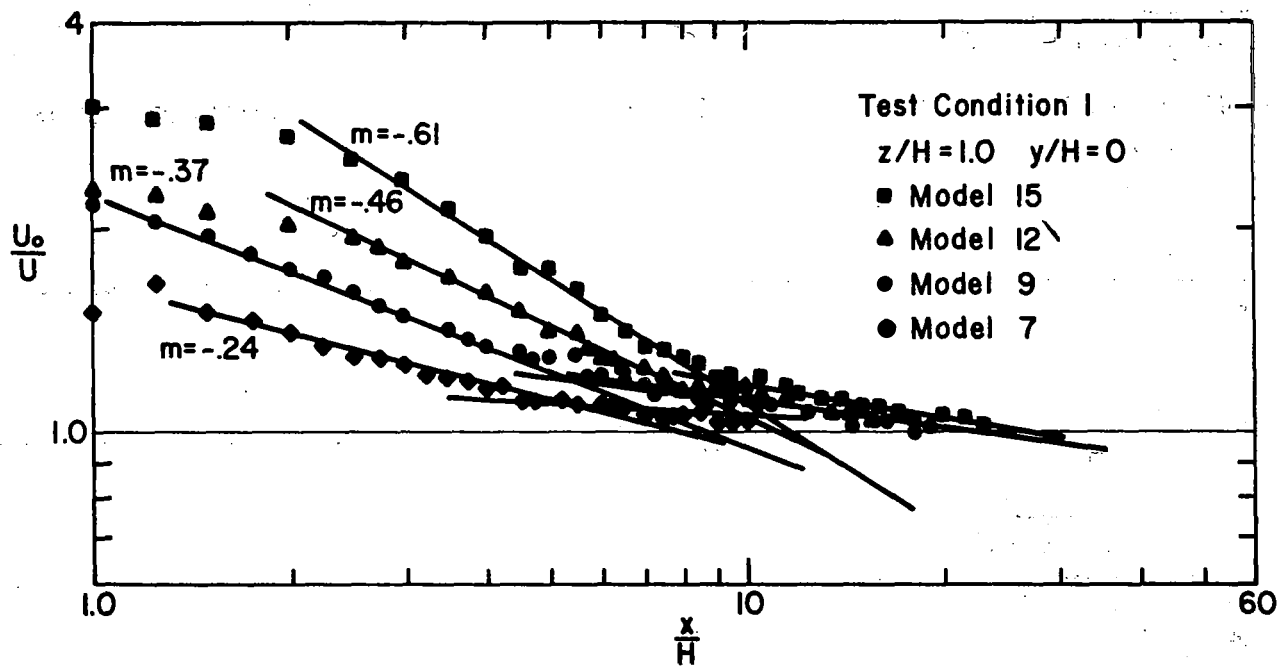
Test Condition 3, models 5,6,7)
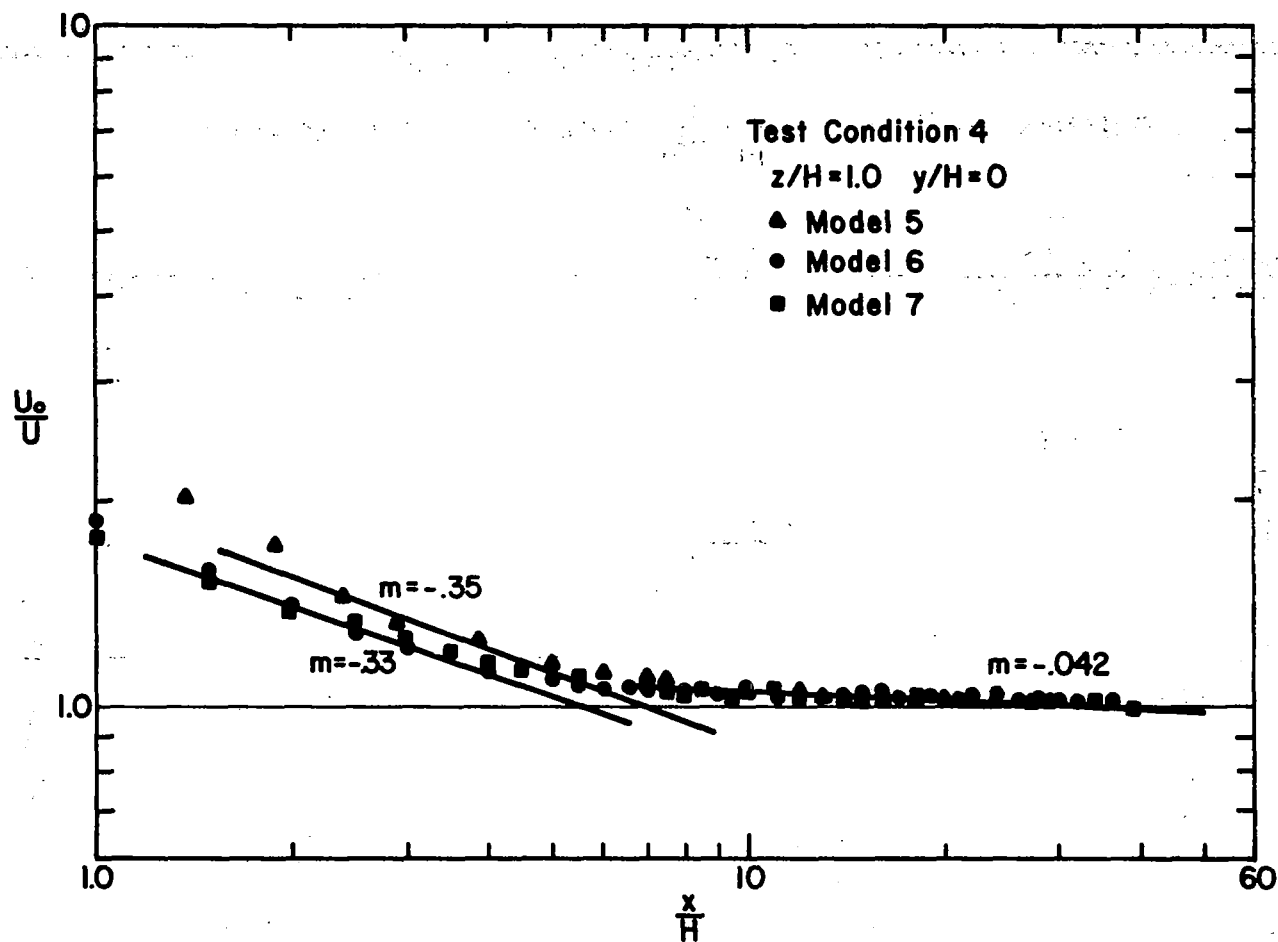
Figure 94. Decay of the Ratio U_o/U along the Centerline
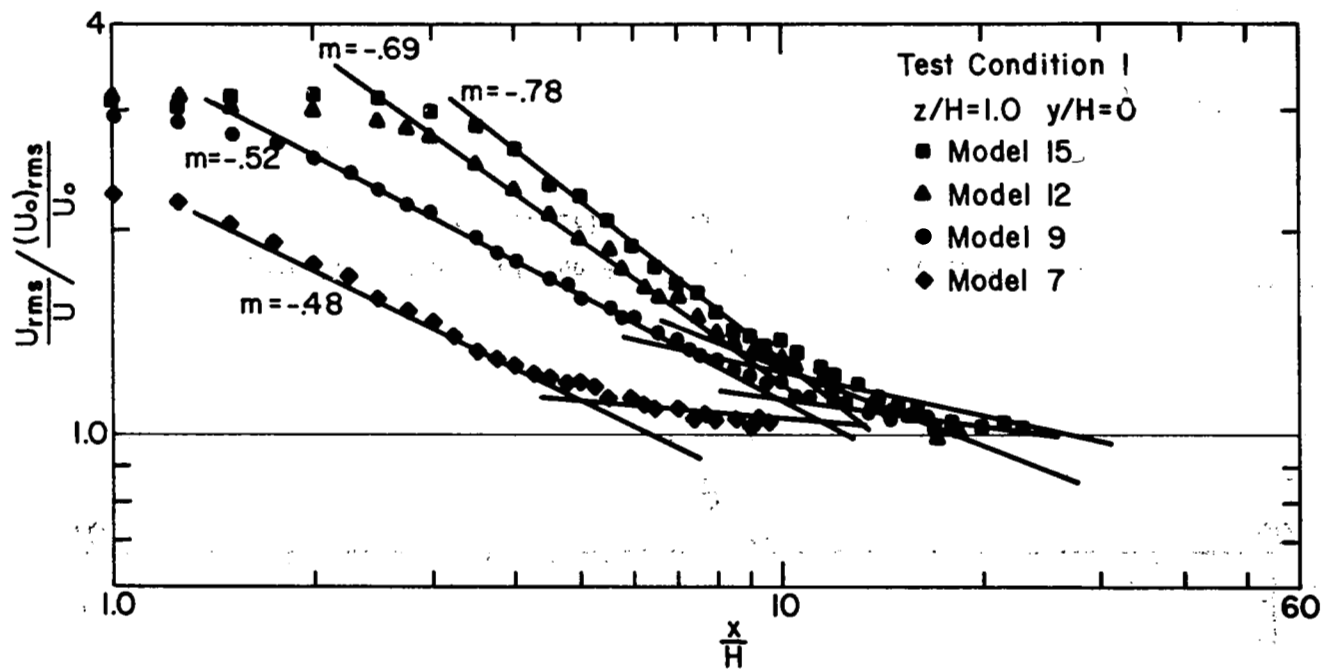(Test Condition 4, models 5,6,7)

Figure 95. Decay of the Ratio $\dfrac{U_{rms}}{U} / \dfrac{(U_o)_{rms}}{U_o}$ along the Centerline

(Test Condition 4, models 5,6,7)
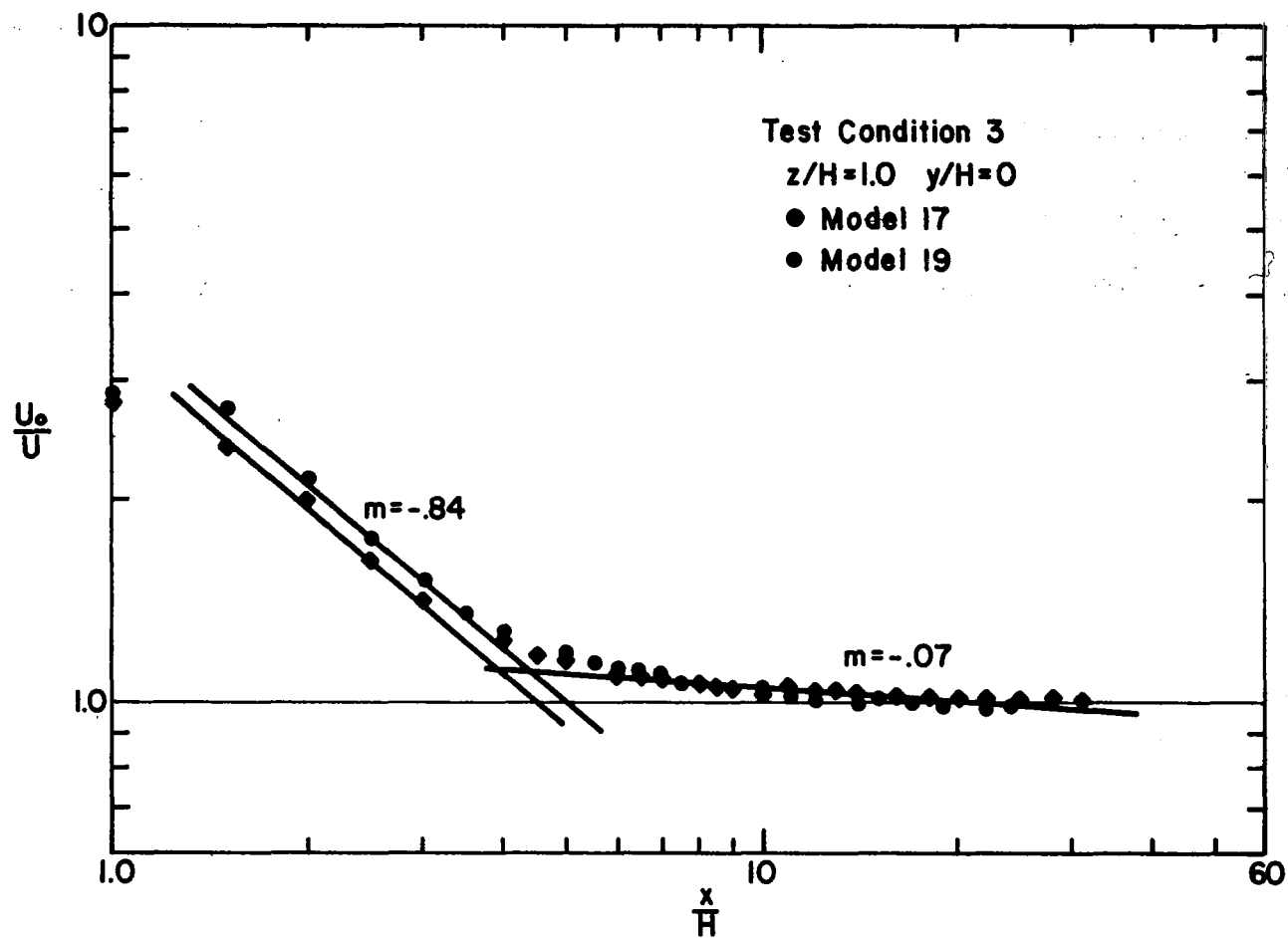
Figure 96.   Decay of the Ratio U_o/U along the Centerline
(Test Condition 3, models 17,19)

Figure 97. Decay of the Ratio $\dfrac{U_{rms}}{U} \Big/ \dfrac{(U_o)_{rms}}{U_o}$ along the Centerline

(Test Condition 3, models 17,19)
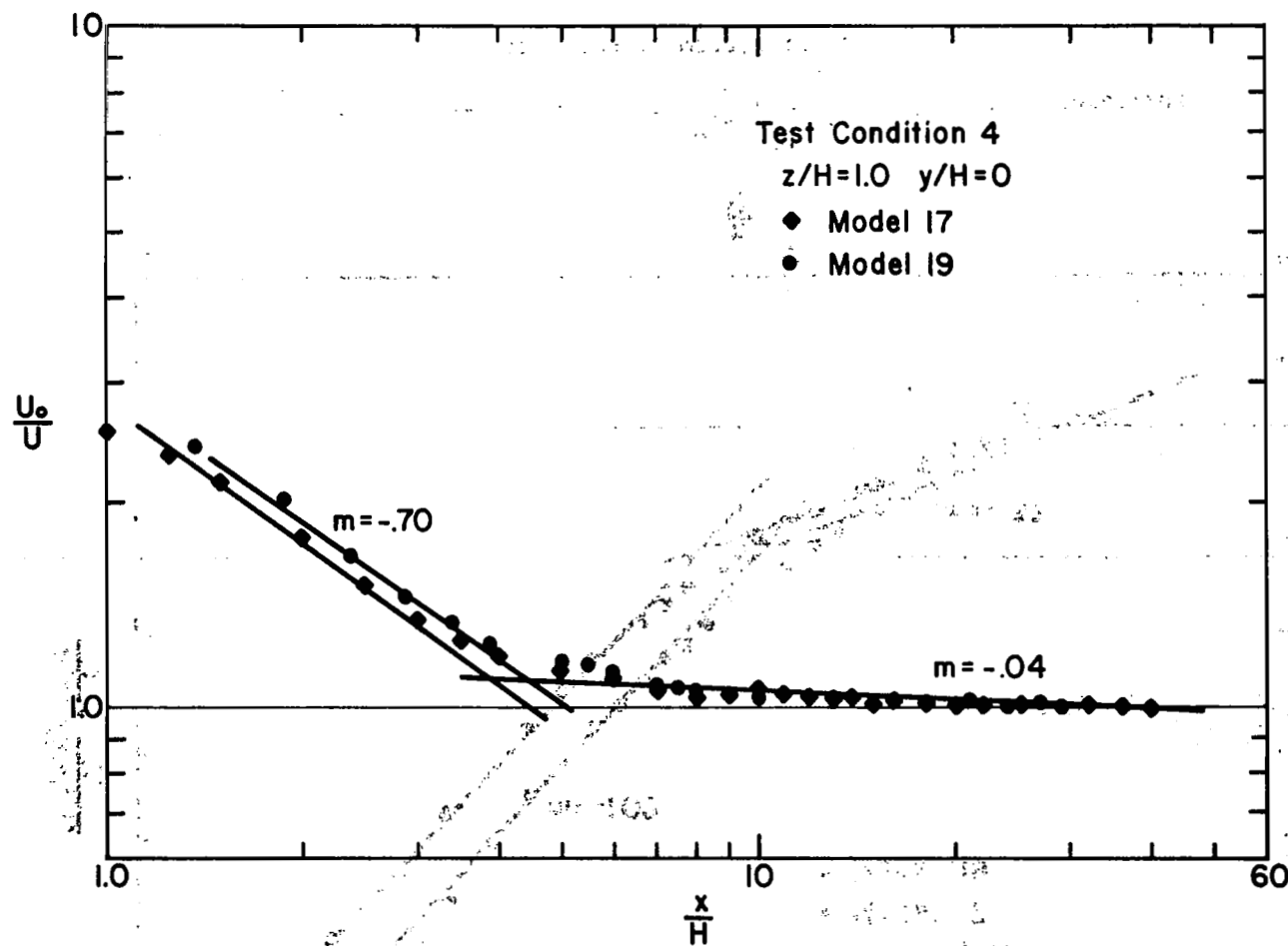
Figure 98. Decay of the Ratio U_o/U along the Centerline
(Test Condition 4, models 17,19)

Figure 99. Decay of the Ratio $\dfrac{U_{rms}}{U} \Big/ \dfrac{(U_o)_{rms}}{U_o}$ along the Centerline
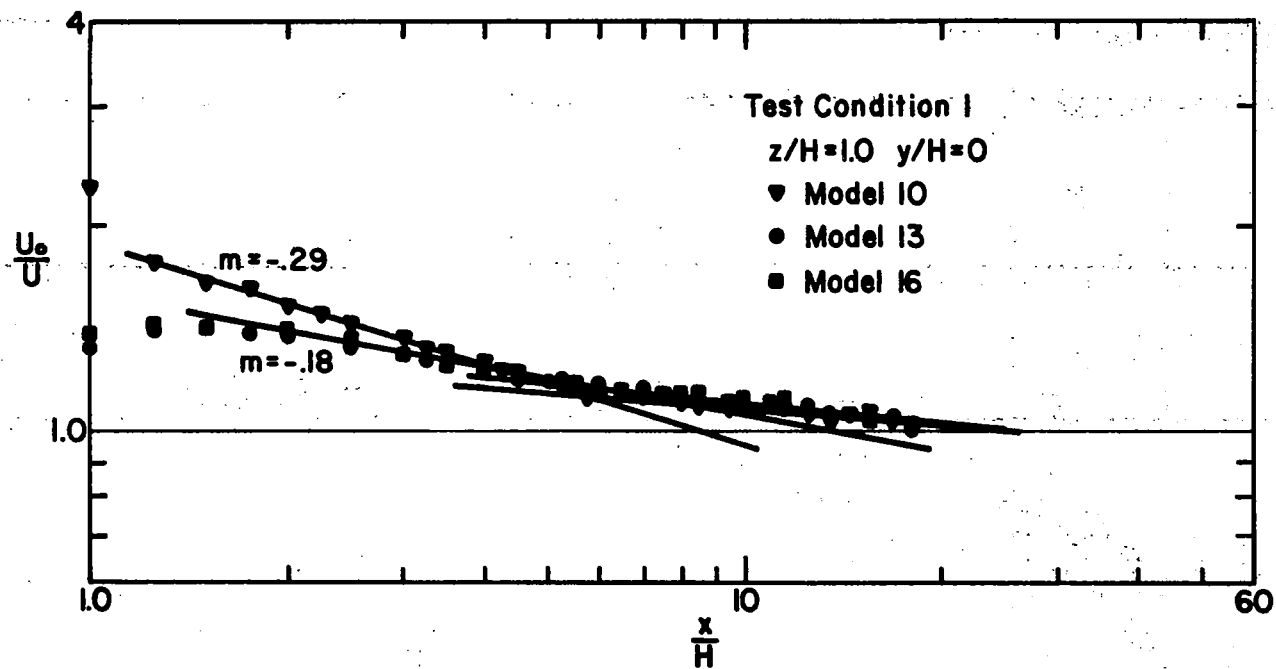
(Test Condition 4, models 17,19)

Figure 100. Decay of the Ratio U_o/U along the Centerline
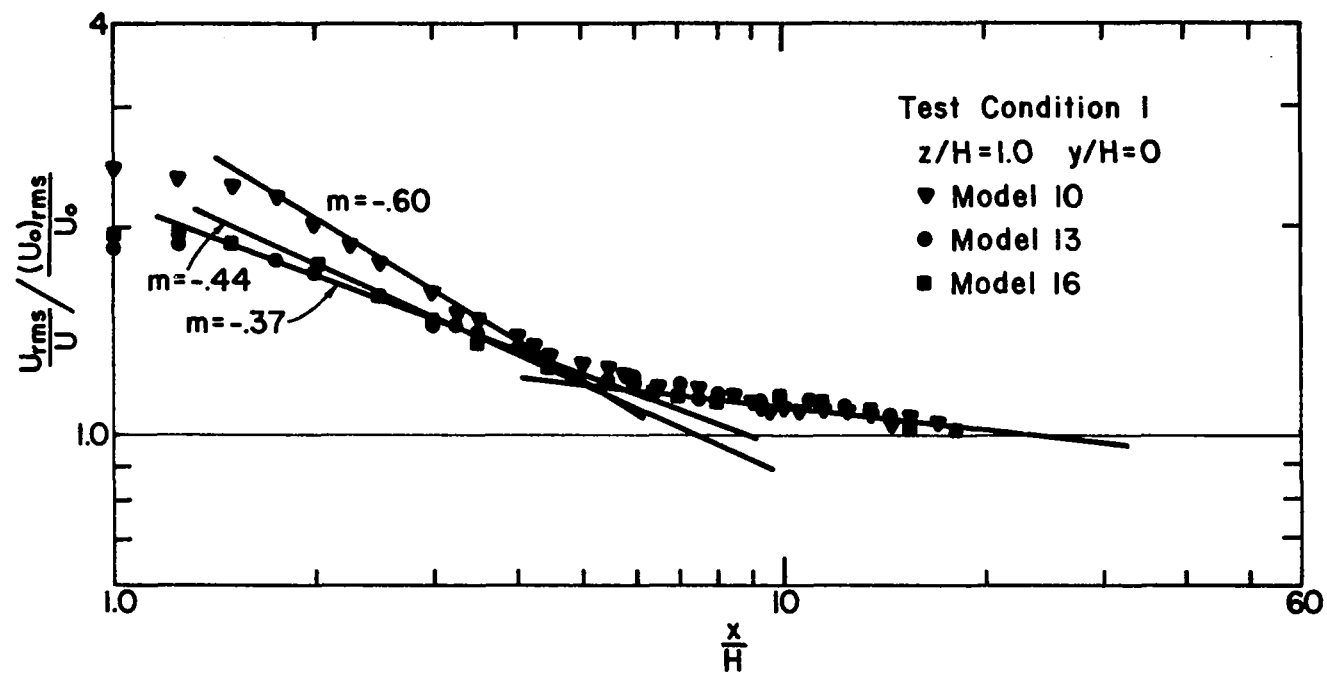(Test Condition 3, models 18,20)

Figure 101. Decay of the Ratio $\dfrac{U_{rms}}{U}\Big/\dfrac{(U_o)_{rms}}{U_o}$ along the Centerline
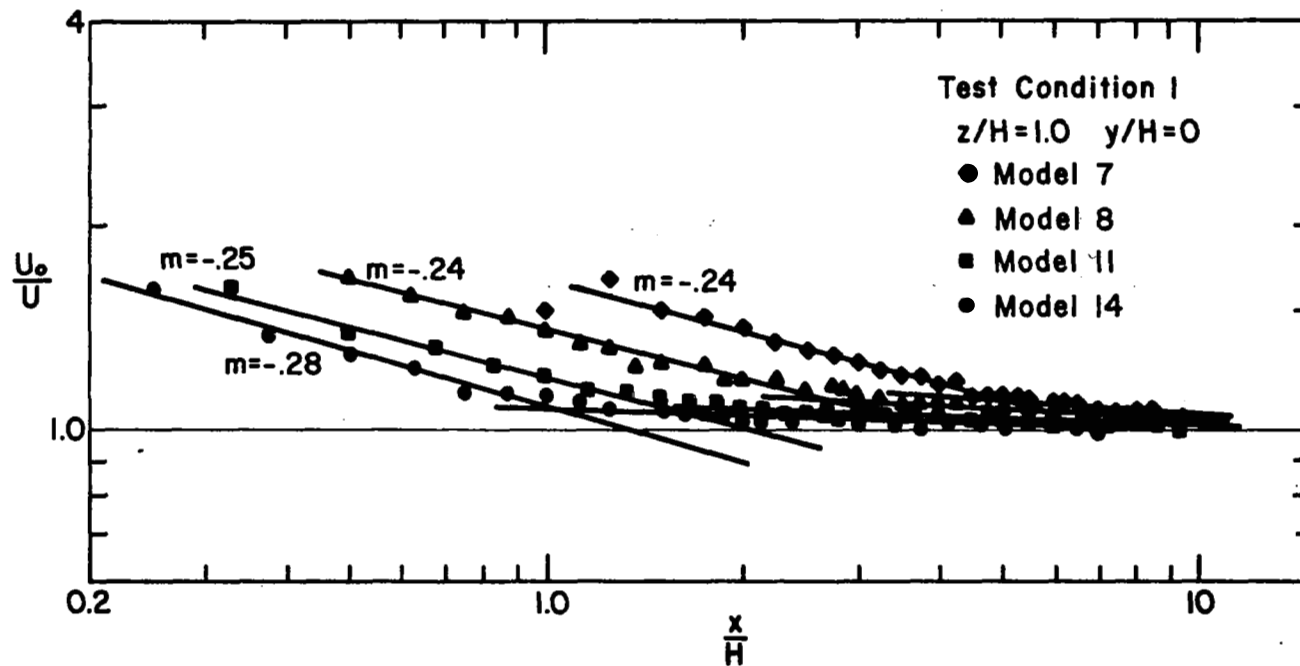(Test Condition 3, models 18,20)

Figure 102.   Decay of the Ratio U_o/U along the Centerline
(Test Condition 4, models 18,20)

Figure 103. Decay of the Ratio $\dfrac{U_{rms}}{U} / \dfrac{(U_o)_{rms}}{U_o}$ along the Centerline

(Test Condition 4, models 18,20)

Figure 104. Decay of the Ratio U_o/U along the Centerline
(Test Condition 1, models 15,12,9,7)

Figure 105. Decay of the Ratio $\dfrac{U_{rms}}{U}/\dfrac{(U_o)_{rms}}{U_o}$ along the Centerline

(Test Condition 1, models 15,12,9,7)

Figure 106. Decay of the Ratio U_o/U along the Centerline
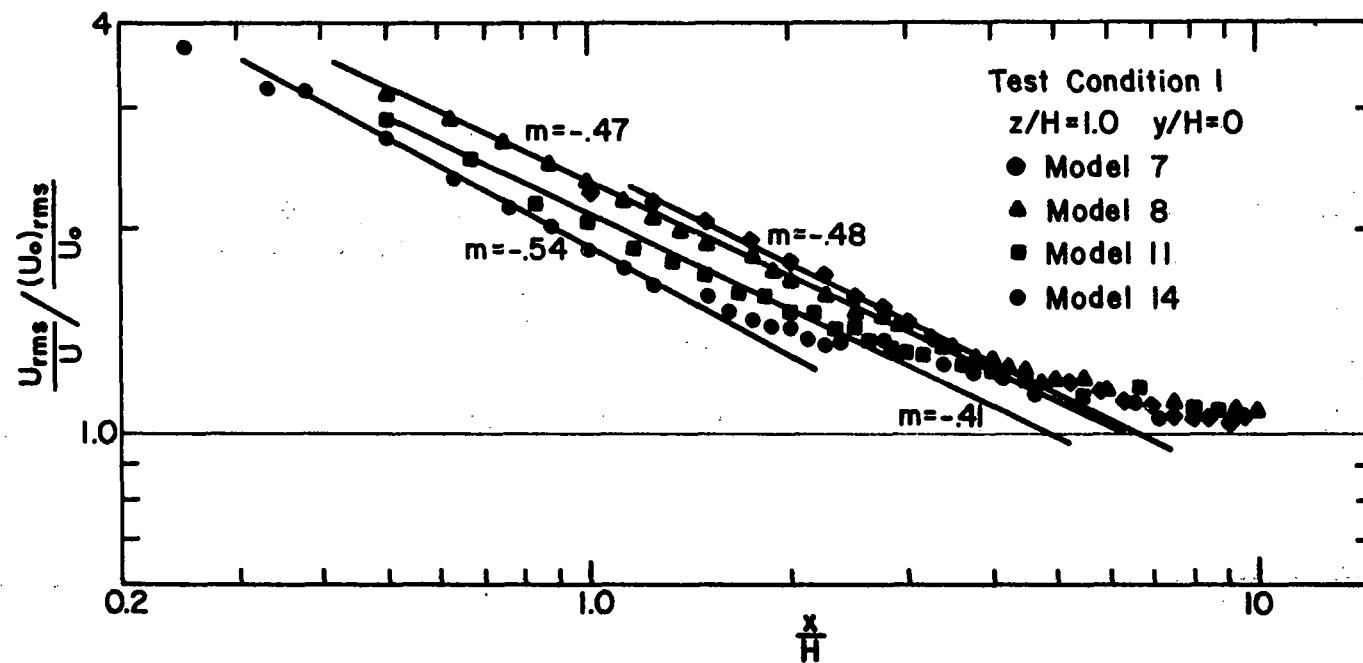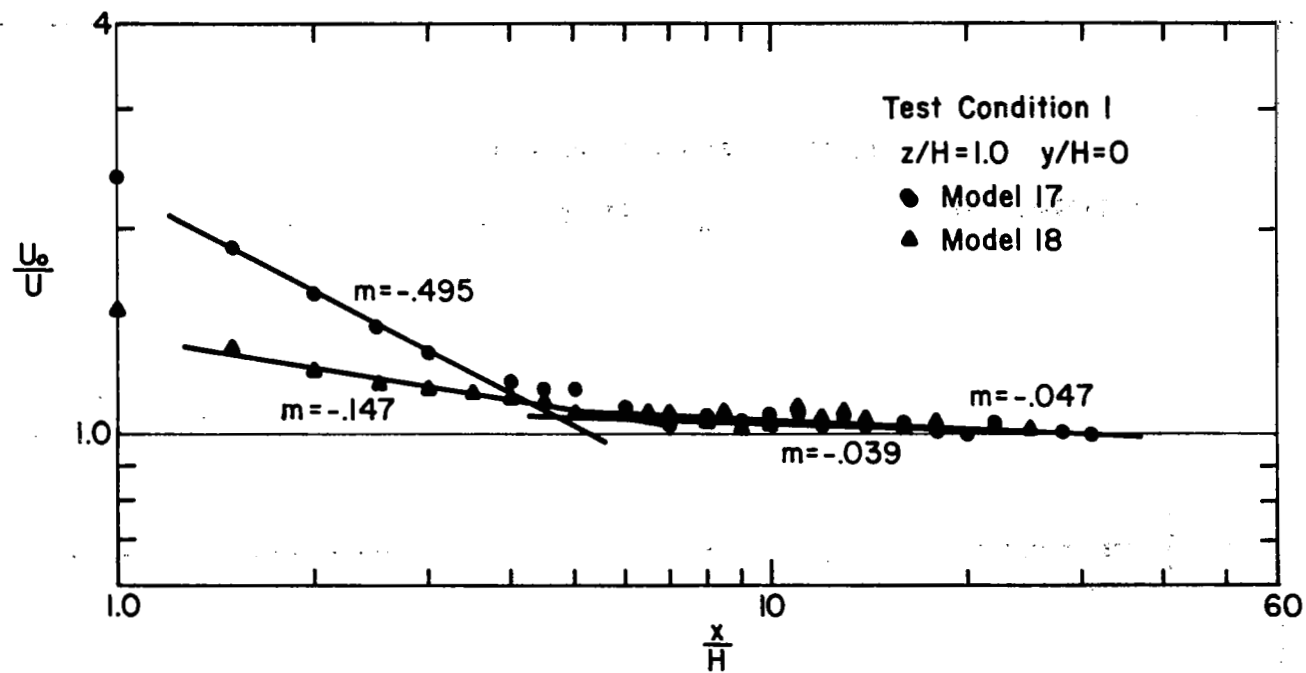(Test Condition 1, models 10,13,16)

Figure 107.   Decay of the Ratio $\dfrac{U_{rms}}{U} / \dfrac{(U_o)_{rms}}{U_o}$ along the Centerline

(Test Condition 1, models 10,13,16)

Figure 108. Decay of the Ratio U_o/U along the Centerline
(Test Condition 1, models 7,8,11,14)

Figure 109. Decay of the Ratio $\dfrac{U_{rms}}{U} \bigg/ \dfrac{(U_o)_{rms}}{U_o}$ along the Centerline

(Test Condition 1, models 7,8,11,14)

Figure 110. Decay of the Ratio U_o/U along the Centerline
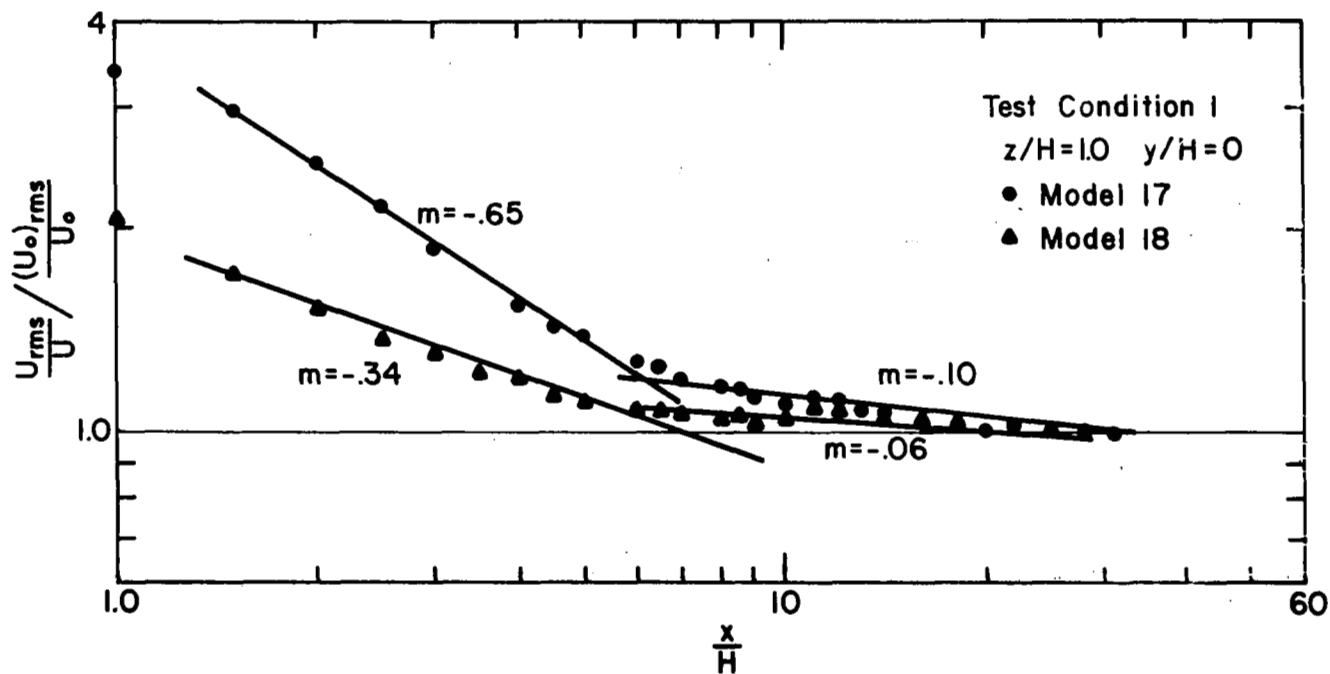(Test Condition 1, models 17,18)

Figure 111. Decay of the Ratio $\dfrac{U_{rms}}{U} \Big/ \dfrac{(U_o)_{rms}}{U_o}$ along the Centerline
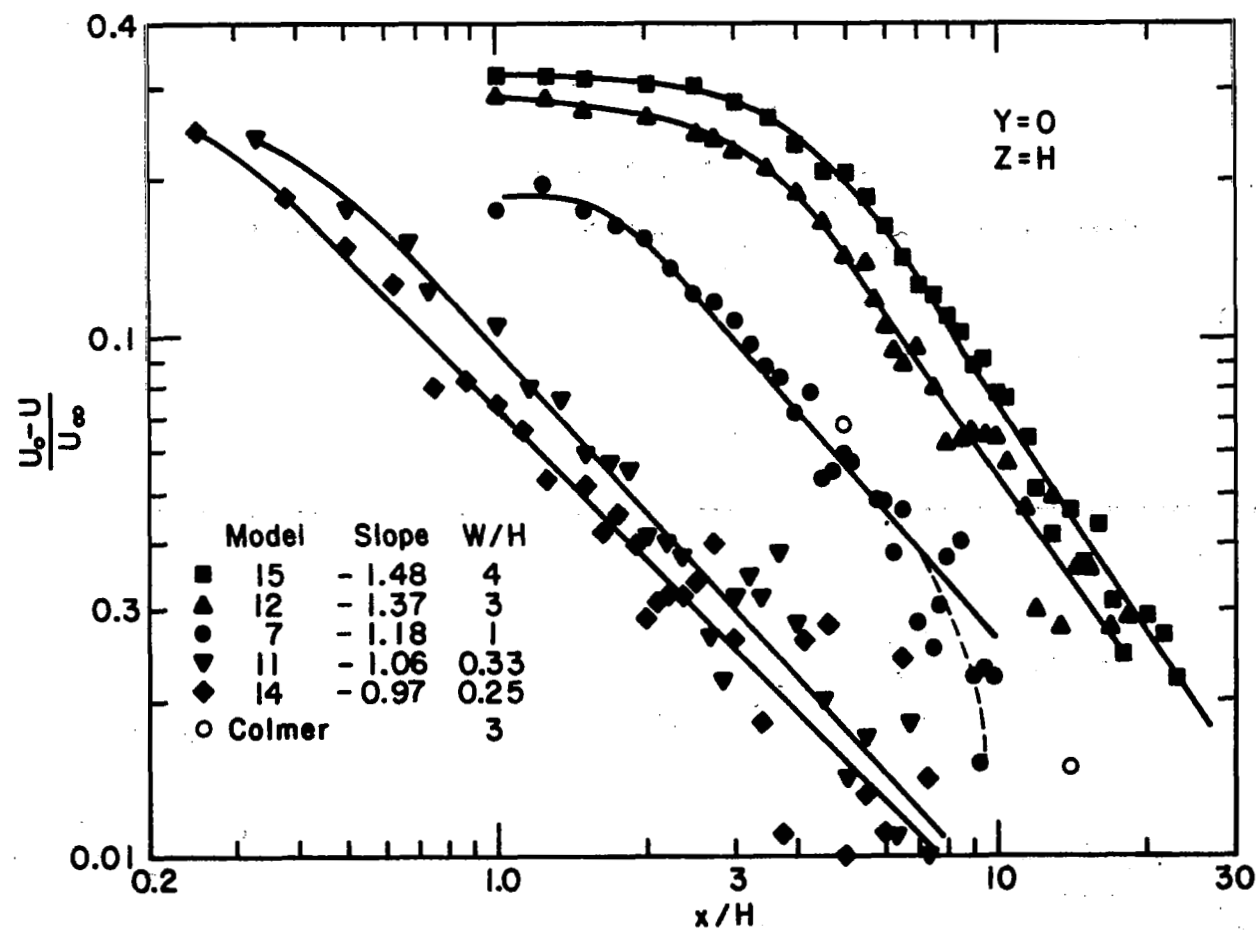
(Test Condition 1, models 17, 18)

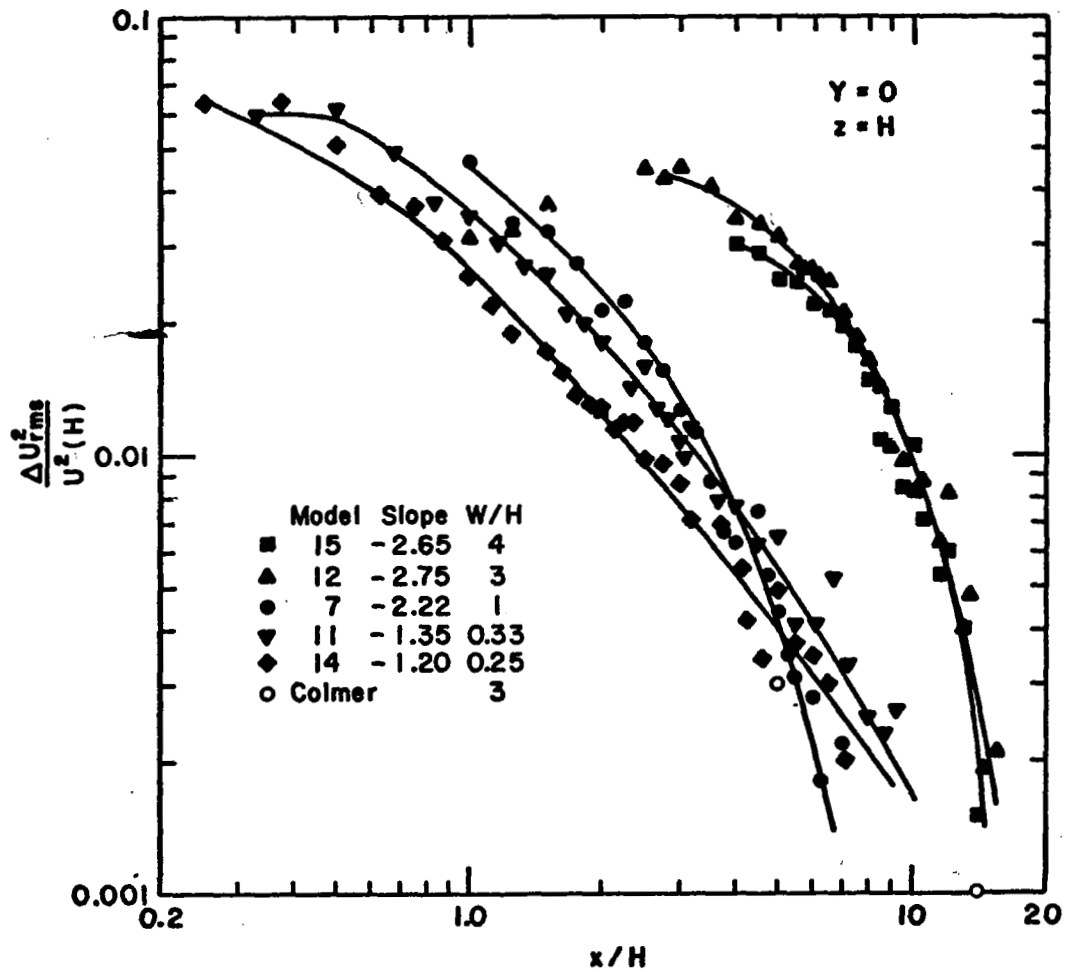Figure 112. Decay of Mean Velocity Defect in the Wake of Several Buildings

Figure 113. Decay of Turbulence Intensity Excess in the Wake of
Several Buildings